Optimal Lifting Surfaces

Including Endplates, Ground Effect & Thickness

David William Fin Standingford, B.Sc (Hons) (Adelaide)

Thesis submitted for the degree of

Doctor of Philosophy

in

Applied Mathematics

at

The University of Adelaide

(Faculty of Mathematical and Computer Sciences)

Department of Applied Mathematics

July 25, 1997

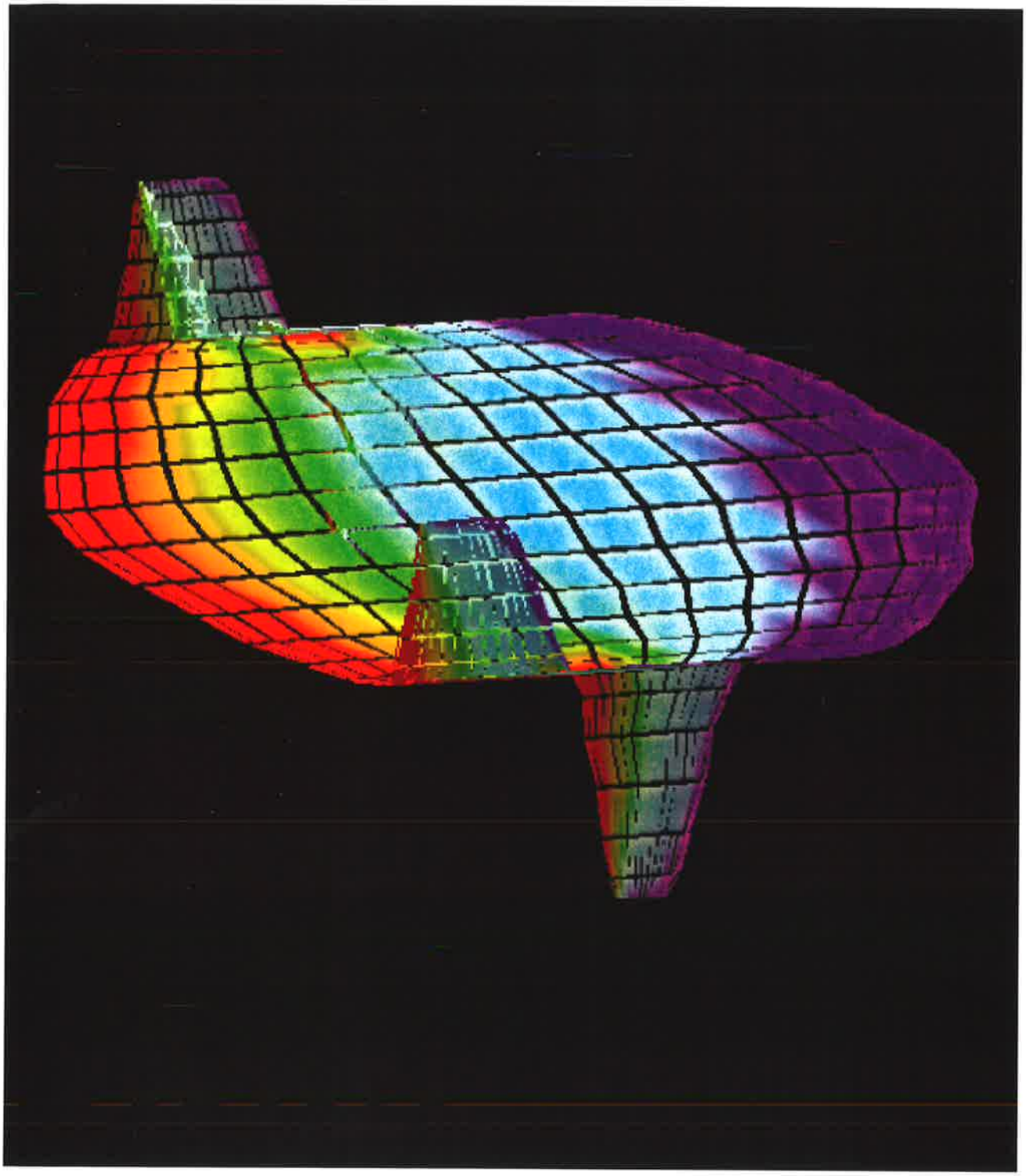

Contents

Abstract x

Signed Statement xi

Acknowledgements xii

Introduction 1

Nomenclature 3

1 Lifting Surfaces 6

1.1 Introduction 6

1.2 Quantities of Interest 8

1.3 Existing Numerical Schemes 8

1.3.1 The Vortex Lattice Method 9

1.3.2 The Airfoil Equation 10

1.3.3 Stark's Scheme 11

1.3.4 Lan's Quasi-Continuous Method 11

1.3.5 Three Dimensionality 13

1.3.6 Spanwise Modifications 15

1.3.7 Spatial Mapping 16

1.3.8 The Panel Method of Tuck 16

1.4 Improved Panel Method 17

1.4.1 Subpanelisation 19

1.4.2 Subpanels in Three-Dimensions 23

1.4.3 Direct Inclusion of Singularity 23

1.4.4 Direct Inclusion in Three-Dimensions 25

1.5 Curved Panels 26

1.6 Results for a Square Wing 29
1.6.1 Lift Coefficient 30
1.6.2 Spanwise Circulation 30
1.6.3 Pointwise Loading 31
1.6.4 Leading-Edge Singularity Strength 33
1.7 Non-Rectangular Planforms 34
1.8 Results for a Circular Wing 35
1.8.1 Lift Coefficient 36
1.8.2 Circulation 38
1.8.3 Pointwise Loading 39
1.8.4 Leading-Edge Singularity Strength 44
1.9 Conclusion 46

2 Suction and Induced Drag **48**
2.1 Induced Drag 48
2.2 Minimum Induced Drag 50
2.3 Evaluation of Induced Drag 51
2.4 Leading-Edge Suction 53
2.5 Results 54
2.6 Discussion 55

3 Endplates **58**
3.1 Introduction 58
3.2 Endplates and Winglets 60
3.3 Design Considerations 62
3.4 Mathematical Formulation 62
3.4.1 Numerical Experience 63
3.5 Optimisation 64
3.6 Optimisation with respect to Total Area 66
3.6.1 Asymptotic Results 67
3.6.2 Optimal Rectangular Endplates 69
3.7 Other Degrees of Freedom 72
3.7.1 Horizontal Offset 72
3.7.2 Flare 74

3.8 More Realistic Optimisation 76
3.8.1 Quasi-Linear Object Function 76
3.8.2 The Search Space 77
3.8.3 Optimal Endplate Angle of Attack 78
3.8.4 Optimal Location 79

4 Ground Effect **84**
4.1 Introduction 84
4.1.1 Classes of Ground Effect 85
4.2 Ekranoplans 86
4.3 Present Formulation 89
4.4 Results for a Rigid Ground Plane 91
4.4.1 Endplates Below the Wing 93
4.4.2 Aspect Ratio Effects 94
4.5 Optimal Placement of Endplates 95
4.5.1 Endplates Above and Below the Wing 96
4.6 Optimal Dimensions 97
4.7 Multiple Wing Configuration 99
4.8 Pitch Stability 103

5 Wave Drag **108**
5.1 Introduction 108
5.2 Three-Dimensional Formulation 109
5.2.1 Hydrodynamic Pressure Due to an Airborne Wing 110
5.2.2 Work Done by a Moving Pressure Distribution 111
5.2.3 Numerical Evaluation of Integral 111
5.2.4 Variation of Wave Drag with Velocity 113
5.3 Pressure Footprints of Wings in Ground Effect 114
5.3.1 Bare Wing 115
5.3.2 Aspect Ratio Effects 116
5.3.3 Wing with Skirts 118
5.4 Wave Drag Versus Aerodynamic Drag 119
5.4.1 Two-Dimensional Airflow 119
5.4.2 Two-Dimensional Wave Drag 121

5.4.3 Magnitude of Three-Dimensional Wave Drag 124

6 Thickness **127**

6.1 Introduction 127

6.2 Suction and Induced Drag 128

6.3 Mathematical Formulation 129

6.4 Single Wing with Endplates 132

6.4.1 Wing with Zero-Thickness Endplates in Free Air 132

6.4.2 Flat-Plate Wing with Thick Endplates 134

6.5 Wing Thickness in Ground Effect 135

6.5.1 Bare Wing 137

6.5.2 Wing with Flat Endplates 137

6.6 Multiple Body Flight Configuration 138

6.6.1 Horizontal Offset 139

6.6.2 Vertical Separation 140

7 Optimization **145**

7.1 Introduction 145

7.1.1 Finite Geometric Representation 146

7.1.2 Grid-Scale Oscillation 147

7.2 A Simple Genetic Algorithm 147

7.2.1 Optimal Wing Planform 149

7.2.2 Optimal Endplate 150

7.2.3 Full Wing-Endplate Optimisation 153

7.3 Conclusion 156

Bibliography **164**

List of Tables

1.1 Corrected matrix A_{ij} 24

1.2 Correction matrix E_{ij} 24

1.3 Relative magnitude of correction matrix E_{ij}/A_{ij} 25

1.4 Lift and moment-slope coefficients for a circular wing 38

1.5 Estimates for the spanwise circulation near the wingtip 39

3.1 Optimal endplate dimensions at fixed locations 72

4.1 Force coefficients for wing one alone 101

4.2 Force coefficients for wing two alone 101

4.3 Force coefficients for wings one and two combined 102

6.1 Downforce compared with one-dimensional analysis 137

List of Figures

1.1 General planar lifting surface 7
1.2 Stark's lattice arrangement 12
1.3 Lan's lattice arrangement 12
1.4 Three-dimensional lattice strip-theory 14
1.5 Spanwise scheme of F. R. DeJarnette 15
1.6 The panel method of E. O. Tuck 18
1.7 Two-dimensional leading-edge correction 20
1.8 Chordwise subpanelisation of a planar wing 21
1.9 Improvement in two-dimensional results by subpanelling 22
1.10 Effect of three-dimensional kernel correction 26
1.11 Rectangular panelisation of a circle 27
1.12 The curved panel method of Lazauskas 28
1.13 Results for a square wing: lift coefficient 30
1.14 Results for a square wing: spanwise circulation 31
1.15 The loading of a square planar wing in free air 32
1.16 Results for a square wing: vortex lattices 33
1.17 Results for a square wing: panel methods 34
1.18 Results for a square wing: leading-edge singularity strength 35
1.19 Oscillatory data for circular wing lift coefficient 37
1.20 Results for a circular wing: lift coefficient 37
1.21 Results for a circular wing: vortex lattices 40
1.22 Results for a circular wing: panel methods 41
1.23 Error propagation from the wingtip 42
1.24 Error propagation removed from the wingtip 43
1.25 Increasing spanwise subpanels changes estimate of singularity strength . . 44
1.26 Changing spanwise collocation alters suction prediction 45

1.27 Extrapolated prediction of suction for circular wing 46

2.1 Wingtip vortices in the clouds 49
2.2 Forces on rectangular wings 55
2.3 Forces on elliptic wings 56
2.4 Forces on delta wings 56
2.5 Relative force errors 57

3.1 Tip sails used to generate thrust from the wingtip vortex flow 59
3.2 Popular winglet design 61
3.3 The loading of a square wing with endplates in free air 65
3.4 Square wing with rectangular endplates 66
3.5 Lift of rectangular wings with endplates of varying height 67
3.6 Lift of a square wing with endplates of varying height and length 68
3.7 Lift coefficient versus endplate location 70
3.8 Lift coefficient versus endplate dimensions 71
3.9 Endplate with independent lower and upper sections 73
3.10 Lift coefficient versus horizontal offset 74
3.11 Upper and lower endplate sections flared to increase lift 75
3.12 Lift versus flare ratio 76
3.13 Variation of linear friction with Reynolds number 78
3.14 Flow parameter function of friction and angle of attack 79
3.15 Effect of flow parameter on optimal endplate angle of attack 80
3.16 Variation in optimal endplate streamwise location with flow parameter . 81
3.17 Variation of force components with streamwise offset 82
3.18 Variation in optimal endplate vertical location with flow parameter . . . 83

4.1 Comparison of the Airfisch 3 with a swan taking off 86
4.2 The Russian "Orlyonok" ekranoplan 87
4.3 The RADACorp C–850 88
4.4 The proposed *Wingship* "Hoverplane" 89
4.5 Variation of lift and drag for a bare wing in ground effect 93
4.6 The wing and ground loading of a bare wing in ground effect 94
4.7 The wing and ground loading of a square wing with full skirts 95
4.8 Lift and drag coefficients for a square wing with endplates 96

4.9 Aspect ratio effects with and without endplates 97
4.10 Optimal endplate horizontal offset in ground effect 98
4.11 Increase in lift due to endplates above as well as below the wing 99
4.12 Optimal geometry as a function of altitude 100
4.13 The form of the optimal geometry below critical altitude 102
4.14 The tandem-wing design of the Jörg TAF VIII 104
4.15 The Taiwanese Chung-Shan tandem-wing transport vehicle 105
4.16 Straight and level flight in ground effect 106
4.17 Passive stability of a three-surface configuration 106
4.18 Loading of a three-surface configuration in ground effect 107

5.1 Gaussian pressure distribution on the water surface 113
5.2 Erroneous wave-drag integrand for Gaussian distribution 114
5.3 Corrected wave-drag integrand for Gaussian distribution 115
5.4 Angle of wave energy propagation versus velocity 116
5.5 Wave drag versus free stream velocity for a Gaussian peak 117
5.6 Pressure on water due to a bare wing 118
5.7 Wave energy spectrum for bare square wing 119
5.8 Close-up of numerical wave energy spectrum near $\theta = \pi/2$ 120
5.9 Pressure footprint of a wing with aspect ratio 10 121
5.10 Wave drag versus span for a rectangular wing 122
5.11 Pressure on water due to a wing with skirts 123
5.12 Two-dimensional wave resistance function 125

6.1 Wing-endplate combination plus image 129
6.2 Thickness distributions for NACA 4-digit wing sections 132
6.3 Lift due to wing thickness and vertically offset endplates 133
6.4 Lift due to wing angle of attack and thickness with offset endplates . . . 135
6.5 Lift due to endplate thickness 136
6.6 Lift versus altitude for a thick square wing in ground effect 138
6.7 Lift due to thickness in ground effect 139
6.8 Two planar wings in proximity 140
6.9 Multiple body efficiency versus horizontal offset 141
6.10 Individual efficiency for wing number 1 versus horizontal offset 142

6.11 Individual efficiency for wing number 2 versus horizontal offset 143
6.12 Combined efficiency versus vertical offset 144

7.1 Grid-scale oscillations in the object function 148
7.2 The rate of convergence versus the generation gap 150
7.3 The optimal wing with aspect ratio 1 151
7.4 The convergence for a horizontally centered endplate 152
7.5 The convergence of individual genes 153
7.6 The optimal centered endplate for a unit wing 154
7.7 Optimal wing-endplate configuration for a flow parameter of 0.1 156
7.8 Optimal wing-endplate configuration for a flow parameter of 0.2 157
7.9 Optimal wing-endplate configuration for a flow parameter of 0.5 158
7.10 Optimal wing-endplate configuration for a flow parameter of 1 159
7.11 Optimal wing-endplate configuration for a flow parameter of 2 160
7.12 Optimal wing-endplate configuration for a flow parameter of 5 161
7.13 Optimal wing-endplate configuration for a flow parameter of 10 162
7.14 The optimal lifting surface configuration 163

Abstract

The design of optimal lifting surface configurations requires a capacity to quickly evaluate derived quantities such as lift and drag of a given lifting surface and an algorithm for improving the geometry based on these quantities. The piecewise-constant vorticity method of Tuck (1993) for solution of the lifting-surface integral equation accurately determines integrated quantities such as the lift produced by planar lifting surfaces. We introduce a modification to this method whereby the accuracy in prediction of local quantities such as the leading-edge singularity strength is dramatically increased for little extra computational effort. Consequently, the leading-edge suction force, and hence the induced drag, may also be calculated accurately. A discussion of endplates and the optimisation of the lift-to-drag ratio for endplates on a given wing leads to the more general problem of the maximization of lift with respect to frictional and induced drag of a lifting surface in ground effect with finite endplates. We also present a discussion of the wave-induced drag when an aerodynamic body flies in proximity to a water surface, and introduce leading-order thickness effects to the aerodynamic analysis program. Finally, we use a genetic algorithm to search a restricted design space of wing-endplate combinations for a range of operational conditions, with the aim of illustrating the change in optimal geometry as we penalise a varying combination of skin-friction and induced drag.

Signed Statement

This work contains no material which has been accepted for the award of any other degree or diploma in any university or other tertiary institution and, to the best of my knowledge and belief, contains no material previously published or written by another person, except where due reference has been made in the text.

I consent to this copy of my thesis, when deposited in the University Library, being available for loan and photocopying.

SIGNED: ..... DATE: 29/7/1997

Acknowledgements

I wish to thank my supervisor, Professor Ernie Tuck for his expertise and enthusiasm for the research work presented in this thesis, as well as the numerous discussions of hydrodynamics and aerodynamics along the way.

I would also like to acknowledge the many useful conversations with Dr. Whye Teong Ang, who visited the department in the early stages of this research. Thanks also to Professor Touvia Miloh, who also visited the department in 1993, during which time many of the issues considered in the first chapter were clarified.

Thanks to Mr. David Beard for his willingness to assist with all computing matters. Many of the numerical results presented in this thesis would not have appeared without Dr. Francis Vaughan, whose management of supercomputing facilities included both a *Thinking Machines* Connection Machine (CM5) and a *Silicon Graphics* Power Challenge. Many sections of this thesis were the result of close work with Mr. Leo Lazauskas, whose knowledge of aerodynamics and the wider fluid dynamics literature have been a great help. I would also like to thank the many people who formed the research group in aerodynamics and hydrodynamics in the Applied Mathematics Department at the University of Adelaide over the period of research, including in particular Mr. David Scullen and Miss Yvonne Stokes.

Thanks also to Miss Deborah Brown, for her help with the optimisation section of this thesis and in particular for her expertise in using genetic algorithms.

I would like to acknowledge useful discussions with Mr. Chris Holloway of RADACorp, whose practical knowledge of ekranoplan design motivated a number of the later sections in this thesis.

I would like to acknowledge the support throughout my candidature of a University of Adelaide Scholarship and an Australian Research Council Scholarship.

Finally, I wish to thank the staff and students of the Departments of Statistics, Pure and Applied Mathematics for friendship and support throughout.

Introduction

The design of optimal lifting surfaces requires the capacity to quickly evaluate the derived quantities such as lift and drag of a given lifting configuration and an algorithm for improving the geometry based on these quantities.

The task of calculating the aerodynamic load distribution on a thin three-dimensional lifting surface or wing of finite aspect ratio at small angle of attack presents difficulties for most numerical methods. The two-dimensional lifting-surface integral equation that must be solved is highly singular, and does not possess analytic solutions, even for simple planform geometries such as rectangles or ellipses. In Chapter 1, we compare some methods that have been used successfully to determine accurate pointwise and integrated loadings, and discuss the underlying numerics. Particular attention is paid to the singularities that occur at the leading edge (LE) and at the tips of finite lifting surfaces, and to the rate at which the results provided by the numerical methods converge to their asymptotic limits. In particular, the constant-vorticity rectangular-panel method of Tuck (1993) has been modified to improve the resolution of the LE singularity. A correction procedure is devised incorporating the inverse-square vorticity variation near the LE, thereby enabling accurate determination of the LE singularity strengths and spanwise loading distributions as functions of the spanwise co-ordinate. The LE singularity strength is important in some applications, such as for induced drag and trailing tip vortices in wing aerodynamics, and (in an equivalent hydrodynamic context) for estimation of the size of the LE splash jet created by a planing surface. In particular, we pay attention to post-processing induced-drag computation, both via a Trefftz-plane method and separately via direct pressure integration. Accurate reconciliation between these two procedures is possible only if the LE suction force, which is proportional to the spanwise integral of the square of the LE singularity strength, is known to adequate accuracy. In Chapter 2, we consider the numerical evaluation of the induced drag for an arbitrary three-dimensional

lifting geometry.

In Chapter 3, we present a discussion of the effect of the addition of endplates to a bare wing in order to increase lift and decrease the induced drag. A limited optimisation of the lift to frictional drag ratio for rectangular endplates on a given wing then leads to the more general problem of the maximization of lift with respect to frictional and induced drag of a lifting surface with endplates.

In Chapter 4, we consider a range of effects that may be manifest when a lifting configuration flies in proximity to a fixed ground plane. In moderate ground effect, the lift is significantly higher than that for the free-air case and the addition of endplates provides a reduction of induced drag. Motivated by a demand for high efficiency wing-in-ground effect vehicles, or *ekranoplans*, we consider the addition of endplates to wings in ground effect and discuss the transition to ground effect in terms of the optimal geometry of a wing-endplate combination as a function of altitude.

In Chapter 5 we consider the additional hydrodynamic wave drag experienced by a lifting configuration flying over water. A numerical scheme is presented for calculating the propagation of wave energy after the evaluation of the aerodynamic forces.

To first order, the thickness effects of a planar wing may be decoupled from the lifting effects. This is not the case when endplates are used, or the wing is in proximity to another wing or the ground. In Chapter 6, the numerical scheme is modified to incorporate leading order thickness effects. We consider the additional forces due to thickness and compare the magnitude with the forces due to angle of attack, proximity to ground and the addition of endplates. We present a discussion and optimisation of the optimal flying configuration for a vertical stack of lifting surfaces with thickness.

Finally, in Chapter 7, we address optimisation issues for lifting surfaces based on the work presented in the preceding chapters. A genetic algorithm is used to optimise the planform of a bare wing and the wing-endplate geometry for a range of operational conditions.

Nomenclature

a	Horizontal offset or displacement
a_w	Wave amplitude
A_0	Wing area
A	Total area, wing plus endplates
A_{ij}	Influence coefficient
A_n	Fourier coefficient for $\Gamma(y)$
α_W	Angle of attack of wing
α_W^*	Optimal angle of attack of wing
α_P	Angle of attack of endplate
AR	Aspect ratio $= s^2/A$
b	Vertical offset or displacement
B	Wing planform
B_n	Fourier coefficient for $Q(y)$
c	Wing chord
C	Trace of trailing vortices in the Trefftz plane
C_{D_i}	Induced drag coefficient
$C_{D_i}^0$	Induced drag coefficient of an elliptically loaded surface
C_f	Coefficient of linear friction
C_L	Lift coefficient based on total area $= L/(\frac{1}{2}\rho U^2 A)$
C_L^0	Lift coefficient based on wing area $= L/(\frac{1}{2}\rho U^2 A_0)$
$-C_M$	Moment coefficient
C_S	Suction coefficient
D_f	Frictional drag
e	Oswald efficiency factor $= C_L^2/[\pi AR(C_{D_i} - C_{D_i}^0)]$
$f^{\pm}, f$	Camber functions

F_h	Froude number based on height $= \sqrt{\rho_A U^2/(\rho_W g h_0)}$
F_L	Froude number based on length $= \sqrt{U^2/(gc)}$
g	Gravitational acceleration
G	Singular potential for a vertical horseshoe vortex
G_1	Non-singular potential for a vertical horseshoe vortex
$\bar{G}$	Composite potential for a vertical horseshoe vortex $= G + G_1$
G_g	Generation gap $= N_p - N_c$
γ	Non-dimensional wave number $= F_L^{-2}$
$\Gamma(y)$	Spanwise lift distribution
h	Endplate height
h_0	Vertical gap between wing and ground or mean sea level
H_w	Water depth
H	Singular potential for a horizontal horseshoe vortex
H_1	Non-singular potential for a horizontal horseshoe vortex
$\bar{H}$	Composite velocity potential for a horizontal horseshoe vortex $= H + H_1$
K	Kernel function
κ	Dimensional wave number $= g/U^2$
ℓ	Endplate length
λ	Natural wavelength of water waves $= 2\pi U^2/g$
L	Lift
m	Number of chordwise panels
$m(x, y, z)$	Source strength distribution
m_g	Number of chordwise panels on the water surface
m_p	Number of chordwise panels on the endplate
m_s	Number of chordwise subpanels
M	Convergence exponent for m
μ	Viscosity
n	Number of spanwise panels
n_g	Number of spanwise panels on the water surface
n_p	Number of heightwise panels on endplate
n_s	Number of spanwise subpanels
N	Convergence exponent for n

N_c	Number of children
N_p	Number of chromosomes in population
η	Two-dimensional water surface elevation
$\hat{\boldsymbol{n}}$	Unit outward normal to a surface
p	Dimensional pressure $= \rho_W U^2 P = -\rho_A U \gamma$
P	Non-dimensional pressure on water
Π_{ij}	Main panel
Π_{ijk}	Sub-panel
$\boldsymbol{q}$	Velocity vector $= (U+u, v, w)$
$Q(y)$	Leading edge singularity strength
R	Two-dimensional wave drag
Re	Reynolds number
ρ	Fluid density
ρ_A	Density of air
ρ_W	Density of water
s	Wing span
S	Singular potential for a source
S_1	Non-singular potential for a source
$\bar{S}$	Composite velocity potential for a source $= S + S_1$
t_P	Endplate thickness parameter
t_W	Wing thickness parameter
u	Streamwise perturbation velocity component
U	Free stream airspeed
v	Spanwise perturbation velocity component
w	Vertical perturbation velocity component
$\bar{w}$	Induced downwash
x	Chordwise coordinate
ξ	Chordwise coordinate
$\bar{\xi}$	Chordwise control point
y	Spanwise coordinate
η	Spanwise coordinate
$\bar{\eta}$	Spanwise control point
z	Vertical coordinate
ζ	Vertical coordinate

Chapter 1

Lifting Surfaces

1.1 Introduction

Lifting surfaces may be wings on airplanes or birds, propeller blades, windmills, racing-car downforce devices, aerodynamic aids such as tails or fins on airplanes or dragsters, frisbees or aerobees, paper planes, kites, control surfaces in air or water, hydrofoils, boomerangs or re-entry space vehicles. In all cases, forward motion induces a pressure difference between the upper and lower sides of a relatively thin surface which is dependent upon the geometry of that surface, and which can be obtained by solving an integral equation over the surface. Accurate solutions to this integral equation have been actively sought by many investigators. Although modifications to the techniques to be discussed do exist to deal with unsteadiness and viscosity, we restrict ourselves here to the steady potential flow of an ideal fluid. Much work has been done on potential flow (Hess and Smith, 1967); however there are numerical issues relevant to flow over thin wings that are at present unresolved.

In particular, for a lifting surface $z = f(x, y)$ that is close to the plane $z = 0$ in an x-directed stream U, the pressure difference or loading is proportional to a bound vorticity $\gamma(x, y)$ which is determined for small f by solution of the lifting surface integral equation (LSIE)

$$\iint_B \gamma(\xi, \eta) W(x - \xi, y - \eta)\, d\xi\, d\eta = -4\pi U f_x(x, y) \tag{1.1.1}$$

over the projection B of the lifting surface onto the plane $z = 0$. The kernel function

$$W(X, Y) = Y^{-2}(1 + X/R), \tag{1.1.2}$$

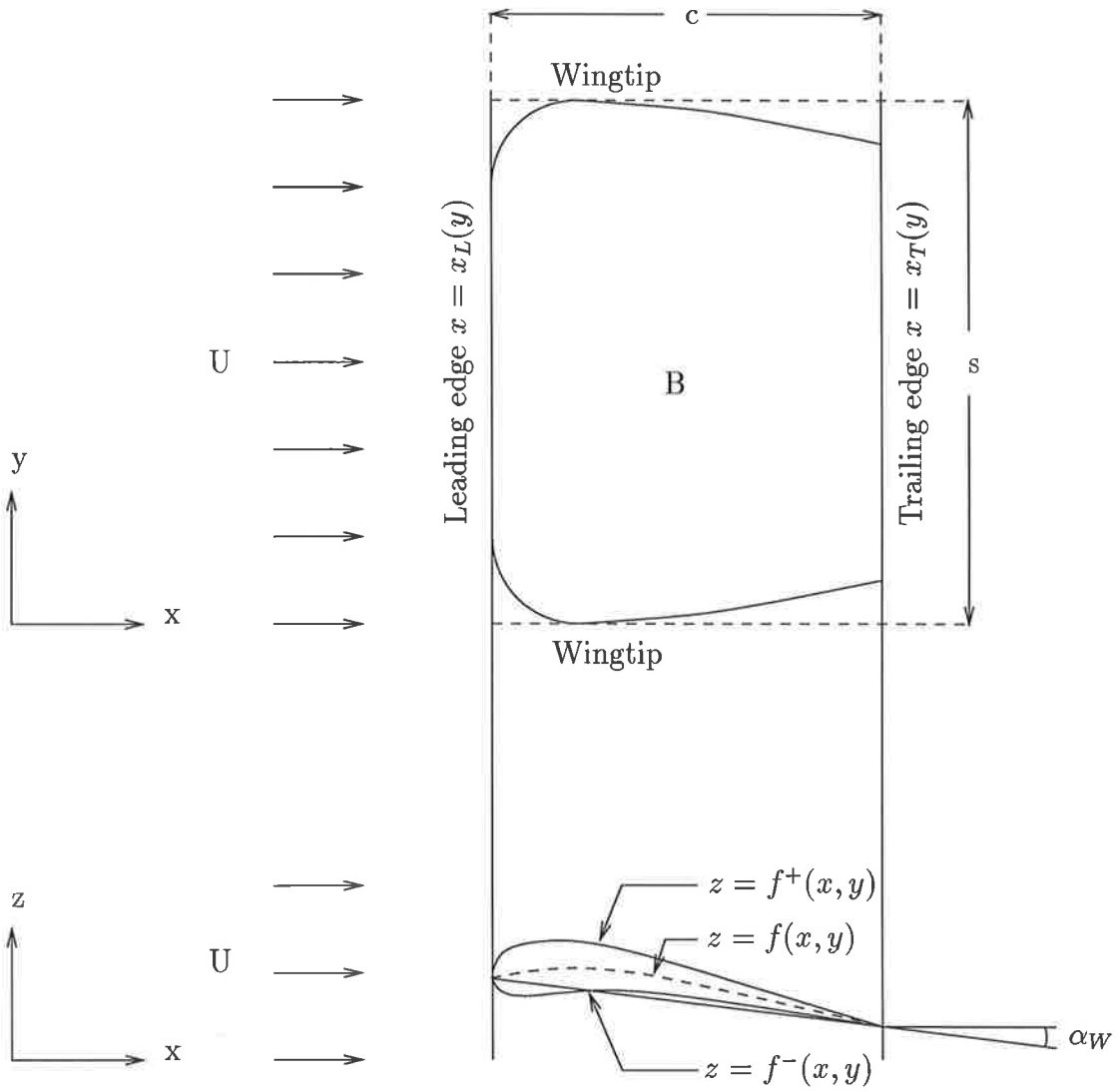

Figure 1.1: *The wing is assumed to have thickness* $t(x,y) = f^+(x,y) - f^-(x,y)$*, mean camber* $f(x,y) = (f^+(x,y) + f^-(x,y))/2$ *and angle of attack* α_W*, which are small when compared to the chord* c*. Under such assumptions, the lifting and non-lifting components may be decoupled to first order.*

with $R = \sqrt{X^2 + Y^2}$, is the downwash induced by a unit horseshoe vortex (Ashley and Landahl, 1965), (Tuck, 1993). Equation (1.1.1) can be integrated once with respect to x and the resulting constant of integration used to satisfy the Kutta condition at each fixed value of y, requiring $\gamma(x,y) = 0$ at the trailing edge of B. No exact analytic solutions of (1.1.1) exist although series solutions have been sought by a number of investigators (Hauptman and Miloh, 1986), (Jordan, 1973), (Jordan, 1971).

1.2 Quantities of Interest

Quantities of engineering and design interest may be determined by the solution of (1.1.1). The relationship between the pressure difference across the upper and lower wing surfaces and the loading $\gamma(x,y)$ is given by

$$p^+(x,y) - p^-(x,y) = -\rho_A U \gamma(x,y). \tag{1.2.3}$$

The chordwise-integrated loading is

$$\Gamma(y) = \int_{x_{LE}(y)}^{x_{TE}(y)} \gamma(x,y)\, dx \tag{1.2.4}$$

and the total lift produced by the surface is given by

$$L = -\rho_A U \int_s \Gamma(y)\, dy. \tag{1.2.5}$$

The lift coefficient, C_L is a useful reference quantity, given by

$$C_L = \frac{2L}{\rho_A U^2 B} = -\frac{2}{UB} \iint_B \gamma(x,y)\, dxdy, \tag{1.2.6}$$

where B is the plan area of the surface. Similarly, the induced drag coefficient C_{D_i} is defined as

$$C_{D_i} = \frac{2D_i}{\rho_A U^2 B}, \tag{1.2.7}$$

where the induced drag force D_i is a function of the trailing vortex sheet and will be discussed further in Chapter 2 with the leading-edge suction force S. The rate at which vorticity is shed at the wingtip directly relates to the strength of the wingtip vortex. Consequently, we present results for the asymptotic behaviour of $\Gamma(y)$ as y tends to the wingtip y_{TIP}.

1.3 Existing Numerical Schemes

A number of popular numerical techniques for approximately solving the linear lifting surface equation have been developed. While there are many variations in gridding and co-ordinate systems, there are essentially two classes of algorithm, namely the vortex lattice methods and the higher order panel methods.

1.3.1 The Vortex Lattice Method

Certainly the most widely used numerical technique for solving the lifting surface equation is the vortex lattice method (Falkner, 1943) in which the unknown function $\gamma(x)$ is replaced by a finite but large number of Dirac delta functions whose strength is to be determined by collocation. This method models the flow by discrete line vortices, rather than by a smooth distribution of vorticity. The location of these vortices and collocation points is crucial to success of the vortex lattice method.

It has evolved with high speed computers into an economical, accurate engineering tool for the design and analysis of such various devices as Darrieus wind turbines (Strickland, 1979) (Zhu, 1981), wind-tunnels (Heltsey, 1976) and marine propellers (Kerwin, 1986), (Kerwin and Lee, 1978). While numerous modifications have been made to the basic method for specific applications, the vortex lattice method seems to produce results for lifting surfaces with a certain serendipity. Essentially the difference between the vortex lattice methods and the other panel methods is the order of representation of the wing loading γ on each panel. While a constant (order 0) or higher (Cunningham Jr., 1971) representation of the loading might be expected to produce a better result than a vortex (order -1 Dirac delta function), the vortex lattice methods have produced "remarkably accurate" solutions (James, 1972). Efforts to represent specific output quantities by higher order functions, such as the spanwise integrated loading (Kálmán et al., 1970) can produce smooth results for that quantity, but often reduce accuracy in some other output quantity. An excellent summary of the trade-off between order of representation and sensitivity to the location of the collocation point within each panel (Ando and Ichikawa, 1983) shows that the vortex lattice method quickly loses accuracy when the panels and collocation points do not correspond to the roots of the Chebyschev polynomial corresponding to the desired number of gridpoints. For higher order methods, the specific discretization is less significant.

Because of its accuracy and ease of numerical implementation, the vortex lattice method is probably the most widely used algorithm for the preliminary design of lifting surfaces in steady, ideal flow. However, because of the sensitivity of the convergence of point loadings to the grid arrangement, the standard technique is usually modifed to suit a particular application. Consequently, the lattices are arranged in a manner based on the anticipated or desired answer. It has also been noted (Hancock, 1971) that while the vortex lattice

method leads to a finite lift, strictly it implies an infinite induced drag since the induced drag of each horseshoe vortex line is in itself infinite. Also, unless some modifications are made to the layout of lattices and collocation points, the Kutta condition requiring smooth flow detachment at the trailing edge is not automatically satisfied (Lan, 1974).

While most investigators agree that a variation on the Chebyschev grid suits most applications, one suggestion (Lowe, 1988) is that a superposition of vortices near the leading edge provides closer modelling of the wingtip behaviour.

Numerous ingenious methods of arranging the lattices and collocation points "determined from the finite sum used to approximate the downwash integral of lifting surface theory" (DeJarnette, 1976), or based on empirical observations have been used to improve the economy and accuracy of the vortex lattice methods. A study of some popular codes based on vortex lattices (Wang, 1974) illustrates that integrated quantities such a lift and pitching moment are relatively easy to obtain numerically, whereas obtaining agreement between the near-field and far-field estimates for the induced drag coefficient can be very difficult. In order to illustrate some of the existing linear collocation methods, consider the two-dimensional analogue of the lifting surface equation.

1.3.2 The Airfoil Equation

The airfoil equation

$$\int_c \frac{\gamma(\xi)}{x-\xi}\, d\xi = f'(x) \tag{1.3.8}$$

is the two-dimensional equivalent of the LSIE (1.1.1), for a given function $f'(x)$, and integrates once to give

$$\int_c \gamma(\xi) \log|x-\xi|\ d\xi = f(x). \tag{1.3.9}$$

An implicit constant of integration in $f(x)$ ultimately determines the unique solution of (1.3.8) satisfying the Kutta condition $\gamma = 0$ on the trailing edge (TE). For example, if the airfoil is a flat plate with $f'(x) = 1, -1 \le x \le 1$, this solution has

$$\gamma(x) = \frac{1}{\pi}\sqrt{\frac{1-x}{1+x}}. \tag{1.3.10}$$

Note the inverse square root leading edge singularity at $x = -1$, and a zero of square-root type at the trailing edge $x = 1$.

Although an explicit analytic solution can be written down as a quadrature (Tricomi, 1965) for any $f'(x)$, the airfoil equation (1.3.8) may also be solved numerically to "remarkable accuracy" (James, 1972) by the vortex lattice method.

1.3.3 Stark's Scheme

Stark (Stark, 1971) showed that the optimum way of dealing with the Cauchy singularity associated with a vorticity distribution behaving like a weight function $W(x)$ is to represent this vorticity distribution by a set of discrete vortices which may be mapped onto the zeros of the orthogonal polynomial associated with $W(x)$. In the lifting surface case, the natural weight function for two-dimensional steady flows is

$$W(x) = \sqrt{\frac{1-x}{1+x}}, \tag{1.3.11}$$

which captures both the leading edge singularity and the trailing edge zero. The associated orthogonal polynomials are the Jacobi polynomials of order $(+1/2, -1/2)$.

Alternatively, if $\gamma(x)/W(x)$ is a polynomial of degree less than or equal to $2m$, then Stark (DeJarnette, 1976) proved that the weighted approximation

$$\int_c \frac{\gamma(\xi)}{x-\xi}\, d\xi = \sum_{i=1}^{m} W_i \frac{\gamma(\xi_i)}{\xi_i - x_j} \qquad j = 1, \ldots, m. \tag{1.3.12}$$

is exact for the following discretization

$$x_i = -\cos\left(\frac{2i-1}{2m+1}\pi\right) \qquad i = 1, \ldots, m \tag{1.3.13}$$

$$\xi_j = -\cos\left(\frac{2j}{2m+1}\pi\right) \qquad j = 1, \ldots, m \tag{1.3.14}$$

$$W_i = \frac{2\pi}{2m+1} \sin\left(\frac{2i-1}{2m+1}\pi\right) \qquad i = 1, \ldots, m, \tag{1.3.15}$$

where x_i, ξ_j and W_i are the vortex location, collocation point and weight function respectively. It is illustrated in Figure 1.2.

1.3.4 Lan's Quasi-Continuous Method

The Quasi-Continuous Method (QCM) of Lan (Lan, 1974) is probably the most widely implemented vortex lattice method variant (Lan, 1974), (Lan, 1976), (DeJarnette, 1976) and (Guermond, 1988).

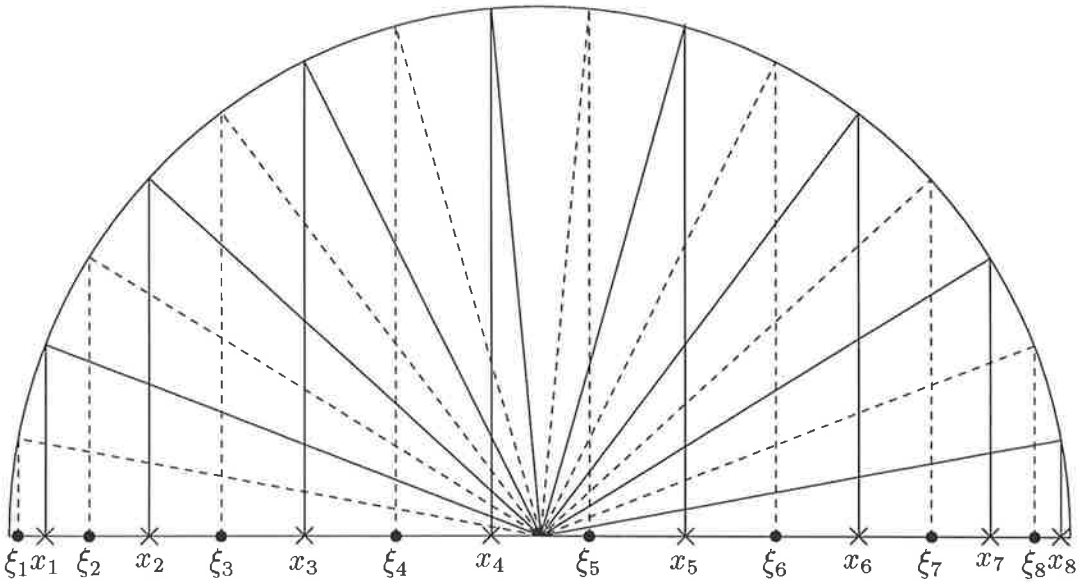

Figure 1.2: *The lattice arrangement of V. E. Stark.*

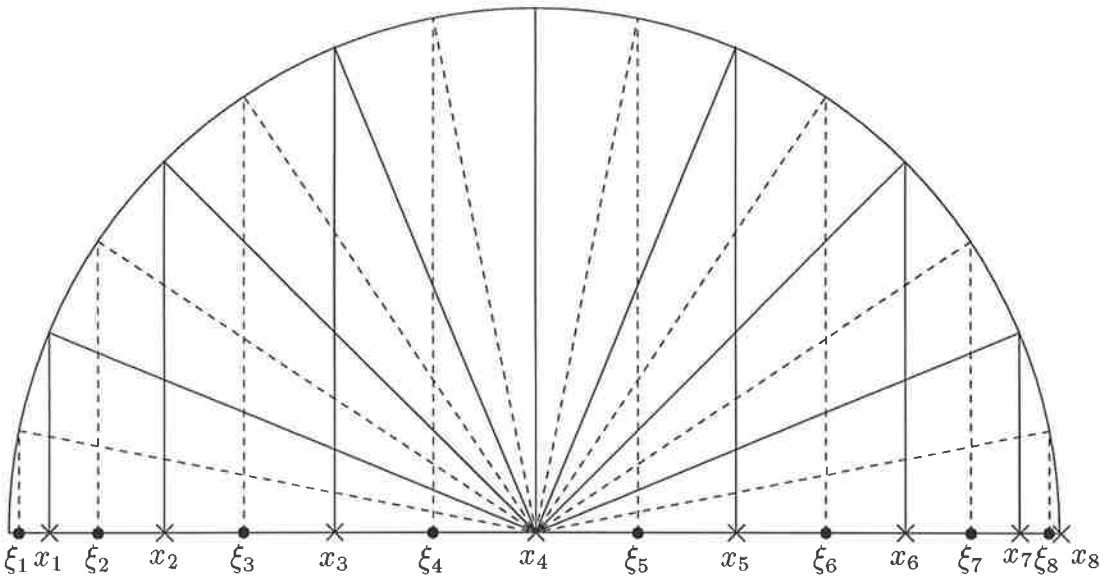

Figure 1.3: *The lattice arrangement of C. E. Lan.*

Lan showed that the continuous distribution of vortices occurring on a wing may be advantageously represented by a set of discrete vortices located at points which may be mapped onto the set of the zeros of the Chebyschev's polynomial of the first kind.

$$x_i = -\cos\left(\frac{2i-1}{2m}\pi\right) \qquad i = 1, \ldots, m \tag{1.3.16}$$

$$\xi_j = -\cos\left(\frac{j}{m}\pi\right) \qquad j = 1, \ldots, m \tag{1.3.17}$$

$$W_i = \frac{\pi}{m}\sin\left(\frac{2i-1}{2m}\pi\right) \qquad i = 1, \ldots, m \tag{1.3.18}$$

This Chebyschev or cosine spacing can also be seen as related to the conformal transformation of a circle into a flat or parabolically cambered plate by the Joukowski trans-

formation (Kerwin, 1986)

While Lan's quadrature is a trapezoidal rule on the mapped segment $[0, \pi]$, Stark's quadrature is a Gaussian rule on the actual segment $[-1, +1]$. As a Gaussian integration, Stark's rule is more accurate and likely to converge faster than Lan's when the ratio $\gamma(x)/W(x)$ differs from a polynomial (DeJarnette, 1976). The motivation for Lan's scheme was to obtain the same accuracy in three-dimensional wing analysis as was possible with the two-dimensional Chebyschev spacing for airfoils.

1.3.5 Three Dimensionality

There are a number of issues beyond those that must be considered for airfoil analysis that effect the accuracy of analogous schemes in three dimensions. The most obvious way to apply the accurate two-dimensional method to the wing is by a strip-theory approximation as illustrated in Figure 1.4. The vorticity strength is piecewise constant in the spanwise direction and optimally spaced in the chordwise direction to capture the leading and trailing edge behaviour. Here the chordwise grid is generated with $m = 1$ and the spanwise grid with $n = 6$. Versions with staggered grids for point vortices and collocation points have also been used, but the spanwise constant vorticity method gives greater accuracy for little extra computational effort. The immediate complication of applying the method in three dimensions is that the vortex lines extending downstream must not intersect any collocation points. For more complicated geometries, this is not always trivial to arrange.

The numerical solution of the three-dimensional lifting surface problem is also complicated because the Cauchy singularity exists not only in the chordwise direction, but also in the spanwise direction. The spanwise wing loading has a square root zero at the wingtip, which should be treated as carefully as the leading edge inverse square root singularity (Guermond, 1988).

Another difficulty is the choice of panel shape. For numerical convenience, quadrilateral panels are usually chosen to model the surface. This choice seems to be legitimate in the case of quadrilateral wings but it is not natural for wings with rounded boundaries. In the latter case a weak logarithmical singularity arises in the calculation of the self-induced velocity coefficients. Since very large velocities occur at the leading edge, no matter how weak the logarithmic singularity may be, one cannot prove that it has no

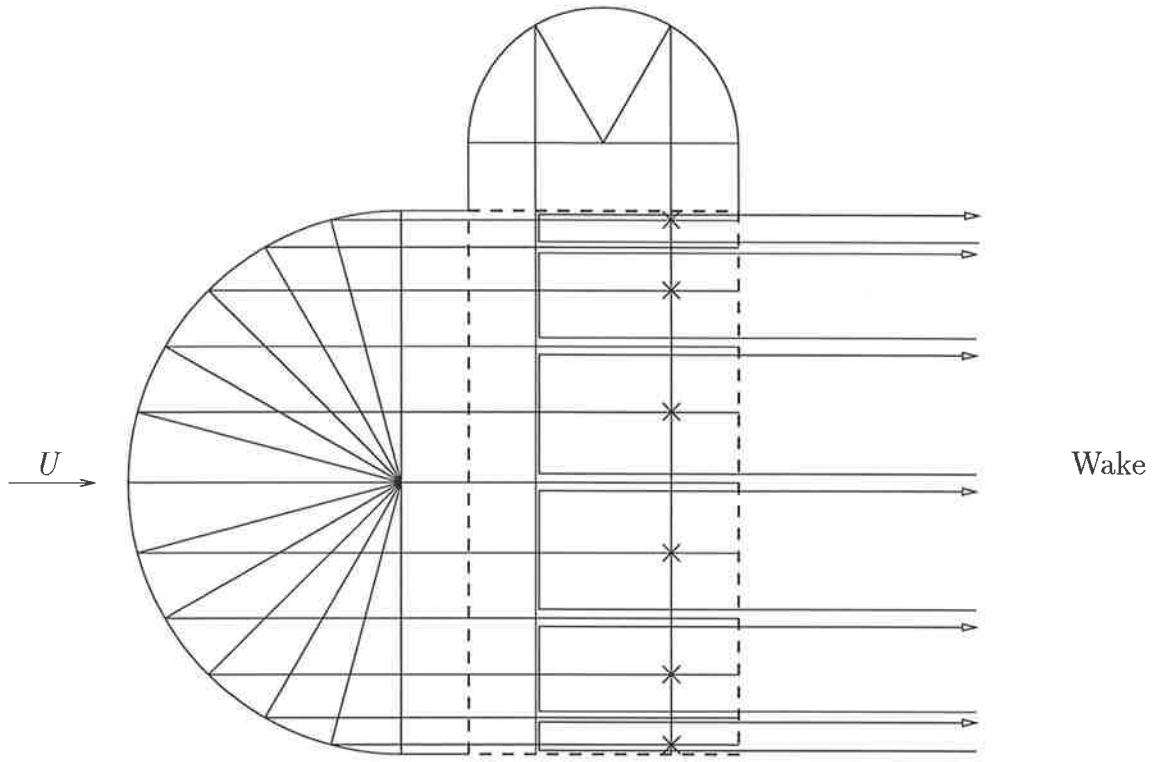

Figure 1.4: *Vortex lattice arrangement for three-dimensional rectangular wing. The lattice points are generated using cosine spacing with* $m = 1$ *and* $n = 6$ *for the chordwise and spanwise grids respectively. Here the vorticity is piecewise constant in the spanwise direction, with orientation determined by the conventional right hand rule.*

perturbing influence on the leading-edge behaviour of the numerical solution (Guermond, 1988).

Another feature of classical methods which is rarely discussed is the control point locations. In the circular wing case, if control points are rigorously located according to Lan's recommendations, then the first and last control points of the tip strips are outside their respective panel. Of course, such a configuration cannot be accepted. Generally the problem is solved by defining the control point location as the mean value calculated from the location of the four vertices of each panel. This rule usually works but has no theoretical basis (Guermond, 1988).

Uncertainty in the control point position can also cause numerical instability for rounded-tip wings when the number of panels increases. In the vicinity of rounded tips, large panel numbers create highly skewed panels for which a slight uncertainty in the control point location may easily result in a wrong calculation of the self-induced velocity coefficients (Guermond, 1988). This problem is often pragmatically solved by giving an arbitrary

non-zero chord length to the tip section. This is discussed further in the section on curved panels.

1.3.6 Spanwise Modifications

Many schemes have been devised to accurately capture the spanwise behaviour of the wing loading, but these have largely been designed with a particular asymptotic behaviour in mind. It is difficult to then apply these methods to analyse the loading in the close vicinity to the wingtip, because the results are grid dependent.

It was found (Rubbert, 1964) that insetting the location of the horseshoe vortices and control points at the wing tips could lead to improved resolution of the known square root zero at the wingtip. Later a one-quarter panel inset in the examination of rectangular and swept wings was applied (Hough, 1973), (Hough, 1976). Using mathematical techniques similar to Lan's, a quasi-continuous spanwise scheme was produced (DeJarnette, 1976) as illustrated in Figure 1.5. In the infinite aspect ratio limit, the three spanwise modifications

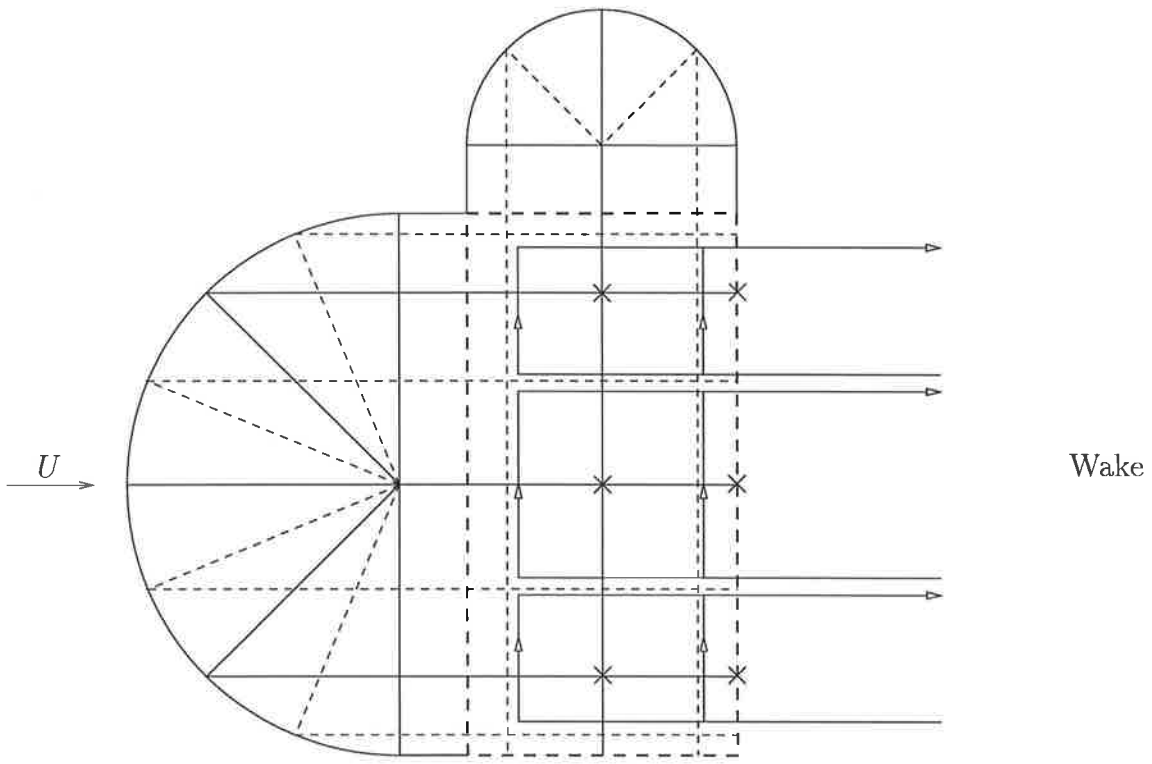

Figure 1.5: *Spanwise scheme of F. R. DeJarnette with $m = 2$ and $n = 3$. The vortices are spanwise inset at the wingtips to capture the wingtip singularity.*

are identical. We use only DeJarnette's scheme for comparison.

For the chordwise discretization, we give comparative results for Stark's and Lan's schemes only. Furthermore, since the performance of the vortex lattice method on wings with curved edges is notoriously poor unless modifications are made at the wing tips, or curvilinear coordinate systems (Guermond, 1988) are used, we will not use these models in the examination of circular wings.

1.3.7 Spatial Mapping

An alternative approach is to map the geometry to a rectilinear space (Guermond, 1988). Guermond's curved panel method is presented as an extension to Lan's Quasi-Continuous Method. The numerical implementation of the mapping is by the inclusion of a Jacobian term in Lan's integral equation. The mapping is certain to be undefined at the wingtips, but elsewhere need not be conformal for the method to work. Although the results for the overall spanwise distribution of the circulation largely seem to agree very well with Jordan's series analytical solution (Jordan, 1973), it is not surprising that the leading edge suction is not captured near the wingtips. There is also no comparison of the spanwise loading very close to the wingtip, and unfortunately no other data is presented with which comparisons can be made.

1.3.8 The Panel Method of Tuck

The panel method of Tuck (Golberg, 1990) for the solution of integral equations with Cauchy-type singularities has been used on a variety of problems in aerodynamics, hydrodynamics and heat transfer (Oertel, 1975) (MacCaskill, 1977) and (Anderssen, 1980).

The method is used to solve the once chordwise integrated version of the LSIE (1.1.1)

$$\iint_B \gamma(\xi,\eta) K_{XY}(x-\xi, y-\eta)\, d\xi d\eta = -4\pi f(x,y) + C(y), \tag{1.3.19}$$

where $K_{XY} = Y^{-2}(X+R)$ and $R = \sqrt{X^2+Y^2}$. The constant of integration $C(y)$ that must be chosen at each spanwise position to ensure satisfaction of the Kutta condition $\gamma(x_{TE}(y), y) = 0$ is calculated as part of the solution procedure. The planform B is divided into a finite number of rectangular panels as illustrated in Figure 1.6 on each of which the loading γ is assumed constant.

While any discretization will in principle work, the favoured method for any planform is to use the Chebyschev scheme illustrated for a circular wing in Figure 1.6. The specific

scheme is as follows, in the order in which the points should be calculated. Note that the chord length of a strip is determined by the Chebyschev midpoint of the strip in the spanwise direction.

$$\eta_j = \frac{s}{2}[1-\cos(j\pi/n)] \quad j=0,\ldots,n \tag{1.3.20}$$

$$y_j = \frac{s}{2}\left[1-\cos((j-\frac{1}{2})\pi/n)\right] \quad j=1,\ldots,n \tag{1.3.21}$$

$$\xi_{ij} = x_L(y_j) + \frac{x_T(y_j)-x_L(y_j)}{2}[1-\cos(i\pi/m)] \quad i=0,\ldots,m \tag{1.3.22}$$

$$x_{ij} = x_L(y_j) + \frac{x_T(y_j)-x_L(y_j)}{2}\left[1-\cos((i-\frac{1}{2})\pi/m)\right] \quad i=1,\ldots,m \tag{1.3.23}$$

Evaluating the left hand side of Equation 1.3.19 on each panel is achieved by considering the value of K, the formal antiderivative of the kernel K_{XY} at each of the 4 corners of panel Π_{ij} Consequently the double integral

$$\iint_{\Pi_{ij}} K_{XY}\, d\xi d\eta = K^{++} - K^{-+} + K^{--} - K^{+-} \tag{1.3.24}$$

is exact for each panel and each collocation point (x,y). In this manner the integral evaluation is computationally efficient and the Hadamard singularity in K_{XY} is avoided. The resulting system of linear equations is solved for the vector of values of γ using any standard dense matrix inversion package.

This method has been used (Tuck, 1993), (Tuck, 1992) to produce seven figure accurate values for the lift coefficient C_L/α_W for rectangular wings. However, close examination of the calculated loading in the vicinity of the leading edge reveals a highly localised inadequacy in the representation of the inverse square-root leading-edge singularity (Standingford and Tuck, 1994), (Tuck and Standingford, 1997).

1.4 Improved Panel Method

All known numerical techniques for solving the LSIE (1.1.1), including the vortex lattice method (VLM) (Lan and Mehrotra, 1979), (Lan, 1974) exhibit a similar inadequacy (Lazauskas et al., 1995) and yet the leading edge singularity strength is of direct aerodynamic significance because it relates to the leading edge suction. One method (Carter and Jackson, 1991) of fixing this problem for the vortex lattice method is to specify a

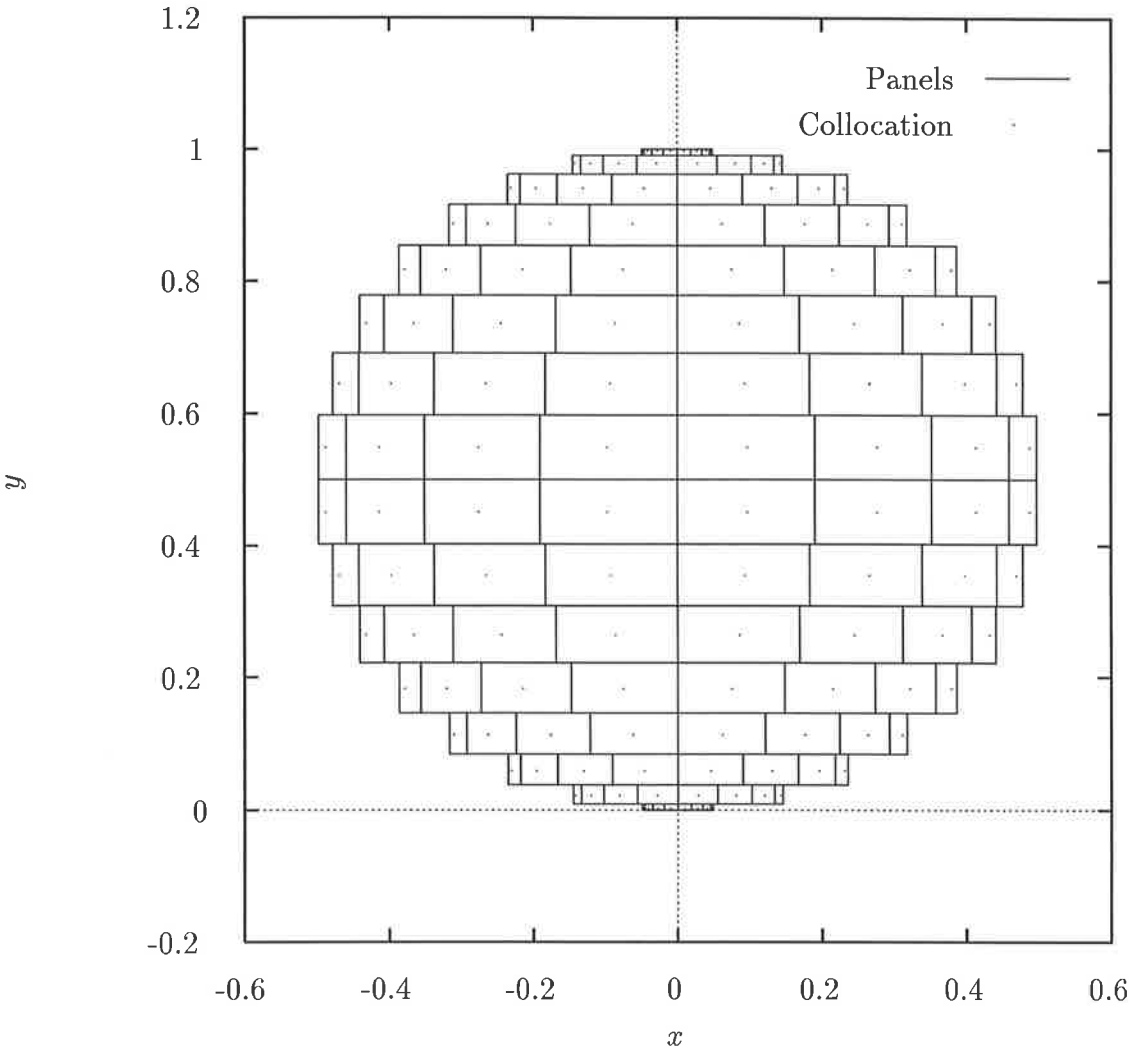

Figure 1.6: *The panel method of E. O. Tuck. This scheme will produce a grid over any single wing planform provided that the leading and trailing edges are given as functions of the spanwise co-ordinate.*

quadratic profile of $\sqrt{x - x_{LE}}\,\gamma(x, y)$ over the first 3 collocation points from the LE. We first turn to the two-dimensional version of the problem to seek an alternative remedy.

At one order of representation higher than the vortex lattice methods, to solve the two-dimensional airfoil equation (1.3.8) in a manner analogous to the three-dimensional method of Tuck (Tuck, 1993), we assume a constant value $\gamma(\xi) = \gamma_j$ on each of m panels, which are Chebyschev spaced, resulting in the discrete set of linear equations

$$\sum_{j=1}^{n} \gamma_j \int_{\xi_{j-1}}^{\xi_j} \log|x_i - \xi|\, d\xi = f(x_i) \tag{1.4.25}$$

where the integral equation is exactly satisfied at each of the m collocation points $x_i, i = 1, \ldots, m$. The integral itself can be evaluated exactly over each panel, and the resulting

algebraic equations

$$\sum_{j=1}^{m} \gamma_j A_{ij} = f(x_i) \tag{1.4.26}$$

require inversion of the influence matrix

$$A_{ij} = \Big[(x_i - \xi)\,(1 - \log|x_i - \xi|) \Big]_{\xi_{j-1}}^{\xi_j} . \tag{1.4.27}$$

Solution of the set of equations (1.4.26) produces an accurate estimate for the overall lift which converges with $O(n^{-2})$ rate. However, inspection of the output values of the function $\sqrt{x}\ \gamma(x)$, which should approach a constant value at $x = 0$ shows instead a distinct *kink* which does not appreciably diminish in amplitude with an increase in the number m of panels used. This numerical artefact is largely local to the first few values of γ from the leading edge and hence the error it contributes to the predicted lift tends to zero rapidly with n, being proportional to the size of the panels, which for a Chebyschev grid are especially small in that vicinity. However, the effect on local properties near the leading edge can be significant. For example (see Figure 1.7) if the first two values of γ_j are used to predict the strength of the leading edge singularity by linear extrapolation to $x = 0$ of $\sqrt{x}\ \gamma(x)$, the accuracy of this prediction will decrease rather than increase with the number of panels used.

To correct this numerical error, the representation of the strength of the inverse square root singularity in the loading function $\gamma(x)$ near the leading edge $x = 0$ must be improved.

1.4.1 Subpanelisation

One method that is quite successful but computationally expensive is *subpanelisation*, illustrated in Figure 1.8 in which we subdivide each main panel into many smaller subpanels, and then modify the numerical integration of the kernel in the integral equation to account for the variation of the relative loads on each of the subpanels, namely, an inverse square root interpolation to the centre of that subpanel, based on the reference value $\gamma_j = \gamma(\overline{\xi_j})$ at the centre of main panel j.

The derivation of the method of subpanelisation is as follows. The expectation from two-dimensional analysis is that

$$\gamma_j \sim \sqrt{\frac{1 - x_j}{1 + x_j}}, \tag{1.4.28}$$

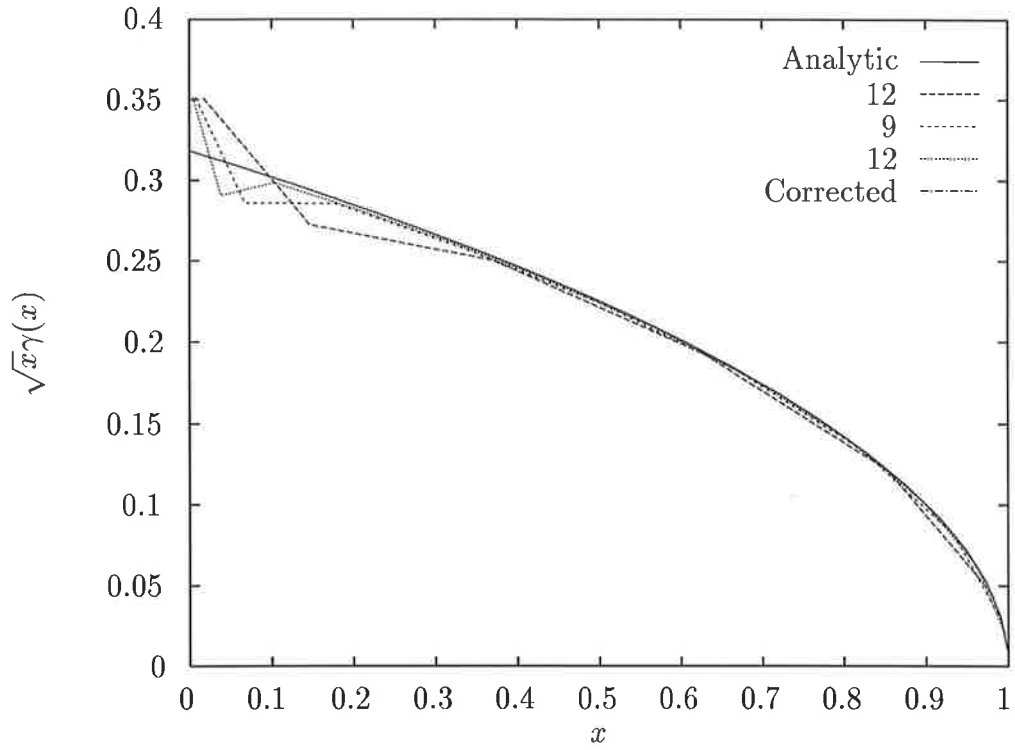

Figure 1.7: *Two-dimensional airfoil loading with square root singularity removed, with* 6, 9 *and* 12 *panels. The kink in the results near the leading edge does not reduce in size with increased numbers of panels. The corrected curve is also shown, and is indistinguishable from the analytic solution.*

over the interval $x_j \in (-1, 1)$. We modify Equation 1.3.8 according to the transformation

$$\xi = -\cos\theta, \tag{1.4.29}$$

whereupon the integral becomes

$$\int_0^\pi \gamma(-\cos\theta)\sin\theta \log|x + \cos\theta|\, d\theta. \tag{1.4.30}$$

The discrete version becomes

$$\sum_j \gamma_j \sin\theta_j \int_{\theta_{j-1}}^{\theta_j} \log|x + \cos\theta|\, d\theta. \tag{1.4.31}$$

Now the integrand here has no formal anti-derivative, so we transform back to ξ-space

$$\sum_j \gamma_j \sin\theta_j \int_{\xi_{j-1}}^{\xi_j} \log|x - \xi| \frac{d\xi}{\sqrt{1-\xi^2}} \tag{1.4.32}$$

and further approximate, by extracting $\sin\theta = \sqrt{1-\xi^2}$ from the integrand, and regarding it as constant over a small subpanel k. Hence

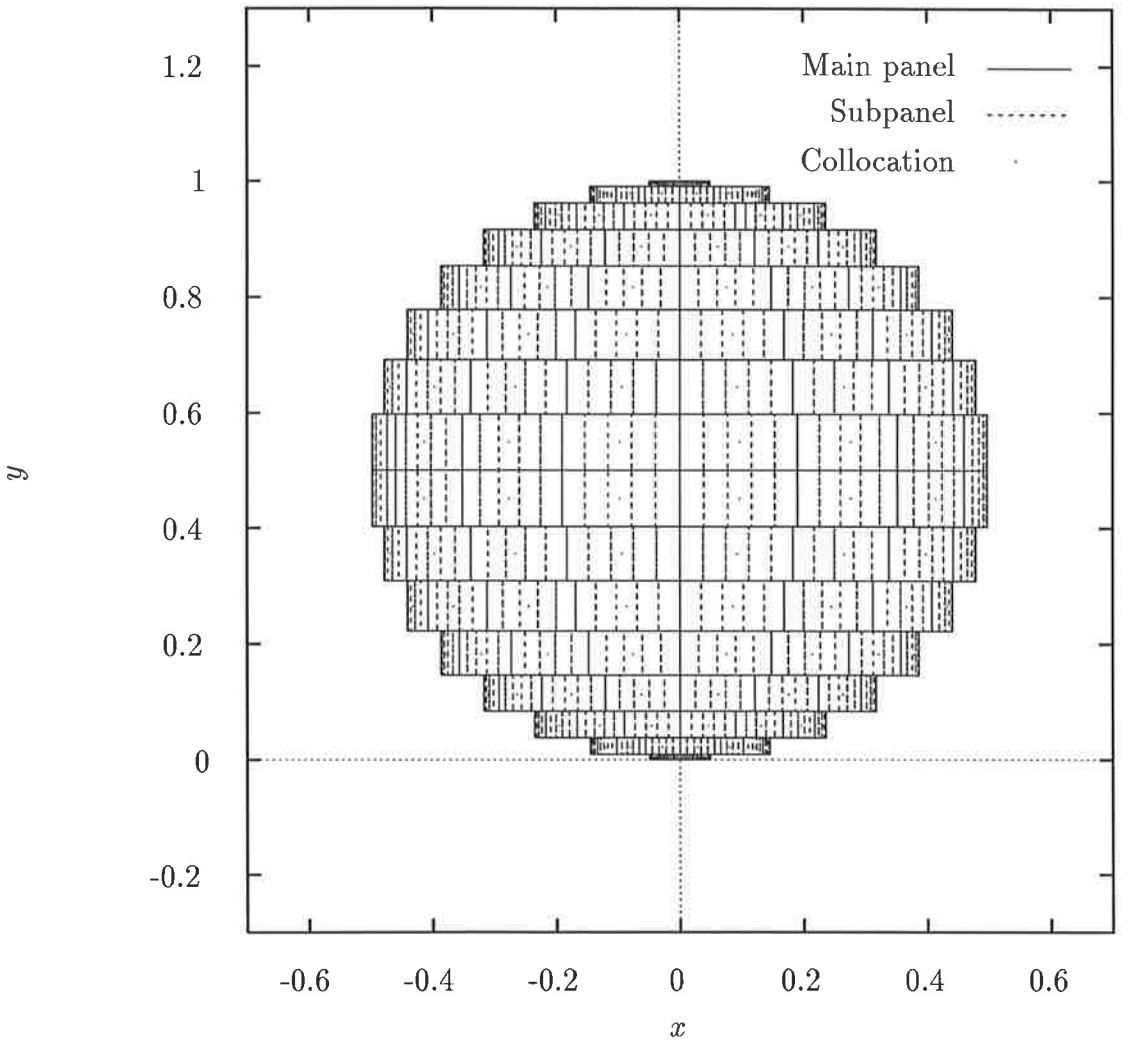

Figure 1.8: *The main wing panels are further divided into chordwise subpanels, on which the relative loads are varied to account for the leading edge singularity.*

$$\sum_j \gamma_j \sum_k (\frac{\theta_j}{\theta_k}) \int_{\xi_{j-1,k-1}}^{\xi_{j-1,k}} \log|x-\xi|\, d\xi. \tag{1.4.33}$$

If the ratio $(\sin\theta_j / \sin\theta_k)$ is close to unity, then this closely approximates Tuck's original method. However, near either the leading or the trailing edge, this ratio approaches infinity (as an inverse square root) and zero (as a square root), respectively.

We may then evaluate the integral more accurately on a given panel by subpanelising. For such a panel, we use the approximation

$$\sum_{k=1}^{M} \frac{1}{\sqrt{1-\bar{\xi}_k^2}} \int_{\xi_{j,k-1}}^{\xi_{j,k}} K_\xi \, d\xi, \tag{1.4.34}$$

noting that the integral is again exact. The inverse square root factor is assumed to

be constant over each subpanel, although the actual location of the $\overline{\xi}_k$ within the kth subpanel is still arbitrary. As the motivation for employing this method arises from the critical ratio for each subpanel ($\sin\theta_j/\sin\theta_k$), $\overline{\xi}_k$ is chosen to lie on a global Chebyschev grid of finer resolution. Treating the approximation as a Riemann integration, the kink in the results for loading can be significantly reduced by using 10 or more subpanels. Figure 1.9 illustrates the improvement in the results. This method has also been successfully employed for the solution to the Planing Splash problem (Tuck, 1994).

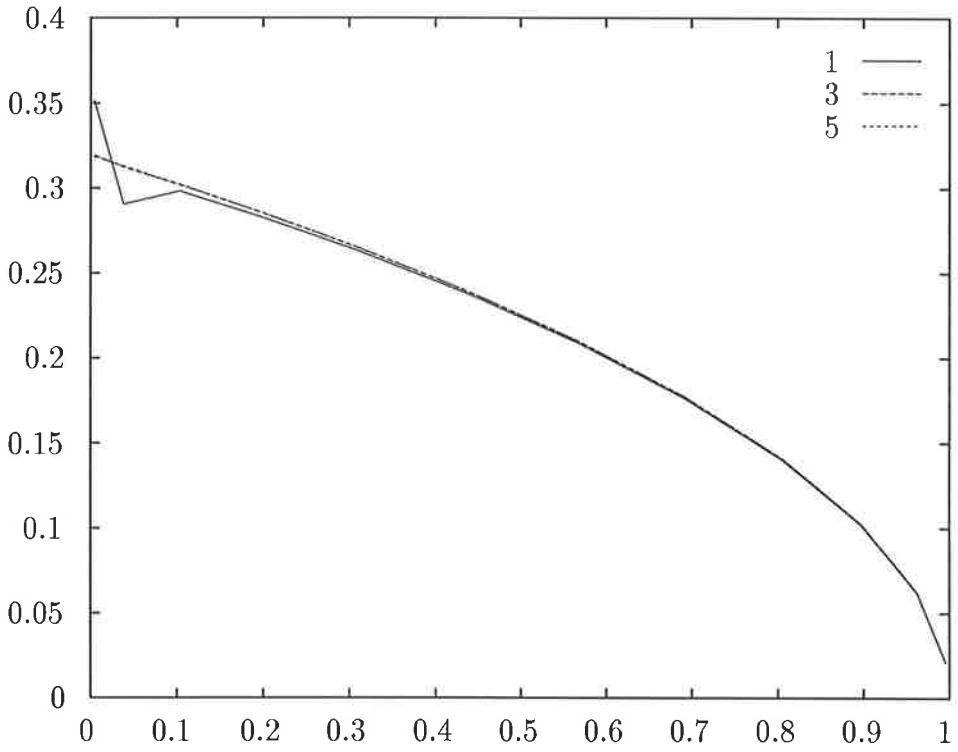

Figure 1.9: *Improvement in the resolution of the leading edge loading by subpanelling with $m_s = 1, 3, 5$ subpanels for a solution to the airfoil equation with $m = 12$. The case $m_s = 1$ corresponds to the case where there are no extra panels on each main panel. Beyond $m_s = 5$, there is no visible improvement in the resolution and in general $m_s = 10$ has been found to improve the point estimate for the leading edge singularity strength to within 3 significant figures of the fully extrapolated estimate for a given m.*

1.4.2 Subpanels in Three-Dimensions

Applying an equivalent chordwise-only subpanelisation to a two-dimensional planform, Equation 1.3.19 is approximated by the discrete version:

$$\sum_{i=1}^{n}\sum_{j=1}^{m}\gamma(\overline{\xi}_j,\overline{\eta}_i)A_{ij} = -4\pi f(x,y) + C(y), \tag{1.4.35}$$

where

$$A_{ij} = \iint_{\Pi_{ij}} K_{XY}(x-\xi, y-\eta)\,d\xi d\eta \tag{1.4.36}$$

is evaluated by

$$\sum_{k=1}^{p}\sqrt{\frac{\overline{\xi}_{ijk}-\xi_{LE}}{\overline{\xi}_{ij}-\xi_{LE}}}\iint_{\Pi^s_{ijk}} K_{XY}(x-\xi, y-\eta)\,d\xi d\eta, \tag{1.4.37}$$

in which $\overline{\xi}_{ijk}$ and $\overline{\xi}_{ij}$ are global Chebyschev points located within the subpanel Π^s_{ijk} and main panel Π_{ij} respectively. The integral

$$\iint_{\Pi_{ijk}} K_{XY}(x-\xi, y-\eta)\,d\xi d\eta \tag{1.4.38}$$

may be evaluated exactly as per Tuck's original method. The concept of subpanelisation has also been extended to the spanwise discretization in an attempt to enhance resolution of the wingtip singularity. This is discussed further in the later section on curved panels. Hence we refer to a complete panel scheme for a particular planform geometry as $(m, n, m_s[1,\ldots,m][1,\ldots,n], n_s[1,\ldots,m][1,\ldots,n])$, the number of chordwise panels, spanwise panels and chordwise and spanwise sub-panels within each main panel respectively, all relatively Chebyschev spaced.

1.4.3 Direct Inclusion of Singularity

Rather than using large numbers of subpanels to achieve greater resolution of the leading edge behaviour, it is possible in two dimensions to specifically include the singularity, by assuming an inverse square root load distribution over all of the m panels, resulting in the influence matrix

$$A_{ij} = \sqrt{\overline{\xi}_j}\int_{\xi_{j-1}}^{\xi_j}\frac{\log|x_i-\xi|}{\sqrt{\xi}}\,d\xi. \tag{1.4.39}$$

The integral in (1.4.39) can also be evaluated exactly, although with slightly more numerical effort, regardless of the particular grid used. When the new matrix A_{ij} is inverted,

1	-0.191386	-0.289623	-0.256148	-0.182541	-0.104447	-0.044738	-0.012201	0.999992
2	-0.101378	-0.426612	-0.332619	-0.224340	-0.131046	-0.061629	-0.022686	0.999977
3	-0.059830	-0.220609	-0.572224	-0.341500	-0.192871	-0.098395	-0.044824	0.999946
4	-0.036050	-0.125994	-0.285674	-0.642983	-0.327320	-0.164022	-0.081616	0.999895
5	-0.020521	-0.073296	-0.161189	-0.320623	-0.642732	-0.291848	-0.140401	0.999817
6	-0.010244	-0.040306	-0.096496	-0.189536	-0.334279	-0.571379	-0.246278	0.999695
7	-0.003903	-0.020458	-0.060113	-0.128624	-0.220412	-0.324656	-0.459530	0.999458
8	-0.000865	-0.011057	-0.043370	-0.102337	-0.179378	-0.251166	-0.341164	0.999278

Table 1.1: *Corrected matrix of influence coefficients A_{ij} for the solution of the airfoil equation with a constantly loaded two-dimensional panel method using $m = 8$ panels with Chebyschev spacing.*

1	-0.007419	-0.010349	-0.005106	-0.002768	-0.001351	-0.000519	-0.000122	-0.000008
2	0.003071	-0.003440	-0.007805	-0.003428	-0.001605	-0.000634	-0.000174	-0.000023
3	0.000880	0.003876	-0.002888	-0.005978	-0.002273	-0.000896	-0.000284	-0.000054
4	0.000450	0.001432	0.003379	-0.002629	-0.004292	-0.001421	-0.000476	-0.000105
5	0.000316	0.000899	0.001411	0.002405	-0.002378	-0.002795	-0.000807	-0.000183
6	0.000267	0.000730	0.001002	0.001062	0.001243	-0.002043	-0.001557	-0.000305
7	0.000249	0.000671	0.000883	0.000816	0.000501	0.000157	-0.001541	-0.000542
8	0.000243	0.000652	0.000849	0.000759	0.000396	-0.000123	-0.000567	-0.000722

Table 1.2: *Correction matrix E_{ij}.*

the kink in the loading effectively disappears while the rate of convergence to the lift coefficient is maintained (See Figure 1.7).

For any given grid, we may now calculate the difference between the influence matrix $A_{ij} = A^C_{ij}$ assuming constant loading, as given by (1.4.27) and the more accurate influence matrix $A_{ij} = A^B_{ij}$ with the singularity built in, as given by (1.4.39). Hence a correction matrix $E_{ij} = A^B_{ij} - A^C_{ij}$ is obtained for any discretization. For a Chebyschev grid the correction matrix E_{ij} is a fixed constant (the size of the smallest panel) multiplied by a set of factors whose only parameter is the number of panels m. For example, for $m = 8$ the corrected influence coefficients A_{ij}, their correction factors E_{ij} and the relative magnitude E_{ij}/A_{ij} are presented in tables 1.1, 1.2 and 1.3 respectively.

1	0.038767	0.035733	0.019933	0.015162	0.012938	0.011603	0.010013	-0.000008
2	-0.030296	0.008063	0.023467	0.015281	0.012250	0.010281	0.007657	-0.000023
3	-0.014716	-0.017567	0.005047	0.017504	0.011785	0.009105	0.006346	-0.000054
4	-0.012489	-0.011367	-0.011828	0.004089	0.013114	0.008666	0.005828	-0.000105
5	-0.015393	-0.012270	-0.008757	-0.007501	0.003700	0.009578	0.005751	-0.000183
6	-0.026095	-0.018103	-0.010388	-0.005605	-0.003719	0.003576	0.006321	-0.000305
7	-0.063880	-0.032792	-0.014688	-0.006346	-0.002271	-0.000485	0.003354	-0.000542
8	-0.281472	-0.058993	-0.019570	-0.007412	-0.002207	0.000491	0.001663	-0.000722

Table 1.3: *Relative magnitude of correction matrix* E_{ij}/A_{ij}.

1.4.4 Direct Inclusion in Three-Dimensions

Since the two-dimensional airfoil equation has an analytic solution and numerical methods are really only needed for lifting surfaces in three dimensions, the influence matrix correction E_{ij} is more useful when applied to the three-dimensional problem. Integrated once in the x direction, the kernel for the three-dimensional LSIE (1.1.1) may be expressed as

$$W(X,Y) = K_{XY} = Y^{-2}(X+R), \tag{1.4.40}$$

where

$$K(X,Y) = X\log(Y+R) + \frac{1}{2}Y\log(X+R) - XY^{-1}(X+R)/2\,. \tag{1.4.41}$$

Now the kernel, K_{XY} is to be integrated over a rectangular panel. We observe that the numerical scheme provides adequate accuracy in the spanwise direction Y and turn our attention to the $X-$integration of K_X. Integrating once with respect to Y, we obtain

$$K_X = \log(Y+R) - Y^{-1}(X+R) + 1 \tag{1.4.42}$$

All of the terms here are analytic with respect to X except when $Y = 0$ and $X \to 0$. In this case there is a weak singularity in $\log(Y+R)$. If we let $Y = 0$, then this is reduced to the two-dimensional kernel and we might expect that a correction factor equal to that used in the two-dimensional case would be appropriate. We use the above formula for K_X as it stands only when $Y = y - \eta > 0$; if this is not so, the identity $\log(Y+R) = 2\log X - \log(Y-R)$ is used. Now when Y takes the same sign on both sides of the panel, the term $2\log X$ is either not present (both Y values positive) or else

cancels out (both Y values negative). On the other hand, when the sign of Y changes from one side of the element to the other (this occurs when the collocation point lies in the same chordwise strip as the panel), the integration over the full panel takes the form

$$\log(Y^+ + R^+) - \log(Y^- + R^-) = \log(Y^+ + R^+) - \left(2\log X - \log\left|Y^- - R^-\right|\right). \tag{1.4.43}$$

There is now a $-2\log X$ term present, so the appropriate three-dimensional correction to the influence matrix A_{ij} is exactly -2 times that for the corresponding two-dimensional kernel. On application of this correction, the leading edge kink in the three-dimensional results for γ disappears, as it did in two dimensions (see Figure 1.10).

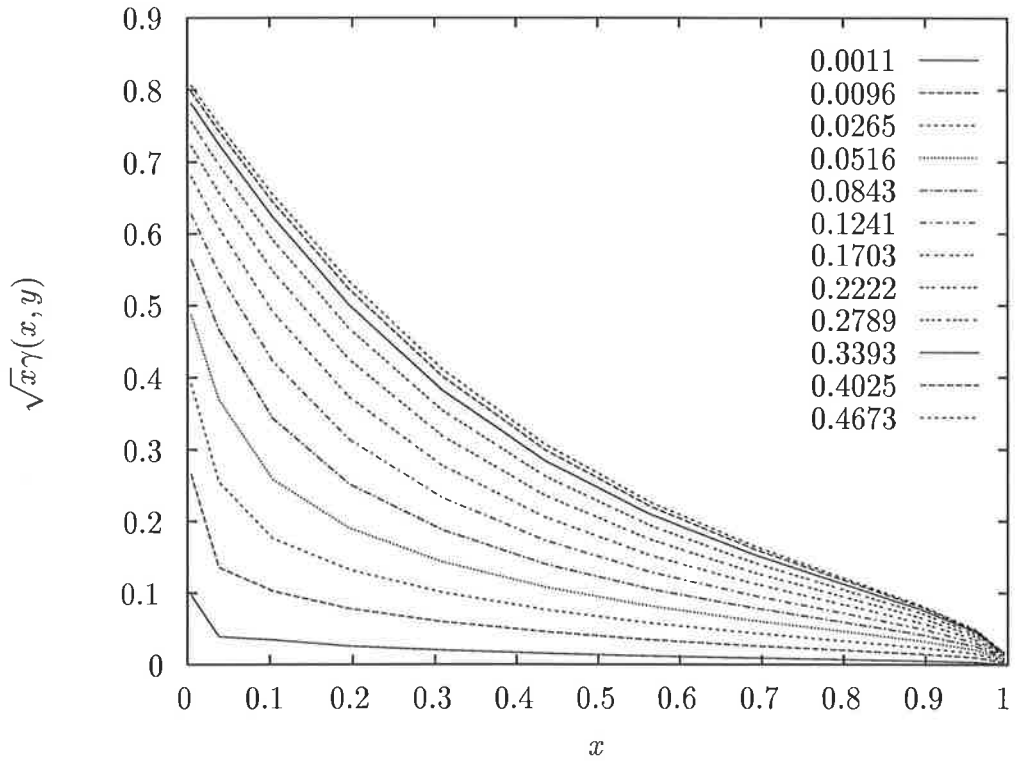

Figure 1.10: *Effect of correcting the leading edge kink for a three-dimensional square planform wing by direct inclusion of the kernel correction term, with* $m = 12$ *and* $n = 12$.

1.5 Curved Panels

The problem of resolving the behaviour of the leading edge loading near the wingtips arguably depends upon the ability to correctly represent the wing planform with non-rectangular panels. It is unclear how the sweep angle of the leading edge effects the load

singularity there and it is plausible that some vital aspect of the geometry might not be adequately captured by a rectangular mesh, no matter how finely approximating the true shape of the wing boundary. On the other hand, all that is sought is an accurate estimate of the influence of the loading on each main panel on each of the collocation points and this ought to be specified to arbitrary accuracy by just such a configuration. Figure 1.11 shows the approximation of a circular geometry by a Chebyschev rectangular mesh as used in Tuck's and the present method.

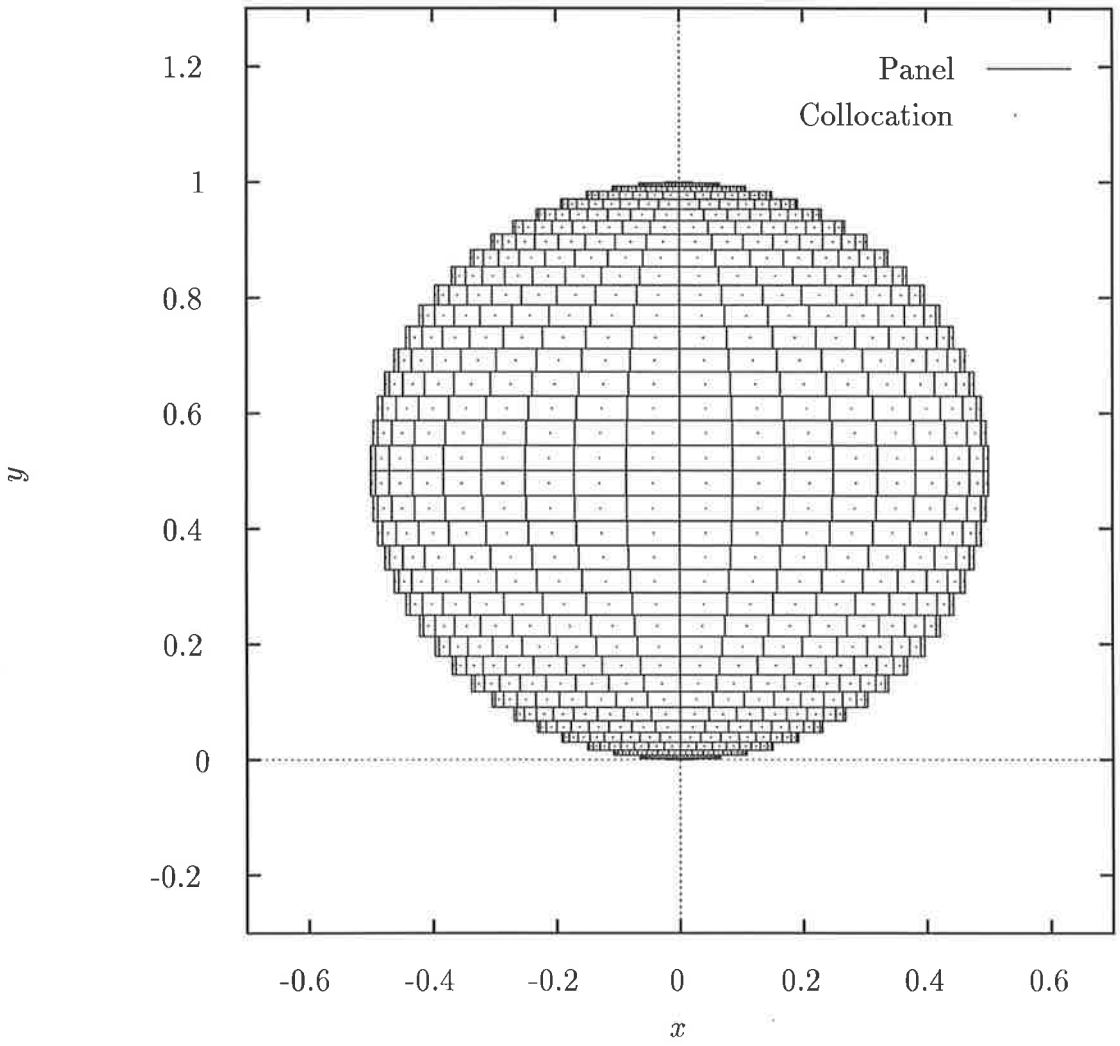

Figure 1.11: *The rectangular panelisation of a circle using a Chebyschev distribution of* $n = 18$ *spanwise strips, each of which has* $n = 18$ *Chebyschev distributed chordwise panels.*

The only obvious shortfall is the self-influence of the panels in the vicinity of the leading edge, where the local geometry might be far from rectangular. Even though the sensitivity of the point loading to the collocation position is far less for the constant loading panel

methods than for the vortex lattice methods, the results for the leading edge singularity strength can be significantly altered by moving the collocation points in the panels close to the leading edge. This in itself is an indication of the art required to produce accurate results for this particular output quantity using any scheme.

The curved panel method of Lazauskas is an extension of Tuck's panel method. It is arguably a misnomer, because the main panels are not actually curved, but are approximated by a spanwise subpanelling technique as illustrated in Figure 1.12.

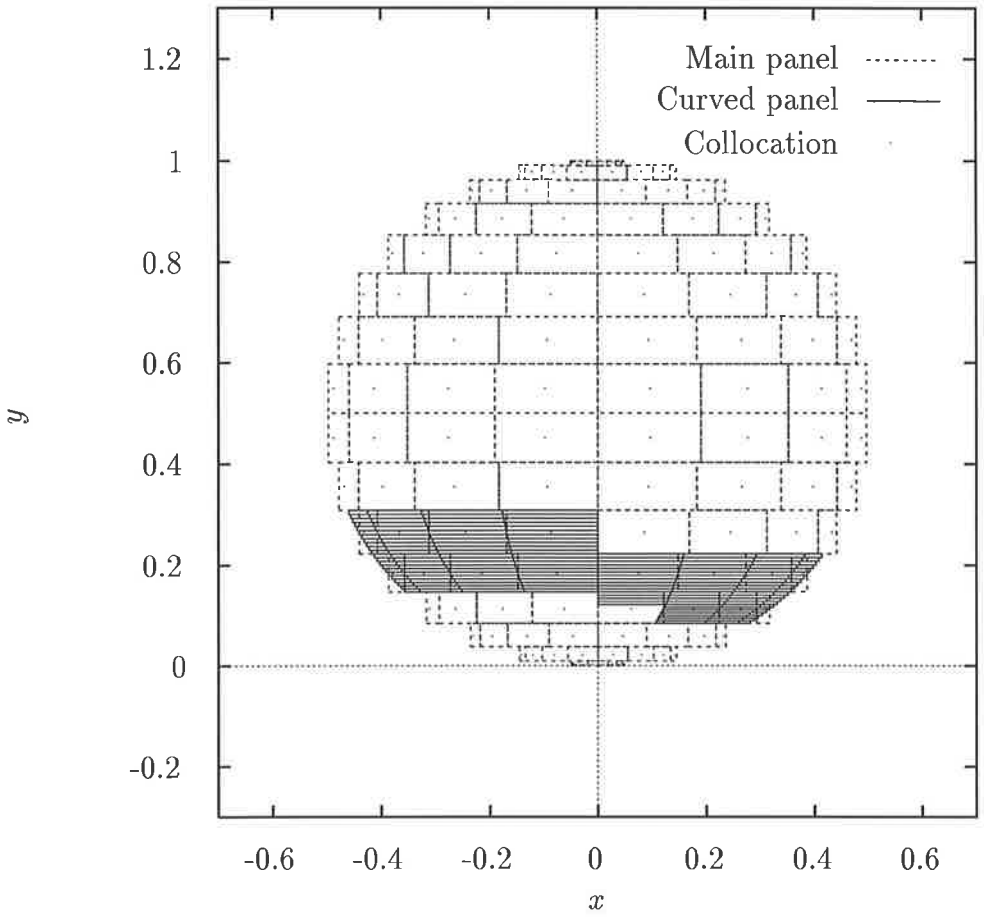

Figure 1.12: *The curved panel method of Lazauskas. For clarity, not all curved panels have been shown. Note that the curved panels are constructed by means of a spanwise subpanelisation and that the original collocation point for the rectangular mesh is still valid as the collocation point for the curved grid.*

The vorticity is assumed constant on each subpanel within a main panel and has the same value as the main panel. In the limit as the number of spanwise subpanels n_s tends to infinity, the planform of the wing will be exactly modelled without the need to invert a matrix where the influence of every subpanel must be considered separately. Like the

chordwise subpanelisation method, this is an attempt to include more information in a matrix prior to inversion. This is a noteworthy point. Since the task of matrix inversion is so computationally expensive, there should be an optimal balance point between work spent on setting up the matrix and work done in solving the resulting system of equations. In the case where the relationship between the system variables and the desired output is complicated by the process of compressing the matrix in this way, there is also the additional work to be done in recovering the meaningful output. Essentially, solving the subpanelised model may be regarded as solving a full system of equations for the loading on each subpanel, where there is a known relationship between the unknowns on the same main panel. Clearly when the wing planform is rectangular, this method is equivalent to the panel method of Tuck.

It is also advantageous to vary the number of subpanels across the span, thereby using more subpanels where the main panels are highly skewed. Two methods have been implemented so far. In the first, the number of subpanels varies linearly from the midspan to the wingtip, and in the second, the distribution of subpanels is based on the first derivative of the function defining the leading edge. This method appeals because of the "automated" allocation of subpanels for arbitrary geometry and the consequent increase in resolution near the tips. In practise, because an enormous number of subpanels are prescribed when the derivative approaches zero (such as at the tip of an elliptic wing), the number of subpanels is "normalised" according to the maximum memory space allocated to subpanelling. For example, on a circular wing with 16 spanwise and 16 chordwise panels, and allowing a minimum number of 4 subpanels, this option allocates the following distribution from midwing to tip $n_s = (4, 12, 22, 34, 50, 76, 134, 412)$.

1.6 Results for a Square Wing

As there are a number of separate numerical issues concerning the representation of curved planform surfaces, we first present comparative results for the simpler case of a square wing plan. Results are given for the various arrangements of the vortex lattice method as well as for Tuck's original panel method and the present panel method with the direct inclusion of the kernel correction.

1.6.1 Lift Coefficient

The most numerically robust quantity to use to compare the various methods is the lift coefficient. Since all the methods to be examined are linear with respect to the angle of attack α_W, the quantity C_L/α_W will be used. A summary of the extrapolated results for the methods discussed is given in Table 1.13.

$$C_L/\alpha_W = C + A \times 10^{-5} \times (10/m)^M + B \times 10^{-5} \times (10/n)^N$$

Method	Chord	Span	C	A	B	M	N
VLM	Lan	Cheb.	1.46022691	-7.44	-6.44	2.853	2.833
VLM	Lan	DeJa.	1.46022702	-7.32	-5.04	2.817	2.660
VLM	Stark	Cheb.	1.46022694	-6.59	-6.42	2.776	2.825
VLM	Stark	DeJa.	1.46022695	-6.73	-5.10	2.802	2.695
Tuck	Cheb.	Cheb.	1.46022679	18.74	-6.41	3.237	2.859
Present	Cheb.	Cheb.	1.46022714	-27.27	-6.41	3.155	2.859

Figure 1.13: *Asymptotic values and convergence rates for the lift coefficient C_L/α_W for a square wing planform. The modifications to the vortex lattice method are listed for the chordwise and spanwise distributions of gridpoints.*

We notice that the error cancellation effect in the lift coefficient of Tuck associated with opposite signs of the coefficients A and B is not apparent in the present solution or any of the vortex lattice methods. In the original method of Tuck, this cancellation can be used to numerical advantage by carefully selecting the number of chordwise and spanwise points. Of the vortex lattice methods, Lan's method is slightly better than the others both in accuracy and convergence. DeJarnette's modifications improve the initial estimates but result in a slower rate of convergence and is not considered further. In any case, all methods tabulated yield a highly satisfactory accuracy of at least 6 figures for C_L/α_W. This accuracy is however, not reproduced by some other output quantities.

1.6.2 Spanwise Circulation

The next most numerically robust output quantity of interest is the spanwise distribution of circulation $\Gamma(y)$. We present a graphical illustration of the degree of similarity between

the various methods in Figure 1.14.

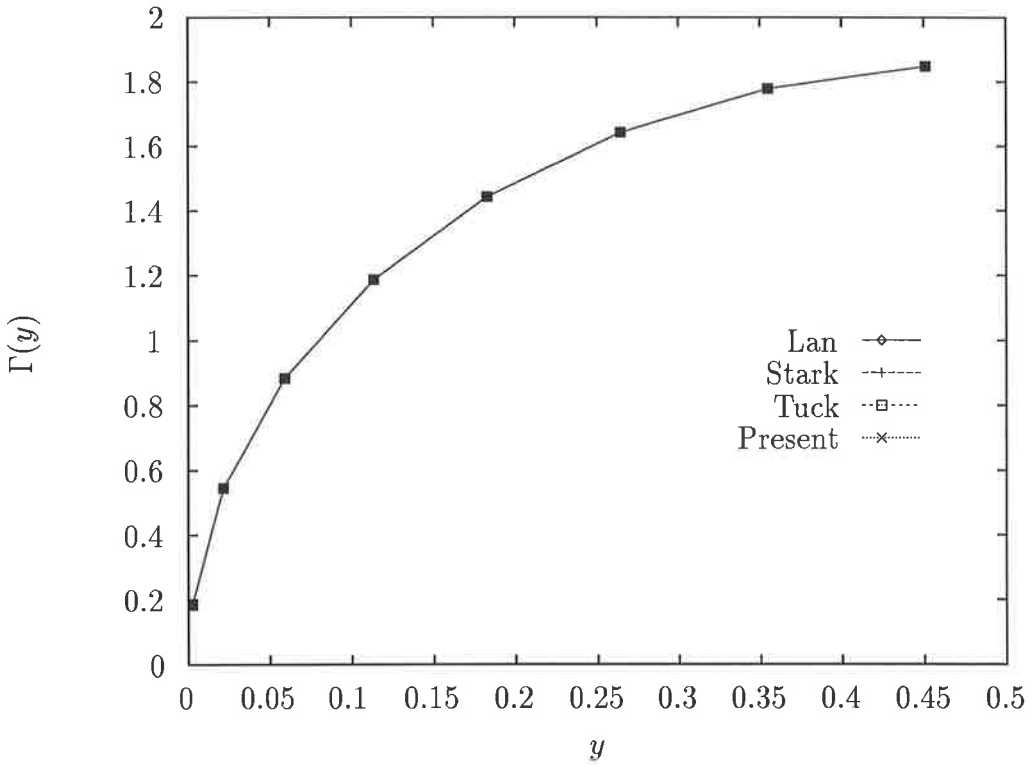

Figure 1.14: *Spanwise circulation* $\Gamma(y)$ *for a square planform wing of unit chord and span. The wingtip is located at* $y = 0$. *Similar results are obtained by Lan's and Stark's schemes for the vortex lattice method, Tuck's panel method and the present panel method. They differ at most in the fifth decimal place. In all cases* $n = m = 16$.

1.6.3 Pointwise Loading

It is possible for a numerical method to obtain acceptable results for integrated forces while examination of the pointwise data reveals relative errors significantly larger than the global error. This may be because of error cancellation, such as grid scale oscillations with approximately zero sum, or because the large relative errors are confined to a small area of the model, where their contribution to global forces is limited.

The loading on a square planar wing in free air is shown in Figure 3a. The loading drops to zero at the wingtips and at the trailing edge.

The accompanying figures in this section compare the pointwise wing loading $\gamma(x, y)$ for the methods described above. Rather than give results for the entire wing, chordwise strips at the midspan and the wingtip are presented as representative. The midspan strip in general provides an indication of the effect of the leading-edge singularity and

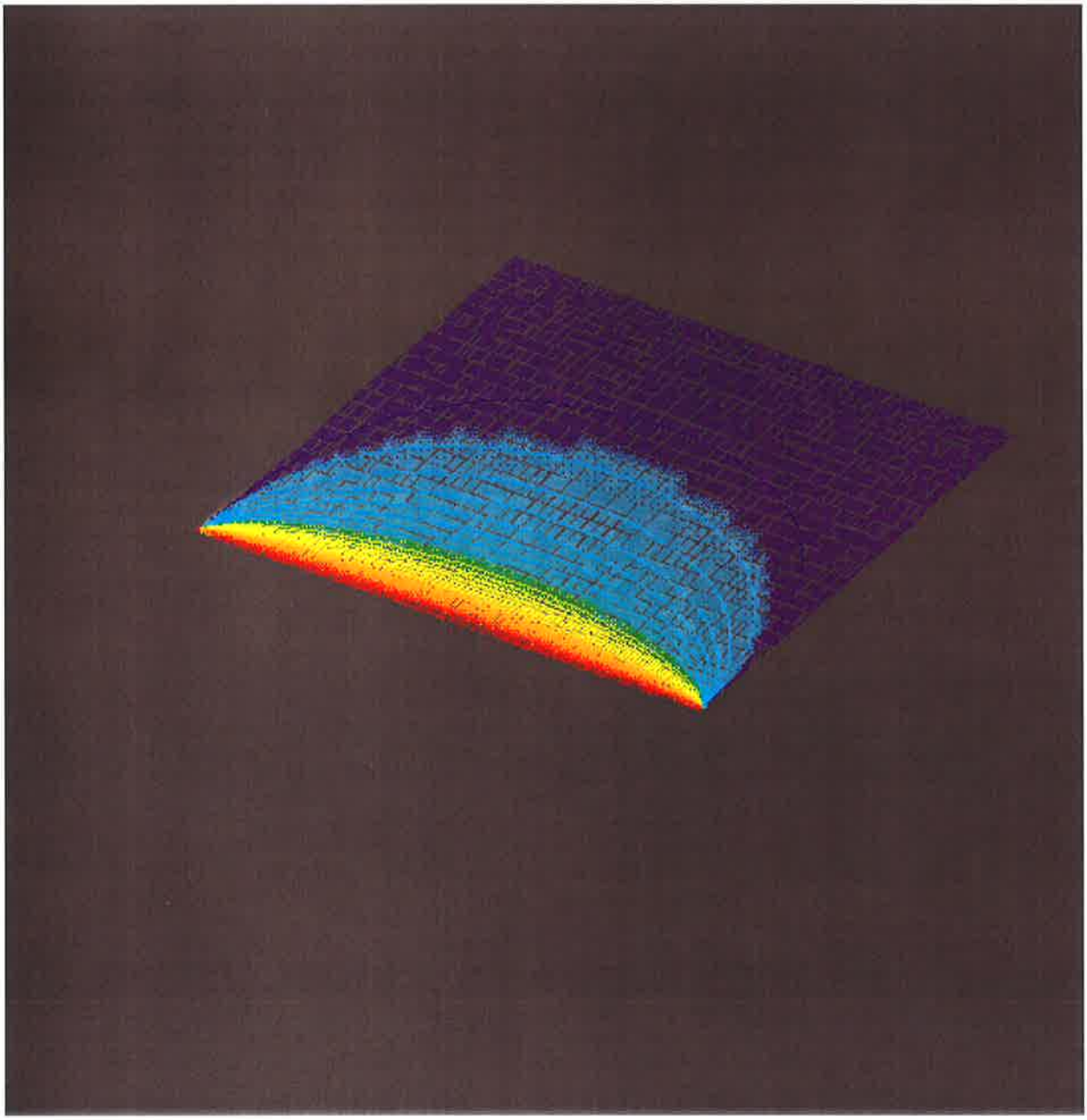

Figure 1.15: *The wing loading of a bare square wing with constant downwash in free air. calculated using* $n = m = 18$ *spanwise and chordwise panels and visualised using the AVS graphics package.*

the wingtip result adds to this the effect of the spanwise singularity. In order to highlight the deficiencies that all methods have with regard to the leading-edge singularity, the quantity plotted is $\gamma(x, y)\ \sqrt{x - x_{LE}}$ versus x. As the singularity at the leading edge is dominantly inverse square root in nature, this graph should have a finite vertical axis-intercept, namely the leading-edge singularity strength $Q(y)$.

Figure 1.16 shows the output for Lan's and DeJarnette's schemes at the midwing $y \simeq s/2$ and at the wingtip $y \simeq 0$ for $n = m = 16$. Note that the spanwise location of the tipmost

section is different for these two vortex-lattice-type methods. Similarly Figures 1.17 shows the output for Tuck's and the present panel scheme. Note that the leading edge kink in the loading in the constant loading panel method of Tuck has been removed in the present improved method at the midwing location. As expected, because of the careful lattice arrangement, the kink at this spanwise location is also negligible in the modified vortex lattice methods. We note here that all four methods illustrate that the singularity is not clearly of a square root nature at the tip.

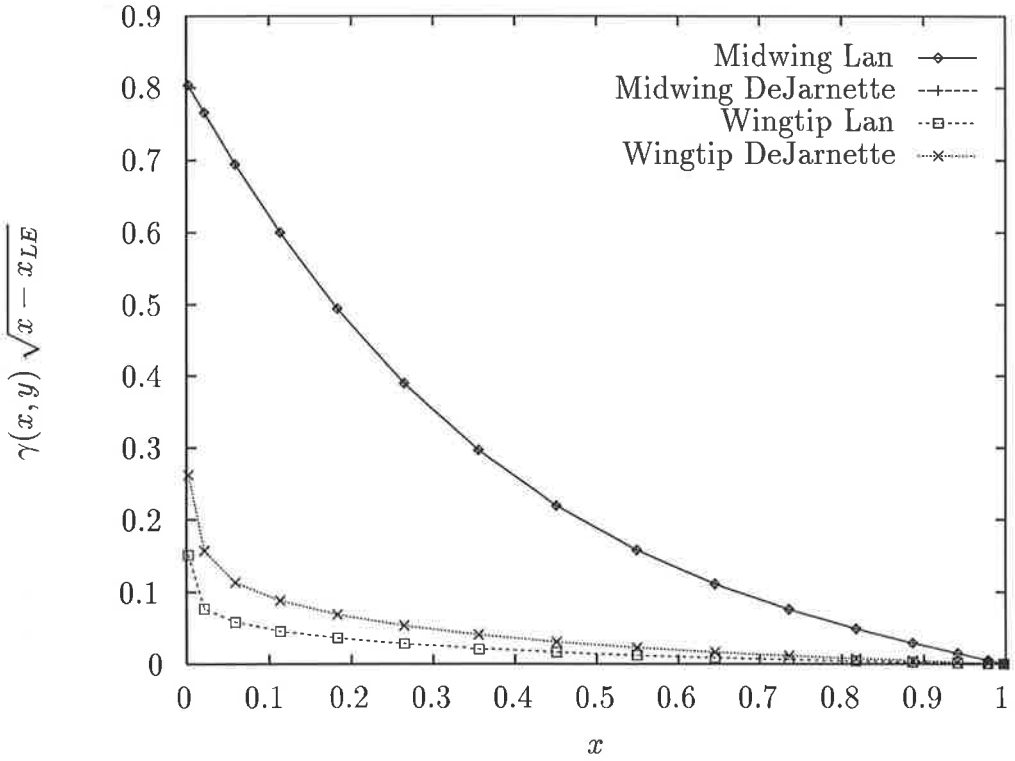

Figure 1.16: *Pointwise loading for a square wing with the square root singularity removed calculated using* $n = m = 16$. *The loading* $\gamma(x, s/2)\sqrt{x - x_{LE}}$ *is plotted over the chord at the tipmost and midwing sections for Lan's and DeJarnette's lattice-type schemes.*

1.6.4 Leading-Edge Singularity Strength

The leading-edge singularity strength (LESS) $Q(y)$ is the coefficient of the extrapolated value of $\gamma(x, y)\sqrt{x - x_{LE}}$ as $x \to x_{LE}$. Figure 1.18 illustrates the form of this coefficient as a function of spanwise location using the present method with 24 spanwise and 24 chordwise panels.

From the previous section, it is clear that Lan's, Stark's and the present method are well correlated for this quantity in the case of a square wing. Consequently, only the data

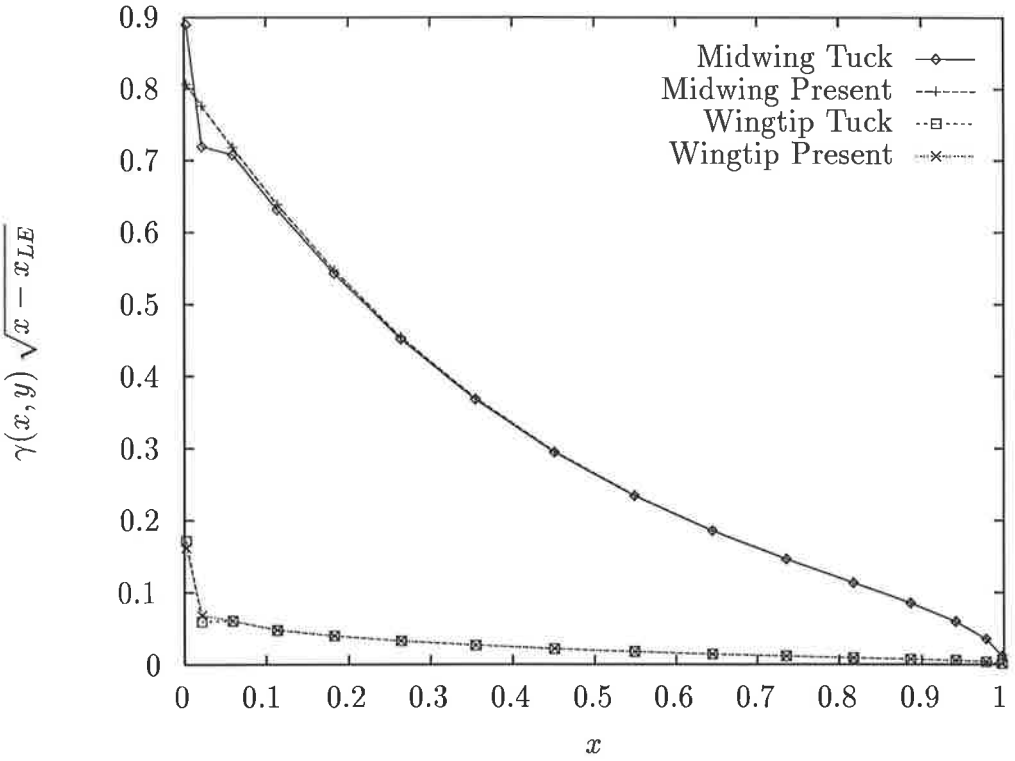

Figure 1.17: *Pointwise loading for a square wing with the square root singularity removed calculated using* $n = m = 16$. *The loading* $\gamma(x, s/2)\sqrt{x - x_{LE}}$ *is plotted over the chord at the tipmost and midwing sections for Tuck's and the present panel methods.*

for the present method is shown. In the case of a circular wing, there will be significant differences.

It is clear that for a square wing the LESS $Q(y)$ tends to zero at the tip $y = 0$ and that there is an infinite slope in the graph of $Q(y)$ as $y \to 0$ at the tip. Numerically determining the precise asymptotic behaviour of $Q(y)$ at the tip is extremely difficult; however based on the data produced with $n = m = 12, 24$ and 48, a two-figure estimate for the zero singularity strength is $Q(y) \sim y^{0.32}$ at the wingtip $y \to 0$.

1.7 Non-Rectangular Planforms

The problem of applying the previous solution methods to a wing where the chord vanishes at the tips lies in the resolution of the leading-edge and wingtip singularities. Determination of the true nature of the of the tip singularity is the key to the complete solution of the analytic problem (Jordan, 1974). Since this information is missing, and collocation methods are based on analytic models, they are particularly unreliable at and

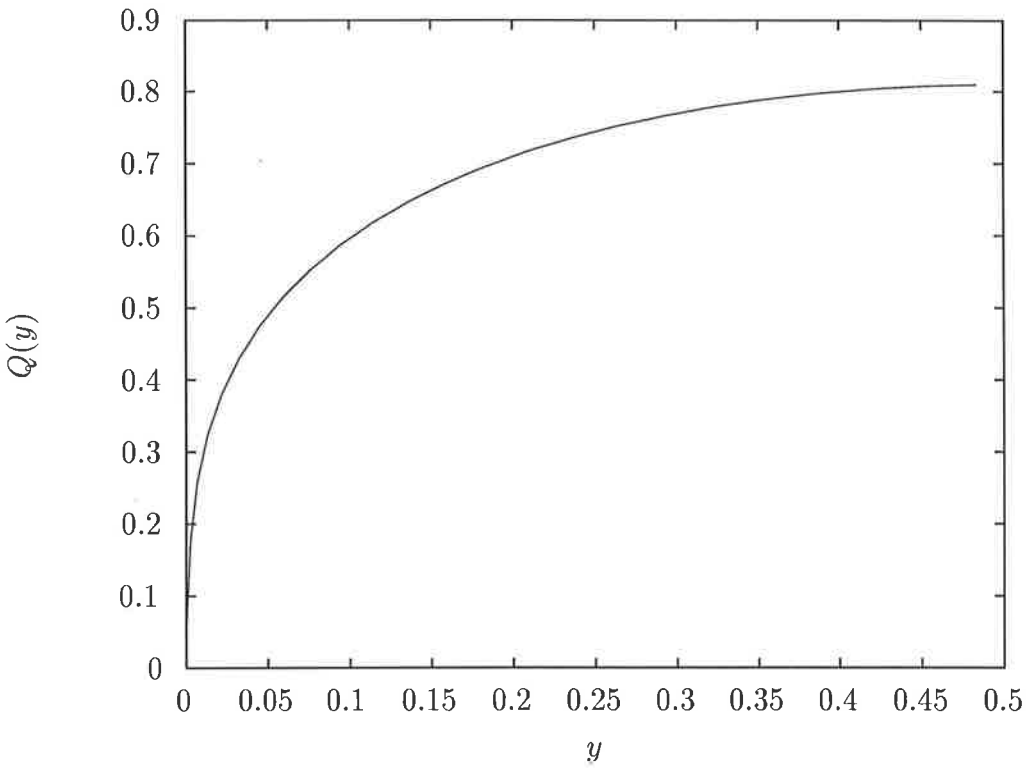

Figure 1.18: *The spanwise variation of the leading-edge singularity strength (LESS) for a square wing, calculated using the present method with* $m = 24$ *and* $n = 48$.

near the tips.

In particular, for a wing whose planform is parabolic at the tips, classical lifting line theory suggests that the strengths of the two singularities should exactly cancel. The two known wing edge pressure singularities, of order $(x - x_{LE})^{-\frac{1}{2}}$ at the leading edge and of order $(x_{TE} - x)^{+\frac{1}{2}}$ at the trailing edge, meet at a single point. It is in fact not very easy to visualize a composite tip singularity which performs a transition between the two different edge singularities (Jordan, 1974).

In this Chapter, we are not interested in the effects of specific geometry or aspect ratio and so the analysis is confined to the simplest planform which exhibits the above property, namely the circle.

1.8 Results for a Circular Wing

As for the square wing, results are given for the various arrangements of the vortex lattice method as well as for Tuck's original panel method and the present panel method with the direct inclusion of the kernel correction.

1.8.1 Lift Coefficient

The accurate numerical computation of the lift coefficient, C_L/α for a circular wing is of distinct interest to the world aerodynamic community. There are two existing analytic solutions for the case of a flat circular wing which differ in their prediction of the lift coefficient in the fifth significant figure. Agreement of the present numerical scheme with either of the two models would provide significant support for the assumptions upon which the favoured analytic model were based. Jordan (1973), whose analysis following Prandtl and Kinner made use of a simple representation of the leading coefficients of the basis Legendre functions, gives $C_L/\alpha = 1.7900230$ whereas Hauptman (Hauptman and Miloh, 1986) proposes the value $C_L/\alpha = 32/(8+\pi^2) = 1.7907503$, also using a series of Legendre functions and representing the circular wing as a degenerate oblate spheroid. Both analytic solutions are expressed as the sums of infinite series, so determination of the correct formulation might provide useful insight into the true nature of the loading at the tips. In subsequent personal communication, the second author of the latter method reported that the Kutta condition was in fact satisfied only in an average manner and therefore that the Jordan result should be regarded as more accurate in this sense.

Using the same method of extrapolation as was applied to the case of the square wing is not entirely satisfactory in the case of the circular planform. Asymptotic coefficients for Tuck's panel method, the present method and the curved panel method of Lazauskas are calculated from results with m and n independently varied with values $12, 24$ and 48. For the curved panel method, extrapolation to an infinite number of subpanels was made using $p = 64, 128, 256$ subpanels.

Unfortunately, for the panel method of Tuck and the present method, such a tableau is of limited value. The results are shown in Table 1.19.

It is tempting to believe that the extrapolated value of $C_L/\alpha_W = 1.79024579$ for the present method is in support of the analytic method proposed by Jordan. However, the tableau used to produce the least squares asymptotic results is somewhat oscillatory, depending on the relative magnitudes of n and m. It is not even possible to obtain an extrapolated value for Tuck's method using this data. This because for rectangular panels, an increase in the number of chordwise panels causes a larger proportion of panels to intersect the edge of the wing. An increase in the number of spanwise panels reduces this proportion. Thus the curved-panel method of Lazauskas is the only scheme with

Tuck	$n = 12$	24	48
$m = 12$	1.7942341775749	1.7918544390226	1.7908781829830
24	1.7942161310811	1.7918749529351	1.7908652637469
48	1.7942128704278	1.7918844214374	1.7908933530325
Present	12	24	48
12	1.7939175509580	1.7915567896180	1.7905968241995
24	1.7941437959117	1.7918047118664	1.7907984861273
48	1.7941957837602	1.7918675769909	1.7908768443562

Figure 1.19: *Results for the lift coefficient C_L/α_W for a wing of circular planform. The data obtained for Tuck's panel method and the present method differ but oscillate with respect to the number of chordwise and spanwise panels.*

which a fully extrapolated value can be found. It is clearly shown in Table 1.20.

$$C_L/\alpha = C - A \times 10^{-4} \times (10/m)^M + B \times 10^{-4} \times (10/n)^N$$

Method	Chord	Span	Collocation	C	A	B	M	N
Curved	Cheb.	Cheb.	Cheb.*	1.78997313	4.725	-22.5	3.5	1.10

Figure 1.20: *The extrapolated value and convergence behaviour for the lift coefficient of a circular planform wing using the curved panel method of Lazauskas. * - Whether the collocation point here is actually Chebyschev spaced given the relative panel geometry is unclear. Determining exactly where the appropriate Chebyschev collocation point is may hold the key to higher accuracy.*

Despite the oscillations in the results for the rectangular panel methods, it is still clear that the results must approach a single value. When the present method is applied with $n = m = 72$, the raw result is a lift coefficient of $C_L/\alpha_W = 1.7905408$. By generating a statistically large number of results with large panel numbers, sufficient evidence might be procured to eliminate one or both of the contending analytic solutions. Another approach is to ensure monotone convergence by setting $n = m$. The present method using $n = m = 12, 24$ and 48 then predicts that $C_L/\alpha_W = 1.7901502968$, with a rate of convergence proportional to $(10/m)^{1.12}$. This is not conclusive evidence against Jordan's

value because the ratio of n to m is arbitrary. By selecting different ratios, one can manipulate the extrapolated value. It seems that there is a numerical issue that is difficult to resolve without the use of non-rectangular panels. The following table, reproduced in part from Hauptman and Miloh (1986) with the current results added, compares the lift and moment slope coefficients for a circular wing. It is reasonably clear that the analytic solution proposed by Hauptman and Miloh is not supported beyond 3 figures by this numerical investigation, though the solution of Jordan is not clearly verified beyond 4 figures, either.

Method	C_L/α_W	$-C_M/\alpha_W$
Present solution	1.7900	0.4661
Hauptman and Miloh	1.790750	0.46882
Jordan	1.790023	0.46617
Kida	1.790	0.466
Levey and Wynter	1.790	0.4663
Kinner	1.81741	0.4679
Van Spiegel	1.7902	0.4663
Krienes and Schade	1.7984	0.466
Robinson and Laurman	1.7596	-
Medan	1.790	0.4662
Watkins *et. al.*	1.7910	0.4694
Prandtl lifting line	2.444	0.611

Table 1.4: *Lift-slope and moment-slope coefficients for a flat circular wing from various sources, both numerical and analytic.*

1.8.2 Circulation

Numerous attempts, both analytic and numeric, have been made to exactly quantify the behaviour of the circulation $\Gamma(y)$ as $y \to y_{TIP}$ for the circular planform flat plate wing (Jordan, 1974, page 473, Equation 6.2) (Hauptman and Miloh, 1986, page 48, Equation 30) and (Boersma, 1989). This is an important matter, because the rate at which vorticity is shed at the wingtips is directly related to the visible wingtip vortices which are the

primary sources of aerodynamic induced drag. A summary of some recent results is given in Table 1.5. Included with this data is an unpublished result (Miloh and Tuck, 1993) obtained upon slight modification to the analysis of Hauptman.

Again, Jordan's result is supported more than any of the others. An extremely large number of panels is likely to be required in order to pursue this matter further. This will also need more than standard double precision for machine accuracy because of the vanishingly small size of the panels near the wingtips with a Chebyschev style grid.

$$\Gamma(y) \simeq A \times \sqrt{y} + B \times y \log y - C \times y + \ldots$$

Method	(Num/Analy)	A	B
Jordan (1974)	Analytic	3.186	-0.2819
Hauptman & Miloh (1985)	Analytic	2.813	-0.497
Miloh & Tuck	Analytic	3.456	N/A
Present	Numeric	3.21	-0.58

Table 1.5: *Estimates for the spanwise circulation* $\Gamma(y)$ *at the wingtip* $y \to y_{TIP}$ *for a circular wing.*

1.8.3 Pointwise Loading

The most obvious negative feature of the pointwise loading predicted by the vortex lattice methods is a catastrophic loss of accuracy at the wingtip, illustrated in Figure 1.21 for Lan's and DeJarnette's schemes. By contrast, the rectangular panel methods produce relatively well-behaved results at both the midwing and the wingtip, as seen in Figure 1.22.

The vanishing chord length at the tip of a circular wing has unsettling effects on all the numerical methods so far discussed. In the schemes primarily suited for two-dimensional flow, such as the vortex lattice methods, highly converged results for the total lift may be produced from pointwise loadings that are rather unsatisfactory at the wingtips. Certainly all methods have a tendency to propagate numerical errors along the leading edge from the wingtip towards the mid-span. The source of the original error may be a catastrophic loss of accuracy near the tip, or the severe grid mismatch in the chordwise

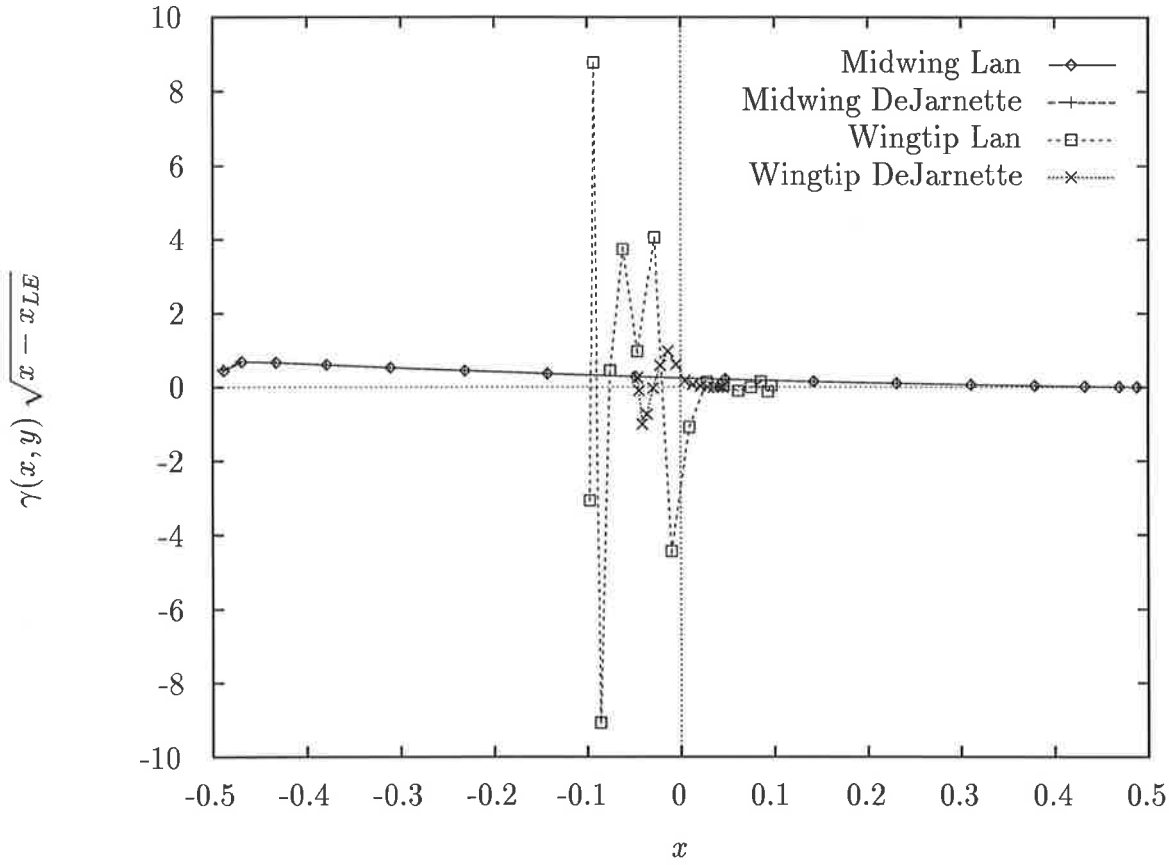

Figure 1.21: *Pointwise loading for a circular wing with the square root singularity removed calculated using* $n = m = 16$. *The loading* $\gamma(x, s/2)\sqrt{x - x_{LE}}$ *is plotted over the chord at the tipmost and midwing sections for Lan's and DeJarnette's lattice-type schemes.*

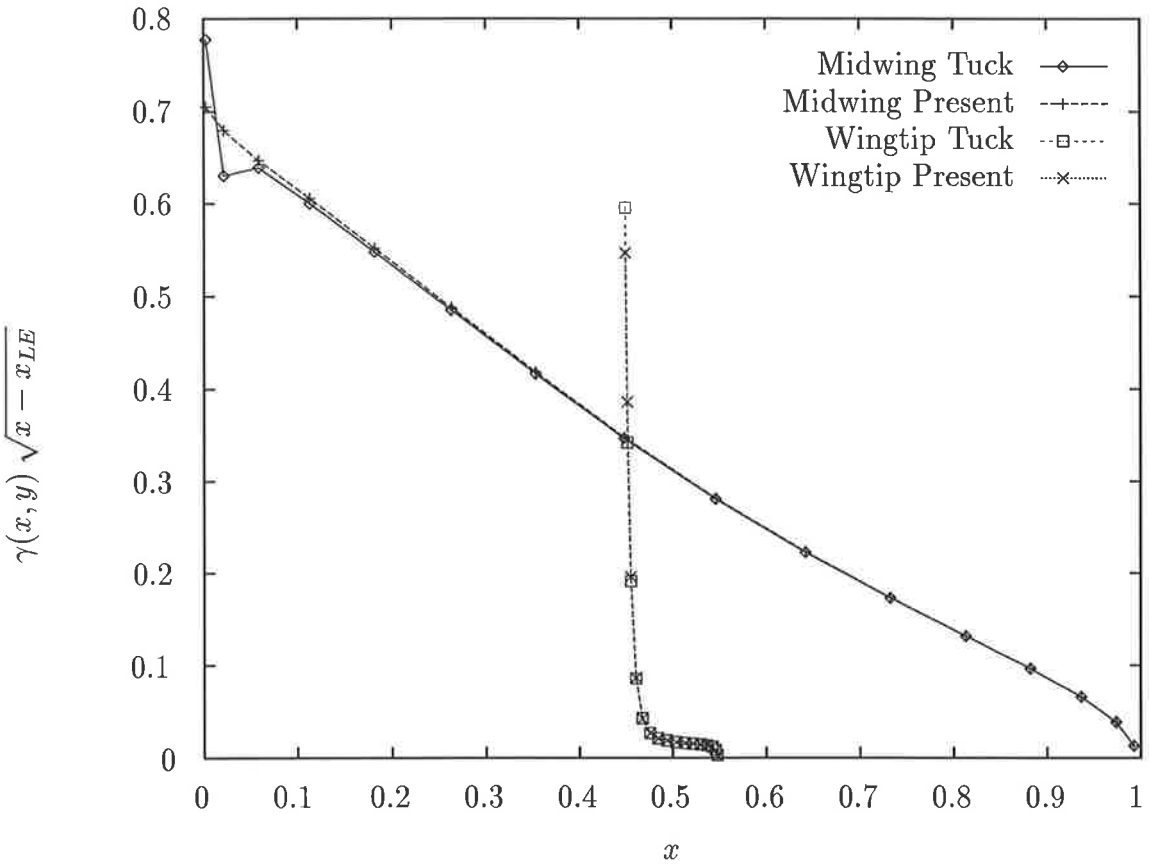

Figure 1.22: *Pointwise loading for a circular wing with the square root singularity removed calculated using* $n = m = 16$. *The loading* $\gamma(x, s/2)\sqrt{x - x_{LE}}$ *is plotted over the chord at the tipmost and midwing sections for Tuck's and the present panel methods.*

dimension at the tip.

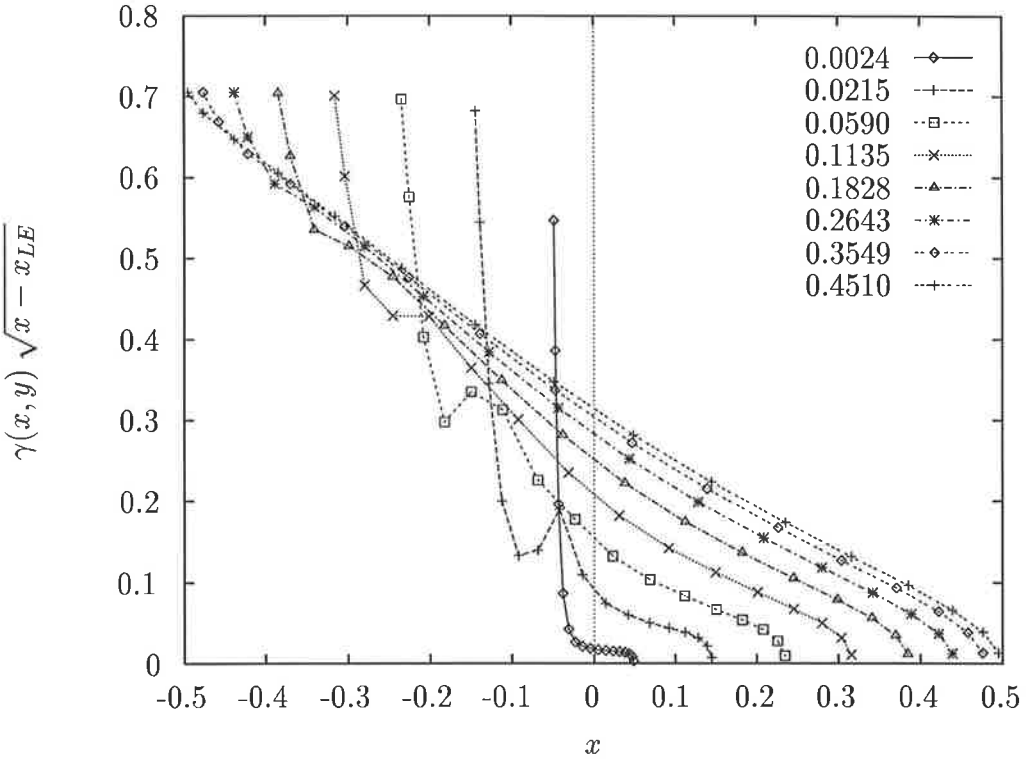

Figure 1.23: *The pointwise loading with leading-edge singularity removed, for a circular wing calculated using the present panel method with* $n = m = 16$. *The extreme numerical error in the pointwise loadings in the present scheme is caused by the spanwise grid mismatch. The leading edge panel for one chordwise strip may be spanwise adjacent to a larger panel that is not at the leading edge of its chordwise strip. There is consequently a false distribution of loading that is propagated spanwise near the leading edge.*

Because of the rectangular panelisation, adjacent chordwise strips for non-rectangular planforms can be significantly mis-aligned, especially at the wingtips. Figure 1.23 shows all chordwise strips of the present panel method solution for the circular wing, using $n = m = 16$. Note that the loading of the tipmost chordwise section using the present method appears to be smooth, but that the section closest to it has a kink, or bulge at the chordwise location of the singularity in its tipmost neighbour. This effect is propagated along the leading edge, although the effect is most pronounced at the tip, where the leading-edge is most swept. One of the appealing aspects of the curved panel method of Lazauskas is that this effect is markedly diminished. Unfortunately, a very large number of subpanels is required to reduce the effect. Figure 1.24 shows the pointwise loading obtained by using the curved panel method with $n_s = 100$ subpanels. The propagated bulge has effectively disappeared, but a kink has been reintroduced to the leading-edge at all

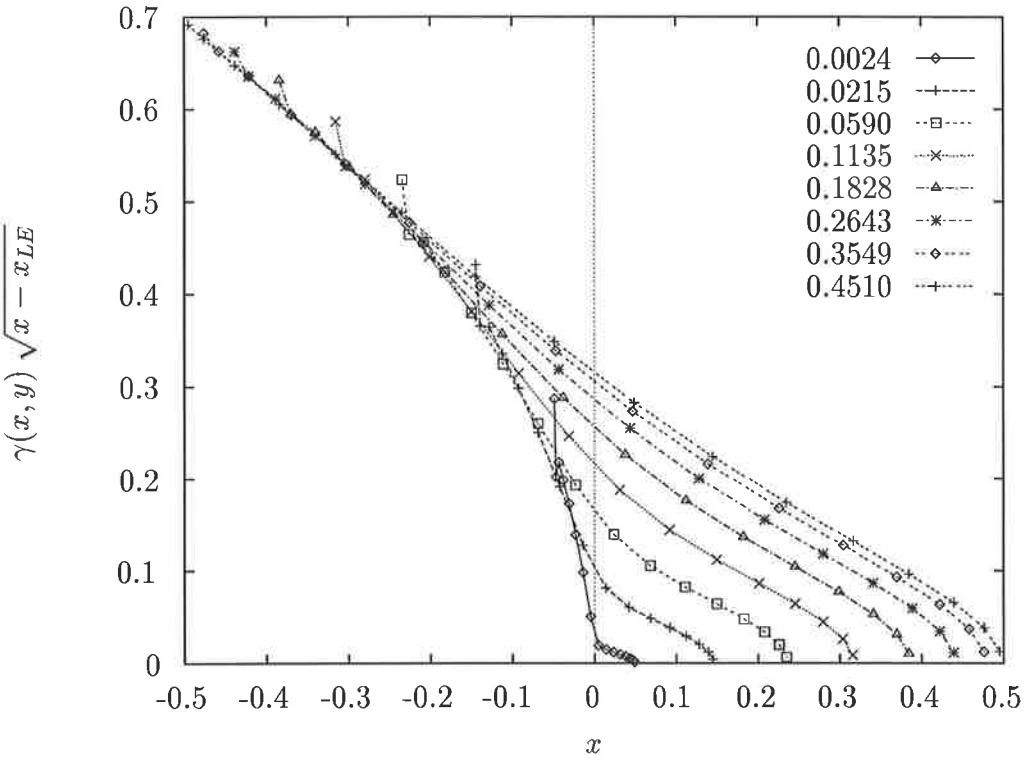

Figure 1.24: *Pointwise loading for the circular wing calculated using the curved panel method of Lazauskas with* $n = m = 16$ *and* $n_s = 100$. *The spanwise propagation of the error caused by grid mismatch has been cured, but at the expense of the resolution of the leading-edge singularity strength.*

spanwise locations. This feature actually also disappears with sufficiently large numbers of subpanels, but the rate of convergence is *logarithmic* with n_s. More importantly, the prediction of the leading-edge singularity strength has completely changed and, as will be shown in the next section, incorrectly.

1.8.4 Leading-Edge Singularity Strength

The leading-edge singularity strength is by far the hardest quantity to determine correctly by any numerical lifting surface method. Noting that the curved panel method and the present method are the same when the number of spanwise subpanels $n_s = 1$, we chart the prediction of $Q(y)$ versus n_s in Figure 1.25.

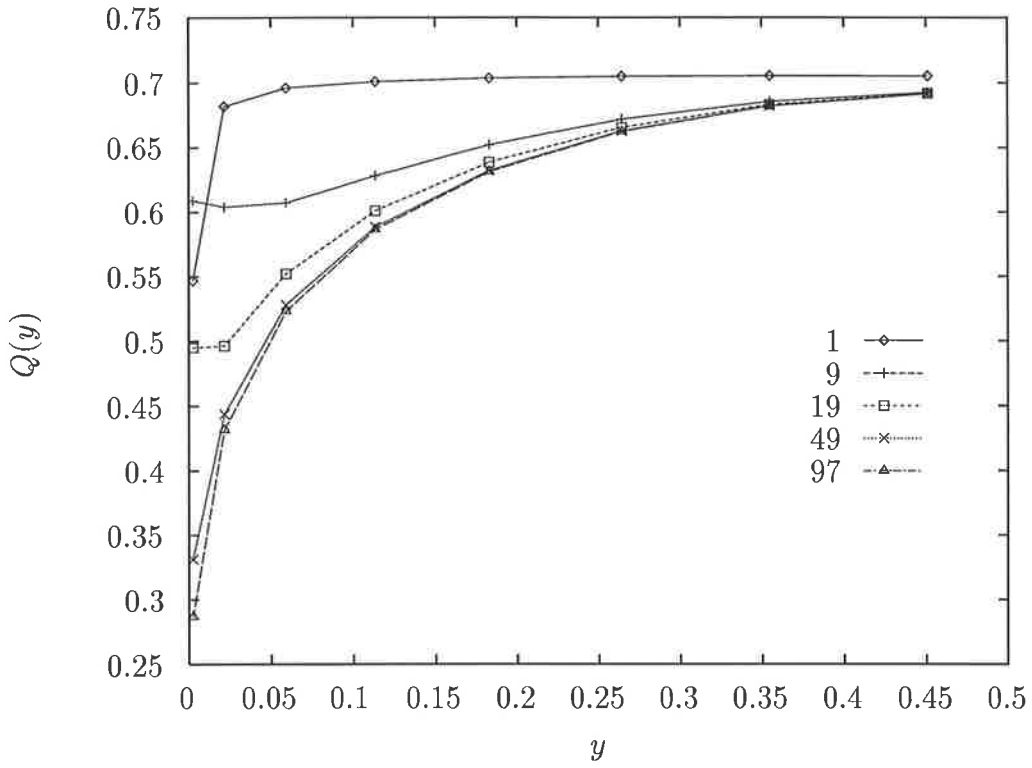

Figure 1.25: *The prediction of the leading-edge singularity strength $Q(y)$ using the curved panel method of Lazauskas with $n = m = 16$ and $n_s = 1, 9, 19, 49$ and 97. There is a distinct change of mode when the panel becomes curved, such that the prediction of $Q(y)$ totally changes.*

It is unfortunate that using the curved-panel method, which so effectively improved the grid mismatching of the rectangular panelisation, introduces such a radical change to the prediction of the leading-edge singularity strength $Q(y)$. The resulting prediction of $Q(y)$ produced an estimate of the leading-edge suction which does not match the corresponding

lift and induced drag estimates. This is presumably due to the extreme change in the self-induced vorticity of the panels near the leading edge and the consequent change in the correct location of the collocation point. In order to demonstrate how sensitive the value of the leading-edge singularity strength is to the choice of collocation points, Figure 1.26 shows how the prediction of $Q(y)$ changes for a rectangular panelisation when the collocation points are moved from the Chebyschev midpoint to the actual midpoint of the panels in the spanwise direction. They are still Chebyschev spaced in the chordwise direction.

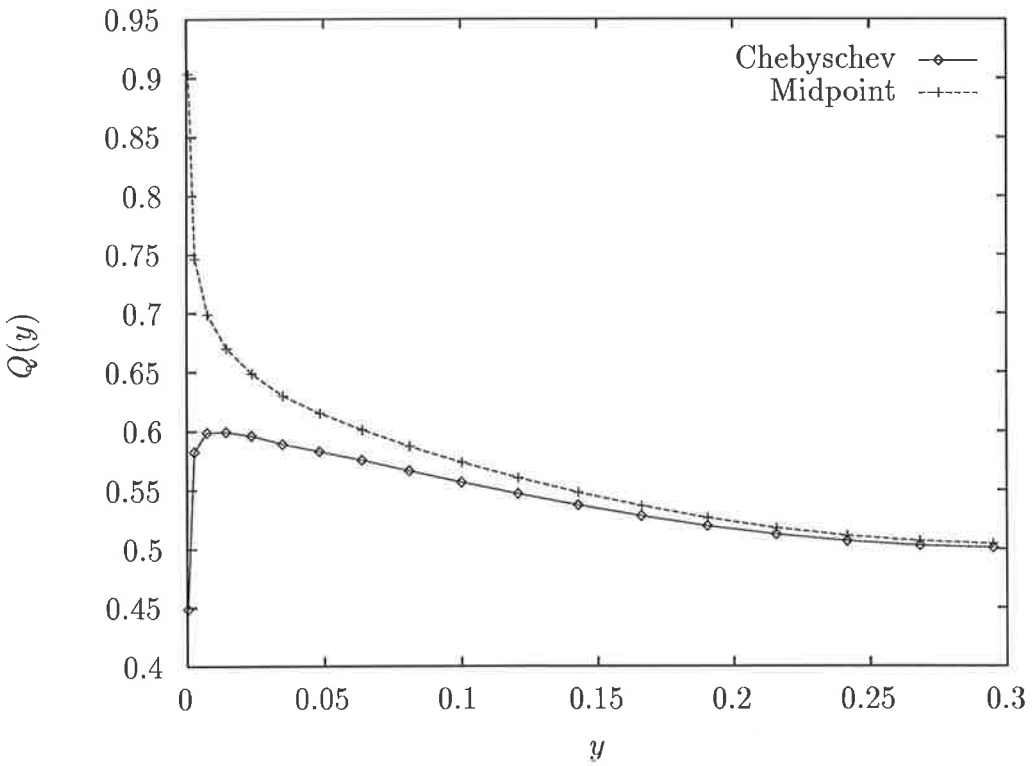

Figure 1.26: *The prediction of the leading-edge singularity strength $Q(y)$ using the present rectangular panel method with leading edge correction. The method is adapted so that the spanwise collocation position is at the actual midpoint of each Chebyschev-proportioned panel. The resulting behaviour of $Q(y)$ differs significantly from the case where collocation is at the Chebyschev midpoint.*

We also compare the prediction of the leading-edge singularity strength with those of Guermond (1989), (1990) and Jordan (1973). Figure 1.27 shows the spanwise variation of the leading-edge singularity strength. Jordan's infinite-series analytic solution predicts a finite value for the leading edge singularity strength at the wingtip, but with an infinite slope as a function of the spanwise co-ordinate, so that the strength drops very rapidly as we move away from the wingtip. For a finite number of panels, the present method (and

Guermond (1989)) suggests incorrectly that the leading edge singularity strength is zero at the wingtip. However, it then rises rapidly to a maximum close to the wingtip, and as the precision of our computation is increased by taking more panels, this maximum moves closer to the wingtip itself, and the results approach those of Jordan.

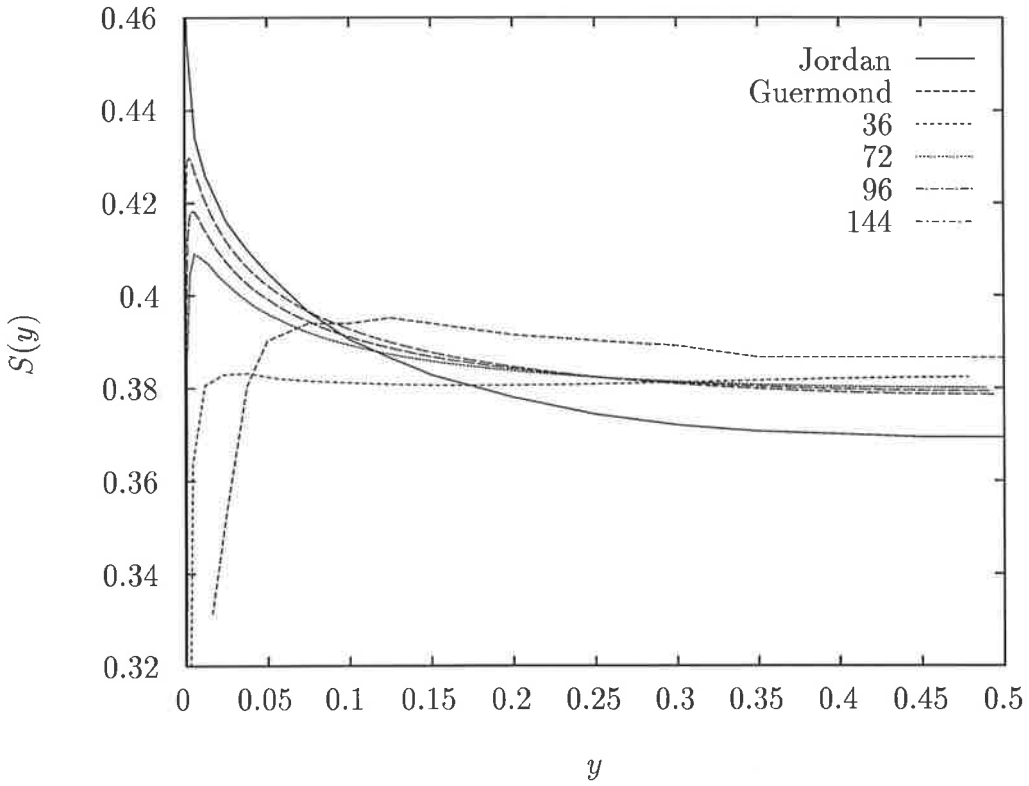

Figure 1.27: *Spanwise variation of the leading-edge singularity strength for a circular planform wing. Results are expressed as the spanwise suction force* $S(y) = \pi/4Q^2(y)$, *where* $Q(y)$ *is the leading-edge singularity strength in the loading* $\gamma(x, y)$, *for* $n = m = 36, 72, 96$ *and* 144.

1.9 Conclusion

The ideal panel method is a marriage of the present rectangular panelisation including the leading-edge kernel correction, with the curved panel method of Lasauskas, in order to obtain spanwise grid continuity. Unfortunately, the use of curved panels to achieve this goal appears to destroy the accuracy in the prediction of the leading-edge suction coefficient.

A large amount of work has subsequently been done in trying to achieve this marriage through correction factors and shifting the collocation points to their "correct" locations,

given the local aggregate panel geometry. No consistent method has been found that will produce both smooth loading and an accurate prediction of the leading-edge suction. Such an investigation, if successful, would hold the key to a fuller understanding of the leading-edge and wingtip singularities.

For the present work however, we shall accept that the present rectangular panel method with the kernel correction provides an accurate estimate for the forces of interest, even with the associated grid mismatching. It is used throughout the remainder of this thesis.

Chapter 2

Suction and Induced Drag

2.1 Induced Drag

Induced drag is a three-dimensional effect that reduces the efficiency of lifting surfaces. Unlike skin-friction drag and parasite drag, which are related to the streamwise flow over the lifting structure, induced drag is a byproduct of the lift force. The pressure difference between the lower and upper wing surfaces tends to circulate fluid from below the wing to above the wing via the wingtips. This causes the wingtip vortices that are illustrated in Figure 2.1. This large rotating fluid body requires energy, which the lifting surface experiences as a drag force. Typically, this induced drag is regarded as representing about half of the total cruise drag of a transport aircraft (Smith and Kroo, 1993), which is directly related to the fuel consumption in straight-and-level flight. Numerous schemes have been proposed for reducing the induced drag of lifting surfaces, including the use of aft swept wing tips following the lunate or crescent-shaped tail fins observable in some birds and fish (Burkett, 1989), (Smith and Kroo, 1993), (Lighthill, 1969); the addition of endplates or winglets which will be discussed in Chapter 3 and flying in close proximity to the ground or water surface which will be addressed in Chapter 4. In nature, birds fly in formations which can increase the overall or group efficiency and squadrons of aircraft, like fleets of ships, often fly in formations which reduce the total drag.

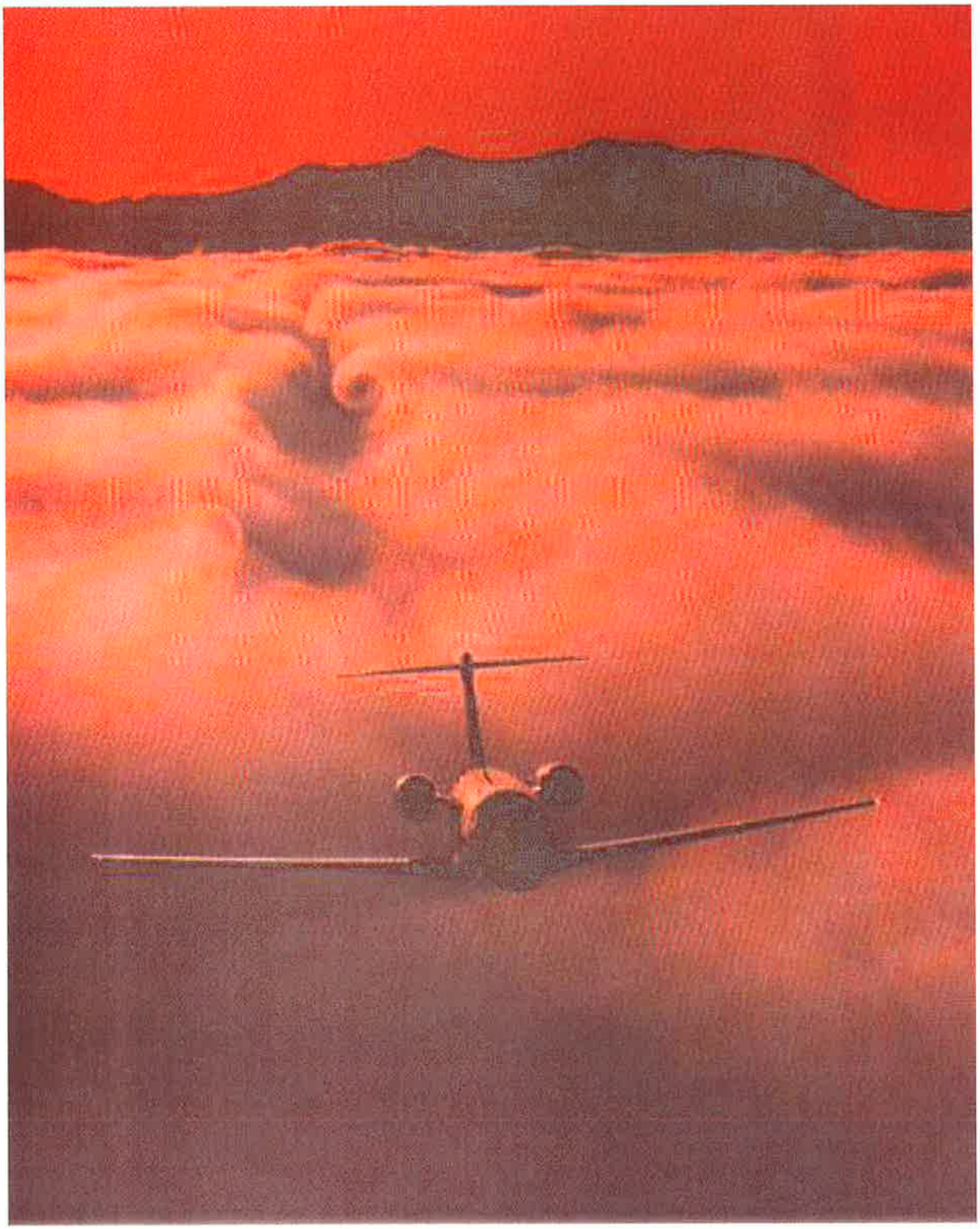

Figure 2.1: *The wingtip vortices are clearly visible in the cloud formation downstream of the Cessna Citation VI. Reproduced from the Gallery of Fluid Motion, special reprint, Physics of Fluids A, Volume 5, number 9, September 1993.*

2.2 Minimum Induced Drag

The field of optimising the ratio of lift to induced drag has been strongly influenced by the work of Max Munk, a student of Ludwig Prandtl. Munk's first theorem, often referred to as the stagger theorem, states that the induced drag of a multiplane system is unaltered if any of the lifting components is moved in the direction of travel, provided that the attitude of the elements is adjusted to maintain the distribution of lift among them. This means that the sweep of a wing is irrelevant to the calculation of induced drag, and that multiple surfaces can be treated simultaneously. All that is important is the distribution of lift in the yz-plane.

The second theorem of Munk allows the induced drag computation to be performed in the Trefftz plane, far downstream of the actual geometry. The benefit of this is that the velocity distribution resulting from the arrangement of trailing vortices is numerically simpler than the fully three-dimensional calculation required locally at the lifting surfaces.

The third theorem of Munk is of specific application to endplates and winglets. It states that when all the elements of a lifting system have been translated longitudinally to a single plane, the induced drag will be a minimum when the component of the induced velocity normal to the lifting element at each point is proportional to the cosine of the angle of inclination of the lifting surface at that point (Blackwell Jr., 1976). This implies that a horizontal lifting surface should have constant downwash and that the sidewash of a vertical component such as an endplate should be zero. This does not mean that the vertical component should have zero loading, but that the sidewash produced on the vertical component by the horizontal wing should be exactly opposed by the sidewash induced on the vertical component by itself. In other words, the induced angle of attack of the vertical component should be zero. This also reduces the downwash and hence induced drag of the wing. In Chapter 3, optimisation with respect to a combination of skin-friction and induced drag will be considered, where Munk's third law will be only asymptotically valid.

Several measures of aerodynamic efficiency are used in the literature to measure lift against induced drag. It is unclear as to which benchmark should be applied, because the theoretical maximum lift to induced drag ratio for a planar wing is undefined when

the wing has infinite aspect ratio. Measures, such as the Oswald efficiency factor

$$e = \frac{C_L^2}{\pi AR(C_{D_i} - C_{D_i}^0)} \tag{2.2.1}$$

may be used to compare the induced drag of an elliptically loaded and therefore optimal wing to a wing of the same span and total lift. This has also been used to define the "effective aspect ratio" of a general lifting surface when endplates are used or when the surface is in ground effect. In such cases the efficiency factor may be greater than one and the effective aspect ratio refers to the aspect ratio of an elliptically loaded wing that provides the same ratio of C_L^2/C_{D_i}. This matter is further discussed in Chapter 3.

2.3 Evaluation of Induced Drag

As stated, the induced drag of a lifting surface (Thwaites, 1960) may be evaluated as the kinetic energy in the Trefftz plane, far downstream and perpendicular to the free stream direction $+x$, namely:

$$D_i = \frac{1}{2}\rho_A \int_{-\infty}^{\infty}\int_{-\infty}^{\infty} (v^2 + w^2)\, dydz. \tag{2.3.2}$$

Assuming a perturbation velocity potential ϕ such that $q = (u, v, w) = \nabla\phi$ then

$$D_i = \frac{1}{2}\rho_A \int_{-\infty}^{\infty}\int_{-\infty}^{\infty} (\phi_y^2 + \phi_z^2)\, dydz. \tag{2.3.3}$$

Stokes Theorem for boundary integration allows us to transform this double integral to a single contour integral

$$D_i = \frac{1}{2}\rho_A \oint_C \phi \left(\frac{\partial\phi}{\partial\hat{n}}\right) ds, \tag{2.3.4}$$

where ds is an element of the trace of the trailing vortices C and $\hat{n}$ is a unit outward normal to this surface. In the case of an infinitely thin trailing vortex sheet, this closed contour integral may be replaced by symmetry by a version where each simply connected segment is traversed only once, namely:

$$D_i = \frac{1}{2}\rho_A \int_C \Delta\theta(s)\bar{w}(s)\, ds, \tag{2.3.5}$$

where $\bar{w}(s)$ is the downwash induced by the vortex distribution on C, according to

$$\bar{w}(s) = \int_C \Gamma(\sigma)\frac{V_{s\sigma}.\hat{n}(s)}{|V_{s\sigma}|^2}\, d\sigma, \tag{2.3.6}$$

where $V_{s\sigma}$ is the vector $(x(s), y(s), z(s)) - (x(\sigma), y(\sigma), z(\sigma))$. It is useful to integrate this double integral once by parts to obtain

$$D_i = \frac{1}{2}\rho_A \int_C \Gamma(s) \frac{d}{ds} \int_C \Gamma(\sigma) \frac{V_{s\sigma}.\hat{n}(s)}{|V_{s\sigma}|^2} \, d\sigma ds. \tag{2.3.7}$$

In the general non-planar case, it is difficult to evaluate this double integral numerically. Some authors (Katz and Plotkin, 1991) present Riemann-based algorithms assuming that Γ has a discrete span-wise representation, but to date we have found these slow to converge with the number of spanwise panels. The vortex lattice method is often used to calculate induced drag, but is known to underpredict the correct value. A spanwise correction factor (Kálmán et al., 1970) has been used to correspondingly renormalize the raw distribution of induced drag over the span. For an elliptically loaded wing, there is an exact relationship between induced drag and lift,

$$C_{D_i} = \frac{C_L^2}{\pi \mathcal{AR}}. \tag{2.3.8}$$

The fact that the wing must be elliptically loaded for the formula (2.3.8) to hold is sometimes not emphasised in the literature. Another occasional misconception is that an elliptic planform at constant angle of attack produces an exactly elliptically loaded wing; this is only true at $\mathcal{AR} = \infty$. These two approximations combined sometimes result in a false "exact value" by which numerical methods are measured.

A graphical means of estimating the double integral has also been presented (Eminton, 1961), but is not generally used. A clever exploitation of the analogy between fluid flow and electrostatics has also been used to produce a rheoelectric-analog device (Lundry, 1968), (Cone Jr., 1962) for the evaluation of the energy in the Trefftz plane for arbitrary geometry wake cross-sections.

In the case of a single planar lifting surface of span s, integration by parts results in the following integral (Ashley and Landahl, 1965).

$$D_i = -\frac{\rho_A}{4\pi} \int_0^s \int_0^s \frac{d\Gamma}{dy} \frac{d\Gamma}{dy_1} \log|y - y_1| \, dy_1 dy. \tag{2.3.9}$$

Assume that $\Gamma(y)$ may be accurately represented as a Fourier sine series

$$\Gamma(y) = Us \sum_{n=1}^{N} A_n \sin(n\theta), \tag{2.3.10}$$

where

$$y = \frac{s}{2} \sin\theta. \tag{2.3.11}$$

Then the induced drag coefficient is given (Ashley and Landahl, 1965) as

$$D_i = \pi \frac{\rho_A U^2 s^2}{8} \sum_{n=1}^{N} n A_n^2. \tag{2.3.12}$$

The induced drag coefficient is then given by

$$C_{D_i} = \frac{\pi}{4} AR \sum_{n=1}^{N} n A_n^2. \tag{2.3.13}$$

In the case of a non-planar wing, an equivalent method has not been found. Whether there are computationally efficient ways to calculate C_{D_i} for non-planar geometries is an interesting question. However, by considering the balance of forces on the body, it should not be necessary to directly evaluate C_{D_i} at all for flat wings. The force perpendicular to a flat wing provided by the pressure jump between its bottom and top sides must balance the drag and leading-edge suction forces, such that $C_S = C_L \sin \alpha_W - C_D$.

In this sense, induced drag might be regarded as the disproportionate reduction in leading-edge suction when compared with lift that occurs when flow becomes three-dimensional.

2.4 Leading-Edge Suction

It may be shown (Milne-Thompson, 1973), (Siekmann, 1965) that there is a non-zero suction force that acts tangent to a sharp (cusped) point on a profile in two-dimensional flow. This force may be regarded as the product of the infinite pressure required to make the fluid negotiate a 180^o turn, times the zero area of an infinitesimal body element on which it acts. It may also be shown that the magnitude of this leading-edge suction force is proportional to the square of the coefficient of the inverse square root leading-edge singularity produced in the pressure field at the cusp.

It has not always been clear (Billington, 1971) that this result is directly portable to three-dimensional flow. However, it has been shown (Tuck, 1995), (Lan and Mehrotra, 1979) that if the suction force is to exist for a three-dimensional thin wing, then it must be given by

$$S = \frac{\pi}{4} \int_0^s Q(y)^2 dy, \tag{2.4.14}$$

where $Q(y)$ is the singularity strength

$$Q(y) = \lim_{x \to x_{LE}} \gamma(x, y) \sqrt{x - x_{LE}}. \tag{2.4.15}$$

Hence for a small angle of attack, we expect the leading edge suction force coefficient to be given by

$$\frac{C_S}{\alpha^2} = \frac{\pi}{4}\int_0^s \left(\frac{Q(y)}{\alpha}\right)^2 dy \tag{2.4.16}$$

At higher angles of attack, for wing planforms with highly swept leading edges, the leading-edge suction analogy may be referred to (Polhamus, 1966), (Er-El and Yitzhak, 1988). This is a method of predicting the increase in lift when the leading-edge vortex detaches and causes an increase in velocity of the fluid on the upper surface of the wing. It is distinct from the linear leading-edge suction of the present analysis. Also in the literature, the definitions of the thrust coefficient C_T and the leading-edge suction coefficient C_S differ. Here we refer to suction in the streamwise direction only, with positive suction opposing drag.

Evaluating the integral in (2.4.16) is made very easy when the integrand is represented as a Fourier series such that

$$\left(\frac{Q(y)}{\alpha}\right)^2 = \sum_n^\infty B_n \sin(n\theta), \tag{2.4.17}$$

where $y = \frac{s}{2}\cos\theta$. In this case, the leading-edge suction force is given by

$$C_S = 2S/A = \frac{\pi^2}{4}B_1. \tag{2.4.18}$$

2.5 Results

For a rectangular wing of $AR = 2$, the suction converges to $C_S = 1.500$ at the rate n_y^{-2}. In order to verify the present computational method, C_L/α, C_{D_i}/α^2 and C_S/α^2 are calculated independently for rectangular, elliptic and delta planform wings of varying aspect ratios. These quantities are plotted in Figures 2.2, 2.3 and 2.4. In all cases, we should find that $C_L/\alpha = C_{D_i}/\alpha^2 + C_S/\alpha^2$. While the unextrapolated results are reasonable ($n_y = n_x = 18$ gives at least 3 figure accuracy for planforms with $AR > 1$), there is a noticeable decrease in accuracy for small AR, especially for the elliptic and delta planforms. Figure 2.5 shows the relative error $(\alpha_W C_L - C_{D_i} - C_S)/(\alpha_W C_L)$ for the rectangular, elliptic and delta planforms. Nonetheless, the absolute error $C_L/\alpha - C_{D_i}/\alpha^2 - C_S/\alpha^2$ tends to zero for all cases with rate n^{-1}.

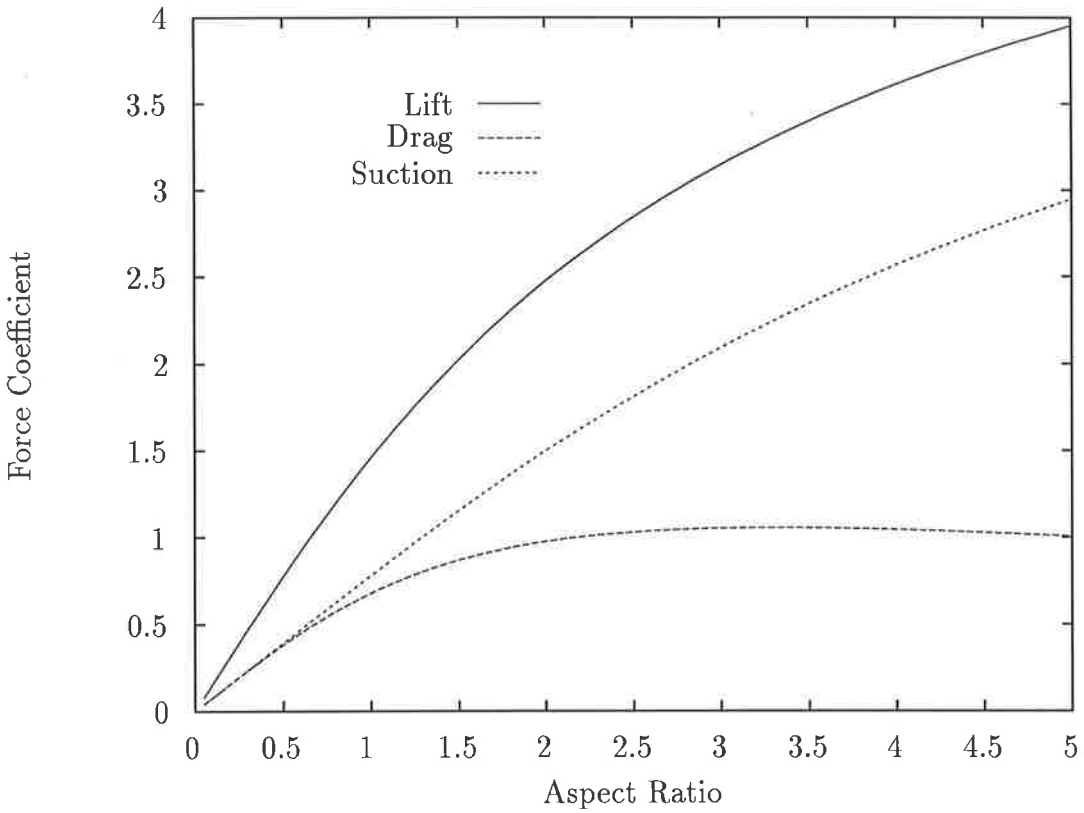

Figure 2.2: *Lift, drag and leading-edge suction on planar rectangular wings of varying aspect ratio. The data has been produced from the present method using* $n = m = 18$.

2.6 Discussion

The power of the current technique is not fully realised for planar wings because it is relatively simple to calculate the induced drag C_{D_i} directly from the Trefftz-plane double integral. However, for lifting-surface geometries that are non-planar, or with multiple components such as endplates or biplane wings, or in ground effect, such direct evaluation of C_{D_i} is computationally difficult.

By comparison, the evaluation of the leading-edge suction force C_S is essentially geometry-independent, once the pointwise loading γ has been accurately calculated by solution of the non-planar equivalent of the lifting-surface integral equation. An immediate consequence is that the induced drag of wings with endplates, thickness and/or ground effect can be confidently tackled (Standingford and Tuck, 1996a).

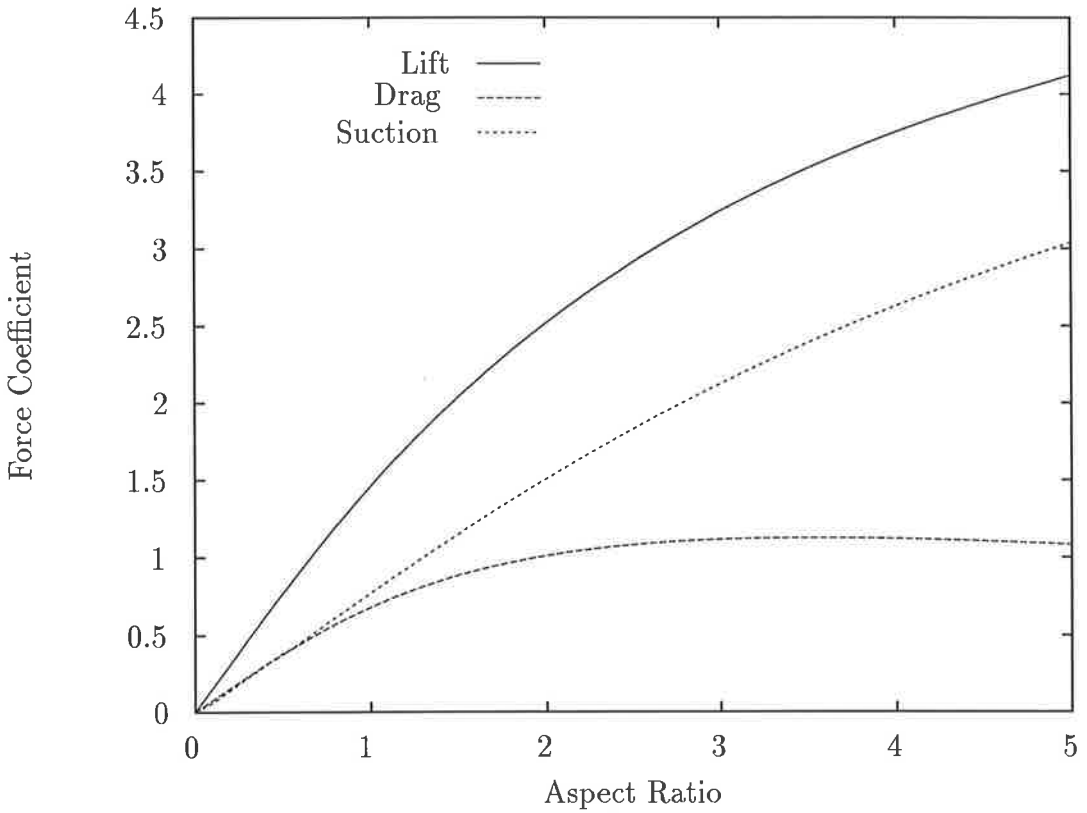

Figure 2.3: *Lift, drag and leading-edge suction on planar elliptic wings of varying aspect ratio. The data has been produced from the present method using* $n = m = 18$.

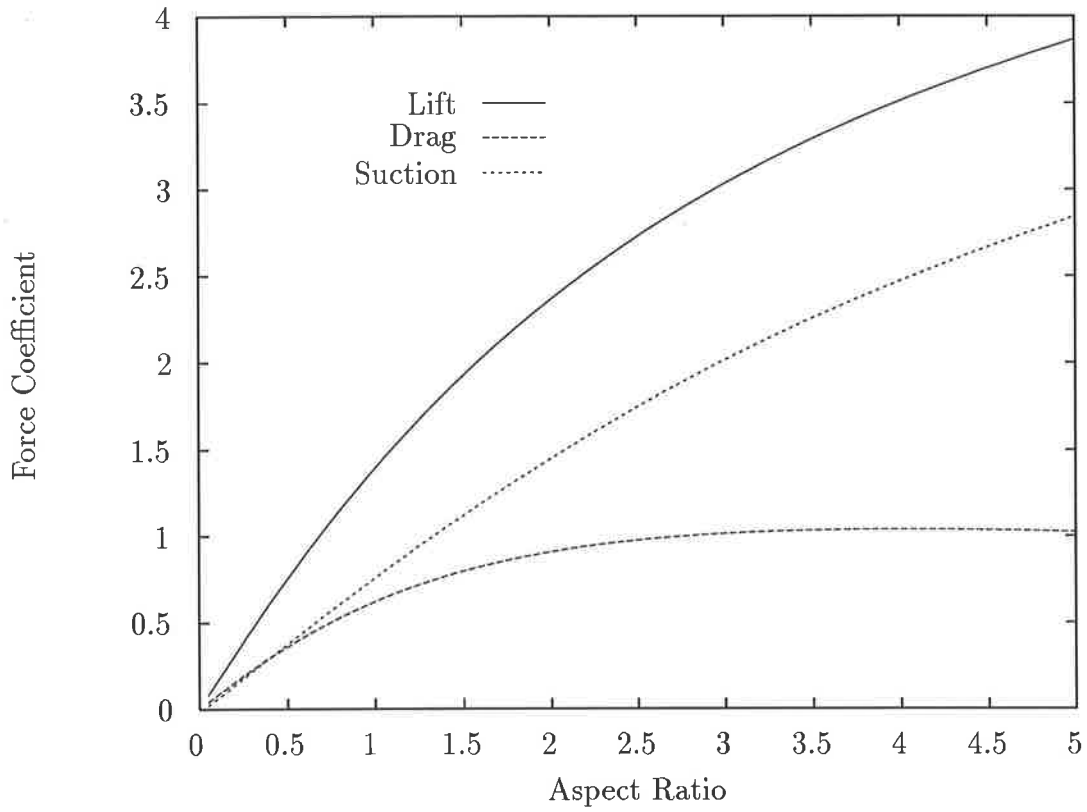

Figure 2.4: *Lift, drag and leading-edge suction on planar delta wings of varying aspect ratio. The data has been produced from the present method using* $n = m = 18$.

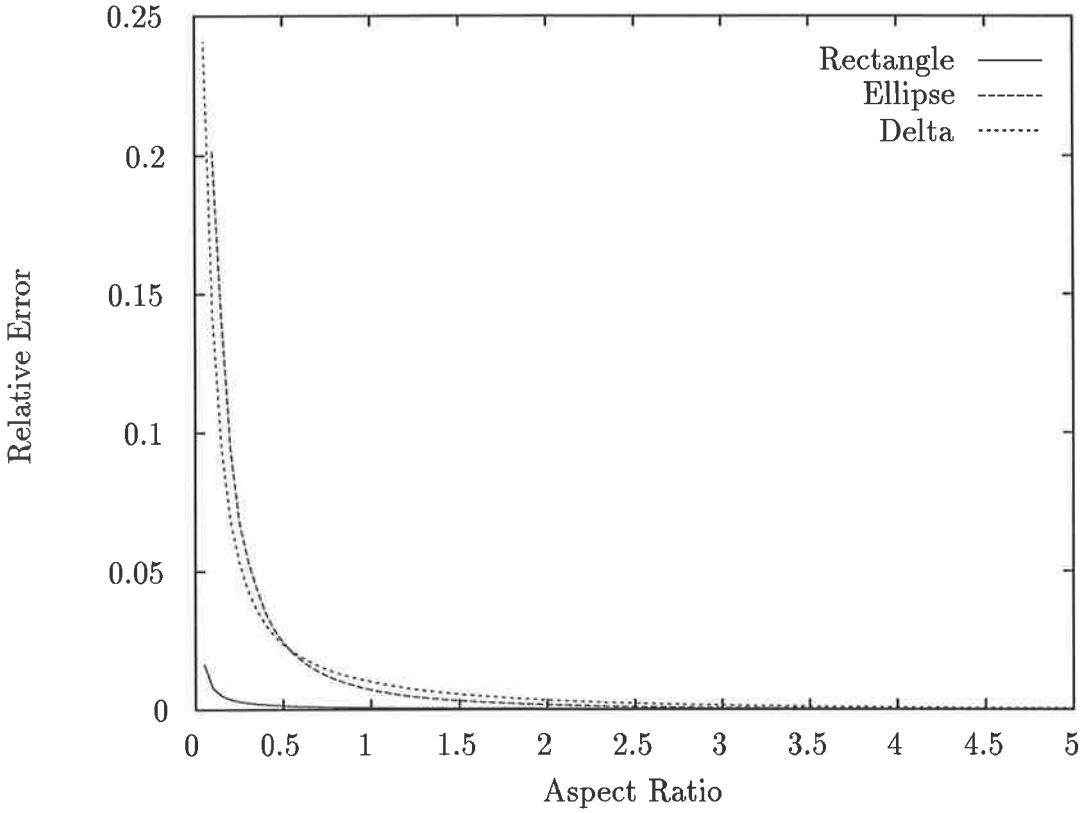

Figure 2.5: *Relative error in the force prediction using the present constantly loaded panel method with kernel correction for wings of rectangular, elliptic and delta planforms. Results computed using* $n = m = 18$ *spanwise and chordwise panels. In all cases, the errors tend to zero at the rate* n^{-1}.

Chapter 3

Endplates

3.1 Introduction

In this Chapter, we address the use of endplates to increase the lift and decrease the induced drag on thin wings in free air. Thickness effects will be considered separately in Chapter 6 and so all surfaces in this chapter are taken to be flat plates with zero camber.

The effect of adding an endplate to a finite-span wing is to inhibit spillage of air from the lower surface to the upper surface, via the tips. This then maintains the lift-creating pressure difference between bottom and top surfaces to a distance closer to the tips than if there were no endplates. Thus the flow becomes more two-dimensional, as if the wing's aspect ratio were larger, and the net lift increases and the induced drag decreases.

This concept is not limited to wings on aircraft. In addition, shrouded propellers, catamarans, vertical axis wind turbines with tip-vanes (van Holten, 1981) and otter boards on fishing nets (Patterson and Watts, 1985), to name a few, all make use of this increase in efficiency when the aspect ratio of a lifting surface is necessarily small.

The significant improvement to the design of the International twelve-metre class yacht made famous when *Australia II* won the America's Cup race in 1983, known as the winged keel is strongly analogous. The keel is designed to act as a lifting surface in opposition to the capsizing force on the sail. In this case, the apparent depth of the keel was increased by the addition of an approximately horizontal plate at the bottom of the keel. The body of knowledge in the study of aerodynamic endplates that had been collected was readily applicable to this kind of ship design (van Oossanen and Joubert, 1986).

The analysis of the effect of adding endplates or winglets to wings is not new. The use of endplates to reduce drag was involved in a patent by Lanchester in 1897 although the first experiments involving endplates did not take place until about 1924 (Spillman, 1978). Since then, names such as "booster tips" have been applied to the various appendages to wingtips to achieve greater operational efficiency. Interestingly, one of the initial names for this class of appendage was "tip sail" because the strong vortex cross flow near the wingtip was seen as a possible source of thrust for an appropriately angled sail. Figure 3.1 shows three such sails attached to the wingtip fuel tank of a "Paris" training aircraft. Pilots noticed a significant improvement in handling on landing, where the high angle of attack leads to large lift and induced drag forces. The similarity with the splayed wingtip feathers of birds on landing is remarkable.

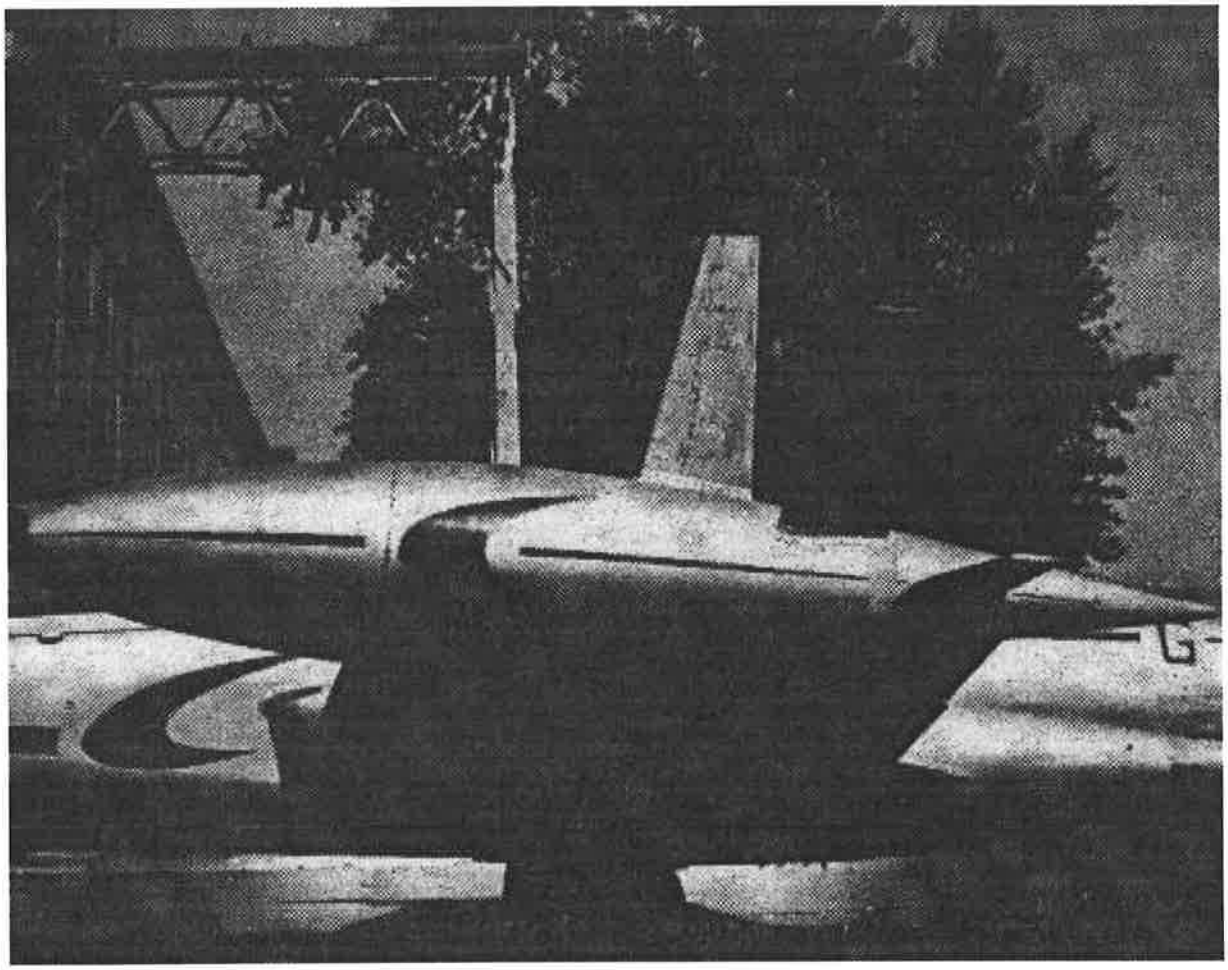

Figure 3.1: *Tip sails, mounted on the "Paris" training aircraft, used to generate thrust from the wingtip vortex flow. Reproduced from Spillman (1978).*

A significant motivation for research has been a perceived value in retro-fitting existing aircraft with devices to improve their fuel consumption, providing an immediate saving,

although the associated parasite drag prevented them from achieving the improvement motivated by the inviscid theory (Whitcomb, 1976).

Hemcke (1927) considered the theory of induced drag by applying a conformal mapping in conjunction with the lifting line theory. He deduced that the reduction in drag, when endplates are used, was sufficiently large to increase the efficiency of the wing. Although the computational power at the time did not support a lifting surface analysis, Hemke made use of windtunnel experiments as well as theoretical analysis to determine that endplate location and shape was crucial to their performance and in particular that endplates designed to minimise induced drag should be positioned towards the wing leading-edge. Since there is no rearward force on the plates due to a lift component when they are at zero angle of attack, the only calculable streamwise force on the plates is the leading-edge suction, which directly opposes the induced drag. This might also be considered to be physical dissipation of the wingtip vortex. Without wishing to decrease the circulation and hence the lift of a lifting system, one can still decrease the kinetic energy of the wingtip vortex system by increasing its core diameter. Basically, the greatest increases in span efficiency occur for modifications which tend to release the major portion of vorticity near the tip and over an appreciable vertical area (Naik and Ostowari, 1990). Similar effects have also been sought by means of spanwise camber, without resorting to the discontinuity of a wing-endplate join (Lowson, 1990).

A portion of this Chapter is reproduced from a technical note (Standingford and Tuck, 1996b), where a limited wing-endplate optimisation is discussed. Here, the author also presents a more detailed literature review; a more complete investigation of the possible wing-endplate configurations and inclusion of induced drag in the optimisation of the wing-endplate geometry.

3.2 Endplates and Winglets

The terms *endplate* and *winglet* are sometimes used interchangeably in the wider literature. Within the context of the present analysis, they have distinct meanings. A winglet refers to a small, nearly vertical wing-like surface, mounted at the wingtip to decrease induced drag (Reynolds, 1979). Winglets are usually aerodynamically shaped, vary in both chord and camber over their span and are also often "canted" outwards. Figure 3.2

shows a popular winglet geometry. Generally it has been found that for minimising induced drag the greatest winglet effectiveness has been achieved with the trailing edge of the winglet near the trailing edge of the wing (Whitcomb, 1976).

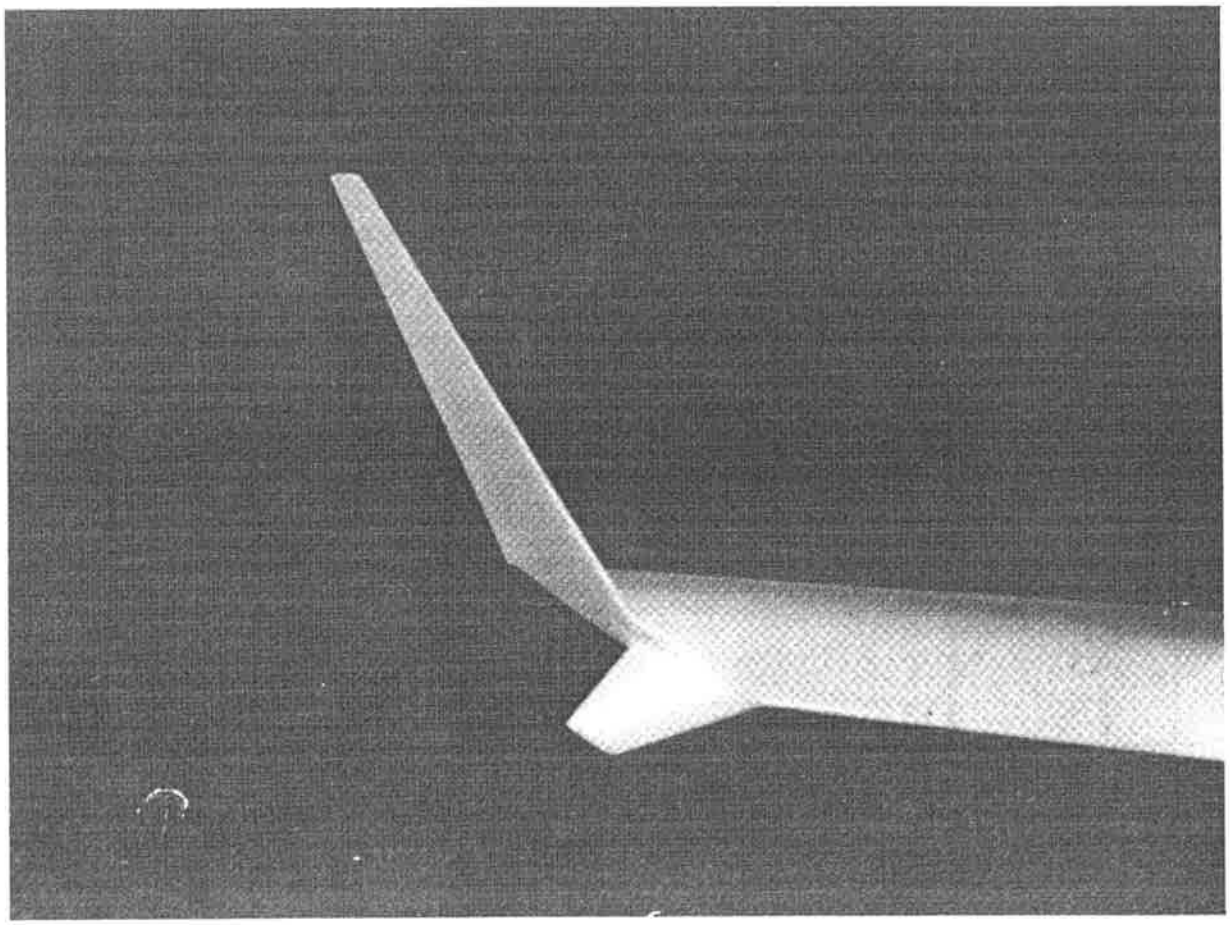

Figure 3.2: *Front view of a popular winglet design, reproduced from Whitcomb (1971). Note the vertical asymmetry, cant angle and horizontal offset of the sections above and below the wing.*

By contrast, an endplate is perfectly vertical, and therefore contributes only indirectly to the total lift. The endplate may be cambered and/or have a non-zero nominal angle of attack α_P to the free stream.

In order to limit the number of variables, we shall only consider endplates here. A common query about endplates is whether they act to increase lift or to decrease drag or both. They can be tuned to perform either of these functions. Endplates on the upper half of the wing only can be "toed out" to create a thrust force from the wingtip vortex thereby reducing the induced drag. Alternatively, they can be "toed in" to increase the lift at the expense of induced drag. Finally, the angle of attack α_P can be be tuned for a specific geometry and flight condition such that an efficiency function combining lift and

induced drag can be optimised. In some cases this will mean that the endplate does not exist at all.

3.3 Design Considerations

The advantages and disadvantages of wingtip treatments in general are debated from varying perspectives. Other things being equal, most designers agree that a single elliptically loaded lifting surface is best. Any additional wingtip structure represents extra manufacturing complexity, increased tip loading that may increase the root bending moment of the wing under gust conditions and a significant contribution to parasite drag at the wing-endplate join. At high speeds and low angles of attack, the skin friction drag penalty often outweighs the reduction in induced drag (Whitcomb, 1976).

However, the wingspans of commercial aircraft are often limited by hangar restrictions and parking space at airports. Other wings, such as on racing cars, or propellers are limited in aspect ratio by design specifications or practical considerations. Generally it is true that the greatest relative improvements to lifting surfaces made by adding wingtip treatments occur when the aspect ratio of the lifting surface is small and thus the bare wing leaves the greatest room for improvement (Kuhlman and Liaw, 1988). It is often suggested that the final designs for the winglets on large modern commercial aircraft are made for aesthetic purposes rather than for performance optimisation (Conley, 1980) (Reynolds, 1979). When aircraft are retro-fitted with winglets, the designer needs to carefully check the change in stability conditions, although in general (van Dam, 1981) the stall characteristic improves.

3.4 Mathematical Formulation

Within thin-wing theory (Ashley and Landahl, 1965), the problem of determining the lift L on a wing-endplate combination at small angles of attack α_W and α_P respectively in a uniform stream U of air of constant density ρ_A relies on the solution of a pair of coupled singular integral equations (Tuck, 1992) for the bound vorticity distribution on both the planar wing and the endplate. The wing and endplate are both assumed thin and the endplate lies within a plane perpendicular to the wing. These equations are just the

generalisation of the lifting surface integral equation presented in Chapter 1 to include the induced downwash of the wing on the endplate and vice-versa. For completeness, the equations are

$$\iint_W \gamma^W(\xi,\eta)\, G_Z(x-\xi, y-\eta, z-\zeta)\, d\xi\, d\eta \tag{3.4.1}$$
$$+ \iint_P \gamma^P(\xi,\zeta)\, H_Z(x-\xi, y-\eta, z-\zeta)\, d\xi\, d\zeta = -4\pi U f_x^W(x,y) \qquad (x,y,z) \in W$$
$$\iint_W \gamma^W(\xi,\eta)\, G_Y(x-\xi, y-\eta, z-\zeta)\, d\xi\, d\eta \tag{3.4.2}$$
$$+ \iint_P \gamma^P(\xi,\zeta)\, H_Y(x-\xi, y-\eta, z-\zeta)\, d\xi\, d\zeta = -4\pi U f_x^P(x,z) \qquad (x,y,z) \in P,$$

where $G(X,Y,Z) = ZF(X,Y,Z)$ is the velocity potential at any point (X,Y,Z) for a unit horseshoe vortex on a wing surface with normal $\hat{n} = (0,0,1)$. Similarly, $H(X,Y,Z) = YF(X,Y,Z)$ is the velocity potential due to a unit horseshoe vortex on an endplate surface with normal $\hat{n} = (0,1,0)$. In these unit horseshoe vortex potentials,

$$F(X,Y,Z) = \frac{1}{Y^2+Z^2}\left[1 + \frac{X}{R}\right], \tag{3.4.3}$$

where $R = \sqrt{X^2+Y^2+Z^2}$. Equations 3.4.1 and 3.4.2 are solved for the bound vortices γ^W and γ^P, subject to the Kutta conditions that $\gamma^W = 0$ on the trailing edge of the wing and $\gamma^P = 0$ on the trailing edge of the plate. In order to simplify the numerical task of satisfying these conditions, both equations are integrated once with respect to X and the resulting kernels expressed as cross derivatives to obtain

$$\iint \gamma^W K_{\xi\eta}^{WW}\, d\xi\, d\eta + \iint \gamma^P K_{\xi\zeta}^{WP}\, d\xi\, d\zeta = -4\pi U \overset{w}{f}(x,y) + \overset{w}{C}(y) \tag{3.4.4}$$
$$\iint \gamma^W K_{\xi\eta}^{PW}\, d\xi\, d\eta + \iint \gamma^P K_{\xi\zeta}^{PP}\, d\xi\, d\zeta = -4\pi U \overset{P}{f}(x,z) + \overset{P}{C}(z)\ , \tag{3.4.5}$$

where $C^W(y)$ and $C^P(z)$ are the constants of integration that are used to satisfy the Kutta condition at each y value on the wing trailing edge and each z value on the endplate trailing edge.

These integral equations have been solved numerically here, using analogous modifications to the ones described in the previous Chapters to enhance the resolution of the leading edge singularities on both the wing and endplate.

3.4.1 Numerical Experience

It is particularly important to achieve a good resolution of the leading-edge singularities for the task of optimising wing-endplate geometries, because numerical artefacts such as

overestimation of the loading at the leading edge can wrongly favour endplates located close to the leading edge. Similarly, there may appear to be a false local maximum in lift when the endplate is attached either completely above (or equivalently below) the wing, due to numerical error in resolving the wingtip singularity. Special care must be taken when the endplate dimensions are either small or large when compared with those of the wing, since there can be interference between the smaller element and the numerical panel scale of the larger element. Most results in this Chapter were computed using a 12×12 rectangular Chebyschev-spaced grid on both the wing and endplate, and are believed to be accurate to at least 3 significant figures.

The convergence of the method was tested on a unit square wing with centrally positioned unit square endplates as illustrated in Figure 3.3. Extrapolation using $n = 3, 6, 12$, where n is the number of panels in each of the spanwise, chordwise and vertical directions gives a value for C_S (using A_0 as a reference area) of 0.922 with convergence rate $O(n^{-2})$.

3.5 Optimisation

Much of the remainder of this Chapter will be concerned with the task of identifying successful wing-endplate geometries for the maximisation of lift with respect to drag. This problem needs careful specification and in particular we must state whether we are optimising with respect to induced drag, skin-friction drag or some combination of the two. It is rare in the literature to find examples of the third option. There is a natural tendency to decouple the two kinds of drag, firstly because they depend upon somewhat different aspects of the design and secondly because the task becomes significantly simpler.

In the absence of a penalisation of skin-friction drag, the optimal endplate geometry for any wing is one where the endplates extend infinitely in all directions, producing effectively two-dimensional flow. In this case artificial constraints on the extent of the total geometry may be imposed. See for example a recent paper using genetic algorithms (Gage et al., 1995) to optimise wing-endplate geometries.

The optimisation of lift with respect to induced drag has been extensively treated in the literature. In this case, Munk's third theorem specifies the optimum distribution of vorticity in the wake for any given total lift and Trefftz plane geometry. This principle has

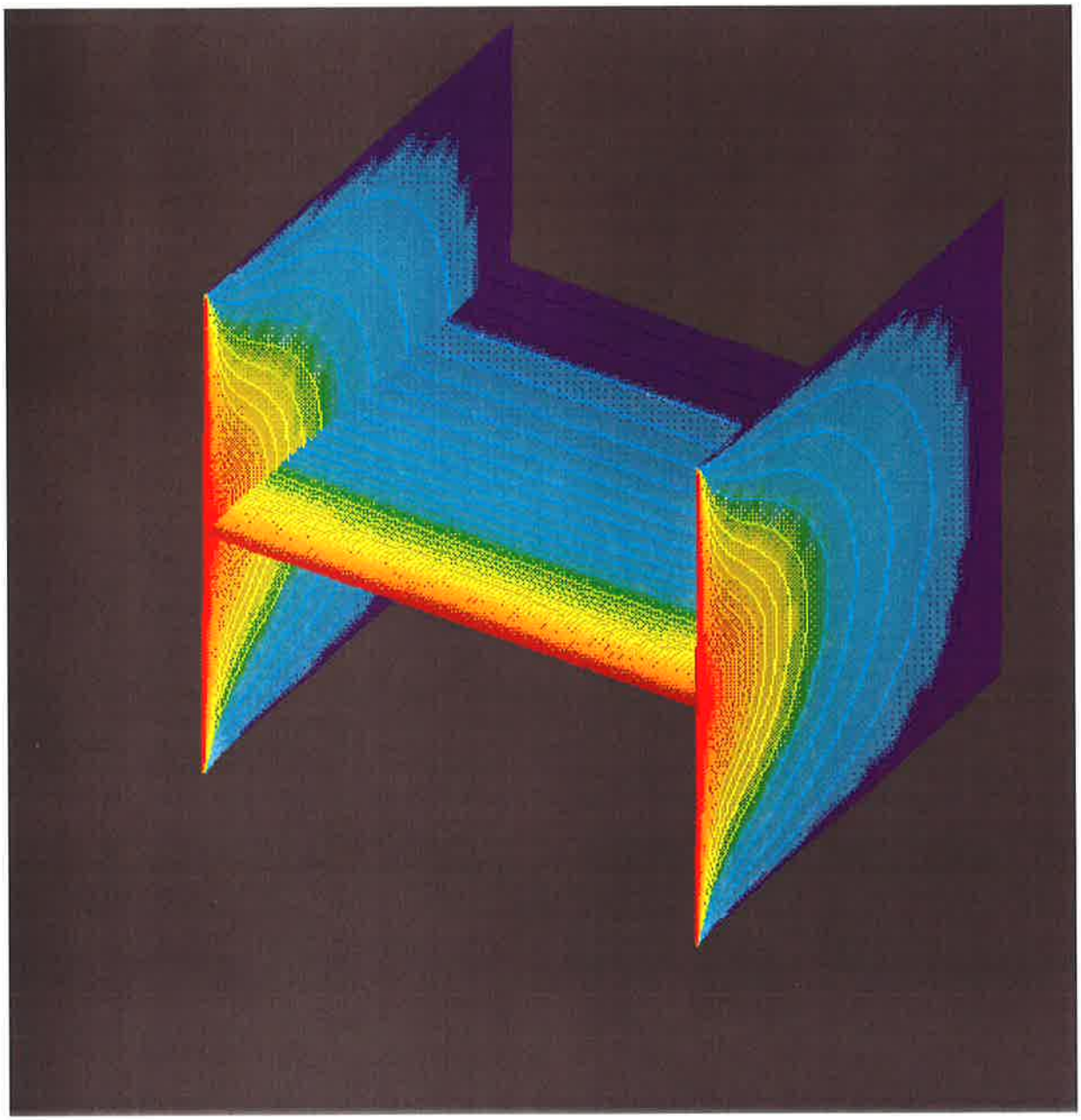

Figure 3.3: *When endplates are added to the square wing, the wing loading becomes somewhat two-dimensional although the plate loading is three-dimensional. Note that the absolute pressure difference is illustrated, and the sign of the pressure jump changes from the lower to the upper portions of the endplate.*

been applied to the design of ship screw propellers (de Jong, 1991) where the designer solves an inverse problem to determine the chord length and camber as functions of spanwise location on the wing and heightwise location on the propeller endplate.

In the absence of a cost for induced drag, the wing and endplate angles of attack should be large and the wing would be of infinite aspect ratio. Because we intend to investigate

the optimisation with respect to some combination of skin-friction and induced drag, we might fix the wing geometry and consider the optimisation of C_L/α_W with respect to D_f. Since skin-friction is only weakly a function of the distribution of the area of the surface itself, to a good approximation the skin-friction may be regarded as a constant multiplied by surface area. Hence an equivalent investigation is the optimisation of the endplate geometry for a fixed wing geometry so as to maximise C_L/α_W based on the total area.

3.6 Optimisation with respect to Total Area

The complete parameter space for single rectangular endplates on a rectangular wing of chord c and span s has been explored. That is, rectangular endplates of arbitrary length ℓ and height h are placed on and perpendicular to both wingtips (i.e. side edges) of the rectangular wing, with their centres offset a horizontally and b vertically from the mid-chord of the wingtip. Figure 3.4 shows the relevant geometry.

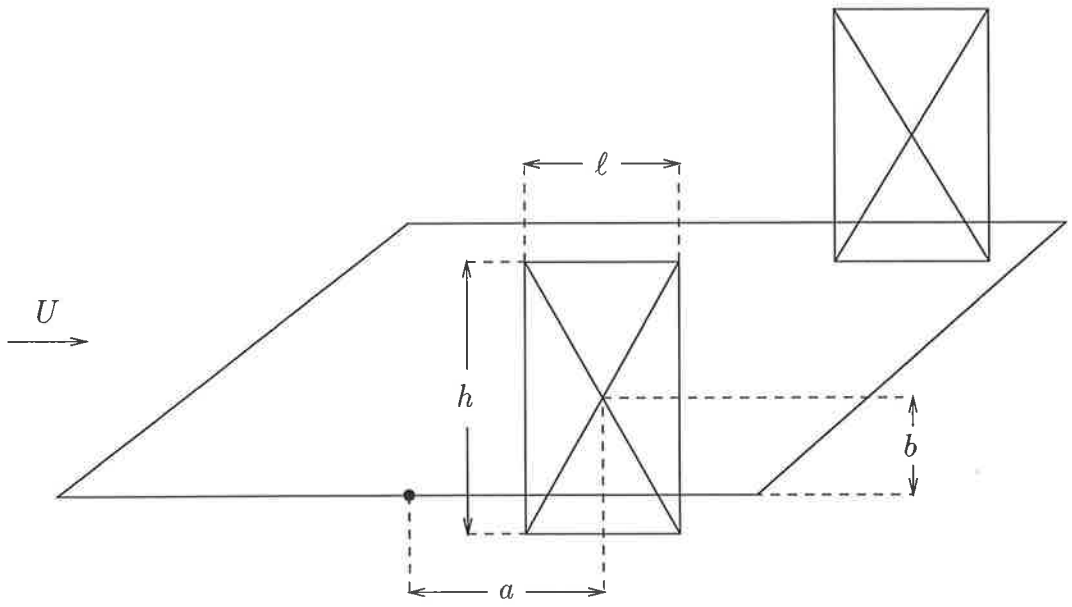

Figure 3.4: *Unit square wing with rectangular endplates of height h, length ℓ, horizontal offset a and vertical offset b. The endplate has angle of attack $\alpha_P = 0$.*

The aim is to maximise the lift coefficient per unit angle of attack C_L/α_W, based on the total (wing plus endplate) area A, by varying all four of the above input plate parameters. In a rough sense, this is equivalent to maximising the lift/drag ratio, if drag is dominated by skin friction and therefore is proportional to the total area A. In the more general optimisation later in this chapter, we include induced drag, which is proportional to α^2.

The results presented here can be alternatively viewed as optimisation at very small angles of attack.

3.6.1 Asymptotic Results

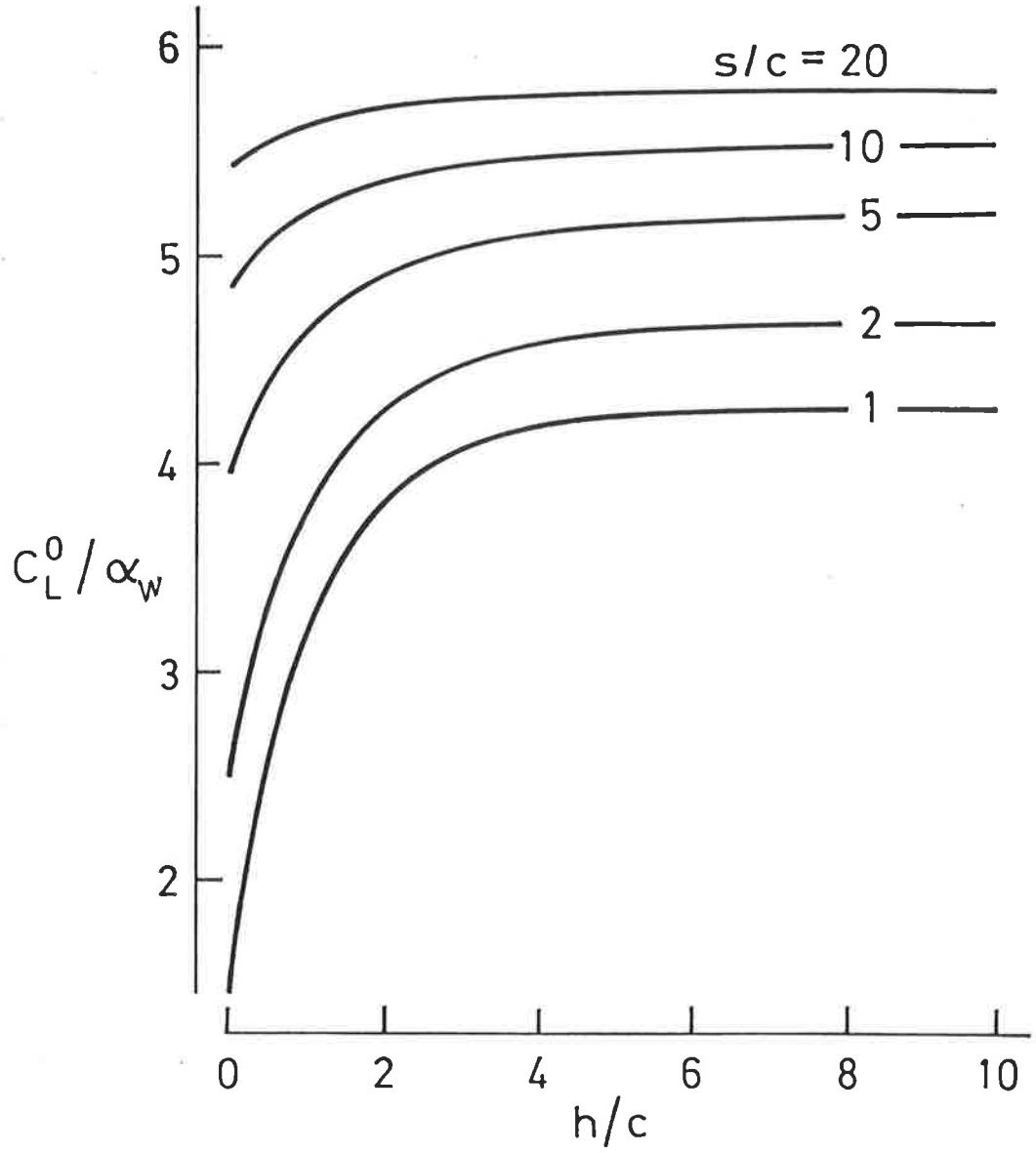

Figure 3.5: *Lift coefficient C_L^0/α_W versus endplate height h/c for endplates with fixed length $\ell = c$ on rectangular wings of varying aspect ratio. Reproduced from Standingford and Tuck (1996b).*

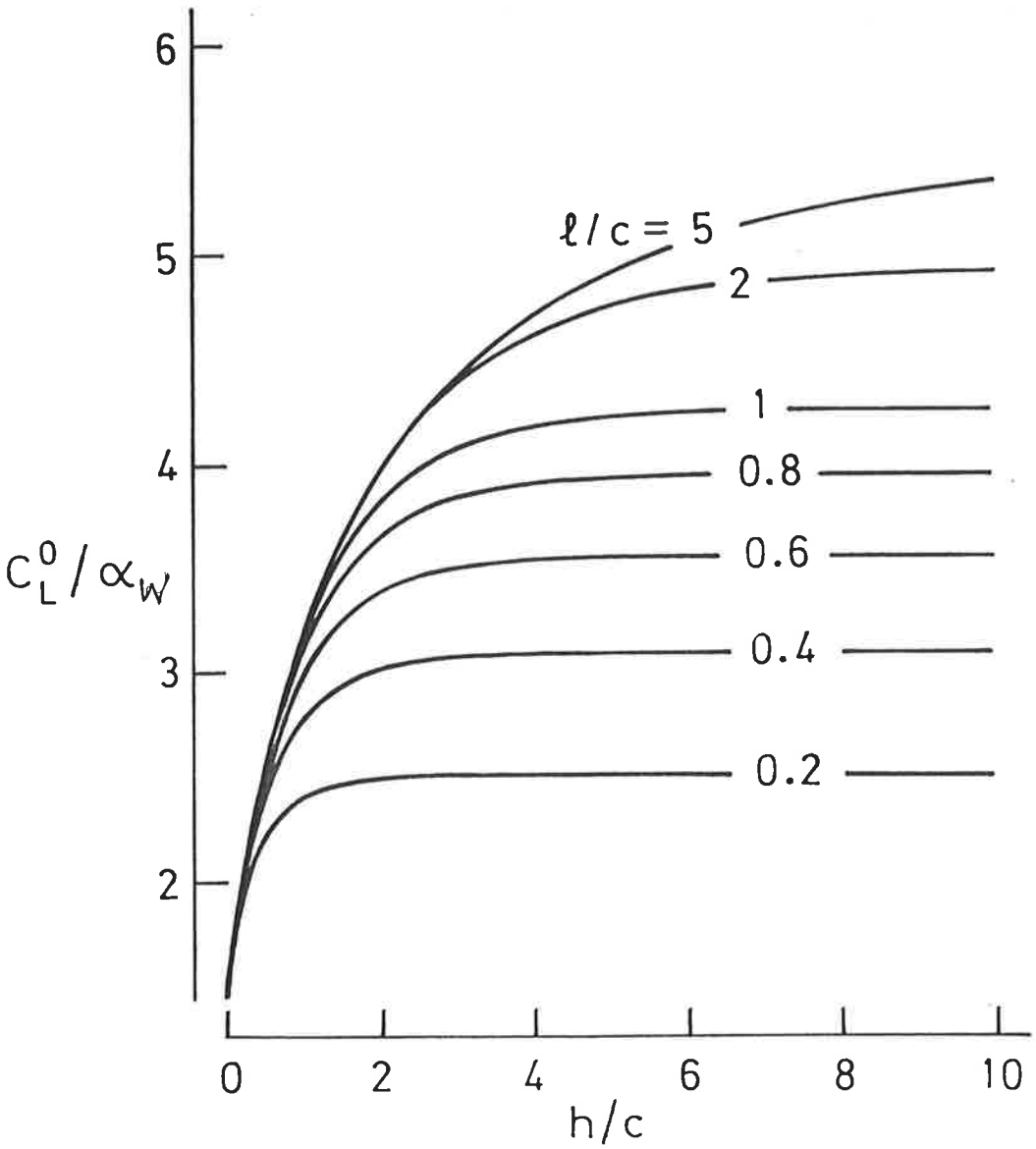

Figure 3.6: *Lift coefficient C_L^0/α_W versus endplate height h/c for endplates of varying length ℓ/c on a square wing. Reproduced from Standingford and Tuck (1996b).*

Figure 3.5 shows the lift increase to a rectangular wing of various aspect ratios s/c, obtained by adding an endplate with $a = b = 0$ and $\ell = c$, as a function of the endplate height h. Thus this endplate has the full wing chord, and is attached flush, leading edge to leading edge and trailing edge to trailing edge. Note that for the purpose of this figure (and the next), the area measure is the area $A_0 = cs$ of the wing only, and these results do not penalise the lift for the extra area of the endplates; C_L^0/α_W is used to emphasize this distinction.

With this family of endplates, fully two-dimensional flow can never be attained even when the height h is infinite. Although the results reach distinct asymptotes as the endplate height increases for each fixed wing aspect ratio, the precise relationship between the asymptotic value for an infinitely high (but finite length) endplate and the wing parameters is not known. Of course, as the wing aspect ratio increases, the results approach the well-known two-dimensional value $C_L^0/\alpha_W = 2\pi$, and endplates provide relatively less benefit.

Since even quite small endplates have a dramatic effect on the square wing with $s/c = 1$, and there are applications such as dirt-track racing cars (Turrill, 1992) and catamarans where wings of approximately square planform are important, we first examine that case.

Figure 3.6 shows the variation with endplate height h of the lift (as C_L^0/α_W, based again on wing area only) for a square wing to which is added centrally placed (i.e. $a = b = 0$) endplates of various lengths ℓ, fixed relative to wing chord c. Again, as h increases, these curves approach an asymptote whose value varies with endplate length, and only approaches the two-dimensional limit of 2π for large ℓ/c, when the endplates become infinitely extended in both directions.

3.6.2 Optimal Rectangular Endplates

Although endplates increase the lift compared to a bare wing, this does not necessarily mean that the lift coefficient slope C_L/α_W as defined above based on total area A increases, since the endplates add to the total area and hence may have a negative affect on the ratio of lift to area. Indeed, it is not difficult to see from the results of Figure 3.6 that no endplate of length ℓ equal to or greater than the wing chord c produces a combined wing-endplate geometry with a C_L/α_W value greater than that of a bare wing. However, it is a different story for shorter endplates.

The optimal dimensions and location of the endplate are shown via contour plots of C_L/α_W in Figures 3.7 and 3.8. In Figure 3.7, the dimensions of the plate are fixed at $\ell = 0.5c$ and $h = 0.5c$ while the offsets a and b are varied. The clear maximum is when the plate is centered on the wing mid-chord, i.e. $a = b = 0$. Figure 3.8 has the offsets fixed at this optimum while the dimensions of the endplate vary. The maximum $C_L/\alpha_W = 1.84$ is attained when $\ell = 0.15c$ and $h = 0.48c$. In this figure, the axes $h = 0$ and $\ell = 0$ represent geometries where the endplate does not exist and hence they have

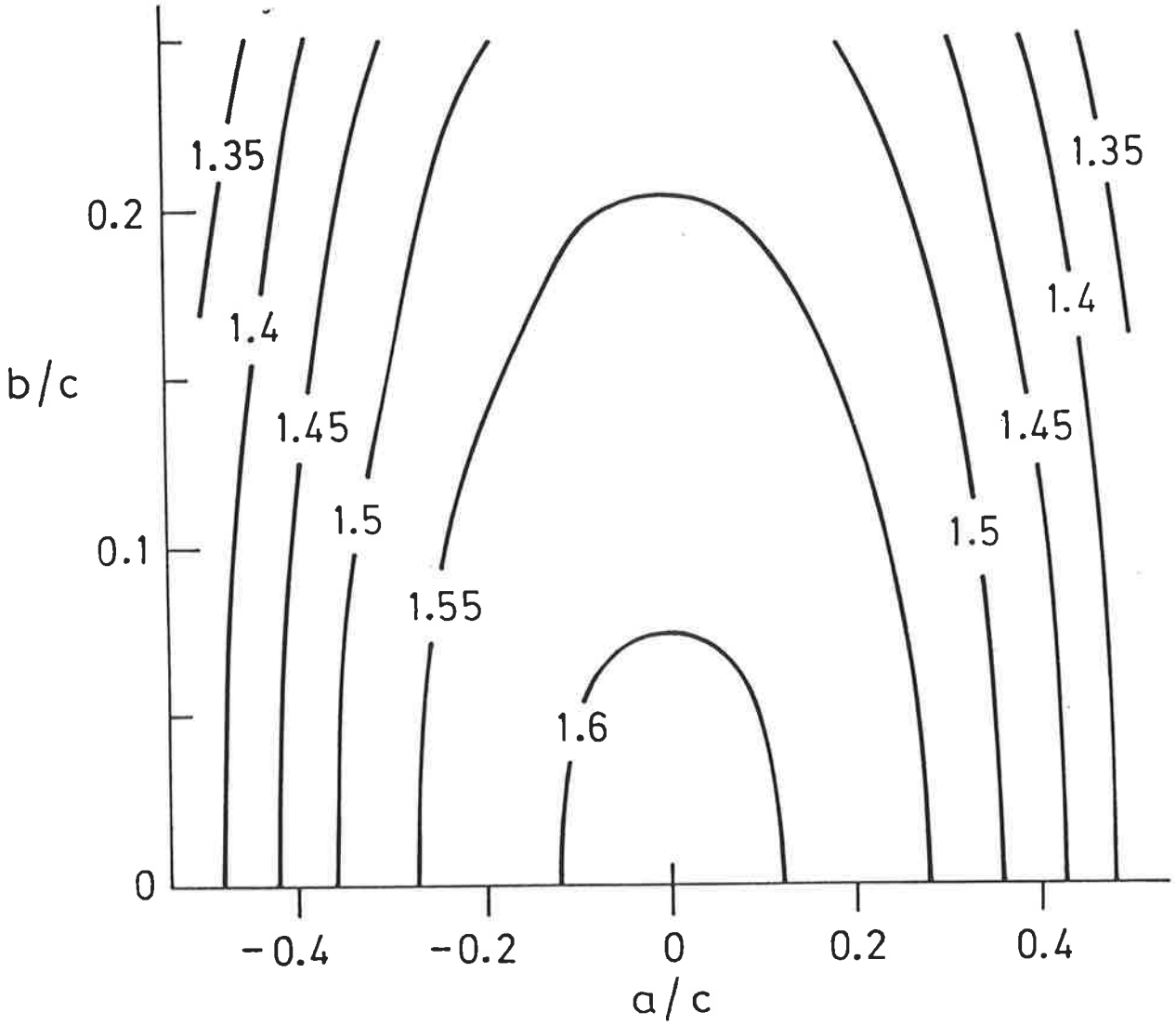

Figure 3.7: *Contour plots of the lift coefficient C_L/α_W based on total area, with endplate dimensions fixed at $\ell = 0.5c$ and $h = 0.5c$ and variable horizontal offset a and vertical offset b. Reproduced from Standingford and Tuck (1996b).*

contour value $C_L/\alpha_W = 1.46$ corresponding to the bare wing. There is another contour with this value which intersects the horizontal and vertical axes at $\ell/c = 1$ and $h/c = 3.1$ respectively. Any choice of h/c and ℓ/c lying within the closed loop thus produced gives $C_L/\alpha > 1.46$, i.e. an improvement on the bare wing.

If one is forced to use a sub-optimal placement of the endplates, i.e. non-zero a,b, then

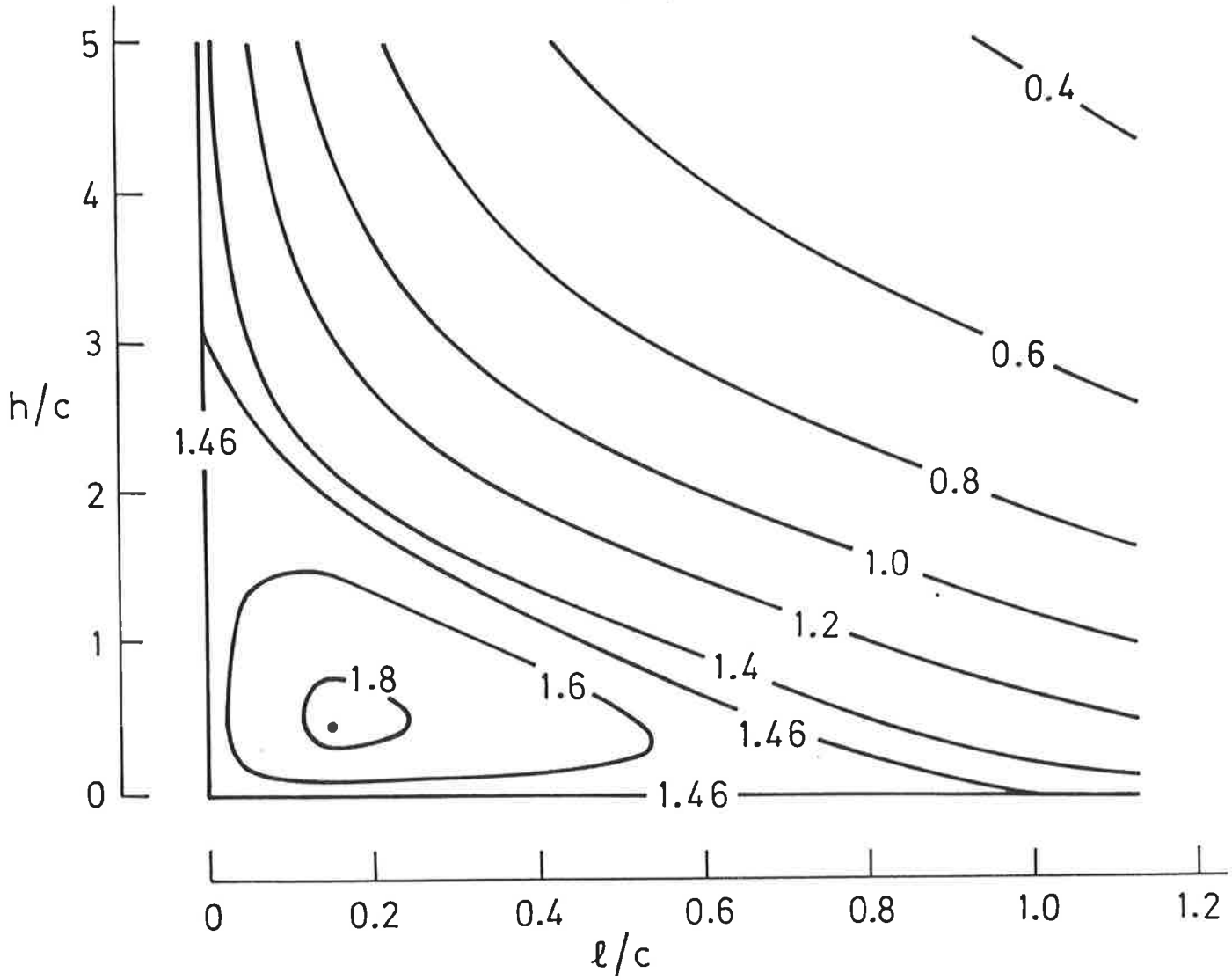

Figure 3.8: *Contour plots of the lift coefficient C_L/α_W, based on total area with the offsets fixed at $a = b = 0$ and variable plate length ℓ and height h. Reproduced from Standingford and Tuck (1996b).*

the optimal endplate dimensions depend upon the offset parameters a and b. Table 3.1 gives the optimal dimensions and the resulting lift slope coefficient when the endplate horizontal offset is $a = -c/2$ (flush with the wing leading edge) or $a = 0$ (horizontally centered at wing mid-chord), and the vertical offset is $b = h/2$ (entirely above wing) or $b = 0$ (vertically centered).

a	b	optimal ℓ	optimal h	optimal C_L/α
$-c/2$	$h/2$	0.28	0.22	1.62
$-c/2$	0	0.25	0.36	1.67
0	$h/2$	0.19	0.28	1.71
0	0	0.15	0.48	1.84

Table 3.1: *Optimal endplate dimensions at fixed locations.*

The bare square wing with no endplates has the value for C_L/α_W given (Tuck, 1993) to 7-figure accuracy as 1.460227. The conclusion is that the same wing with single rectangular endplates of length $c = 0.15c$ and height $h = 0.48c$, centered both horizontally and vertically at the mid-chord of the wing ($a = b = 0$) has $C_L/\alpha = 1.84$. If the extra area of magnitude $0.144c^2$ due to these two optimal endplates were instead added to the span of the previously square wing, so making a rectangular bare wing of aspect ratio $s/c = 1.144$, this wing would have only $C_L/\alpha_W = 1.63$. It is thus better to use this area in the form of (optimal) endplates rather than increased (full-chord) span.

3.7 Other Degrees of Freedom

There are infinitely many ways in which the parameter space for the optimisation can proceed from these baseline results. Rather than immediately attempt to determine a global optimum for the design of a wing-endplate configuration, we shall restrict ourselves to a small number of additional parameters which yield insight into the problem.

3.7.1 Horizontal Offset

As a first extension we now allow the endplate sections above and below the wing to move independently in the chordwise direction. The horizontal offset o measures the distance between the leading edges of the top and bottom sections of the endplate as illustrated in Figure 3.9.

The new parameter space to be explored is (ℓ, h, o), and it will be assumed that the solution space is otherwise symmetric in the parameters a and b. In the case where o is non-zero, b will indicate the average horizontal offset of the endplates from the wing mid-

chord. It is anticipated that there will be two mechanisms which will jointly determine the optimal geometry, namely (i) that the most area-efficient location for an endplate is centred, both vertically and horizontally on the wing mid-chord and (ii) that since area is penalised, each endplate should be as highly loaded as possible. Consequently an endplate should not be in the immediate vicinity of another endplate, whose function is the same. Such endplates would tend to shadow each other, resulting in inefficient usage of both. The task is to gain insight into the relative importance of these two features. As with the previous Section, we consider skin-friction drag only.

Figure 3.10 shows the variation in C_L/α_W for a unit square wing with endplates at angle of attack $\alpha_P = 0$ and geometry ($\ell = 0.5c, h = 0.5c, a = 0, b = 0, -1 < o < 1$). The graph is symmetric about the vertical axis, indicating as would be expected that the endplate can be reflected in the x-axis with no change in the wing loading. There is a clear maximum when the endplates are offset such that $o = \ell$ or equivalently when $o = -\ell$, such that the endplates are just touching leading-edge to trailing-edge. This result is true no matter where the centroid of the split endplate is, and is a particularly significant result as it limits the search space to the two-parameter specification $(\ell, h, o = \ell)$.

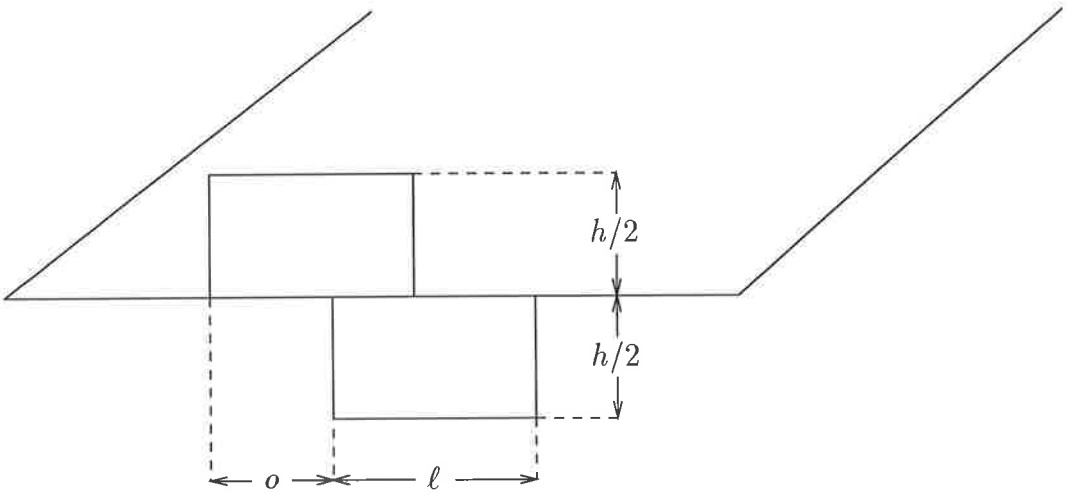

Figure 3.9: *Endplate with independent sections above and below the wing. The horizontal offset o of the two sections is measured as the distance between their leading edges and is positive when the upper plate is forward.*

The optimisation, previously performed with the single rectangular endplates is repeated with the new endplate specification. Qualitatively, the results are the same, but with a higher optimum value. It is interesting to note that the optimal geometry ($\ell = 0.17c, h = 0.53c, o = \ell$) gives the value for $C_L/\alpha_W = 1.91$, which is significantly greater than the

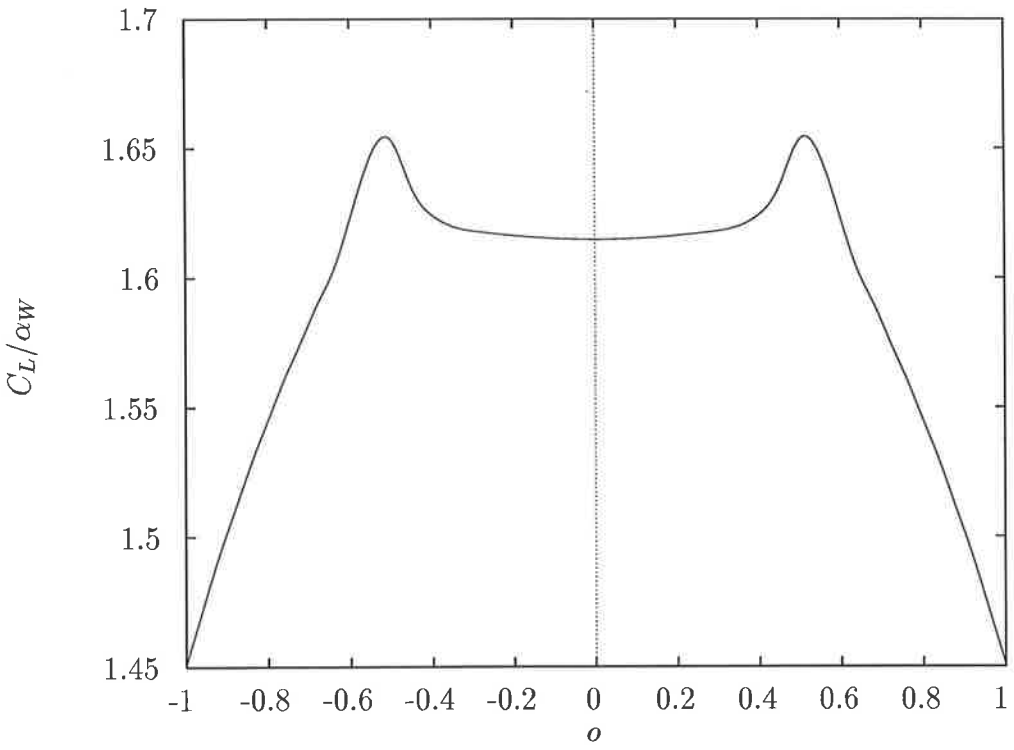

Figure 3.10: *Lift coefficient C_L/α_W versus the horizontal offset o of the top and bottom endplate halves on a unit square wing. The centroid of the combined endplate is such that $a = b = 0$ and the endplate has angle of attack $\alpha_P = 0$.*

optimal value $C_L/\alpha_W = 1.84$ produced using $(\ell = 0.15, h = 0.48, o = 0)$ for a single rectangular plate. The actual area of the split plate geometry is also greater than that of the single plate, and is thus producing 7% more lift. An important optimisation principle is highlighted here, namely that the optimal dimensions of the endplate increase with their loading.

3.7.2 Flare

In order to further load the endplates and procure higher values of C_L/α_W, the endplates will be *flared*, whereby the top and bottom sections will be pitched at angles of attack α_P and $-\alpha_P$ respectively such as to increase the pressure difference between the lower to upper wing surfaces. In the literature, setting a wingtip device at an angle of incidence to the direction of travel is sometimes referred to as "toe-out" when the leading edge of the device is outboard of the trailing edge and "toe-in" when the leading edge is inboard of the trailing edge. Figure 3.11 illustrates the case of positive flare, which refers to the case where lift is increased by having toe-in above the wing and toe-out below.

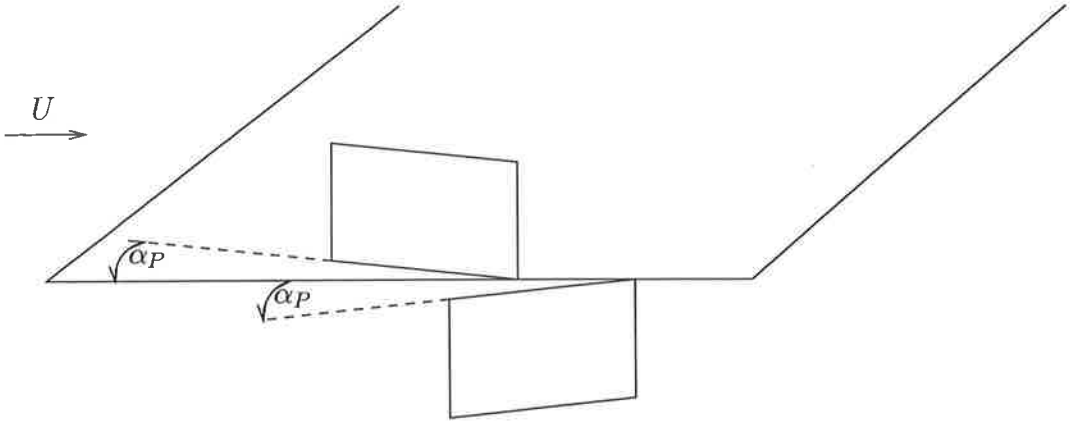

Figure 3.11: *Split endplate with top and bottom endplate sections flared to increase lift. The case of positive flare is illustrated, whereby the upper portion of the endplate is "toe-in" and the lower portion is "toe-out."*

For the present linear analysis, we use the flare ratio α_P/α_W between the endplate angle of attack and the wing angle of attack as our measure of flare. Figure 3.12 illustrates the effect of varying the flare ratio from 0 to 1 starting with the optimal endplates from the previous section. In one sense the result is uninspiring because it is, of course, a straight line under the present linear analysis. However, it does provide a estimate for the magnitude of the extra attainable lift by flaring the endplates. More subtly, the slope of the graph is a measure of the relative significance of endplates on the overall configuration. Indirectly, the lift-curve slope of these endplates is $C_L/\alpha_P = 0.5$, based on total area of wing plus endplates. This is a significantly high value, given that there is no direct lift force on the endplates. Of course, under the present scheme there is no limit to the flare angle, and the possible increase of the lift coefficient is unbounded. It will be shown that the optimal ratio α_P/α_W is naturally attenuated when we consider induced drag, but let us first consider the present situation when $\alpha_P = \alpha_W$.

Within this new paradigm, the optimisation of the lift coefficient with respect to the geometric parameters $(a = 0, b = 0, \ell, h, o = \ell)$ produces the optimal plate geometry $(\ell = 0.25, h = 0.95)$, yielding $C_L/\alpha_W = 2.54$, a staggering 33% improvement on the optimum with no flare in the previous section and, as the optimal area has also increased, an actual increase in lift of 66%.

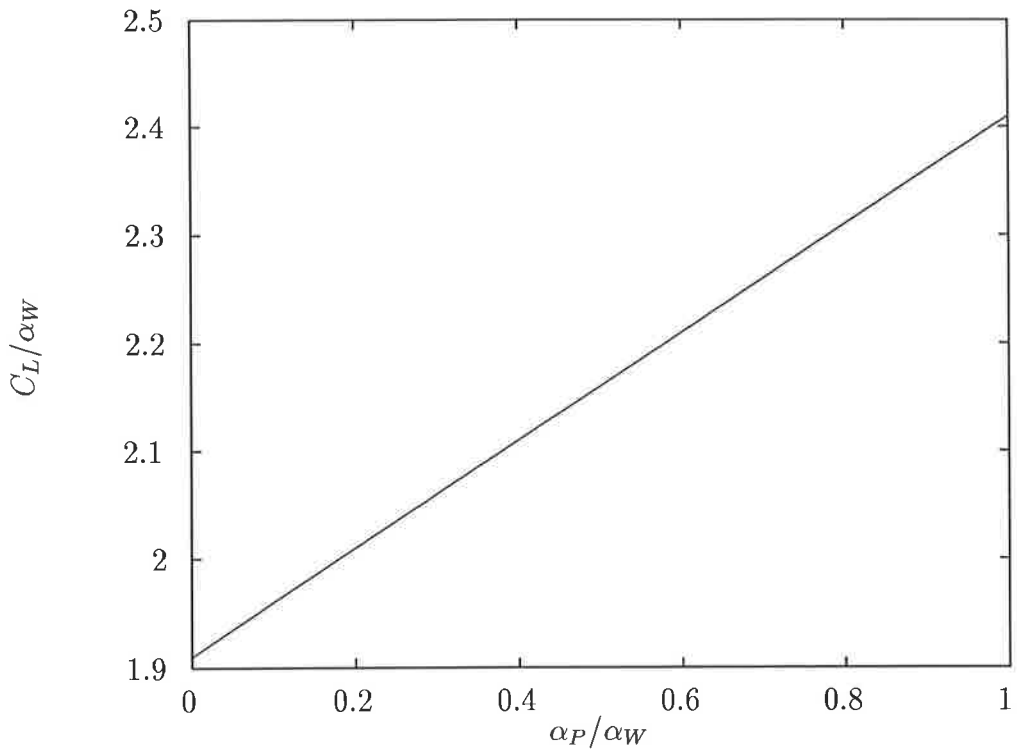

Figure 3.12: *Lift coefficient C_L/α_W versus linear flare measured as α_P/α_W for endplates defined by $(a = 0, b = 0, \ell = 0.17, h = 0.53, o = \ell)$ mounted on a unit square wing.*

3.8 More Realistic Optimisation

Having established some basic principles of endplate optimisation with respect to area, or skin-friction only, we turn to the inclusion of induced drag. Ideally for a single wing with endplates we should be able to do this within the existing linear formulation.

3.8.1 Quasi-Linear Object Function

We wish to consider an object function which favours high lift and penalises some combination of induced and frictional drag. There are a number of possible existing options, such as the Oswald efficiency factor $e = C_L^2/(C_D - C_{D_0})\pi AR$ or the so-called subsonic endurance parameter $C_L^{3/2}/C_D$ (Gall and Smith, 1987). It seems natural in the linear case to adopt a function whose dependence upon angle of attack is restricted to the relative importance of the two forms of drag. In general, frictional drag will be given by

$$D_f = \int_{W+P} \mu \frac{\partial U}{\partial \hat{n}}\, dS. \tag{3.8.6}$$

If we assume that the relative geometry of the wing does not significantly alter the frictional characteristics, then we may make the simplifying assumption that

$$C_f = \mu \frac{\partial U}{\partial \hat{n}} \Big/ \left(\frac{1}{2}\rho_A U^2\right). \tag{3.8.7}$$

The total drag coefficient is then given by

$$C_{D_T} = C_{D_i} + C_f, \tag{3.8.8}$$

and if we define the optimisation task to be maximising the value of

$$\frac{C_L^2}{C_{D_T}} = \left(\frac{C_L}{\alpha_W}\right)^2 \Big/ \left(\frac{C_{D_i}}{\alpha_W^2} + \frac{C_f}{\alpha_W^2}\right), \tag{3.8.9}$$

then the only quantity external to the existing linear algorithm is C_f/α_W^2. Since it is inversely dependent upon the square of α_W, it may span several orders of magnitude. There is also a weak dependence of C_f upon **Re** as shown in Figure 3.13 which is reproduced in part from Rosenhead (1963). Whether the boundary layer is modelled as laminar or turbulent, for subsonic aircraft the linear friction coefficient may be assumed to lie within the range $0.001 < C_f < 0.01$. If we fix $C_f/\alpha_W^2 = 1$, this corresponds to a range of angle of attack $1.8^o < \alpha_W < 5.7^o$. Rather than independently select values of C_f and α_W for specific applications, it is more useful at this stage to chart the general trends in optimal geometry as we vary the combination C_f/α_W^2. It should be noted that the results for the present work converge to the previous results for optimisation with respect to area only in the limit $C_f/\alpha_W^2 \to \infty$. The ranges of values for C_f and α_W corresponding to the parameter C_f/α_W^2 are illustrated in Figure 3.14.

3.8.2 The Search Space

There are a very large number of variables to be considered when setting out to find the best three-dimensional lifting surface. Even without variable camber, the chord must be specified as a function of y and z over the wingspan and the vertical extent of the plate respectively. While this is an admirable ultimate aim, we shall begin by examining the relative effects of a smaller number of geometric parameters, where possible determining their dependencies. In order to restrict the search we will again presume that the wing is a unit square. Thus the only variables are those describing the size, location and relative angle of attack of the endplates. To emphasise the immediate effect of including induced drag in the calculation, we start with a determination of the optimal angle of attack of the endplates α_P/α_W.

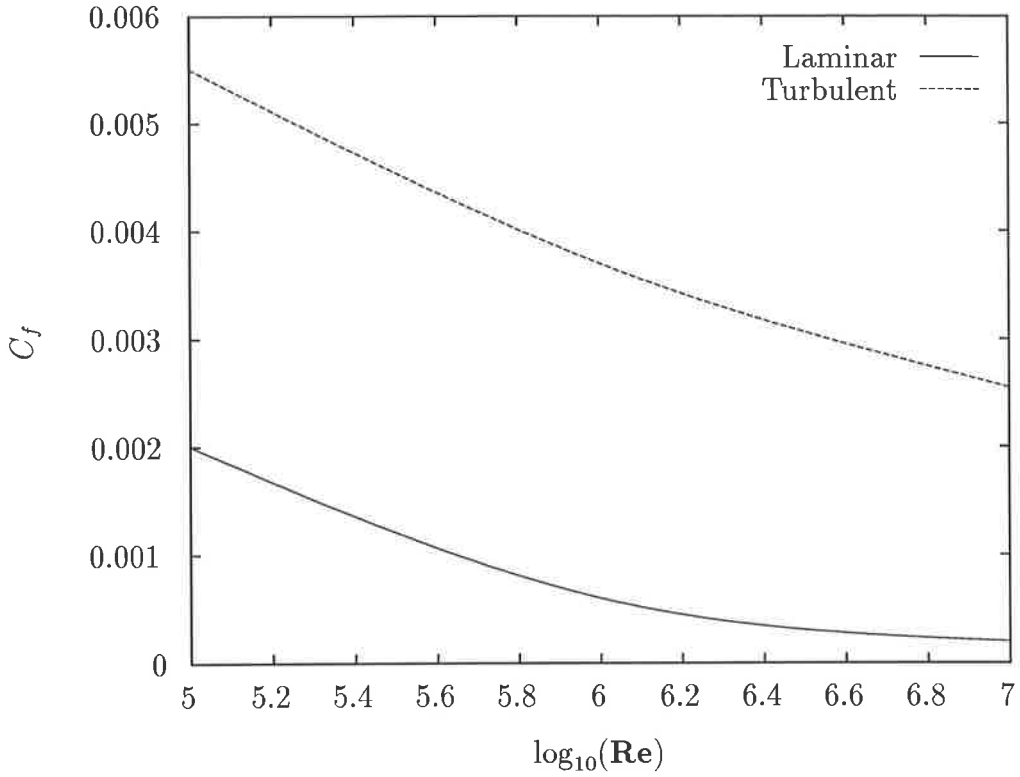

Figure 3.13: *Variation of the linear friction coefficient C_f with the Reynolds number* ***Re****. After Rosenhead (1963). Whether the model of the boundary layer used is laminar or turbulent, the linear friction coefficient lies well within the range* $0.001 < C_f < 0.01$.

3.8.3 Optimal Endplate Angle of Attack

In the optimisation of C_L^2/C_{D_T}, Munk's third theorem concerning optimal wake vorticity distribution suggests a trade-off between loading on the plates and the resultant induced drag. Before exploring this optimisation, we must explicitly include the drag component due to the angle of attack of the endplates, since the force perpendicular to the endplates now has a component parallel to the direction of travel.

In order to incorporate this effect, the total drag component of the objective function is modified according to

$$C_{D_i} = \left(\frac{C_{D_i}}{\alpha_W^2}\right)\alpha_W^2 = \left(\frac{C_L}{\alpha_W}\right)\alpha_W^2 + 2\left(\frac{C_{L_P}}{\alpha_W}\right)\left(\frac{\alpha_P}{\alpha_W}\right)\alpha_W^2 - \left(\frac{C_S}{\alpha_W^2}\right)\alpha_W^2, \quad (3.8.10)$$

where the endplates on both sides of the wing have been included. Note that each of the required output quantities is still available from the current linear formulation.

For simplicity, we again consider the case of a unit square wing, with unit square endplates centered both horizontally and vertically on the wing mid-chord. Figure 3.15 shows the variation in the object function C_L^2/C_{D_T} with the flare ratio over the range from

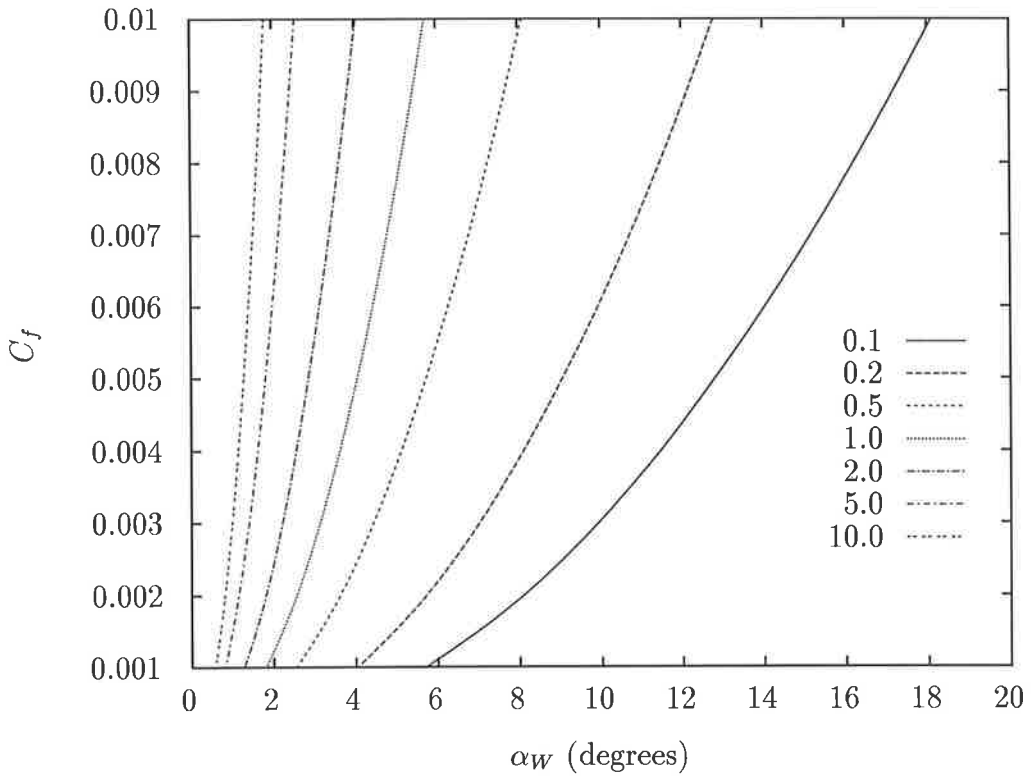

Figure 3.14: *Ranges of the frictional coefficient* $0.001 < C_f < 0.01$ *and angle of attack* α_W *corresponding to the parameter* $C_f/\alpha_W^2 = 0.1, 0.2, 0.5, 1, 2, 5$ *and* 10.

$-5 < \alpha_P/\alpha_W < 5$ for various values of the flow parameter $0.1 \leq C_f/\alpha_W^2 \leq 10$. The negative values for α_P/α_W indicate that the flare on the endplates is acting to reduce the lift, which actually creates a geometry with zero lift but finite drag when $\alpha_P/\alpha_W = -1.7$. When the flare is positive however, the trend in optimal design is clear. For low values of C_f/α_W^2, since there is no penalty on area, the endplates should be used with small angle of attack. For higher values of C_f/α_W^2, the optimal flare ratio approaches infinity because any available area must be as highly loaded as possible. It is interesting to note that for $C_f/\alpha_W^2 = 1$, the optimal endplate angle of attack is $\alpha_P/\alpha_W = 1.5$.

3.8.4 Optimal Location

We already know that the optimal endplate location corresponding to a large value of C_f/α_W^2 is centered both horizontally and vertically on the wing mid-chord. What effect will the inclusion of induced drag have on the optimal placement? Firstly we consider a unit square wing with endplates of dimensions $(\ell = 0.5, h = 0.5)$. Figure 3.16 shows the variation in C_L^2/C_{D_T} as the horizontal offset varied over the range $-0.5 < a < 0.5$. The endplate is maintained at the vertically central position.

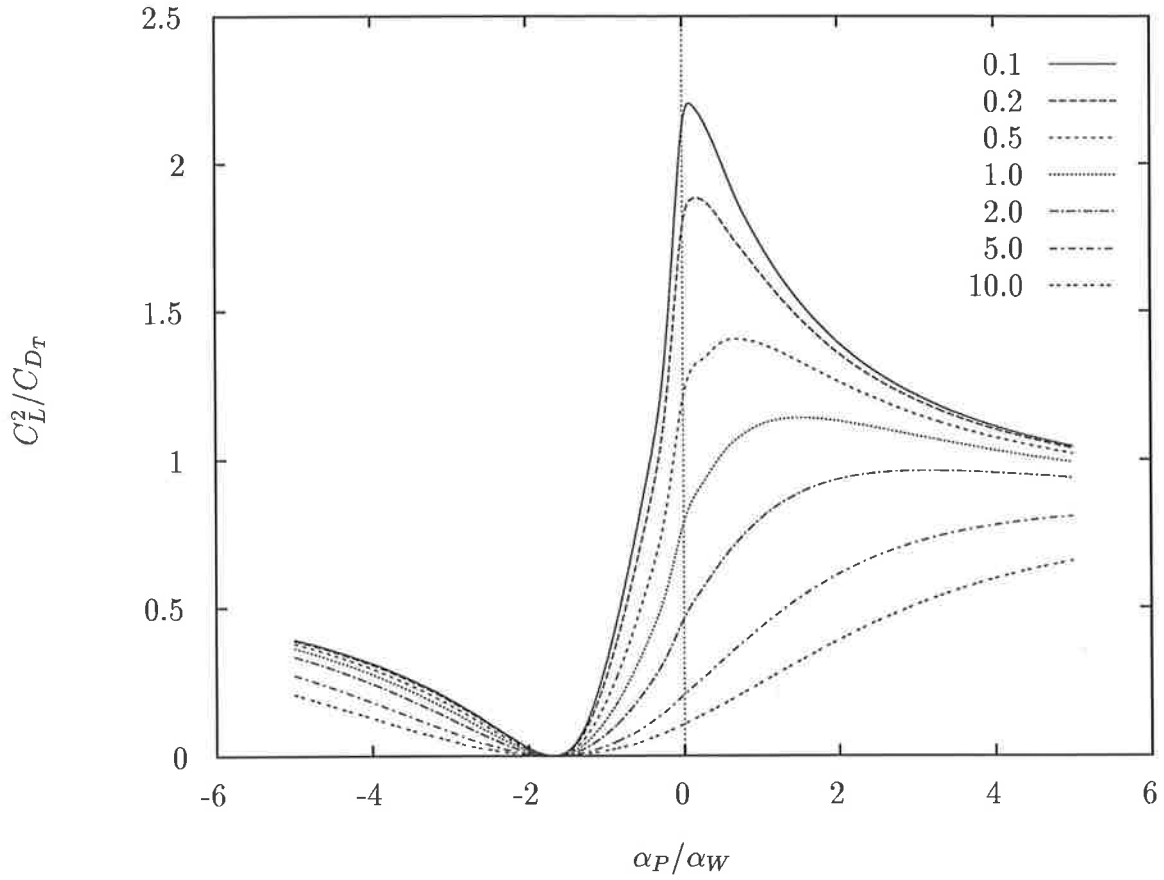

Figure 3.15: *Variation in the object function C_L^2/C_{D_T} including both induced and frictional drag versus the flare ratio α_P/α_W for a unit square wing with unit square endplates. The flow parameter takes values $C_f/\alpha_W^2 = 0.1, 0.2, 0.5, 1, 2, 5$ and 10.*

The smooth transition is fairly clear, with a horizontal offset $a = 0$ as expected for high values of the flow parameter yielding to a forward placement of the endplates to reduce induced drag as was found by Hemcke (1927) when the flow parameter is small. The optimum placement for small values of the flow parameter C_f/α_W^2 is flush with the wing leading edge, thereby maximising the leading edge suction on the endplate. Figure 3.17 shows the lift, total leading edge suction and resultant total induced drag components separately for the linearised $\alpha_W = 180^o/\pi$ case.

It is also interesting to see whether there are any induced drag effects on the optimal vertical location of the endplates. Figure 3.18 shows the variation in C_L^2/C_{D_T} with the vertical offset b of the same endplates, maintaining the streamwise central location. For the range of flow parameters $0.1 < C_f/\alpha_W^2 < 10$, the optimal location is vertically centered, although in all cases the gradient is very small. It is likely that this feature could be easily sacrificed to increase the efficiency with respect to another design parameter.

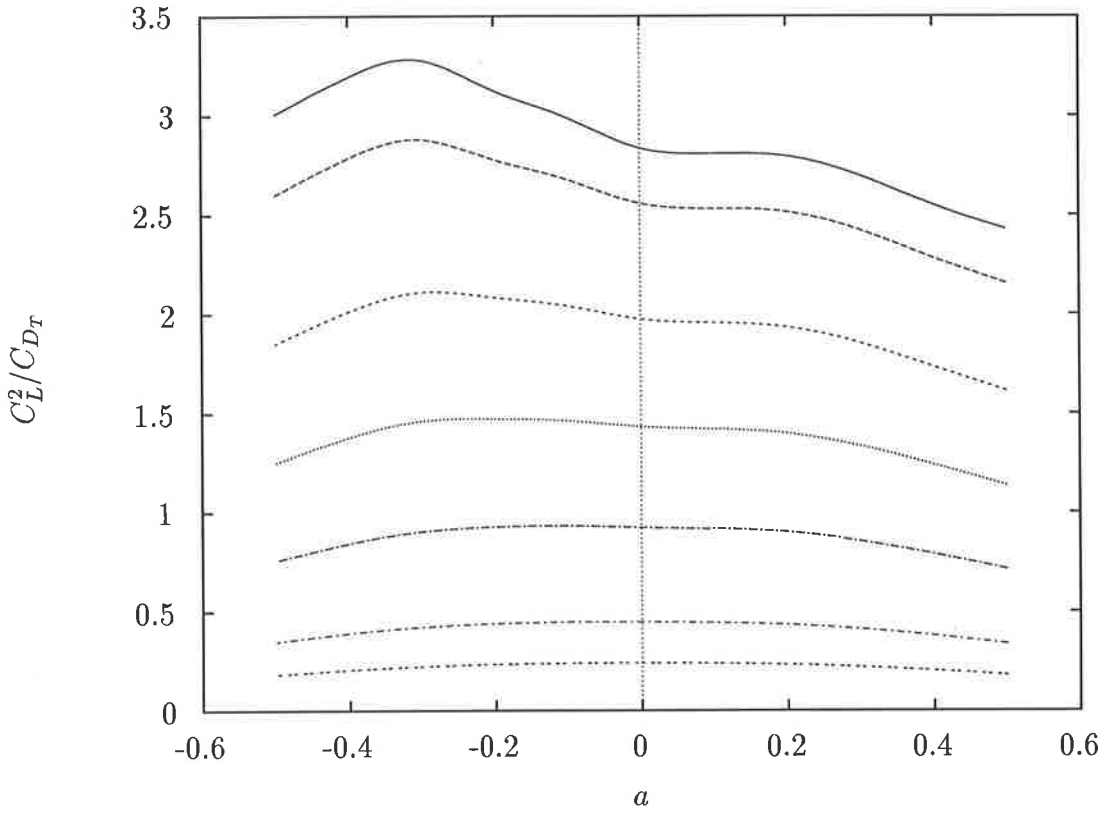

Figure 3.16: *Variation of the object function* C_L^2/C_{D_T} *as the endplate horizontal offset is varied over* $-0.5 < a < 0.5$ *for values of the flow parameter* $C_f/\alpha_W^2 = 0.1, 0.2, 0.5, 1, 2, 5$ *and* 10. *The highest value curve corresponds to* $C_f/\alpha_W^2 = 0.1$, *down to the lowest which corresponds to* $C_f/\alpha_W^2 = 10$.

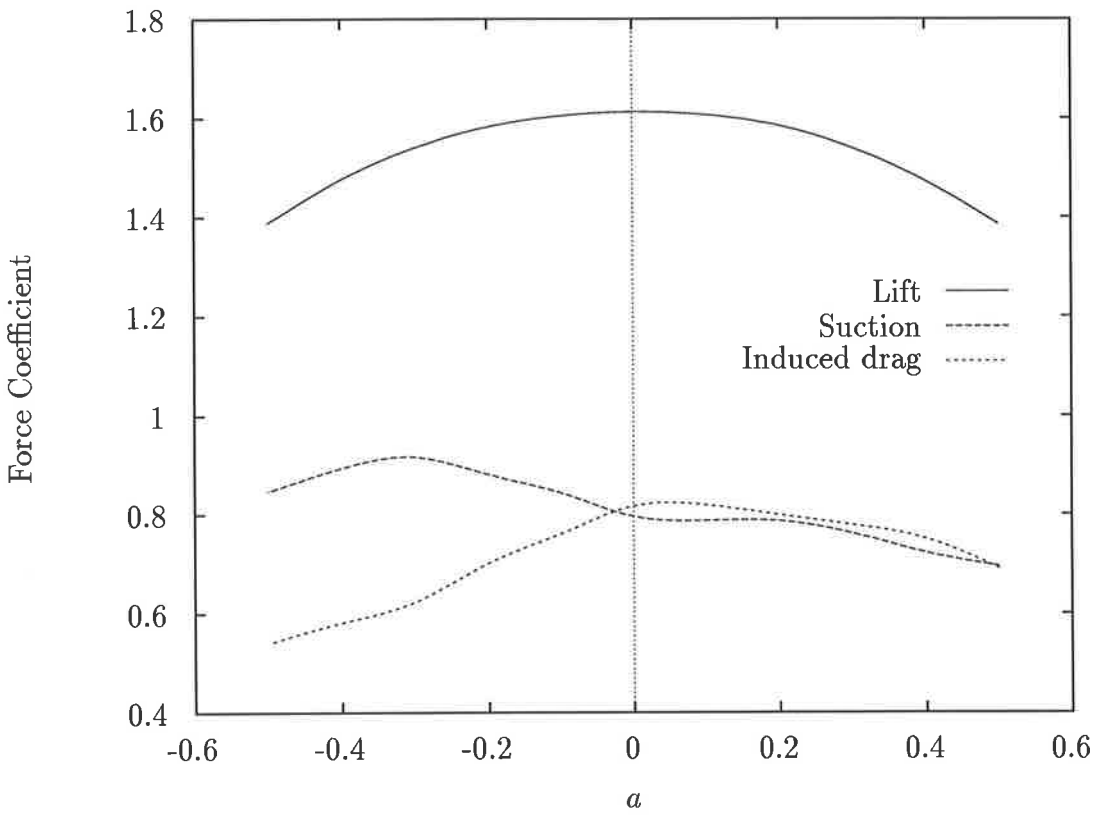

Figure 3.17: *Variation in the individual linearized force components* C_L/α_W, C_S/α_W^2 *and* C_{D_i}/α_W^2 *versus the streamwise endplate offset a for the case of a unit square wing with square endplates defined by* $(\ell = 0.5c, h = 0.5c)$.

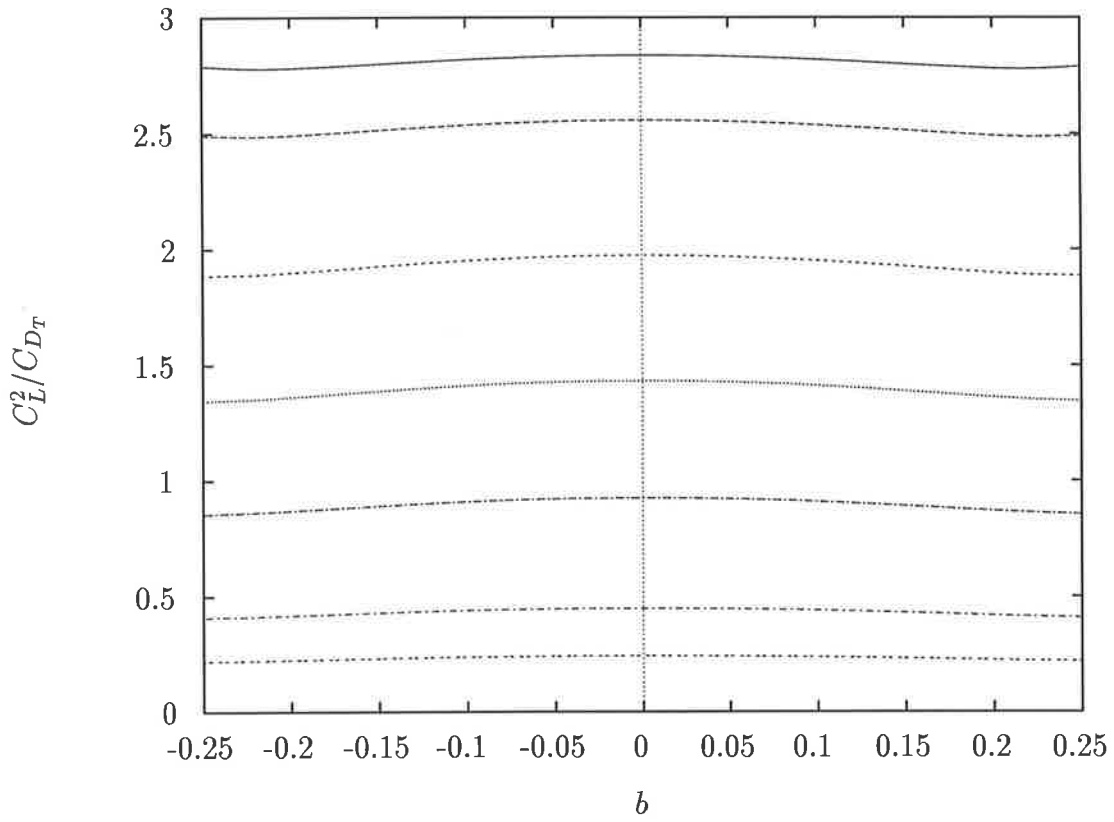

Figure 3.18: *Variation of the object function* C_L^2/C_{D_T} *as the endplate vertical offset is varied over* $-0.25 < b < 0.25$ *for values of the flow parameter* $C_f/\alpha_W^2 = 0.1, 0.2, 0.5, 1, 2, 5$ *and* 10, *with the highest value curve corresponding to the lowest value of the flow parameter.*

Chapter 4

Ground Effect

4.1 Introduction

Ground effect is the term used to describe the modification to the forces experienced by a body when moving in the vicinity of a planar fluid boundary. The boundary may be rigid as in the case of solid ground or a sea bed (Tuck, 1974) or it may be a deformable free surface, analogous to the case of an interfacial wave (Grundy, 1986b). In the latter case, the boundary may be effectively planar such as for a large scale object moving at high speed in air over a calm water surface (Rozhdestvensky and Synitsin, 1993) or be geometrically complicated by natural and/or artificial features. It is not uncommon when considering an air/water interface to consider the aerodynamics over a steady water surface undergoing hydrostatic deformation (Tuck, 1975), (Grundy and Tuck, 1987).

This Chapter contains material already published (Standingford and Tuck, 1996a) concerning the effect of introducing a rigid ground plane to the free air analysis presented in Chapter 3. The specific application is the design of a *Wing-In-Ground-Effect* (WIG), otherwise known as an *ekranoplan*. [Note: *ekrano-plan* = Russian for *screen-plane*, or a craft whose aerodynamic characteristics are dominated by the presence of a (reflective) fluid boundary]. Here we also present a more comprehensive literature review and an examination of the effect of wingspan on ground effect.

4.1.1 Classes of Ground Effect

Ground effect can be divided into three regimes, namely small (clearance far in excess of chord), moderate (clearance comparable to chord), and extreme (clearance small compared to chord). Tuck gives a full derivation of the extreme ground effect theory in two dimensions (Tuck, 1978), (Tuck, 1980) and (Tuck, 1981) which adds work on trailing-edge flaps and stability, and (Tuck and Bentwich, 1983) which gives theory and computations for wings of finite aspect ratio.

Extreme ground effect is nonlinear, with large deviations from free-stream velocity in the gap zone, and hence large forces. The lift coefficient can be of the order of unity, and in particular is not proportional to the small angle of attack. Instead, it is more closely related to the *contraction ratio* of the gap zone, or leading-edge clearance to trailing-edge clearance.

The papers mentioned so far assume that the ground plane is solid. Some other papers (Tuck, 1975), (Tuck, 1984) and (Grundy and Tuck, 1987) assume a water surface which is allowed to deform hydrostatically under the influence of the aerodynamic pressure in the gap. There is then a strong nonlinear coupling between aerodynamics and hydrostatics, since the deformation of the water surface affects the air flow and vice versa. The assumption that the water surface deformation is hydrostatic is also questionable, but incorporation of true hydrodynamic effects into the coupled nonlinear extreme ground-effect problem is very difficult (Grundy, 1986b).

Moderate ground-effect (clearance comparable to chord) is more conventional. The problem then reverts (for small angle of attack) to linear aerodynamics, with small lift coefficients proportional to the angle of attack, though with a coefficient of proportionality substantially different from the open-air value. This regime was studied (Tuck, 1971) for a general non-wing-like body (e.g. an automobile) and for wing-like leaflet valves near a plane wall (Tuck, 1982c), (Tuck et al., 1982). The aerodynamic effect of moderate ground effect on standard wing design is available in the literature (Katz and Plotkin, 1991), (Kuchemann, 1978),

4.2 Ekranoplans

Flying in ground effect is an attractive option for military and commercial aircraft because of the high lift and low drag, as well as radar avoidance considerations. In recent years, the work on aerodynamic design specifically for flying in ground effect has been significant. Figure 4.1 shows the comparison between a swan taking off and an *Airfisch 3*, manufactured by Fischer Flugmechanik.

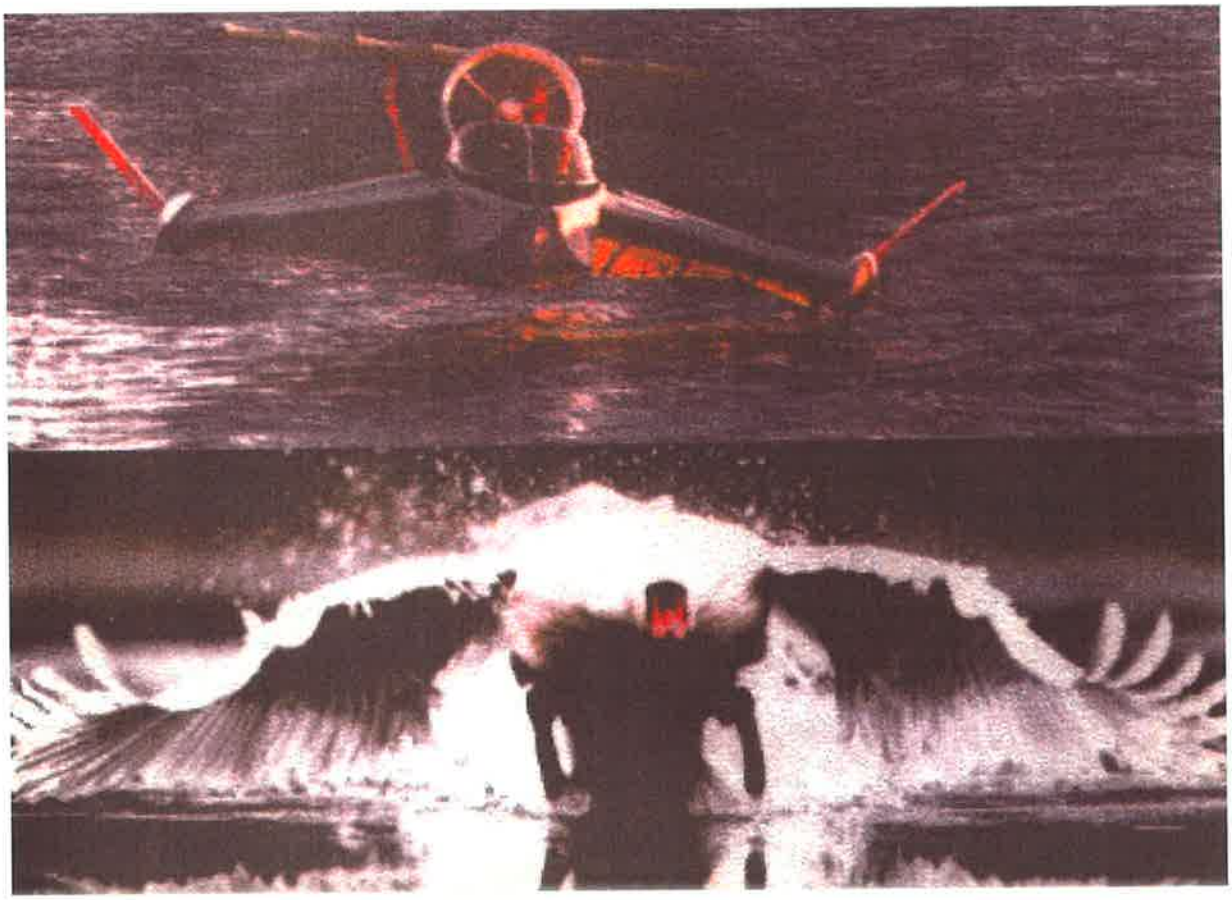

Figure 4.1: *Comparison of the Fischer Flugmechanik "Airfisch 3" with a swan taking off. Reproduced from "Ekranoplans and Very Fast Craft" (1996).*

A number of highly specialized groups worldwide are considering the various problems concerning the commercialization of ekranoplan technology. Aside from the original Wright brothers flyer, which arguably never flew out of ground effect, the Russian models such as the "Orlyonok" illustrated in Figure 4.2 otherwise known as the "Caspian Sea Monster" were the first to receive serious attention.

Although some early investigation from the British and United States' defence sectors explored the possibility of applying ground-effect technology to similar large vehicles, it

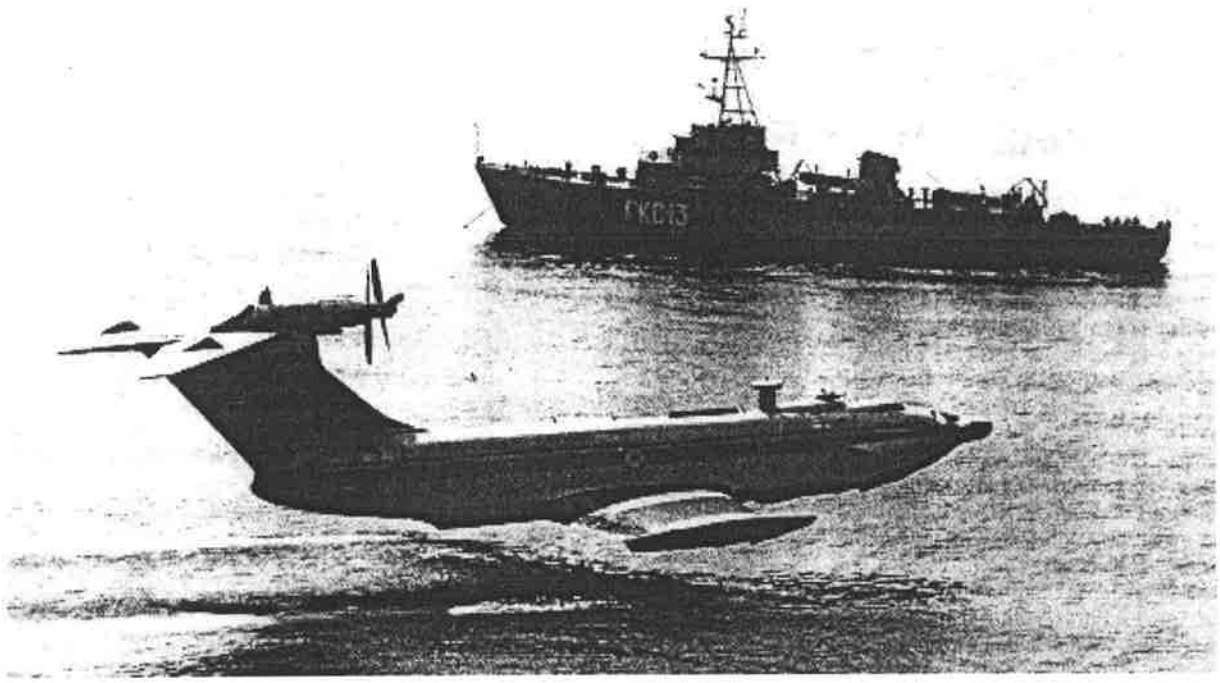

Figure 4.2: *The 120 tonne "Orlyonok" is one of the largest Russian ekranoplans. First launched in 1972, it has a length of 60 metres, a cruising speed of 400 kilometres per hour and a range of 1000 kilometres. Reproduced from "Engineers Australia" (1996).*

is only now that the United States is considering the manufacture of a large transport "Wingship" (Hooker, 1996). It is now accepted that the original Russian vehicles do not compete in efficiency with modern transport aircraft, but the large payload combined with the flexibility of landing on any open water surface rather than on an airstrip means that they are still in use.

One must be careful when distinguishing between the craft flying in aerodynamic ground effect and those making use of a static air-cushion analogous to a hovercraft. The term "ekranoplan" has been applied to a number of commercial craft that use a partial flexible hovercraft-like skirt to produce lift. Throughout this Chapter, ground effect will refer only to vehicles deriving their lift from aerodynamic forces. There is current debate also as to the various classes of ekranoplan and whether they should be able to sustain flight out of ground effect for safety reasons. This forms part of a wider discussion about whether the relevant regulatory body should be Maritime or Aviation (Bogdanov and Maskalik, 1996).

It is generally accepted that future ekranoplans will have to have integrated functionality

so that the body acts as a lifting surface and the transition from the body to the wing becomes smooth (Hooker, 1996). For very large craft with reasonably efficient aspect ratios, root bending moment considerations suggest that distributed payload systems would offer a considerably lighter structure for a given payload. The free air "spanloader" has been the subject of considerable research for this reason (Lange, 1988). The design process involved in producing such a vehicle is made difficult because the functionality of individual components is not unique. An appealing design among the smaller categories of vehicles operating in ground effect that exhibits this integrated design philosophy is the *RADACorp* "C–850" illustrated in Figure 4.3.

Figure 4.3: *The RADACorp C–850 shows the trend in future designs for ground effect vehicles. Although integrated wing-body designs are more complicated for aerodynamic analysis, they offer superior parasite drag characteristics and market appeal. Reproduced with permission.*

Despite the theoretical advantages of flying in ground effect, there are a number of generally accepted challenges that the so-far embryonic industry must face before successful production vehicles can be made. When the ground surface actually refers to a fluid surface like an ocean, the stability requirements on the design of the craft mean that that service must be either limited to very calm water or that the size of the vehicle must be

Figure 4.4: *The proposed* Wingship *Hoverplane concept ground effect vehicle. The Hoverplane is expected to be large enough to be able to fly safely above 8 metre waves. Reproduced with permission.*

large when compared to the size of the largest waves likely to be encountered. One such proposed design is the *Wingship* "Hoverplane" which is intended to be large enough to safely fly over 8 metre waves. While a passively stable design is the ultimate aerodynamic aim, it is likely that a certain amount of the near-surface control will be automated to improve stability and ride quality.

4.3 Present Formulation

A feature of moderate ground effect is that when the ground plane is replaced by a water surface there is, to leading order no coupling between the aerodynamics and hydrodynamics. Hence one can solve the combined aero-hydro problem in serial stages, first computing the aerodynamic problem for a rigid ground plane, then applying the resulting ground pressure distribution to the water surface, so generating a hydrodynamic flow due to an apparent "hovercraft" with that pressure distribution. A more detailed justification of this approach is presented in Chapter 5 .

Here we first include rigid ground effects to the lifting-surface computational tools de-

veloped and applied in the previous Chapters. When one is including a ground plane (in principle quite straightforward by the method of images) it is important to maintain maximum numerical accuracy of determination of the pressure distribution on the wing and ground plane. This is particularly difficult when the wing is close to the ground (i.e. when $h/c < 0.1$) and large numbers of chordwise panels are required to capture the pressure distribution in the gap zone.

The linear model also loses validity when the wing loadings are very high because of backwash. Lan (1976) noted that the image vortex system may in some cases be strong enough to decrease the velocity on the wing enough to reduce the lift to below the free air value.

An important inclusion in the present thesis is the computation of the effect of the ground plane on the induced drag of a wing, both with and without endplates. Information is provided here on the optimum size and positioning of wingtip endplates, which become full skirts touching the ground for heights less than about one-half of the wing's chord.

Once we have a good algorithm for determination of the pressure distribution on the ground plane, it is only necessary to apply that distribution as a free-surface forcing term to determine the hydrodynamics of the flow in the water. The required formula is well known (Wehausen and Laitone, 1960), and all that is needed is an accurate double numerical integration over the whole free surface, noting that the aerodynamic pressure is felt everywhere, not just immediately beneath the wing.

Some wave resistance computations have been made in this way, and will be reported in the next Chapter. However, the general conclusion seems to be that the wave resistance of a wing in ground effect is negligible relative to the aerodynamic induced drag, for vehicles traveling at speeds high enough that there is adequate aerodynamic lift. This is so for two reasons. In the first place, there is a factor involving the small air/water density ratio between the water and air drags, expressing the fact that the size of the traveling pressure distribution is proportional to the air density, but has to create a disturbance proportional to the water density. Secondly, the Froude number is likely to be of the order of $F_L \simeq 10$, which is far in excess of the usual naval architectural values, and any water-borne vehicle is an inefficient wave generator at such Froude numbers.

However, at low velocities the wave drag may be significant. The ground-effect industry is acutely aware of the *hump drag* that must be overcome when a vehicle accelerates

to take off from a hydrostatic mooring. This is the well understood increase in hydrodynamic wave resistance up to a critical velocity, sometimes called the hull-speed of a non-planing ship. Beyond this critical velocity, the wave resistance is inversely proportional to the speed. In order to make this transition as easily as possible, ground-effect vehicles sometime have take-off aids. One such addition, called power-augmented ram (PAR) (Lange, 1988) makes use of the backwash phenomenon previously mentioned to create stagnation pressure beneath the wing. This technique requires a large amount of power and ingenious alternatives are likely to be developed.

4.4 Results for a Rigid Ground Plane

The aerodynamic induced drag of a bare wing in ground effect increases as altitude decreases. It is a misconception that as a lifting surface approaches a rigid ground the flow becomes more "two-dimensional" in nature. What really happens is that the pressure beneath the wing drives the fluid sidewards out from under the wing and around the wingtip at a rate proportional to the pressure drop in the gap zone, and since that pressure drop increases as the altitude decreases, this undesirable sideslip velocity also increases.

The only thing that can prevent sidewards flow is the addition of some barrier. In open-air aerodynamics, such barriers are called endplates, or in a somewhat different role, winglets. In racing-car design for downforce, barriers that effectively touch the ground, so blocking all sideways flow, were called "skirts" when used very effectively in Formula 1 racing in the late 1970's (Tuck, 1983), (Incandela, 1990). Skirts were later banned from Formula 1 in an attempt to reduce dependence upon ground effect. We shall use the term skirt here to denote an endplate that lies only below the wing, extending for its full chord, and touching the ground.

In the case of open-air aerodynamics, it has been shown (Standingford and Tuck, 1996b) that even quite small endplates located halfway along the wing chord and vertically centered on it (symmetrically above and below) can dramatically increase the lift coefficient.

As a wing approaches the ground, the character of the pressure distribution changes significantly. On a thin lifting surface in open air, there is both a pressure increase

beneath the wing and a pressure decrease above the wing, relative to free-stream pressure, and these effects essentially contribute equally to the lift-creating pressure difference across the wing. This pressure difference becomes large only very near the leading edge. In extreme ground effect, although there is still a pressure decrease above the wing of comparable magnitude to that in open air, the net pressure difference is dominated by a vastly increased pressure on the lower wing surface. That surface may be considered to be the upper boundary for a converging channel flow between the wing and the ground. There is a rapid fall in velocity near the entrance to the channel, followed by a slower return to free-stream velocity at the trailing edge exit. This produces a large rise in pressure extending over most of the forward part of the channel .

For wings of finite aspect ratio, whether in ground effect or not, the pressure difference between the upper and lower wing surfaces becomes zero at the wingtips. This both reduces the lift, being the integrated pressure difference, and also causes an induced drag which is seen in the vortices which trail behind the wing, driven by the flow of air around the wingtip from bottom to top.

For evaluating the induced drag of a planar wing in ground effect, we may verify our present leading-edge suction formulation with the Trefftz-plane double integral, which must include a term for the image of the wing in the ground plane, viz

$$D_i = \frac{1}{2}\rho_A \int_W \Gamma(y) \frac{d}{dy} \int_W \Gamma(\eta) \left(\frac{1}{y-\eta} - \frac{(y-\eta)}{(y-\eta)^2 + 4h_0^2} \right) d\eta dy. \qquad (4.4.1)$$

Since the quickly-convergent method of evaluating this integral by means of a Fourier transformation discussed in Chapter 2 has no analogue when the non-singular part is concluded in the kernel, a Riemann-type approach is used instead. While the results agree with those predicted by the suction method, the rate of convergence with the number of spanwise panels is very slow, and so the suction method is used from now on.

Figure 4.5 shows our computations of the lift and induced drag coefficients as a function of ground clearance for a bare planar square wing with aspect ratio $AR = 1$. What is clear from this Figure is that lift and induced drag both increase dramatically as the ground clearance is reduced, ultimately both varying inversely with mean ground clearance or altitude h_0/c. Substantial lift increase is indeed obtained from ground effect, but at the expense of increased induced drag. For a bare wing, there is no indication that ground effect makes the flow more two-dimensional, or reduces the relative importance of induced drag. The loading for the case of a bare wing in ground effect is shown in Figure 1.15. In

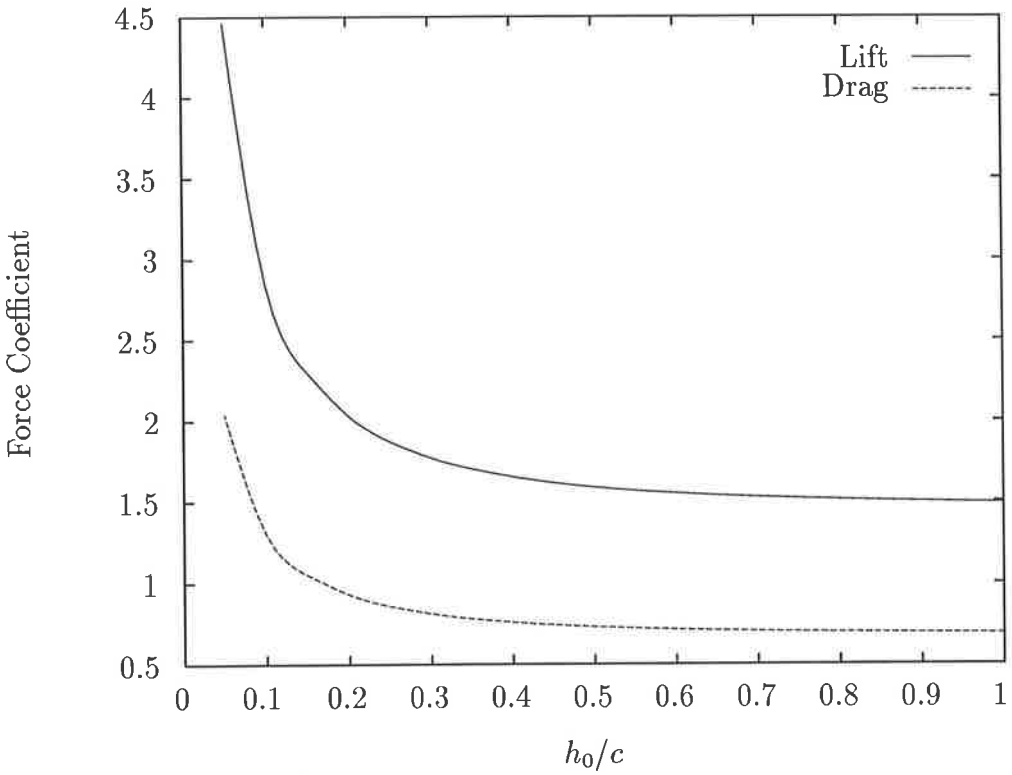

Figure 4.5: *Variation of the lift and induced drag coefficients for a bare square wing in moderate ground effect.*

all cases, the absolute pressure distribution is shown on the ground surface. The actual pressure distribution will be discussed in Chapter 5.

These Figures illustrate the importance of including endplates or full skirts into the design of vehicles operating in ground effect. Without them, the actual efficiency of the vehicle is likely to be similar to a vehicle operating in free air, with the exception that a higher lift coefficient will allow a smaller angle of attack and a greater resulting reduction in the induced drag coefficient.

4.4.1 Endplates Below the Wing

Since the main aim is to increase the lift due to ground effect and reduce the effect of induced drag, we first consider the addition of endplates to the bottom half of the wing only, along the full wing chord and extending to the ground. Specifically we shall examine the addition of rectangular skirt-like endplates to a square wing.

When such endplates are added (see Figure 4.8) we find that the lift is vastly increased but the induced drag changes hardly at all. The flow has been made significantly more

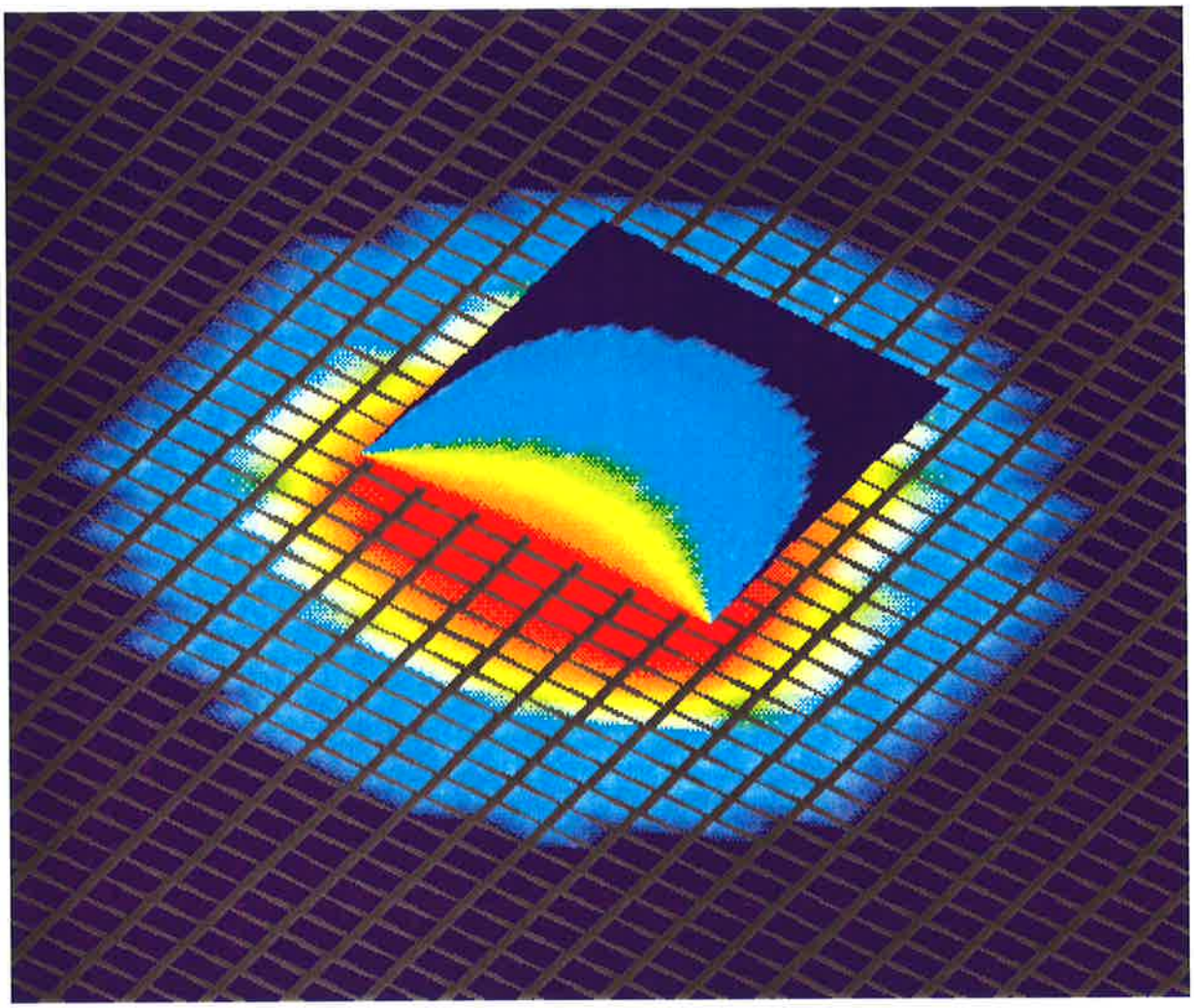

Figure 4.6: *When a bare wing flies over a ground plane, there is a pressure exerted on the ground, but the flow remains three-dimensional, no matter how small the clearance.*

two-dimensional by the endplates. Below an altitude of $h = 0.15c$, where c is the wing chord, the induced drag of a wing with endplates is actually less than that of the bare wing, even though the lift is many times higher.

4.4.2 Aspect Ratio Effects

It is well accepted that in open air, the aspect ratio AR of a wing is crucial to its performance, and the higher the aspect ratio the better. Since the two-dimensionality of the flow over a bare wing is unaffected by the presence of a rigid ground, this is also true in ground effect. For a bare wing at altitude $h_0 = 0.1c$, the lift coefficient is more than doubled by increasing the aspect ratio from $AR = 1$ to $AR = 2$ (see Figure 4.9). On the other hand, the more nearly two-dimensional flow over the same wing with skirts already

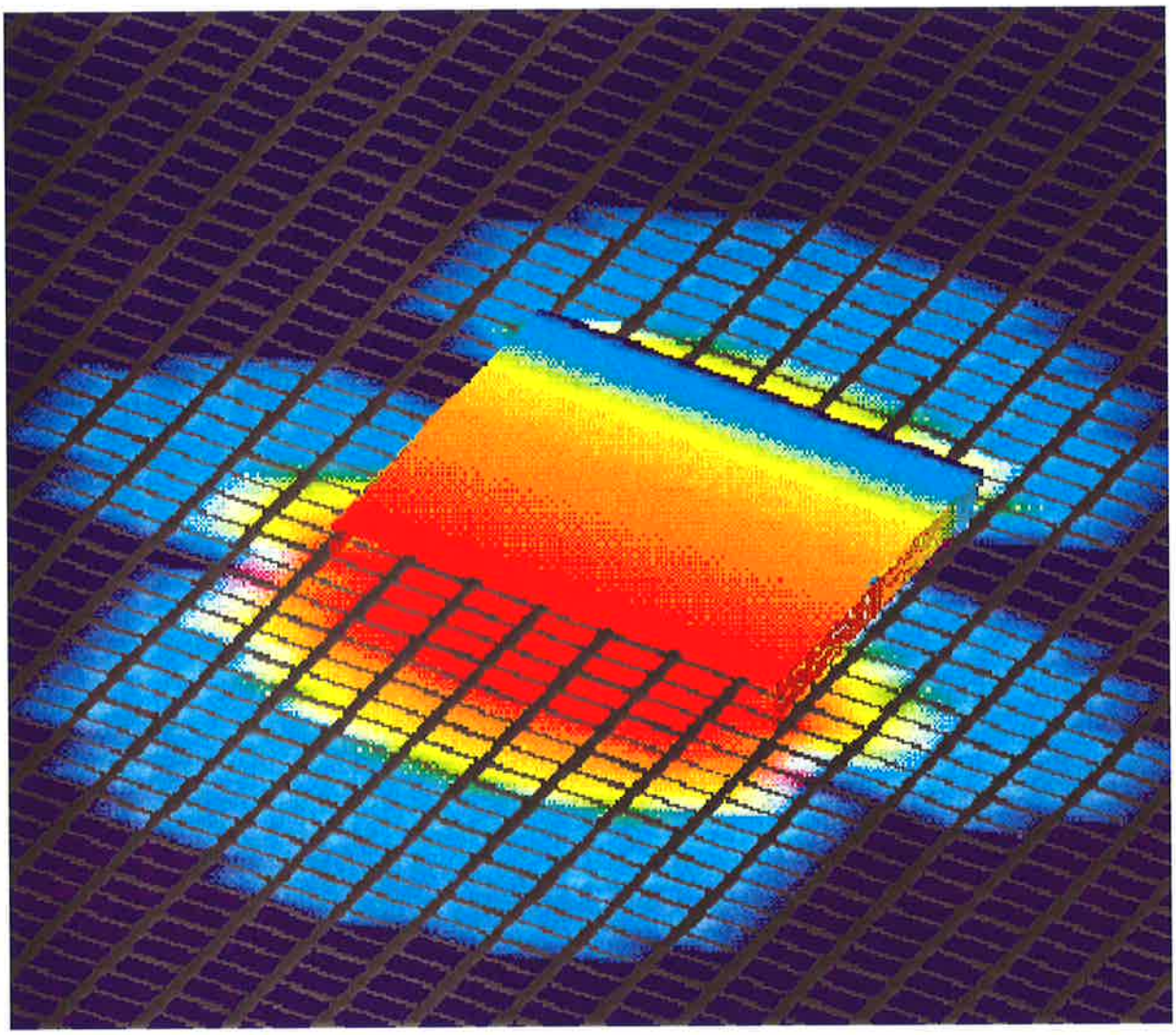

Figure 4.7: *When endplates or skirts are added to the wing in ground effect, the flow becomes effectively two-dimensional.*

has a much higher lift coefficient, and the extra increase in lift due to the same change in aspect ratio is less than 5%. Hence skirts enable effective use to be made of wings of much lower aspect ratio than is conventional in open air.

As the aspect ratio of a bare wing increases from $AR = 1$ to $AR = 2$, the induced drag coefficient at altitude $h_0 = 0.1c$ increases by more than 50%, whereas the same wing with skirts has a corresponding decrease in induced drag of 50%.

4.5 Optimal Placement of Endplates

It has been established in Chapter 3 that if lift is to be maximised by the placement of finite endplates on the wingtips tips of a given rectangular lifting surface in open air,

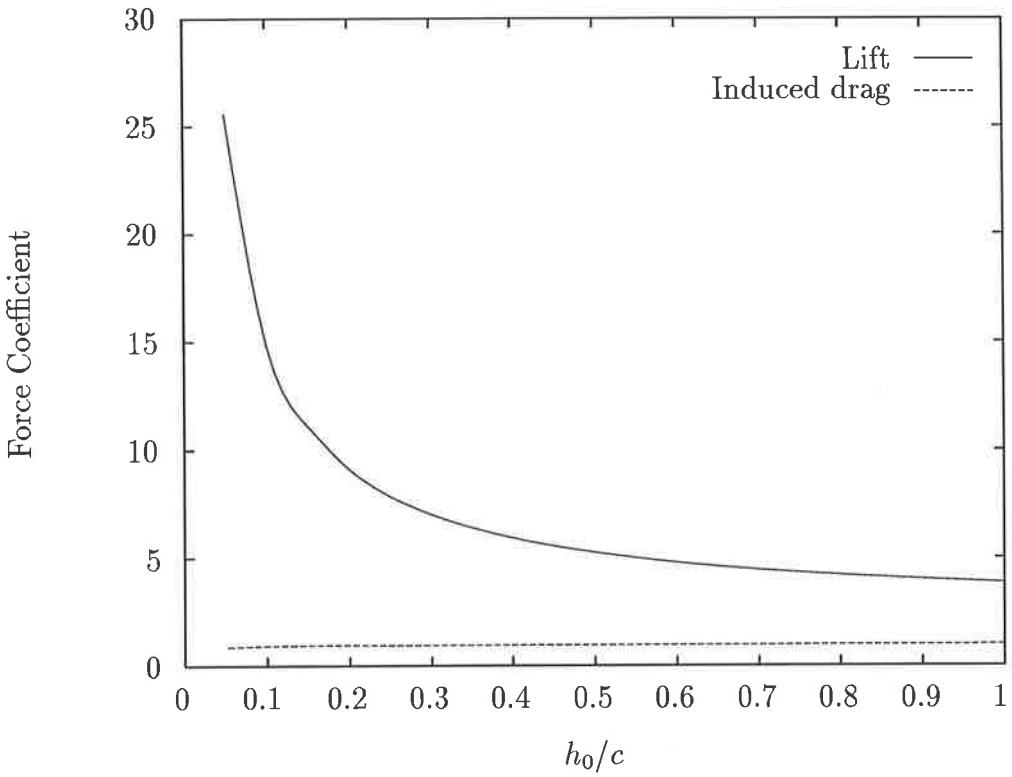

Figure 4.8: *Lift and induced drag coefficients for a square wing with lower full-chord endplates in ground effect. Note that the lift coefficient increases with the inverse of the altitude while the induced drag remains constant. While the lift force is proportional to the pressure realised on the body, the potential for induced drag is in some sense proportional to the product of the pressure and the cross sectional area of the gap flow.*

then the endplates should be centered on the wingtip mid-chord. The optimal size of the endplates depends upon the various flow parameters and the aspect ratio of the wing.

It has already been stated that the character of the flow in ground effect is fundamentally different to that in free air. The first test is whether this difference affects the optimal chordwise location of a given plate. Figure 4.10 illustrates that the optimal placement of an endplate whose length matches the length of the wing itself is somewhat forward of center. The lift itself is a maximum when the endplate is at the mid-chord position, but the induced drag may be decreased as for the free air case by moving it slightly forwards.

4.5.1 Endplates Above and Below the Wing

Endplates that extend above the wing could also be used, but their influence is similar to that in open air, whereas endplates below the wing directly influence ground effect, and hence are more effective in maintaining the increased pressure in the channel flow

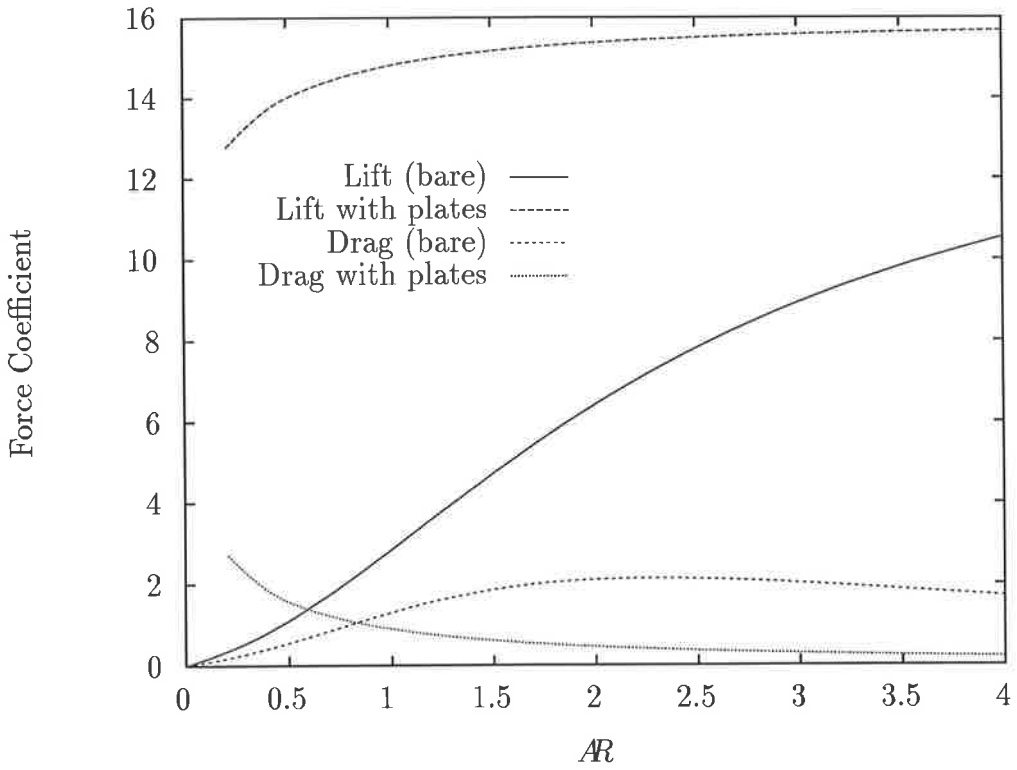

Figure 4.9: *Variation of the lift and induced drag coefficients against the aspect ratio of a square wing with and without full-chord skirts at an altitude* $h_0 = 0.1c$.

there. However, the present computer program can also compute easily the effect of above-wing endplates, and Figure 4.11 shows some results. Even though the intention of use of endplates is to increase the lift due to ground effect, it is impracticable to operate a wing at altitudes less than about $h = 0.1c$. We may then be interested in extracting every little extra lift possible out of wings that are not of very high aspect ratio, and above-wing endplates may aid in this objective. By how much, then can the lift due to accelerated flow over the top surface be increased by the addition of endplates above the wing?

4.6 Optimal Dimensions

It is interesting to see how the presence of a rigid ground alters the optimum dimensions of an endplate. As in Chapter 2, we now take as our function to maximise the lift coefficient C_L/α_W based on total area, ignoring induced drag for this study, and assume that the wing is square ($AR = 1$). As the wing is lowered to the ground, there will presumably be some point when the optimal endplate will touch the ground and become

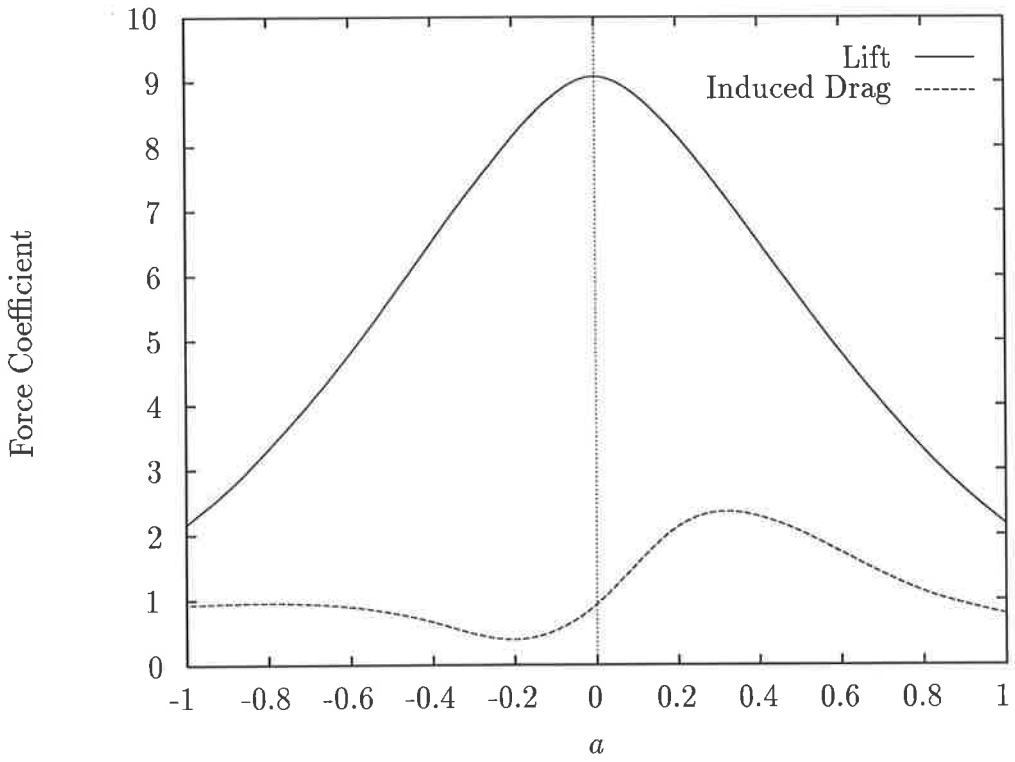

Figure 4.10: *Variation of the lift and induced drag coefficients for a unit square wing at altitude $h_0 = 0.1c$ with skirts of length $\ell = c$ and horizontal offset a. As for the free air case, the endplate produces maximum lift when flush with the wing. Induced drag reductions may be made by shifting the endplate slightly forwards. The total drag including a frictional component should be used to determine the specific optimum.*

a skirt. Figure 4.12 suggests that this happens when the altitude is approximately one half of the chord. The best size for the part of the endplate above the wing remains essentially unchanged (with a length of about $\ell = 0.15c$ and a height of $h = 0.24c$) no matter what the altitude. What does change is the size of the optimal lower part of the endplate, which increases rapidly, until below the critical altitude $h_0 = 0.5c$, it becomes a full-chord skirt touching the ground, illustrated in Figure 4.13.

When the optimisation procedure is repeated for a wing of aspect ratio $AR = 2$, similar results are obtained. In particular, there appears to be little dependence of this result upon the wingspan. Within the aviation industry, it is generally regarded that the "float" effect on landing due to the ground is first experienced at an altitude proportional to the wingspan, rather than the chord length. This is caused by the vertical compression of the flow field in ground effect, giving rise to an increase in the apparent aspect ratio. It thus represents a decrease in induced drag rather than an increase in lift due to the streamwise gap contraction ratio. We must therefore consider two distinct modes of ground effect.

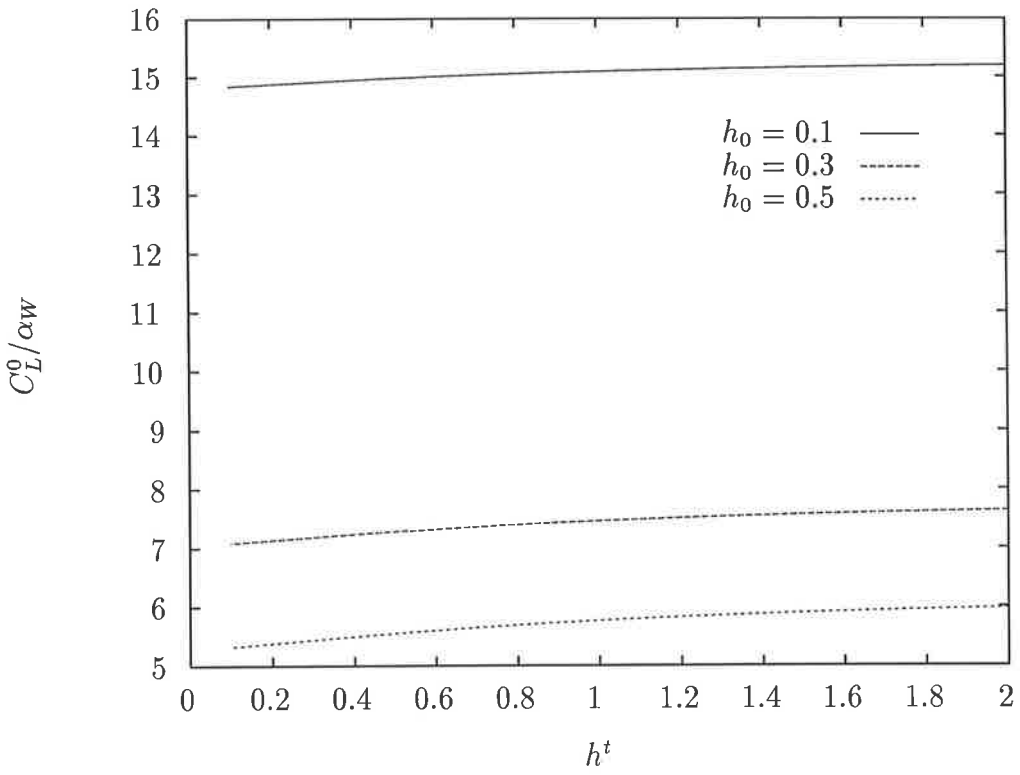

Figure 4.11: *The increase in lift coefficient C_L^0/α_W based on the wing area only, due to the addition of full-chord endplates above the wing of height h^t to a square wing in ground effect with full skirts for parameter values of the altitude $h_0 = 0.1c, 0.3c$ and $0.5c$. The relative change in the lift coefficient C_L^0/α_W based on wing area only shows that the endplate section above the wing is significantly less effective than the lower section when the altitude is small. As the altitude approaches infinity, the upper and lower sections become equally effective.*

4.7 Multiple Wing Configuration

In this section, we consider the optimisation of the lift-to-drag ratio of a tandem wing configuration in ground effect, by varying the angles of attack of two separate wings. Because the angle of attack is to be varied, we shall consider an object function that is dependent upon lift, rather than the square of lift, namely:

$$\frac{L}{D_f + D_i} \tag{4.7.2}$$

where L = lift, D_f = frictional drag assumed to be given by area times linear friction coefficient and D_i is the induced drag as previously calculated.

Before considering the two-wing combination, we optimise the angles of attack of two flat, unit square wings in ground effect independently. The first wing is located at an

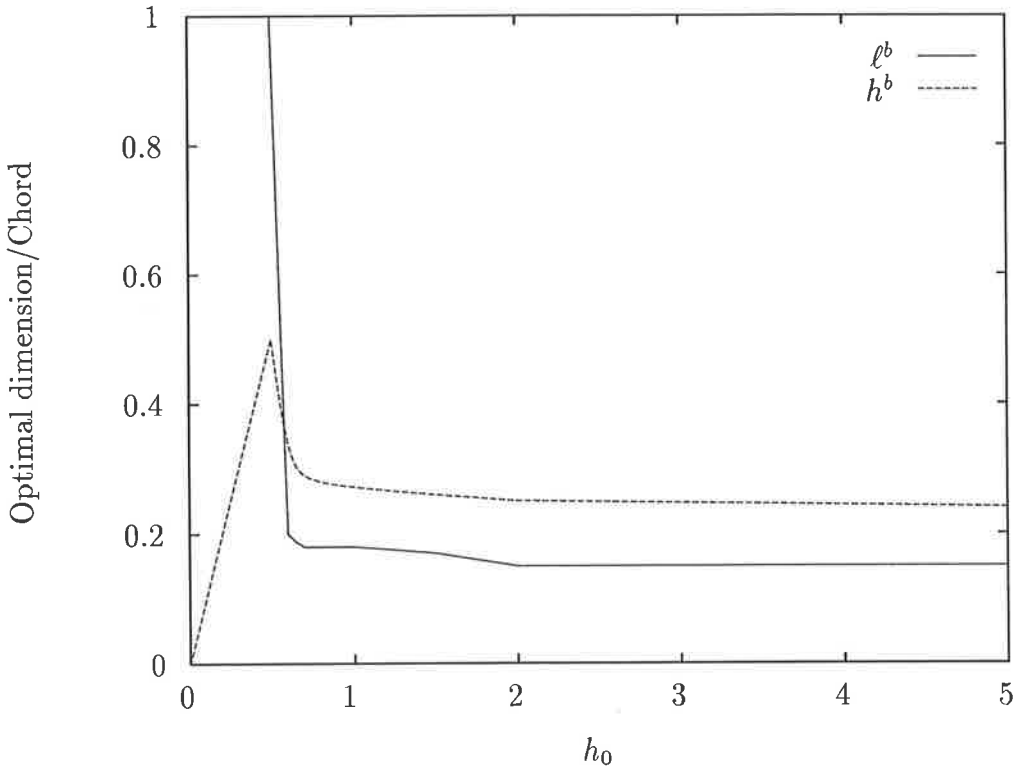

Figure 4.12: *The optimal lower endplate geometry for a unit square wing as a function of altitude. The lift coefficient C_L/α_W with respect to toal area is maximised at each altitude h_0. It is clear that beyond $h_0 = 2c$, the wing is effectively in free air. There is a dramatic change when the wing flies at an altitude $h_0 < c/2$. Below this altitude, the optimal configuration is a full-chord skirt, such that the length of the lower plate $\ell^b = c$ and the height of the lower plate $h^b = h_0$.*

altitude $h_0 = 0.1c$ in a uniform stream $U = 1$. The optimum angle of attack $\alpha_W = \alpha_W^*$ occurs when $D_i = D_f$, such that the object function $L/(D_i + D_f) = 15.167$. The lift, drag and suction coefficients are also shown in Table 4.1.

The second wing is a flat unit square located at an altitude $h_0 = 0.2c$, for which the optimal angle of attack is higher. The force coefficients are shown in Table 4.2.

Note that the decrease in ground effect for the second wing has resulted in lower lift L for the same induced drag D_i.

The interesting question is how the optimal angles of attack and the forces on the two wings change when they interact. For the purposes of this test, they separately maintain their altitude, but the second wing follows directly behind the first, such that the leading edge of wing number 2 is $0.1c$ directly above the trailing edge of wing number 1. In this case, the angles of attack are varied independently so as to maximise the total lift-to-drag

α_W^*	6.1111^o
L	0.1517
D_f	0.0050
S	0.0112
D_i	0.0050
C_L	0.3033
C_{D_i}	0.0100
C_L/α_W	2.8440
C_S/α_W^2	1.5433
$L/(D_i + D_f)$	15.167

Table 4.1: *Lift, drag and suction force coefficients for wing one alone.*

α_W^*	7.2027^o
L	0.1277
D_f	0.0050
S	0.0111
D_i	0.0050
C_L	0.2554
C_{D_i}	0.0100
C_L/α_W	2.0318
C_S/α_W^2	1.0987
$L/(D_i + D_f)$	12.770

Table 4.2: *Lift, drag and suction force coefficients for wing two alone.*

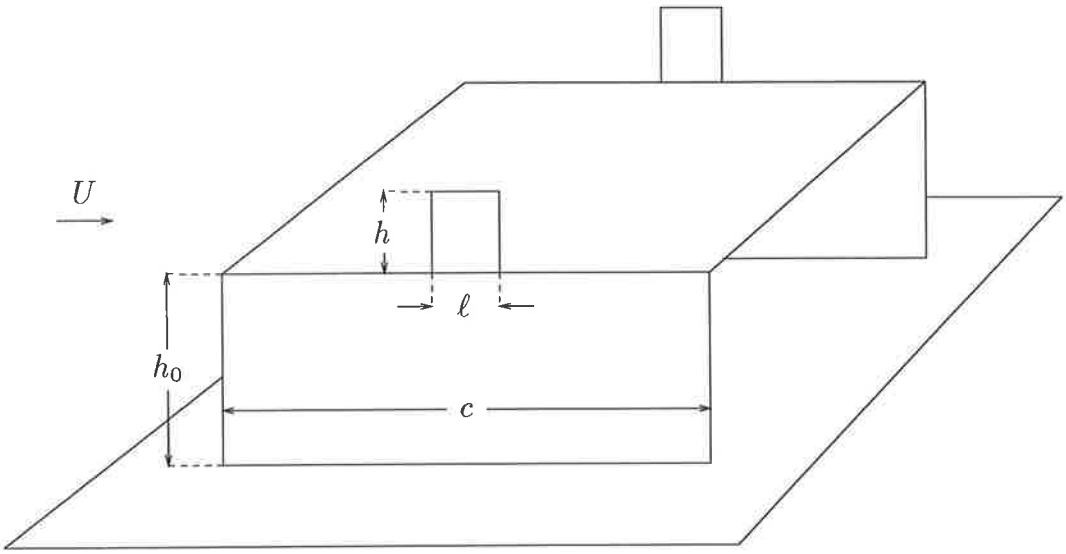

Figure 4.13: *Below the critical altitude $h_0 = c/2$, the optimal endplate geometry for the lower plate is a full-chord skirt. The optimal geometry of the upper plate does not change significantly from the free air case $h = 0.24c$ and $\ell = 0.15c$.*

ratio. The force coefficients for the combination are shown in Table 4.3.

α^*_W	8.9407°	4.6013°
L	0.2204	-0.0029
D_f	0.0050	0.0050
S	0.0239	0.0003
D_i	0.0100	
C_L	0.2175	
C_{D_i}	0.0100	
C_L/α_W	2.8249	-0.0715
C_S/α^2_W	1.5398	0.0719
$L/(D_i + D_f)$	10.878	

Table 4.3: *Lift, drag and suction force coefficients for wings one and two, optimised together.*

The results are consistent with the result for a single wing. The optimal configuration again requires that $D_f = D_i$ for the combination. However, the lift force on wing number 2 is negative. Wing number one is at a higher angle of attack than if it were alone, and consequently produces both more lift and induced drag. This induced drag is reduced

by wing number 2, which experiences an negative induced angle of attack due to the downwash of wing 1 that is greater than its own nominal positive angle of attack. The net angle of attack is negative and the second wing acts to reduce the energy in the vortices trailing wing 1.

Wing number 2 might also be considered to be the ground-effect equivalent for the upper surface of wing 1. This *ceiling effect* speeds up the flow over the upper surface of wing number 1 and thereby increases the pressure jump from the lower surface to the upper surface. This is in a sense sacrificial as the flow is also accelerated under wing number 2, causing a downward force. It should be noted that the value of $L/(D_i + D_f)$ for the combination is less than the optimal value for either of the wings alone. The aspect ratio of the combination is half that of either wing individually, because of the arrangement. Wing 2 is providing the same function as a very inefficient endplate, because its only contribution is in blocking vortex flow, but this has a direct reduction in the total lift, whereas an endplate does not reduce the lift at all.

In Chapter 6 we consider the streamwise separation in free air for which the combination is aerodynamically better that either of its constituents independently (birds for example which fly in a vertical arrowhead formation). The real advantages may only be seen when a certain bank angle in ground effect is required, forcing the lead wing to have a small aspect ratio.

4.8 Pitch Stability

The heave-pitch stability of a single wing in ground effect has been considered by a number of investigators (Tuck, 1981), (Kuhmstedt and Milbrandt, 1995), (Rozhdestvensky, 1992). There has been a general acceptance of the theory of Gallington (Gallington et al., 1972) that a single wing in ground effect is always heave-pitch unstable and this has been the motivation for the enormous tailplanes of the Russian models. This is because the centre of aerodynamic pressure in free air lies close to the quarter chord $x = 0.25c$ for a symmetrical airfoil but shifts back to $x = 0.4c$ when in ground effect. When subject to a upward gust of air, this shift causes the centre of pressure to move forward and the ground effect vehicle tends to flip backwards.

Other than simply using a large tailplane to counter the natural instability of a single

lifting surface, there are several other methods that have been implemented. Firstly the wing design illustrated in Figure 4.14 and, later in Figure 4.15 increases the pitch stability by using a large channel flow with two similar lifting surfaces in tandem.

Figure 4.14: *The tandem-wing design of the Jörg TAF VIII is used to counteract the natural pitch-heave instability of a single wing in ground effect.*

Adding a tailplane is an established solution to this problem, but to counter the pitch instability of a large wing in ground effect, the tailplane must be huge and far from the ground. This means a large tailplane support structure. However, a canard wing when appropriately positioned and sized can also provide a measure of pitch stability. It is not within the scope of this thesis to present an analysis of the pitch stability of a three-surface configuration However, ground effect does introduce a difference in the linear case between chordwise camber, whose effect upon lift is well understood, and multiple connected surfaces at differing altitudes and angles of attack, because of the change in ground clearance of each component with global pitching.

Without presenting a stability analysis of the configuration, the loading is illustrated in Figure 4.18.

Figure 4.15: *The Taiwanese Chung-Shan transport vessel also incorporates the tandem wing design. Larger vehicles along similar design lines are expected from Taiwan in the near future.*

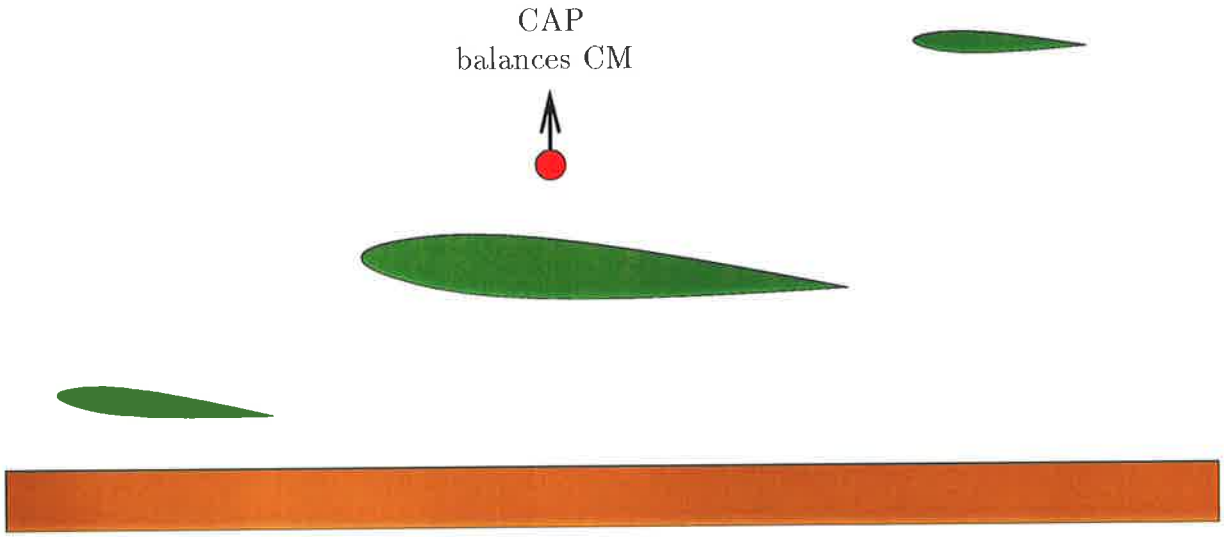

Figure 4.16: *Straight and level flight in ground effect. The canard in this configuration is relatively highly loaded, at a high angle of attack and in extreme to moderate ground effect. The main wing is in moderate ground effect and the tailplane remains in effectively free air. The center of aerodynamic pressure (CAP) balances the center of mass (CM).*

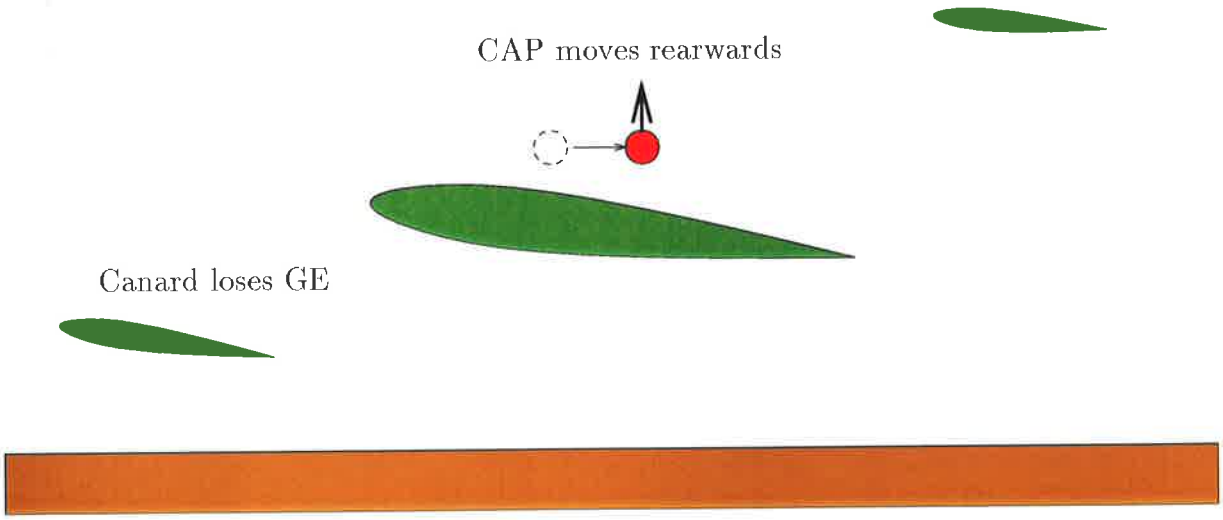

Figure 4.17: *Ideally the three-surface configuration should be passively stable to pitch. When a gust causes the configuration to pitch, the loss of ground effect (GE) on the canard wing moves the center of aerodynamic pressure rearwards, restoring the flight attitude.*

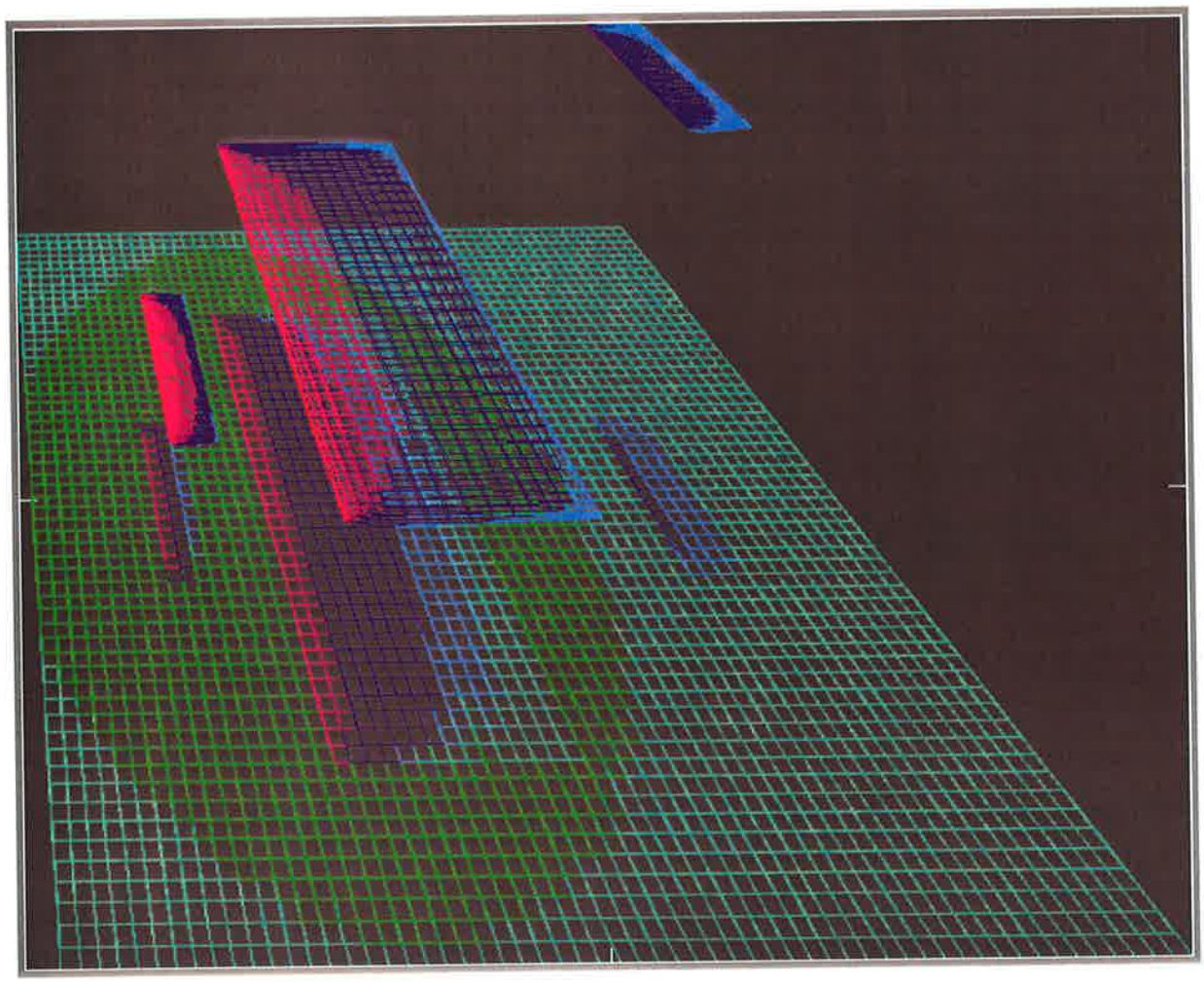

Figure 4.18: *The loading of a three-surface configuration in ground effect.*

Chapter 5

Wave Drag

5.1 Introduction

When a body flies in air close to a water surface, the shape of the water surface is modified. In this Chapter, we consider whether or not this significantly effects the problem of optimising the geometry of a large, high speed wing-in-ground-effect (WIG) vehicle flying over water.

For bodies that do not pierce the water surface, much of the work in this chapter is analogous to the calculation of the wave resistance of air cushion vehicles (Monacella and Newman, 1967), (Doctors and Sharma, 1970). In the absence of spanwise skirts in addition to chordwise skirts, the present numerical evaluation of the pressure on the water due to the lifting surfaces is favoured instead of the analytic work appropriate to air cushion vehicles.

The present algorithm for determining the aerodynamic lift and drag on a three-dimensional finite lifting surface with endplates in moderate ground effect is to be used with the addition of the drag associated with the waves made on the surface of the water. The vertical gap between the wing and the water plane is denoted h_0 and we assume that this gap is $O(1)$ when compared with the wing chord c. The method of images will be employed to account for the aerodynamic ground effect. This is justified on the basis that the angle of attack α_W is small relative to the gap h_0. Consequently the deflection of the water surface makes far less relative difference to the aerodynamic forces than it does to the hydrodynamic ones.

There are a number of ways to estimate the deflection of the water surface given the velocity discontinuity across the lifting surfaces. If the limit as h_0/c tends to zero, the pressure "footprint" registered on the water is asymptotically the same as the pressure $p^-(x, y)$ on the lower surface of the wing. This would involve no additional computational effort but would be inaccurate for greater altitudes. Also, the resulting discontinuity in pressure across the projection of the leading edge on the water surface would cause numerical difficulty in evaluating the wave drag. This may be overcome by using a smoothing function as applied to air-cushion vehicle analysis (Doctors, 1997) but this is clearly less appropriate for vehicles without hovercraft-like skirts.

The present method explicitly determines the velocity influence at each point on a finite grid on the ground from all airborne lifting-surface panels. The resulting matrix is then used to evaluate the wave drag W using a two-dimensional wave resistance integral (Wehausen and Laitone, 1960) which estimates the wave energy propagated by a moving pressure disturbance in all directions.

5.2 Three-Dimensional Formulation

In order to determine the wave drag W due to an airborne vehicle flying above a water surface, we must determine the pressure on the water surface due to the vehicle. In principle, this may be achieved to a first order approximation by considering the velocity potential on the water surface due to the lifting surface perturbation to the free stream and then applying Bernoulli's law. A Michell-like integral (Tuck, 1989) is then used to estimate the wave drag associated with this pressure distribution.

The lifting surface integral and the wave drag integral are sufficiently different in structure as to warrant two distinct numerical grids for quadrature. However, these must be linked in such a way as to minimise numerical error, which can be relatively large. This Section will explore some of the sources of these errors as well some remedies. An examination is also made of the different pressure footprints made by bare and skirted wings and the dependence of the wave drag on the planform of the wing.

5.2.1 Hydrodynamic Pressure Due to an Airborne Wing

The hydrodynamic pressure distribution $p(x,y)$ on the water surface due to the presence of the airborne lifting surface must be calculated. This is easily done by considering the linearised Bernoulli's equation in terms of the small perturbation velocity $q = (u,v,w)$ so that

$$\begin{aligned} p &= \frac{1}{2}\rho\left[U^2 - \left((U+u)^2 + v^2 + w^2\right)\right] \\ &\sim -\rho U u. \end{aligned}$$

Now the u velocity component can be determined on the water surface by finding the x-derivative of the velocity potential $\phi(x,y,z)$, knowing already the loading $\gamma(x,y,h_0)$ on the wing. The potential of a unit horseshoe vortex (Ashley and Landahl, 1965) may be used directly to evaluate the influence of the wing and endplate on the streamwise velocity on the water surface. The potentials are

$$\phi(X,Y,Z) = G(X,Y,Z) = ZF(X,Y,Z)$$

for a line of vertical dipoles and

$$\phi(X,Y,Z) = H(X,Y,Z) = YF(X,Y,Z)$$

for a line of horizontal dipoles where $F(X,Y,Z)$ is the kernel of the conventional lifting surface equation

$$F(X,Y,Z) = \frac{1}{Y^2+Z^2}\left[1 + \frac{X}{R}\right].$$

Thus the perturbation velocity $u = \phi_x$ may be determined at any point in space as the contributions from the wing-endplate combination plus the image in the water surface:

$$\begin{aligned} u(x,y,z) \;=\; & \int_0^s \int_0^c \gamma(\xi,\eta)\; K^{GW}(x-\xi, y-\eta, z-h_0)\; d\xi d\eta \\ & - \int_0^s \int_0^c \gamma(\xi,\eta)\; K^{GW}(x-\xi, y-\eta, z+h_0)\; d\xi d\eta \\ & + \int_0^h \int_0^\ell \gamma(\xi,\zeta)\; K^{GP}(x-\xi, y-\eta, z-\zeta)\; d\xi d\zeta \\ & - \int_0^h \int_0^\ell \gamma(\xi,\zeta)\; K^{GP}(x-\xi, y-2s+\eta, z-\zeta)\; d\xi d\zeta \\ & + \int_0^h \int_0^\ell \gamma(\xi,\zeta)\; K^{GP}(x-\xi, y-\eta, z+\zeta)\; d\xi d\zeta \\ & - \int_0^h \int_0^\ell \gamma(\xi,\zeta)\; K^{GP}(x-\xi, y-2s+\eta, z+\zeta)\; d\xi d\zeta. \end{aligned} \tag{5.2.1}$$

In the case where $z = 0$ on the water surface, this becomes

$$\begin{aligned} u(x,y,0) \;=\; & \int_0^s \int_0^c \gamma(\xi,\eta)\left[K^{GW}(x-\xi,y-\eta,-h_0) - K^{GW}(x-\xi,y-\eta,h_0)\right]\, d\xi\, d\eta \\ & + \int_0^h \int_0^\ell \gamma(\xi,\zeta)\Big[\; K^{GP}(x-\xi,y-\eta,-\zeta) - K^{GP}(x-\xi,y-2s+\eta,-\zeta) \\ & \qquad + K^{GP}(x-\xi,y-\eta,\zeta) - K^{GP}(x-\xi,y-2s+\eta,\zeta)\Big]\, d\xi\, d\zeta. \end{aligned} \tag{5.2.2}$$

The new kernel functions are

$$\begin{aligned} K^{GW}(X,Y,Z) &= \arctan\left(\frac{XY}{RZ}\right) + \arctan\left(\frac{Y}{Z}\right) \\ K^{GP}(X,Y,Z) &= \arctan\left(\frac{XZ}{RY}\right) + \arctan\left(\frac{Z}{Y}\right) \end{aligned} \tag{5.2.3}$$

where the obvious vertical symmetry has been exploited in the actual computer algorithm.

5.2.2 Work Done by a Moving Pressure Distribution

An expression for the rate of work done on a water surface by a moving pressure distribution is given (Wehausen and Laitone, 1960, page 598) as

$$W = \frac{\nu^2}{\pi\rho U}\int_0^{\frac{\pi}{2}} d\theta \sec^5\theta \left[P^2(\theta) + Q^2(\theta)\right], \tag{5.2.4}$$

where

$$P(\theta) = \int_{-\infty}^{\infty}\int_{-\infty}^{\infty} dx\; dy\; p(x,y)\; \cos\left[\nu \sec^2\theta\,(x\cos\theta + y\sin\theta)\right], \tag{5.2.5}$$

$$Q(\theta) = \int_{-\infty}^{\infty}\int_{-\infty}^{\infty} dx\; dy\; p(x,y)\; \sin\left[\nu \sec^2\theta\,(x\cos\theta + y\sin\theta)\right], \tag{5.2.6}$$

and $\nu = g/U^2$.

5.2.3 Numerical Evaluation of Integral

Numerically, the computation of the θ integral is complicated by the oscillatory nature of the integrand. Filon's quadrature (Tuck, 1987) is implemented and the method becomes

$$P(\theta) \approx \sum_{j=1}^{N_y} \Delta y \sum_{i=1}^{N_x} \Delta x\; w_i\; w_j\; p(x_i,y_j)\; \cos\left[\nu \sec^2\theta\,(x_i\cos\theta + y_j\sin\theta)\right], \tag{5.2.7}$$

where the weights for Filon's quadrature are given by

$$\begin{aligned} w_k &= 4(\sin K - K\cos K)/K^3 && (k \text{ even}) \\ w_k &= (3K + K\cos 2K - 2\sin K)/K^3 && (k \text{ odd}) \end{aligned}$$

where $K = \nu \sec\theta \Delta x$.

Care must be taken with the numerical implementation of this algorithm. The number of panels on the wing must be large enough that the water surface grid does not falsely include energy associated with waves of the grid scale on the wing. Having too large a number is prohibitive in terms of CPU time, because the influence from each aerodynamic panel must be calculated for each water surface panel.

In order to limit the number of parameters while determining the numerical behaviour of the integral 5.2.4 we consider the wave resistance of a Gaussian pressure distribution

$$p(x, y) = \exp(-x^2 - y^2) \tag{5.2.8}$$

illustrated in Figure 5.1 for which the wave drag integral 5.2.4 may be written analytically as

$$W = \frac{\nu^2}{\pi\rho U}\int_0^{\pi/2} \sec^5(\theta)\pi^2 \exp\left(-\nu^2 \sec^4(\theta)/2\right) d\theta. \tag{5.2.9}$$

The value for W does not appear to converge reliably with increased numbers of gridpoints on the water surface. Depending upon the free stream velocity U and the number of values of θ into which the outer integral is partitioned, the value for W can converge or vary wildly.

The grid implemented on the water surface is regular in each of the x and y directions separately and has $n_g = m_g$ points distributed over an (8×8) domain centered on the origin. Extending the grid further does not significantly effect the results. Figure 5.2 shows the θ integrand from $0 < \theta < \pi/2$ for $m_g = 60, 120$ and 240 for a free stream $U = 5$. The integral is in each case dominated by peaks which occur at different values of θ. When the algorithm is modified such that the contribution is neglected when fewer than two data points are present for each period of the integrand within the P and Q integrals for a particular value of θ, these spurious peaks disappear and the integrand curves are replaced by those in Figure 5.3. These curves predict a wave drag which converges to $W = 0.0004043$ with rate of convergence $O(m_g^{-4})$. The exact solution for $U = 5$ is $W = 0.00040469$.

For values of the energy propagation angle approaching $\theta = \pi/2$, correspondingly large values of m_g and n_g are required to capture the diverging wave pattern. In general, $m_g = 120$ has been found to estimate the wave drag to two significant figures. As increasing these parameters is rewarded with diminishing marginal returns on overall accuracy, this is regarded as sufficient at least in the first instance.

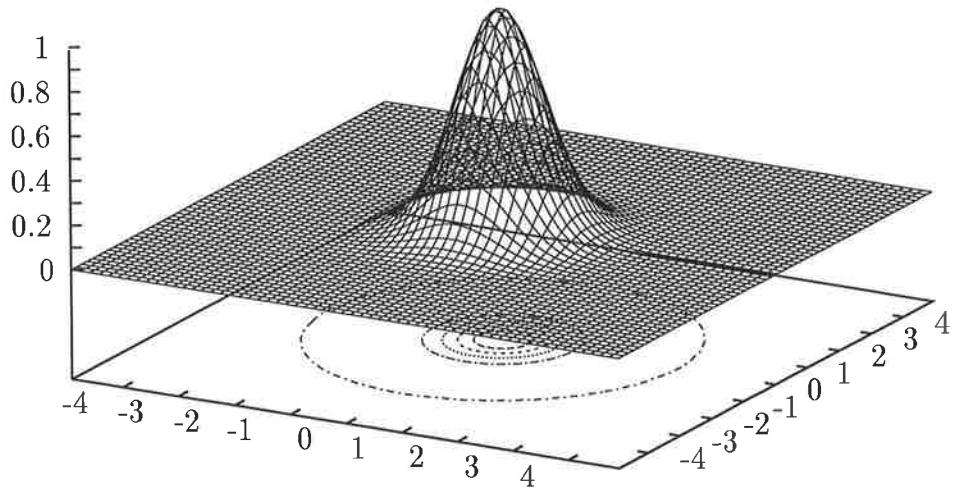

Figure 5.1: *Gaussian pressure distribution on the water surface given by the expression* $p(x, y) = \exp(-x^2 - y^2)$. *This is to be used to test the accuracy of the numerical scheme for the wave integral, independent of the aerodynamic calculations and the calculation of the resulting pressure on the water plane.*

5.2.4 Variation of Wave Drag with Velocity

The magnitude and distribution of the wave energy spectrum $0 < \theta < \pi/2$ varies with the parameter $\nu = g/U^2$. Figure 5.4 shows the change in the energy spectrum as U varies from 1 to 10. The curves have been normalised with respect to their definite integral so that their forms may be compared. At low velocity U, the energy is mainly associated with waves at small angles θ to the free stream. As the velocity increases, the

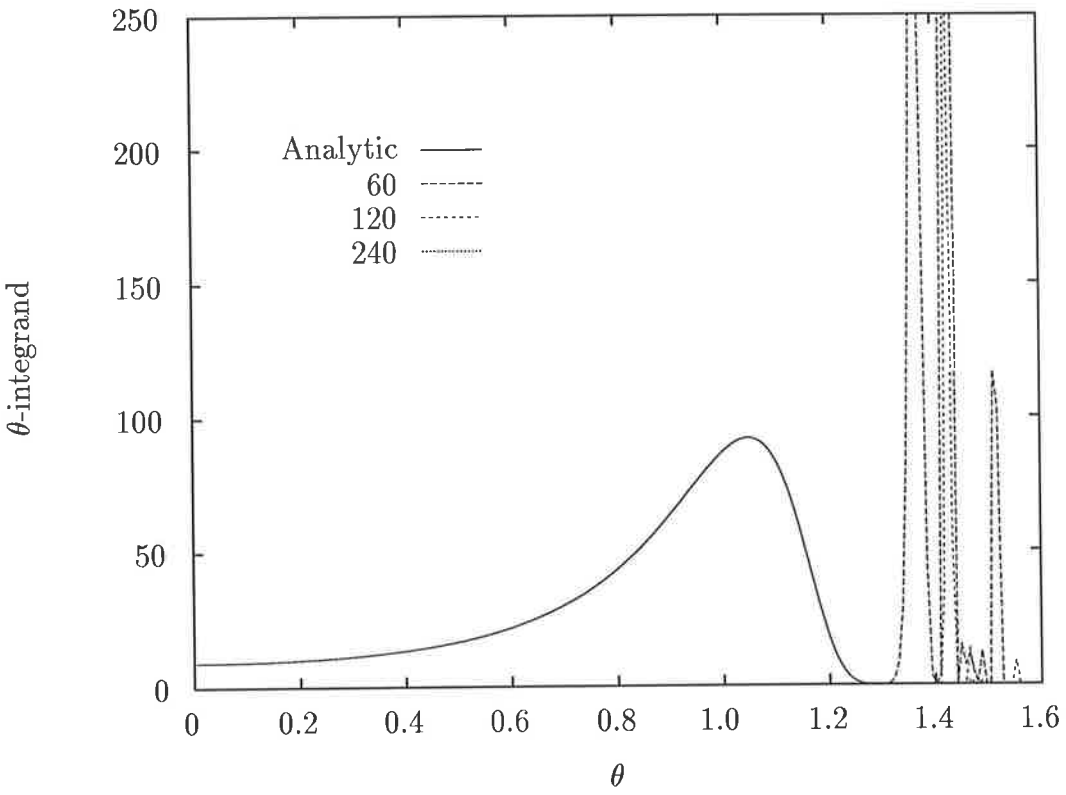

Figure 5.2: *Wave drag θ-integrand including spurious peaks for $m_g = 60, 120$ and 240 for a Gaussian pressure distribution traveling with velocity $U = 5$.*

energy is largely contained in the diverging waves near $\theta = \pi/2$. Figure 5.5 shows the corresponding variation of the drag integral W. As the velocity increases, the wave drag initially associated with waves propagating in the streamwise direction increases slowly until reaching a sharp increase and then a maximum. Thereafter, increase in velocity reduces the wave drag until the only waves produced are transverse or at right angles to the direction of the free stream. In the limit as the velocity U tends to infinity, the wave drag W tends to zero with rate $W \sim U^{-1}$.

5.3 Pressure Footprints of Wings in Ground Effect

Different wings flying over water leave different pressure footprints. In general, some parts of the water surface will experience a reduction in pressure and some an increase even though the wing exerts a net downward force on the water. The addition of endplates or skirts to a wing in ground effect markedly alters the form of the pressure footprint and in general increases the deflection of the water surface.

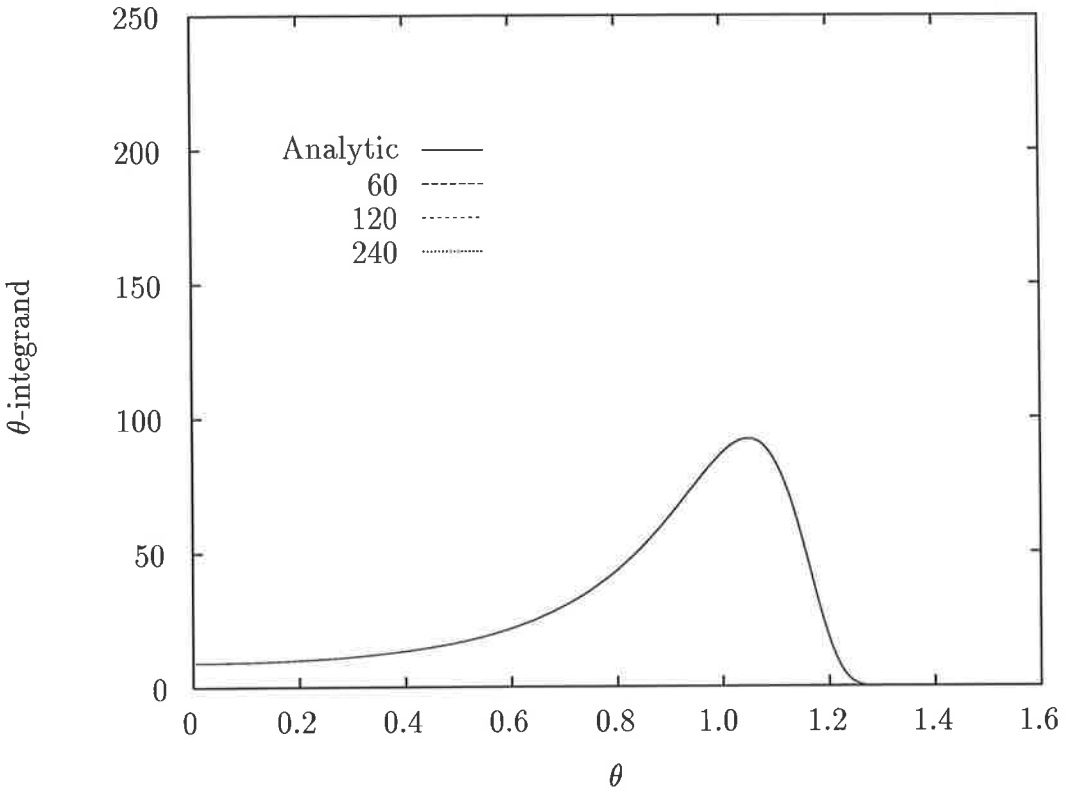

Figure 5.3: *Corrected wave drag θ-integrand with spurious peaks removed for $n_g = m_g = 60, 120$ and 240 for a Gaussian pressure distribution traveling with velocity $U = 5$.*

5.3.1 Bare Wing

The pressure footprint made by a unit square wing at angle of attack $\alpha_W = 5^\circ$, altitude $h_0 = 0.1c$ and free stream $U = 5$ is illustrated in Figure 5.6. The high pressure region beneath the wing is matched in magnitude by the low pressure immediately surrounding it. The corresponding energy distribution is shown in Figure 5.7. Note that the curves calculated using $n_g = m_g = 40, 60, 120$ appear to converge, but retain peaks and troughs in the integrand near $\theta = \pi/2$. These represent real information about the influence of the wing geometry on the wave drag. The curve calculated using $n_g = m_g = 240$ is significantly higher than the others. This is numerical error caused by the mismatch in grid scales on the wing and the ground. Figure 5.8 is a zoom-in of Figure 5.7 near $\theta = \pi/2$. It appears that the oscillations in the θ-integrand are at least partially independent of the grid on the ground. The grid on the wing is a standard Chebyschev with $n = m = 18$ so the 240×240 grid on the ground is in places far denser. Consequently, the ground grid resolves the grid scale behaviour of the loading on the wing and attributes high frequency wave energy to the discontinuous panel loading. In order to achieve highly accurate estimates for W, the wing panelling must also be significantly dense or else

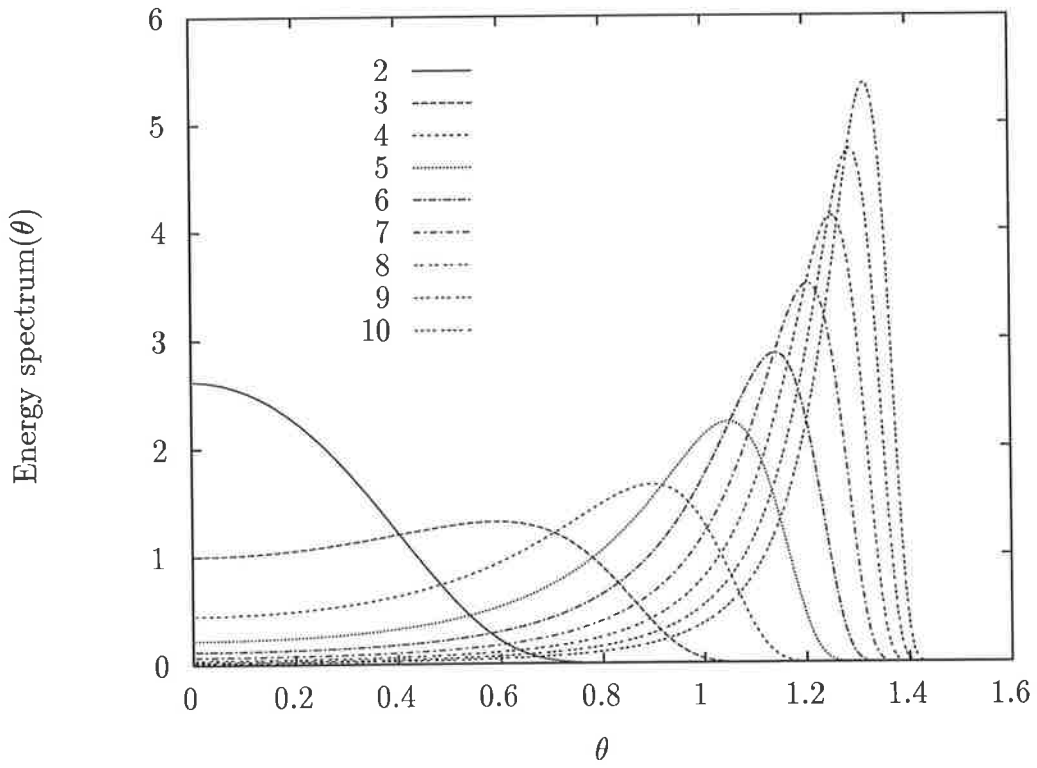

Figure 5.4: *Normalised wave drag θ-integrand representing the wave energy spectrum of a Gaussian surface pressure distribution moving with velocity $U = 2, \ldots, 10$. Calculated numerically using a (8×8) ground plane grid with $n_g = m_g = 120$ panels in both the chordwise and spanwise directions.*

another method must be used to transfer the wing loading to the water surface.

5.3.2 Aspect Ratio Effects

As the wing aspect ratio $AR = s^2/A$ increases we might expect a greater contribution to W from the waves in the streamwise direction and greater cancellation of the diverging waves. From slender hull theory we expect $W \sim AR^2$ for small AR. Figure 5.9 shows the form of the pressure footprint of a rectangular wing with aspect ratio $AR = 10$. Relative to the unit square wing, the only differences are that the increased aspect ratio has increased the magnitude of the pressure on the surface and that the resulting pressure distribution on the water surface is one average closer to that on the wing itself, because the encroachment of the low pressure region at the wingtips is relatively less significant to the total geometry.

We wish to examine the behaviour of the wave drag W as the aspect ratio is varied. Because of the extreme numerical sensitivity to mismatch of the aerodynamic and hydro-

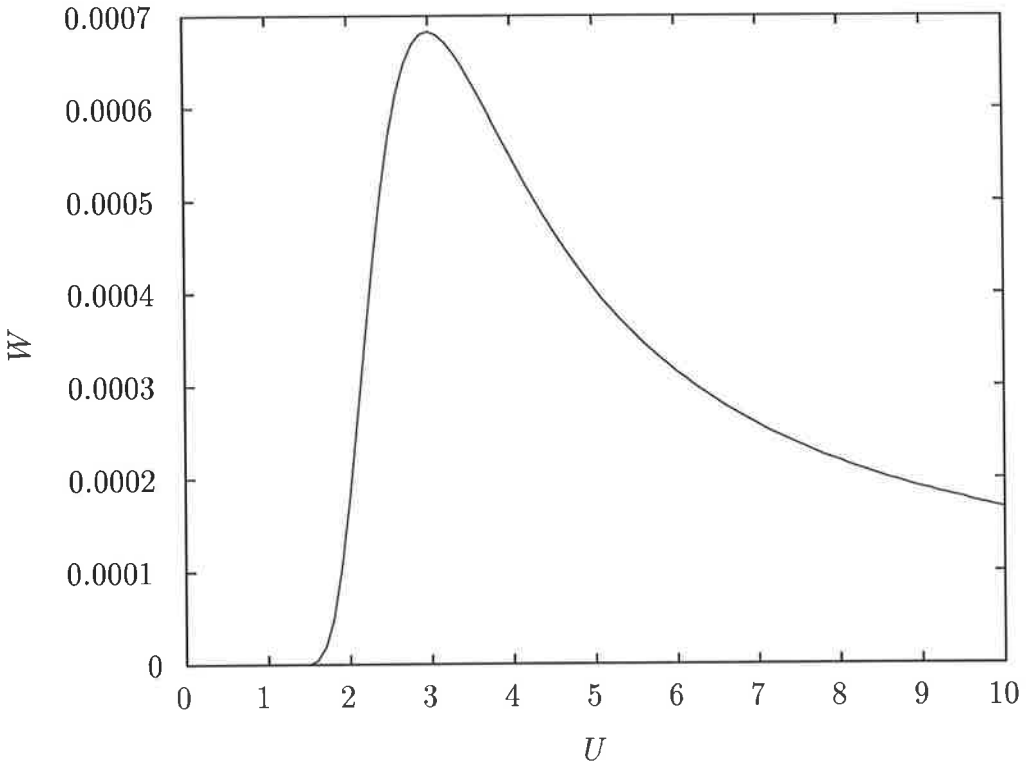

Figure 5.5: *Wave drag W of a Gaussian pressure distribution versus the free stream velocity U. Calculated numerically using a (8×8) ground plane grid with $n_g = m_g = 120$ panels in both the chordwise and spanwise directions.*

dynamic grids, we introduce a special scheme to reduce the grid-interference noise from the real results. The pressure footprints have been calculated previously on a ground-plane grid which is the dimension of the wing plus a fixed margin of 2 units on all sides. In the y-direction, we now use a margin which is half of the wingspan for the particular wing being evaluated. Prior to calculating the pressure footprint on the ground, the loading on the wing is interpolated onto a regular grid *on the wing* which coincides exactly with the grid on the ground-plane. While the grid-scale oscillations still present numerical difficulty, the variation in the wave drag W is plotted for the range of aspect ratios $0 < AR < 4$ for a rectangular wing moving with velocity $U = 5$ and angle of attack $\alpha_W = 5^o$. Wave interference from the two side-edges of the pressure footprint causes real oscillations in the graph, shown in Figure 5.10. Since the natural wavelength of water-surface waves in infinitely deep water is $\lambda = 2\pi U^2/g$, and the wave pattern propagates at an angle of $\arctan(1/3)$ behind the vessel (Newman, 1977), then we expect to see an interference effect when $s = \lambda/6 = 2.67$. In fact, we also resolve the behaviour on the scale of the chord-length, corresponding to a variation in span of $s = c/3 = 0.33$.

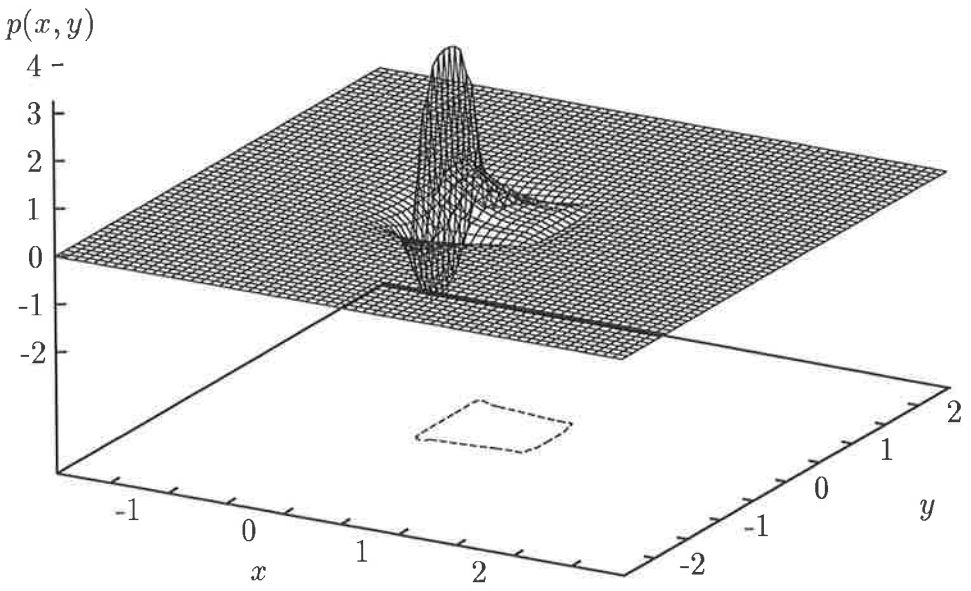

Figure 5.6: *Water surface pressure footprint of unit square wing in ground effect, at angle of attack* $\alpha_W = 5^o$ *and velocity* $U = 5$. *The projection shows the zero pressure contour line. Clearly the region beneath the wing has dominantly higher pressure that the free stream and elsewhere the pressure is reduced.*

5.3.3 Wing with Skirts

The lift and induced drag force on a wing in ground-effect are significantly changed when endplates are added as full-chord skirts below the wing. Figure 5.11 shows the pressure distribution on the water surface due to a unit square wing at angle of attack $\alpha_W = 5^o$ moving with velocity $U = 5$ at altitude $h_0 = 0.1$ with full skirts. This may be directly compared to Figure 5.6, where the skirts are omitted. The magnitude of the pressure in the case with skirts is significantly higher as we expect from the lift forces generated, but we also note regions of high pressure extending upstream and also downstream of the configuration. This is largely due to the endplate vorticity, which accentuates the blockage to the flow created within the channel.

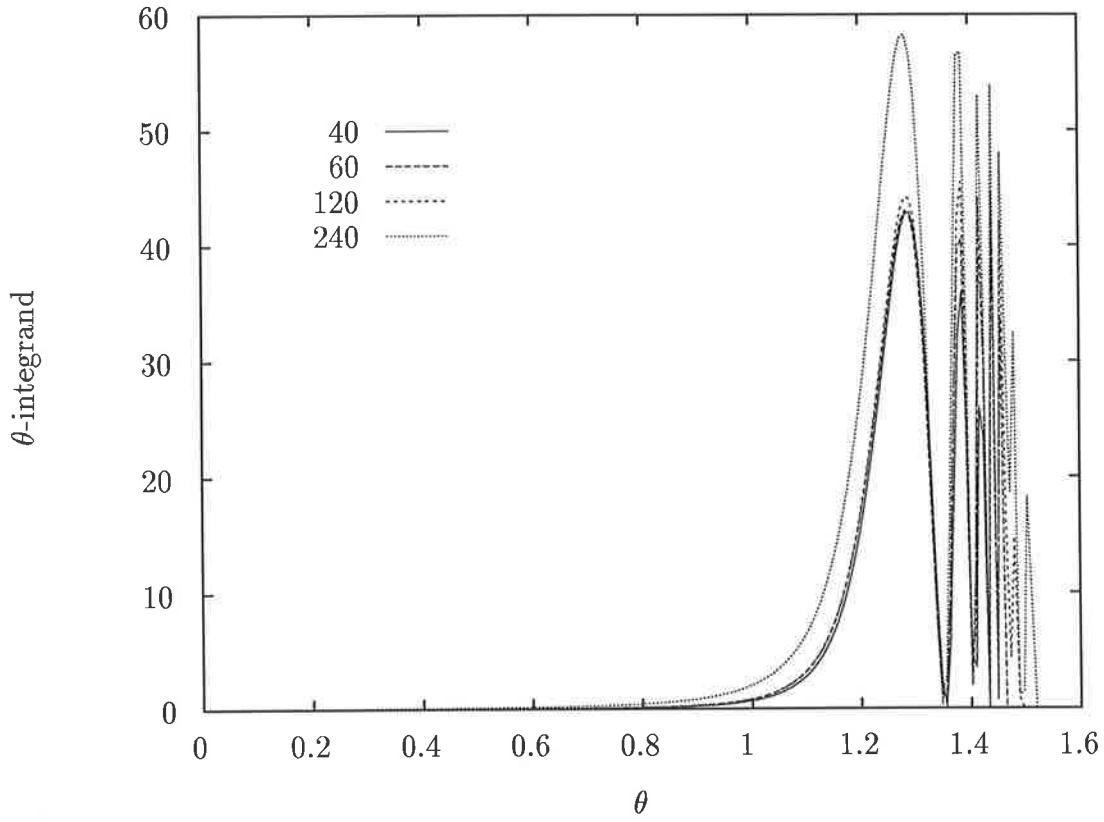

Figure 5.7: *Wave energy spectrum for a unit square wing at angle of attack* $\alpha_W = 5^o$ *traveling with velocity* $U = 5$ *in ground effect over a water surface with clearance* $h_0 = 0.1c$. *Curves are shown for ground-plane panel numbers* $n_g = m_g = 40, 60, 120$ *and* 240.

5.4 Wave Drag Versus Aerodynamic Drag

Although it is clear that the present scheme may be used to predict the wave drag of a wing-in-ground effect flying over water, the level of computational complexity required to produce accurate results suggests that this facet of the algorithm be avoided when possible. We now consider the circumstances under which we may assume that the wave drag will be significantly smaller than the corresponding aerodynamic drag, starting with a two-dimensional approximation for the circulation resulting from an inclined flat plate in ground effect.

5.4.1 Two-Dimensional Airflow

The flow field associated with a general lifting surface in ground effect is not two-dimensional. However, in Chapter 4 it was shown that the addition of full chord skirts to a wing in ground effect can provide reasonably two-dimensional conditions within the

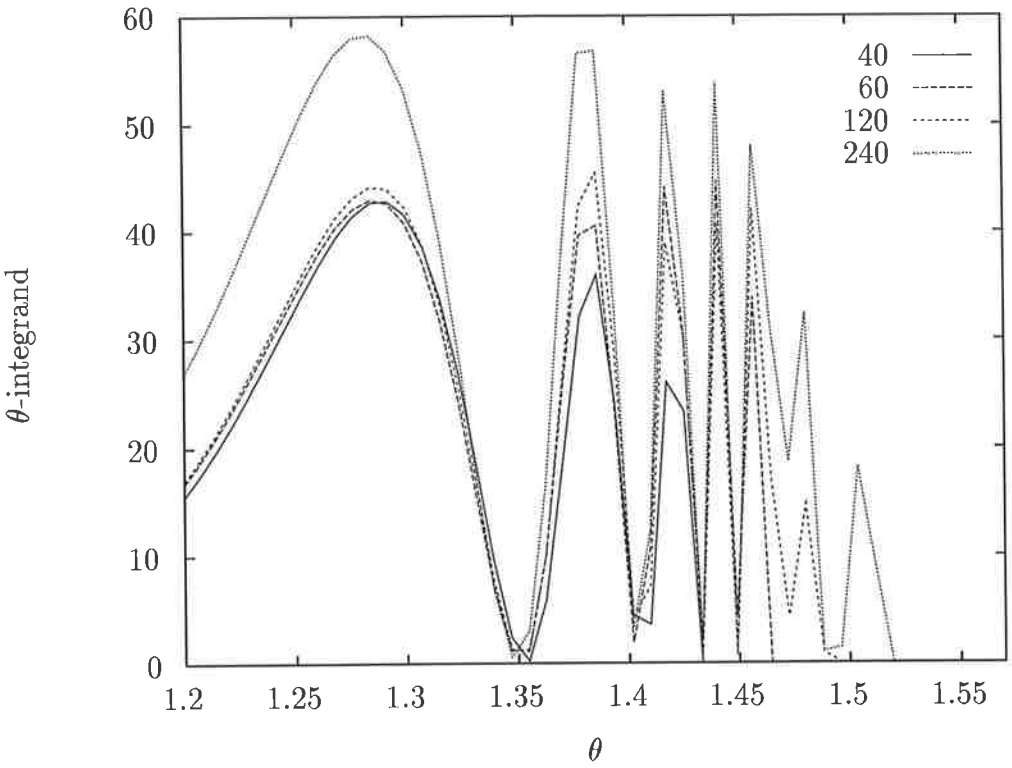

Figure 5.8: *Zoom-in of the wave energy spectrum for unit square wing in ground effect near* $\theta = \pi/2$. *Curves for* $n_g = m_g = 40, 60, 120$ *and* 240 *are shown.*

gap. It is also clear that the hydrodynamic forces associated with wings in ground effect are very much higher when full skirts are used. If we consider a small gap of length c and clearance $h = h_0 + \alpha_W(c - x), \quad 0 \leq x \leq c$ then Bernoulli's equation applied to the gap region becomes

$$\frac{p(x)}{\rho_A} + \frac{1}{2}q(x)^2 = \frac{p_0}{\rho_A} + \frac{1}{2}U^2. \tag{5.4.10}$$

If we the air velocity in the gap be approximated by the linear theory, such that

$$\frac{p - p_0}{\frac{1}{2}\rho_A U^2} = 1 - \left(\frac{h_0}{h_0 + \alpha_W(c - x)}\right)^2, \tag{5.4.11}$$

and assume that $p_0 = 0$, then

$$\frac{2}{\rho_A U^2}\int_0^c p(x)\,dx = \frac{\alpha_{\underset{\sim}{w}} c^2}{h_0 + \alpha_{\underset{\sim}{w}} c}. \tag{5.4.12}$$

If the gap clearance is $O(1)$ when compared to the wing chord, whereas the angle of attack α_W is small compared to the wing chord then $\alpha_W/h_0 \simeq 0$ and

$$\frac{2}{\rho_A U^2}\int_0^c p(x)\,dx = \alpha_{\underset{\sim}{w}} \frac{c^2}{h_0}. \tag{5.4.13}$$

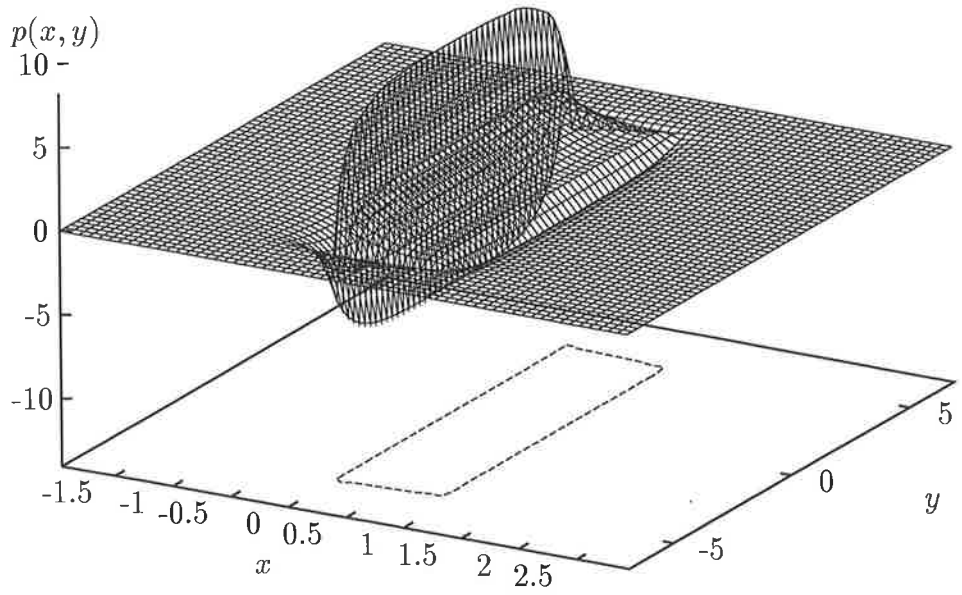

Figure 5.9: *Pressure footprint of a rectangular wing with AR = 10 in ground effect at altitude $h_0 = 0.1c$, angle of attack 5° and velocity $U = 5$. The only lines shown on the contour plot are where pressure $p(x, y) = 0$.*

Thus we may approximate the circulation generated by an inclined flat plate in moderate ground effect as

$$\frac{\Gamma}{U\alpha} \approx -\frac{c^2}{2h_0}. \tag{5.4.14}$$

5.4.2 Two-Dimensional Wave Drag

We now consider the wave drag R of a finite two-dimensional surface pressure distribution. It may be shown (Lamb, 1932, page 415) that the resistive force per unit span on a disturbance advancing with velocity $U < \sqrt{gH}$, where H is the depth of water is

$$R = \frac{1}{4} g \rho_W a^2 \left(1 - \frac{2\kappa H}{\sinh 2\kappa H}\right), \tag{5.4.15}$$

where $\kappa = g/U^2$ is the wave number. As we are dealing with water of infinite depth H, then this reduces to

$$R = \frac{1}{4} g \rho_W a_w^2, \tag{5.4.16}$$

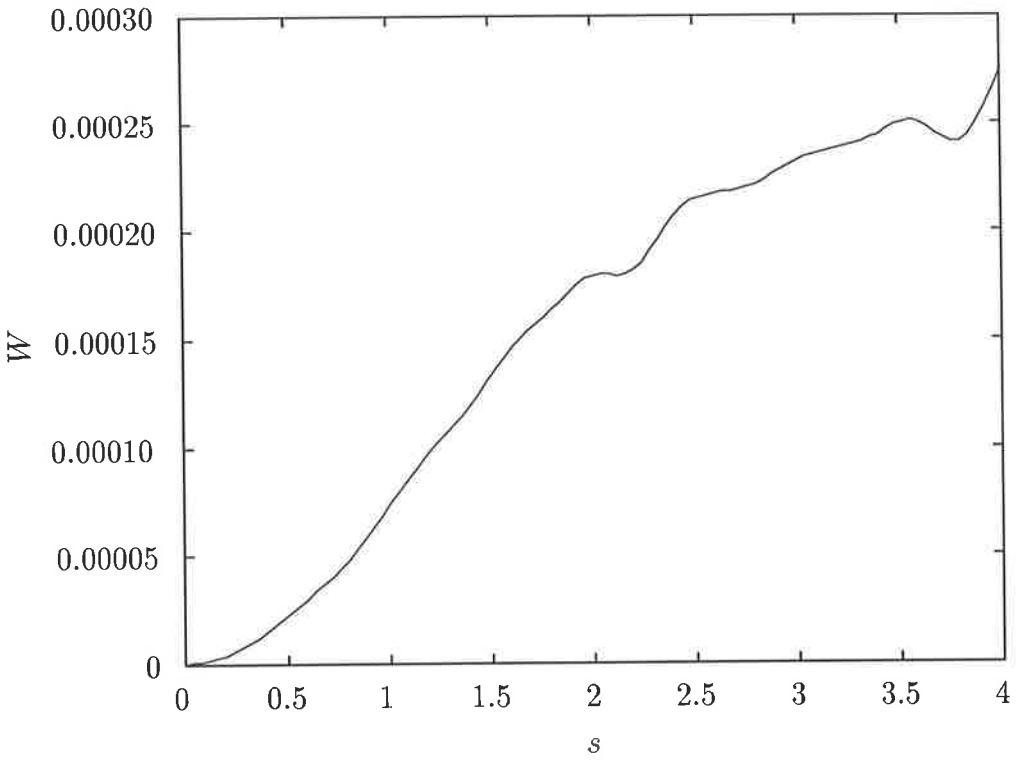

Figure 5.10: *Wave drag W versus span s for a rectangular wing flying at altitude $h_0 = 0.1c$ at velocity $U = 5$ and angle of attack $\alpha_W = 5^o$.*

where a_w is the amplitude of the wave train following the object. This wave amplitude may be determined (Grundy, 1986a), (Tuck, 1982a, page 245), (Tuck, 1982b) and (Lamb, 1932, page 403) by the planing equation, which specifies the surface elevation $\eta(x)$ resulting from a finite pressure distribution p as

$$\eta(x) = \int_0^c P(\xi) K_0'(x - \xi)\, d\xi, \tag{5.4.17}$$

where the integrated kernel function (for numerical convenience) is

$$K_0(x) = -\frac{\pi U^2}{g} f(\frac{gx}{U^2}) + \begin{cases} \frac{2U^2}{g}\cos(\frac{gx}{U^2}) - 1, & x > 0 \\ 0, & x < 0 \end{cases}, \tag{5.4.18}$$

where f is the auxiliary function for the sine and cosine integrals (Abramowitz and Stegun, 1965, Page 232) defined as

$$f(x) = \mathrm{Ci}(|x|)\ \sin x - \mathrm{si}(|x|)\cos x\ \mathrm{sgn} x. \tag{5.4.19}$$

We are not necessarily interested in the near-field form of the waves, only the amplitude far downstream. As $x \to +\infty$ then

$$\eta(x) \to 2\sin(\gamma x) \int P(\xi) \left(\frac{g}{U^2}(x - \xi)\right) d\xi. \tag{5.4.20}$$

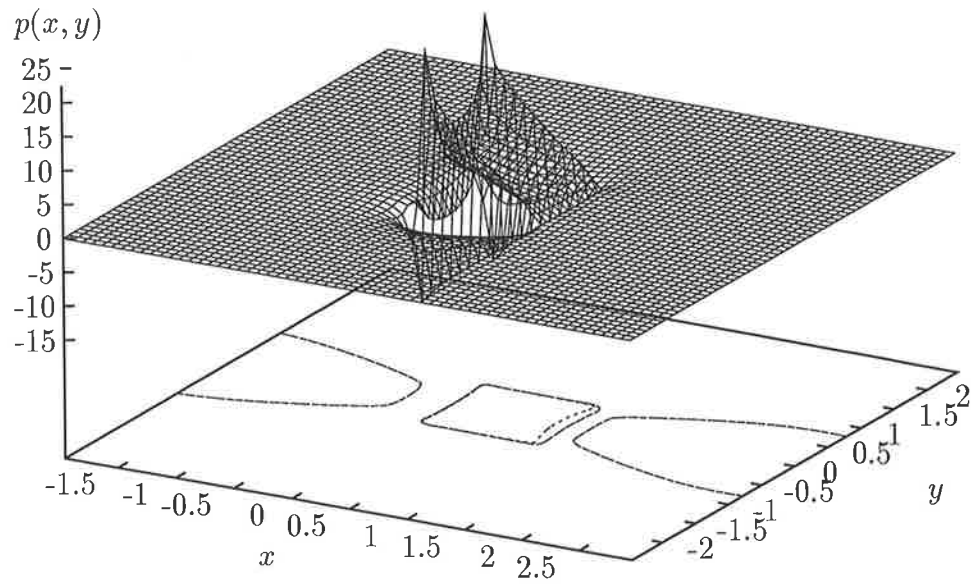

Figure 5.11: *Water surface pressure footprint of unit square wing in ground effect, at angle of attack $\alpha_W = 5°$ and velocity $U = 5$ with full-chord skirts. The projection shows the zero pressure contour lines. In addition to the high pressure region directly beneath the wing, the pressure is increased upstream and downstream by the partial blockage represented by the channel flow region. The pressure still drops as the leading edge is approached from upstream as for the case of the bare wing.*

For general $P(\xi)$, this integral must be calculated numerically. However, we shall assume that the previous assumption regarding two-dimensional airflow is valid and that there is a linear variation in velocity from the leading edge to the trailing edge within the gap zone. While this strictly implies a parabolic variation in pressure, for numerical convenience and because we are only interested in the magnitude of the forces rather than their variation with the gap geometry, we shall assume a linear variation from leading-edge to trailing-edge, where the perturbation pressure is zero. We may then define a factor $F(\gamma)$, which gives the wave-train amplitude following a linear two-dimensional pressure distribution per unit chordwise integrated pressure as

$$F(\gamma) = \int_c P(\xi)\, d\xi = \frac{4}{\gamma^2}\left[\sin(\lambda+\gamma) - \sin(\lambda) - \gamma\cos(\lambda)\right] \tag{5.4.21}$$

where

$$\lambda = \arctan\left(\frac{\cos(\gamma) - 1}{\sin(\gamma) - \gamma}\right). \tag{5.4.22}$$

The parameter $\gamma = F_L^{-2}$ is based on the length Froude number F_L given by

$$F_L = \sqrt{\frac{U^2}{gc}}. \tag{5.4.23}$$

Assuming that the pressure within the gap is constant with respect to z, then we may relate the pressure on the water surface to the loading on the wing by

$$p(x) = \rho_W U^2 P(x) = -\rho_A U \gamma(x). \tag{5.4.24}$$

We may therefore approximate the wave resistive force R per unit span, due to a two-dimensional pressure disturbance from a lifting surface in moderate ground effect, where the forces are dominated by a linear channel flow as

$$R = \frac{1}{4} g \rho_W \left(\frac{\rho_A}{\rho_W}\frac{\Gamma}{U} F(\gamma)\right)^2. \tag{5.4.25}$$

5.4.3 Magnitude of Three-Dimensional Wave Drag

In order to compare the relative magnitudes of the aerodynamic induced drag and the hydrodynamic wave resistance, we must consider the three-dimensional analogue of the two-dimensional resistance formula above, because the induced drag is a strictly three-dimensional phenomenon. If we accept that full skirts on the wing make the flow effectively two-dimensional, then an approximation to the three-dimensional wave drag may be given by extending the expression for the two-dimensional wave drag along the span

$$D_W = \int_0^s R(y)\, dy. \tag{5.4.26}$$

If we assume in addition that the two-dimensional resistance is spanwise constant, then we may further simplify by setting $R(y) = R$ from Equation 5.4.25, obtaining

$$\frac{D_W}{\alpha^2} = \frac{1}{4} g \frac{\rho_A}{\rho_W} \int_s \left(\frac{\Gamma(y)}{U\alpha} F(y, \gamma)\right)^2 dy. \tag{5.4.27}$$

Thus the wave drag coefficient realised on the wing is

$$\frac{C_{D_W}}{\alpha^2} = \frac{g}{2A_0 U^2}\frac{\rho_A}{\rho_W} \int_s \left(\frac{\Gamma(y)}{U\alpha} F(y, \gamma)\right)^2 dy. \tag{5.4.28}$$

On substitution of 5.4.14 into 5.4.28, we obtain a likely magnitude for the three-dimensional wave drag coefficient based on locally two-dimensional flow past a full-skirted wing in moderate ground effect

$$\frac{C_{D_W}}{\alpha^2} = \frac{g}{2A_0U^2}\frac{\rho_A}{\rho_W}\int_s \left(\frac{c^2}{2h_0}F(y,\gamma)\right)^2 dy. \tag{5.4.29}$$

If we assume that the wing is rectangular and the flow is uniform with respect to y, then

$$\frac{C_{D_W}}{\alpha^2} \approx \frac{1}{8}\frac{\rho_A}{\rho_W}\left(\frac{c}{h_0}\right)^2 \gamma F^2(\gamma). \tag{5.4.30}$$

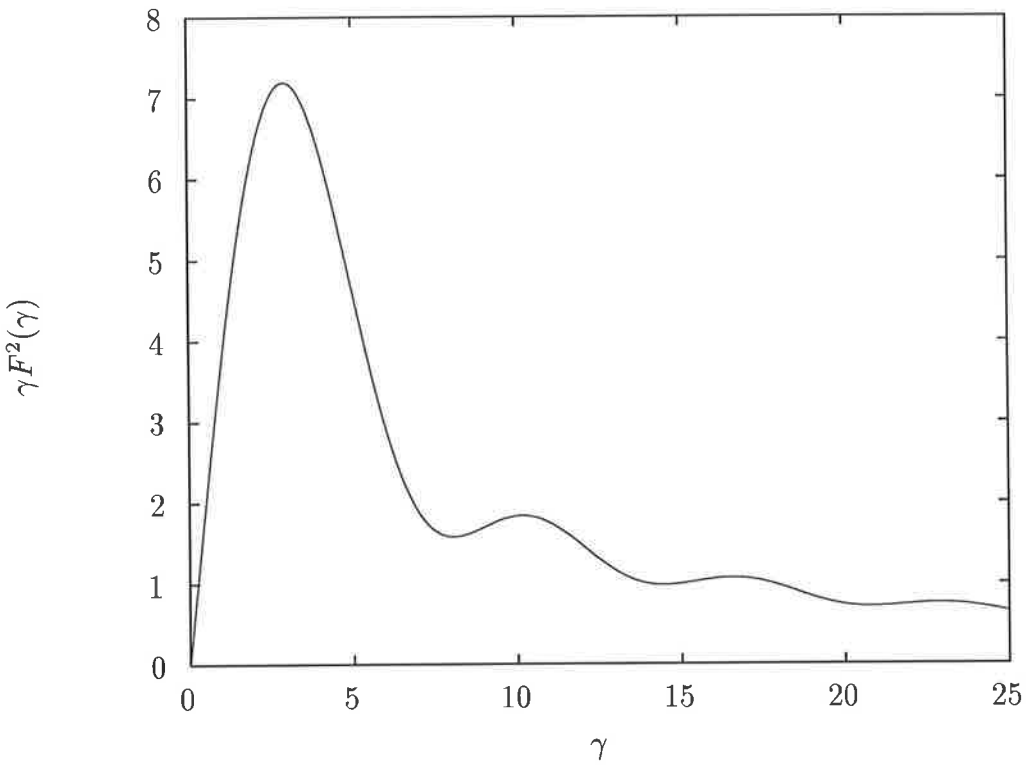

Figure 5.12: *Plot of the wave resistance function $\gamma F^2(\gamma)$ versus the wave number γ. The maximum value is 7.2 when $\gamma = 2.9$.*

The function $\gamma F^2(\gamma)$ is illustrated in Figure 5.12. Clearly the function tends to zero as γ tends to either zero or infinity, but there are an infinite number of local maxima and minima in between. The largest value of $\gamma F^2(\gamma)$ is 7.2, when $\gamma = 2.9$. This corresponds to a chord length $c = 2.9U^2/g$, which either requires an enormous aircraft or a very low velocity. Assuming that such a figure could be obtained, then the corresponding maximum possible wave drag coefficient would be approximately given by

$$\frac{C_{D_W}^{\max}}{\alpha^2} \approx \left(\frac{c}{33h_0}\right)^2. \tag{5.4.31}$$

For a coefficient of the order of one, this requires an altitude less than 5% of the chord length.

Thus it is highly unlikely that wave drag will be significant relative to aerodynamic induced drag for wings in ground effect unless they also directly pierce the water surface. The only situation in which a low velocity and a low altitude are experienced is during take-off and possibly landing, when specific aids are often required. We may conclude that for the optimisation of a wing-in-ground effect vehicle in cruise mode, the wave drag may be regarded as far less significant than the aerodynamic drag.

Chapter 6

Thickness

6.1 Introduction

In the previous Chapters, thickness effects have been treated as distinct from the lifting flow calculations. It is certainly true in the case of a single thin wing with no endplates in free air that the thickness may to leading order be decoupled from the lifting equation (Ashley and Landahl, 1965); however this is not true if any of the above conditions are violated. Any thick body lying in a plane other than that of a lifting surface will induce a velocity difference across that surface, which may be considered as an apparent angle of attack. Alternatively, a formal perturbation series may be used to determine the effect of thickness on the kinematic boundary conditions on the upper and lower surfaces (Kinnas, 1992). The result is that thickness may be explicitly included prior to the loading calculation and does not significantly increase the computational complexity of the problem. In the case where mean camber surfaces deviate significantly from the plane (Hsin et al., 1991) Kinnas shows that it is necessary to first calculate the loading for zero thickness before adding a thickness correction factor to the free stream in order to obtain the coupled solution. We shall consider here only systems of surfaces which deviate from planes by a small amount and under such circumstances, the two formulations are equivalent.

It is consistent with the present formulation to model the thickness of any thin surface by a source distribution on the center plane of that surface. While this source distribution will influence the velocities on the upper and lower surfaces equally, and thereby contribute nothing to the pressure difference between them, it will significantly modify the potential

across all other planes in the flow domain. This Chapter deals with thickness as it effects endplates, ground effect and the case of two or more wings flying in proximity.

6.2 Suction and Induced Drag

Under the present formulation, the lift and suction are regarded as sufficient to determine the induced drag with and without thickness. However if this approach had not been taken, then it would be necessary to consider the coupling of lifting and thickness to second order in angle of attack, in order to correctly determine the induced drag. Such an analysis (Tuck, unpublished notes on aerodynamics) for a single wing with thickness shows that the resulting drag may be evaluated as

$$D_i = \iint_B [p(x,y,0^+)f_x^+(x,y) - p(x,y,0^-)f_x^-(x,y)]\,dxdy \tag{6.2.1}$$

$$= D_S + D_V + D_I, \tag{6.2.2}$$

where

$$D_S = -\rho_A \iint_B dxdy \iint_B d\xi d\eta\, m(x,y)m(\xi,\eta)G_z(x-\xi,y-\eta,0) \tag{6.2.3}$$

is the contribution from the sources alone,

$$D_V = \rho_A \iint_B dxdy \iint_B d\xi d\eta\, \gamma(x,y)\gamma(\xi,\eta)H_z(x-\xi,y-\eta,0) \tag{6.2.4}$$

is the contribution from the vortices alone, and

$$D_I = \rho_A \iint_B dxdy \iint_B d\xi d\eta\, m(x,y)\gamma(\xi,\eta)[G_{1z} - H_{1z}](x-\xi,y-\eta,0) \tag{6.2.5}$$

is the contribution from the interaction between sources and vortices, where G, H, G_1 and H_1 refer to the singular and non-singular kernels for the influences of source and horseshoe vortex distributions respectively.

The only way in which such a complicated interaction could be manifest in the current formulation is through a thickness modification to the linearized leading-edge suction coefficient. Although a number of investigators have considered the nonlinear attenuation of the suction phenomenon with angle of attack for real airfoils (Lan and Su, 1987) and the variation of leading-edge suction with camber (DeLaurier, 1983), the reduction of leading-edge suction with linear thickness is unclear. Such an investigation is beyond the scope of this thesis, but would no doubt make an interesting study. For the purposes of the remainder of this thesis it will be assumed that linear leading-edge suction is not affected by wing thickness.

6.3 Mathematical Formulation

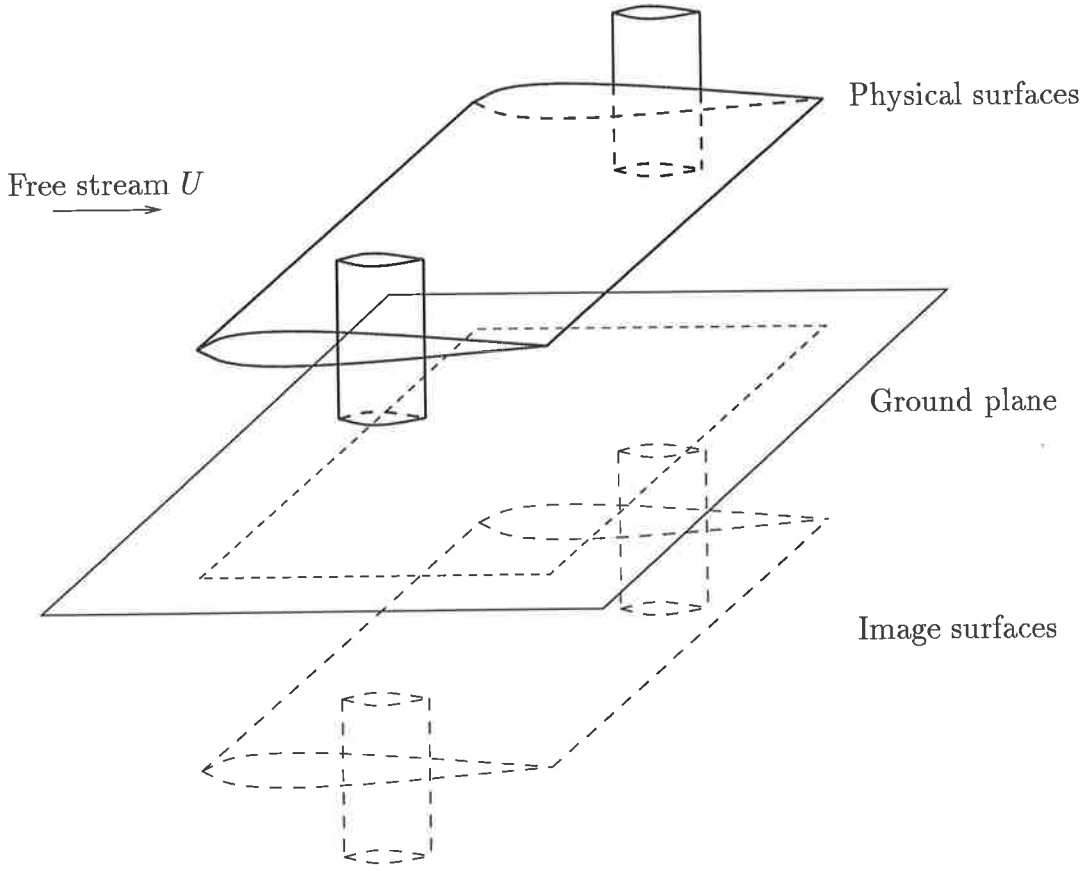

Figure 6.1: *Wing-endplate combination plus image.*

In order to properly formulate the thickness problem, we need to specifically consider the inclusion of ground effect. Ground effect in the presence of a rigid ground plane can be modelled as in Figure 6.1 using an image as though reflected in the ground plane. Let the velocity be given by

$$\boldsymbol{q} = \boldsymbol{\nabla}\left(Ux + \phi(x,y,z)\right) \tag{6.3.6}$$

where ϕ is the velocity potential

$$\begin{aligned}\phi(x,y,z) &= \iint_W \gamma(\xi,\eta)\overline{H}(x-\xi,y-\eta,z-\zeta)\,d\xi d\eta \\ &+ \iint_P \gamma(\xi,\zeta)\overline{G}(x-\xi,y-\eta,z-\zeta)\,d\xi d\zeta \\ &+ \iint_W m(\xi,\eta)\overline{S}(x-\xi,y-\eta,z-\zeta)\,d\xi d\eta \\ &+ \iint_P m(\xi,\zeta)\overline{S}(x-\xi,y-\eta,z-\zeta)\,d\xi d\zeta. \end{aligned} \tag{6.3.7}$$

The composite potential functions include the image contributions such that

$$\overline{H} = H + H_1 = H(x-\xi, y-\eta, z-\zeta) - H(x-\xi, y-\eta, z+\zeta) \quad (6.3.8)$$

$$\overline{G} = \mathcal{G} + \mathcal{G}_1 = \mathcal{G}(x-\xi, y-\eta, z-\zeta) + \mathcal{G}(x-\xi, y-\eta, z+\zeta) \quad (6.3.9)$$

$$\overline{S} = S + S_1 = S(x-\xi, y-\eta, z-\zeta) + S(x-\xi, y-\eta, z+\zeta). \quad (6.3.10)$$

Maintaining the previous notation, H is the potential function for a unit horseshoe vortex on the wing, G is the potential function for a unit horseshoe vortex on the plate and S is the potential for a source on either the wing or the plate. For convenience, it will be assumed that when S refers to a source on the plate, the influence of both endplates is included. In the special case where one endplate only is to be included, we shall use S^* instead. Then

$$\begin{aligned}\frac{\partial \phi}{\partial z} &= \iint_W \gamma \overline{H}_z \, d\xi d\eta + \iint_P \gamma \overline{G}_z \, d\xi d\zeta \\ &+ \iint_W m\overline{S}_z \, d\xi d\eta + \iint_P m\overline{S}_z \, d\xi d\zeta. \end{aligned} \quad (6.3.11)$$

Taking the limits above and below the surface of mean camber $z \to h \pm 0$ gives

$$\begin{aligned} Uf_x^{\pm} &= \lim_{z \to h\pm} \left\{ \iint_W \gamma \overline{H}_z \, d\xi d\eta + \iint_P \gamma \overline{G}_z \, d\xi d\zeta + \iint_W m\overline{S}_z \, d\xi d\eta + \iint_P m\overline{S}_z \, d\xi d\zeta \right\} \\ &= \iint_W \gamma \overline{H}_z \, d\xi d\eta + \iint_P \gamma \overline{G}_z \, d\xi d\zeta \pm \frac{1}{2} m + \iint_W m S_{1_z} \, d\xi d\eta + \iint_P m\overline{S}_z \, d\xi d\zeta \end{aligned} \quad (6.3.12)$$

Subtracting the two halves of Equation 6.3.12 and solving for m gives

$$m(x,y) = U\left(f_x^+ - f_x^-\right) = U\frac{\partial}{\partial x}(\text{Wing Thickness}). \quad (6.3.13)$$

Taking the average of the two halves of Equation 6.3.12 and substituting the mean camber $f_x = (f_x^+ + f_x^-)/2$ gives

$$Uf_x = \iint_W \gamma \overline{H}_z \, d\xi d\eta + \iint_P \gamma \overline{G}_z \, d\xi d\zeta + \iint_W m S_{1_z} \, d\xi d\eta + \iint_P m\overline{S}_z \, d\xi d\zeta. \quad (6.3.14)$$

Thus the first of the coupled lifting-surface equations for wings and endplates in ground effect with leading-order thickness is

$$\iint_W \gamma \overline{H}_z \, d\xi d\eta + \iint_P \gamma \overline{G}_z \, d\xi d\zeta = -\iint_W m S_{1_z} \, d\xi d\eta - \iint_P m\overline{S}_z \, d\xi d\zeta + Uf_x \quad (6.3.15)$$

Similarly, the second equation is

$$\iint_W \gamma \overline{H}_y \, d\xi d\eta + \iint_P \gamma \overline{G}_y \, d\xi d\zeta = -\iint_P m S_y^* \, d\xi d\zeta - \iint_W m\overline{S}_y \, d\xi d\eta + Ug_x, \quad (6.3.16)$$

where S^* is the contribution to the velocity potential $\overline{S}$ due to the second endplate only. In the case of multiple wings or wing-endplate combinations in or out of ground effect, the contribution of sources from every other surface and its image must also be included.

Once these equations have been integrated once with respect to x, we need only calculate the additional kernel functions based on the velocity potential for a source

$$S(X,Y,Z) = -\frac{1}{4\pi R}, \tag{6.3.17}$$

where $R = \sqrt{X^2+Y^2+Z^2}$. Thus

$$K_Y^S = \int \frac{\partial S}{dy}\,dx = \frac{1}{4\pi}\frac{XY}{(Y^2+Z^2)R} \tag{6.3.18}$$

$$K_Z^S = \int \frac{\partial S}{dz}\,dx = \frac{1}{4\pi}\frac{XZ}{(Y^2+Z^2)R}. \tag{6.3.19}$$

Since there is no formal antiderivative to these kernel functions analogous to the kernel for a horseshoe vortex in the present method, we model the thickness using a Riemann-type summation. For numerical convenience, we assume that the thickness is constant on each panel with a value given by the standard NACA 4-digit section distribution evaluated at the collocation point. This distribution is given (Abbott and von Doenhoff, 1958, page 113) as

$$\pm y_t = \frac{t}{0.20}\left(0.29690\sqrt{x} - 0.12600x - 0.35160x^2 + 0.28430x^3 - 0.10150x^4\right), \tag{6.3.20}$$

where t is a thickness parameter expressing the maximum thickness as a fraction of the chord length and the chord is defined for $0 < x < 1$. In fact, this distribution describes a foil which is slightly longer than $c = 1$, but as it is a standard in the literature it will be used without modification. Figure 6.2 shows the thickness distributions over $0 < x < 1$ for various values of t.

With the exception of the case of a single wing without endplates in free air, thickness effects are significant to first order for every wing or wing-endplate combination in or out of ground effect. In the context of the previous Chapters, there are three cases that should be described, namely the influence of thickness when adding endplates to a single wing in free air, the effect of wing thickness with and without endplates in ground effect, and the effect of a second lifting configuration in proximity to the first.

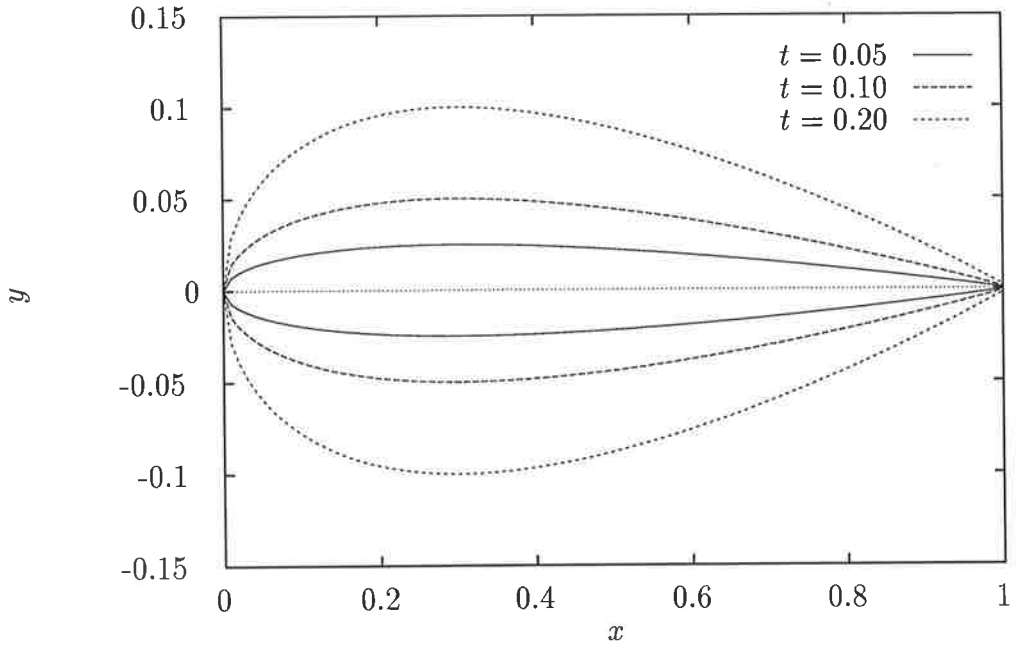

Figure 6.2: *Thickness distributions for NACA 4-digit wing sections for various values of the thickness parameter t.*

6.4 Single Wing with Endplates

From the thickness modification to the mathematical formulation of the lifting surface integral equations presented in Section 6.3 of this Chapter, it is easy to see that the thickness of any component of a wing-endplate configuration alters the apparent angle attack of every component other than those in the same plane as itself. However, it is not always clear what effect this will have on the lift distribution.

In order to develop some intuition on these coupled effects, an examination is made of a single wing with endplates. The case where the wing has thickness while the endplates do not is considered first, then the case of a flat plate wing with thick endplates. It will be seen that even a flat plate at nominal angle of attack $\alpha_W = 0^\circ$ will produce lift when there is a vertically asymmetric distribution of thickness on the endplates.

6.4.1 Wing with Zero-Thickness Endplates in Free Air

We take a unit square wing with unit square endplates. The endplates have no thickness and the wing has spanwise uniform thickness parameter $t(y) = t$. We chart the variation

of C_L against the vertical offset b of the endplates from the central position for various values of t. We maintain the horizontal symmetry $a = 0$ as before. For clarity these results are presented in Figures 6.3 and 6.4. Figure 6.3 shows the variation in lift with the vertical location of the square endplate for a wing at angle of attack $\alpha_W = 0^o$. The thickness parameter t/c takes the values $0\%, 2\%, 4\%, 6\%, 8\%$ and 10%.

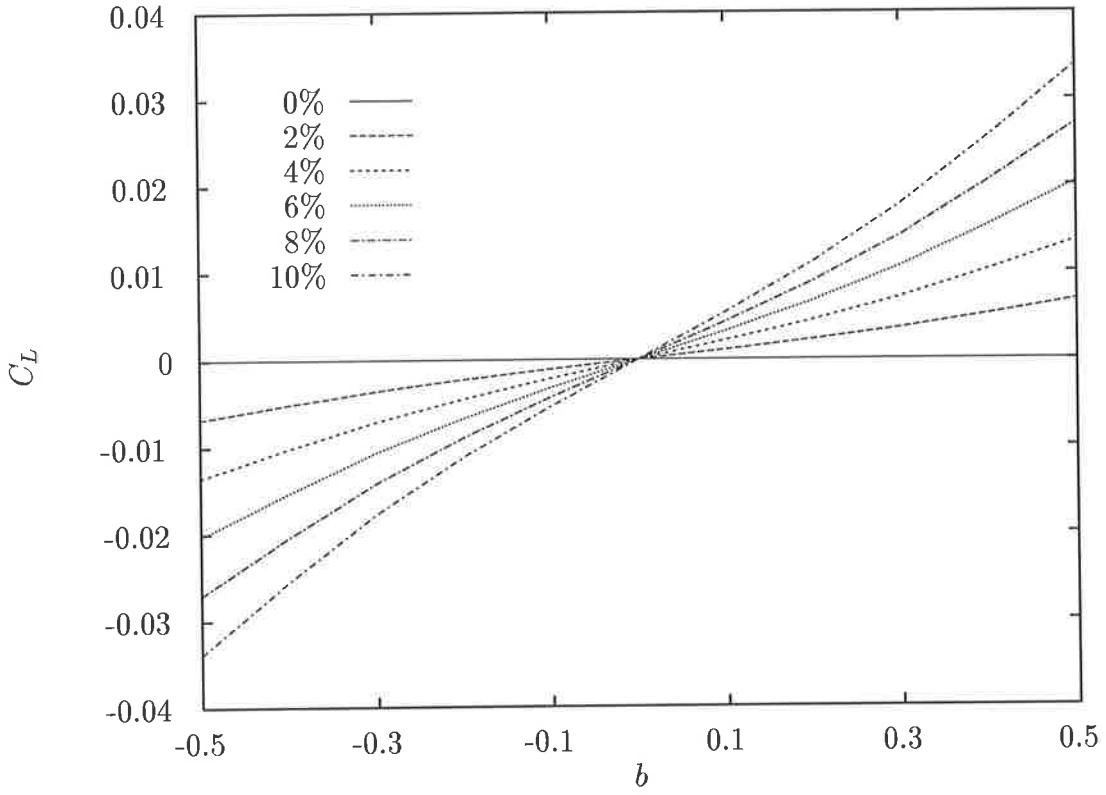

Figure 6.3: *Plots of C_L against the vertical offset b of the zero thickness endplates from the central position for $\alpha_W = 0^o$ and $t/c = 0\%, 2\%, 4\%, 6\%, 8\%$ and 10%. Note that thickness causes a downforce when the endplate is on the lower half of the wing only.*

Note that when the wing has thickness, asymmetry in the position of the endplate causes a net lift or downforce on the wing, even though the wing is at zero nominal angle of attack. This is because the wing thickness accelerates the flow on both upper and lower surfaces in the same way as fluid is accelerated through a Venturi and the pressure is consequently reduced. When the endplate is is symmetrically located, this effect is equal on both upper and lower surfaces and the pressure difference between the surfaces caused by the thickness is zero. When the endplate is asymmetrically positioned, the Venturi effect is greater on the surface where flow is more two-dimensional. Thus if the endplates are dominantly below the wing, the two-dimensional flow on the lower surface produces a lower average pressure than on the upper surface and the wing experiences a

net downforce. For a zero camber airfoil, this effect is vertically symmetric. Figure 6.4 includes the information from Figure 6.3 but also shows the relative effect of this additional 'thickness lift' to flat-plate lift for the square-wing, square-plate geometry at angles of attack $\alpha_W = 0^o, 2^o, 4^o, 6^o, 8^o$ and 10^o. It is clear that thickness effects are not significant whenever the endplates are vertically central. Maximum lift no longer always occurs when the endplates are vertically central. In contrast to the flat-plate case, there is now a balance to be struck between the two lift-generating mechanisms. For positive angles of attack, thickness reduces the high pressure below the wing and increases the suction above the wing. It is consequently worth offsetting the endplate such that $b > 0$ to make the flow over the wing more two-dimensional and the flow below the wing less two-dimensional.

6.4.2 Flat-Plate Wing with Thick Endplates

Introducing thickness to endplates is another way to increase the lift of a system with the same planform geometry. In order to compare this effect with the lift of a flat plate and the thickness-related lift of a thick wing, thickness is added to the endplate *above the wing only.* This will accelerate the flow over the upper wing surface and cause a lift force. Figure 6.5 shows the variation in lift of a square flat-plate wing at angle of attack $\alpha_W = 0^o$ against vertical offset b of square planform endplates. Curves are shown for the parameter t_P, being the thickness of the endplate above the wing. The endplate has zero thickness below the wing.

Note that there is still an optimal vertical offset b even though the wing and lower plates have zero thickness. The section of the endplate below the wing still has a role to play in maintaining the difference in pressure between upper and lower wing surfaces by preventing the relatively high pressure air below the wing from circulating around the wingtip to the low pressure region created by the Venturi between the thick upper endplates. In this case, the balance is struck when the endplate is almost entirely above the wing. By comparing Figures 6.3 and 6.5 we see that the thickness effect of the endplates is certainly of the same order as that of the wing and in the case of the square planforms, creates a lifting force roughly three times greater than for the same thickness on the wing.

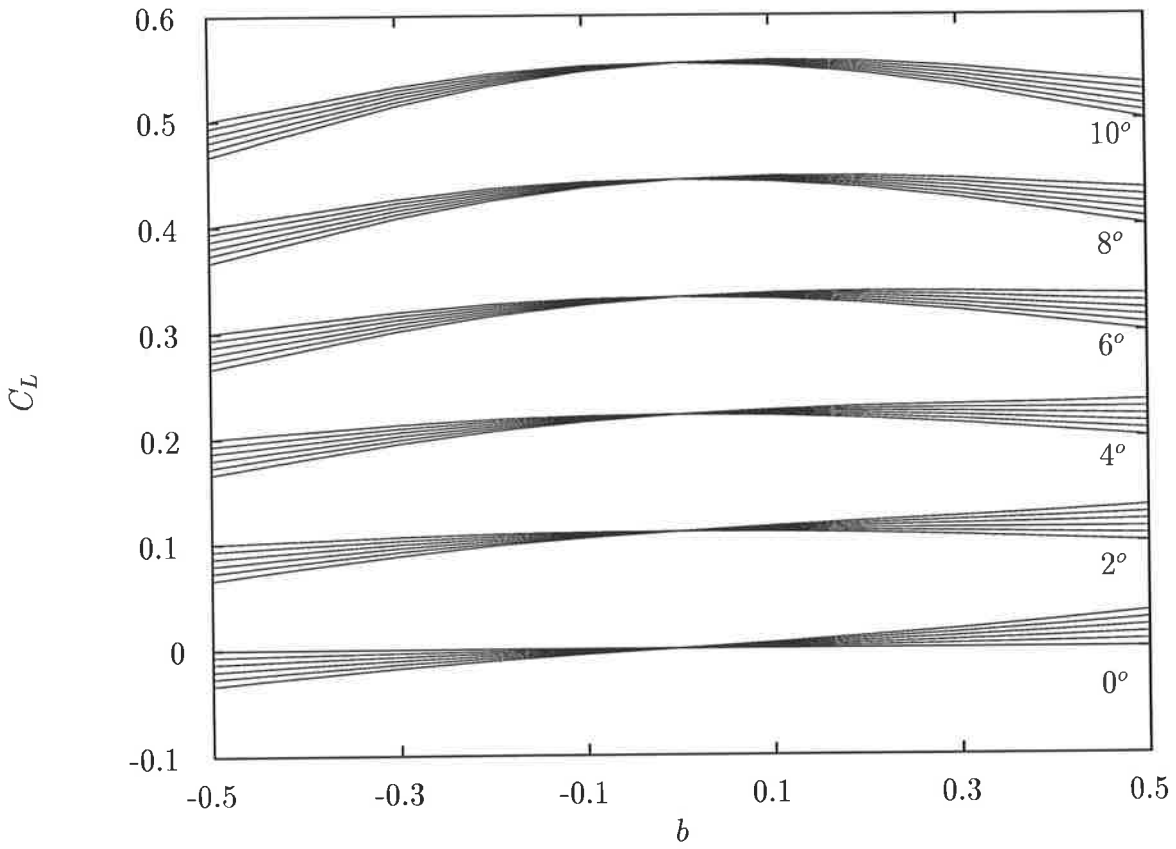

Figure 6.4: *Plots of C_L against the vertical offset b of the endplates from the central position. The group of curves for each of the angles of attack $\alpha_W = 0^o, 2^o, 4^o, 6^o, 8^o$ and 10^o shows the effect of $t/c = 0\%, 2\%, 4\%, 6\%, 8\%$ and 10%. In every case the greatest variation in lift occurs for the thickest wing. At higher angles of attack, the thickness related lift is relatively less significant than the flat-plate lift. In all cases, finite thickness makes the optimal endplate displacement b positive, rather than zero as already shown for a wing of zero thickness.*

6.5 Wing Thickness in Ground Effect

Having developed an insight into the effect of thickness in free air, we turn to the case of a single wing in ground effect. Rather than repeat the work of the previous section, we consider only the cases of wing thickness with and without flat endplates. Before proceeding with the geometries of specific interest, it is prudent to verify the numeric implementation. In the previous Chapter on ground effect, it was found that even in moderate ground effect, the wing grid scale can cause large inaccuracies when image vortices are close to surface panels. It is reasonable to assume that image sources will have similar numerical behaviour. One test of the numerics is to compare the predicted

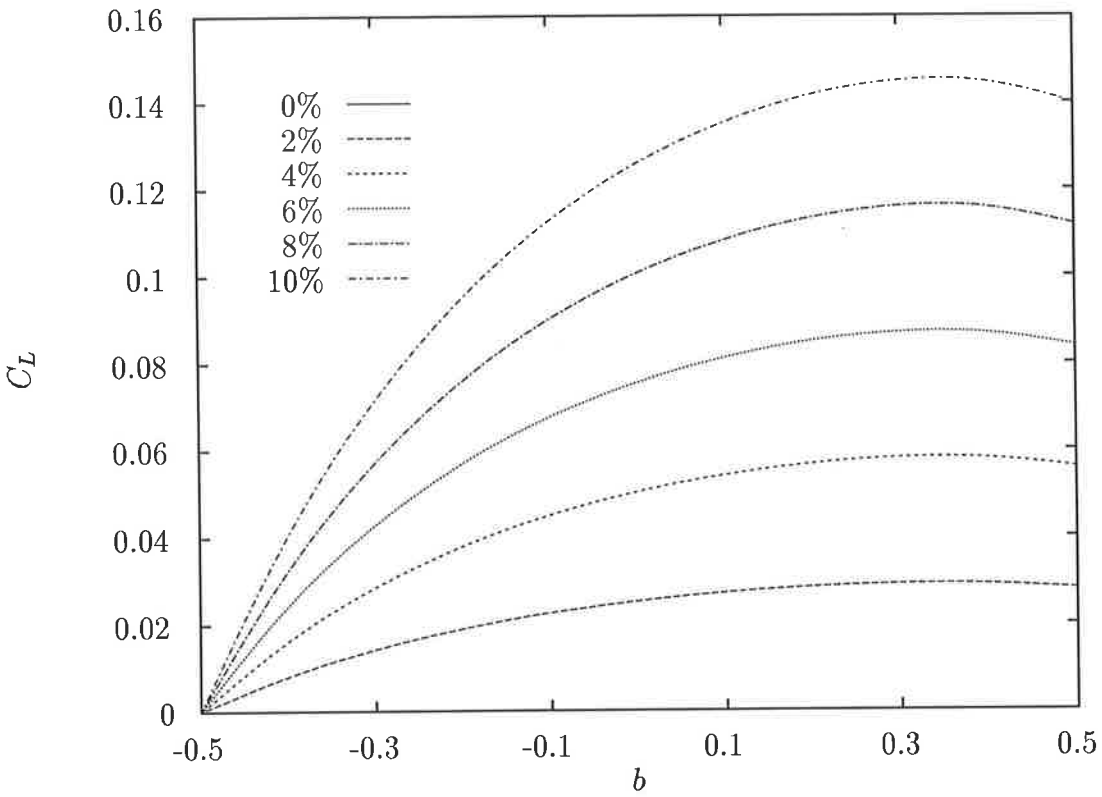

Figure 6.5: *Plots of C_L against the vertical offset b of the endplates from the central position. The endplate has thickness parameter $t_P = 0\%, 2\%, 4\%, 6\%, 8\%$ and 10% above the wing and zero thickness below the wing.*

downforce of a single wing at zero nominal angle of attack with full endplates with that estimated by the one-dimensional channel flow

$$p(x) = p_0 + \frac{1}{2}\rho_A U^2 \left(1 - (h_0/h(x))^2\right), \tag{6.5.21}$$

where h_0 is the nominal altitude of the wing and $h(x)$ is the actual clearance. In this case $h(x) = h_0 - y_t(x)$. Since it is only the ratio $h_0/h(x)$ that determines the pressure distribution beneath the wing, we may calculate the exact value of the total downforce for any given thickness parameter t. For $t = h_0/10$ the lift coefficient $C_L = -.0729$.

Numerically it is difficult to reproduce this result using the three-dimensional code because computational effort must be expended to include sufficiently large endplates so as to make the flow effectively two-dimensional. Also, the grid scale must be fine enough to resolve the influences of image sources located beneath the ground plate. Using flat rectangular endplates which extend from one chord length upstream of the leading edge to one chord length behind the trailing edge, and from the ground to two chord lengths above the wing we obtain the data presented in Table 6.1.

h_0	t	C_L
0.100	0.0100	-0.0440
0.050	0.0050	-0.0525
0.025	0.0025	-0.0581
$1/\infty$	$h_0/10$	-0.0694

Table 6.1: *Downforce produced on a unit square wing with thickness parameter* $t = h_0/10$. *Endplates have no thickness and are full skirts to produce effectively 2-dimensional flow. In the limit as* $h_0 \to 0$, *1-dimensional channel flow predicts that* $C_L \to -0.0729$. *Extrapolation is used to match the one-dimensional case.*

While increased endplates and consequently increased numbers of panels asymptotically improve the results for this test, they are regarded as sufficient code verification for the following sections.

6.5.1 Bare Wing

The thickness in ground effect of a bare square wing with thickness parameter t is to be considered. Since the effects of aspect ratio and angle of attack have been covered in the previous Chapter 4 we consider only the parameters h_0 and t. Figure 6.6 shows the variation of C_L with the altitude h_0 for various thickness parameters t.

As with the case of negative angle of attack and no thickness, the downforce varies linearly with the thickness parameter t and inversely with the altitude h_0. In order to increase the downforce, we can add endplates as full skirts.

6.5.2 Wing with Flat Endplates

By adding skirts to the wing in ground effect, we limit the flow of air into the low pressure zone directly beneath the wing. Figure 6.7 shows the variation of the lift coefficient C_L with the altitude for various thickness parameters.

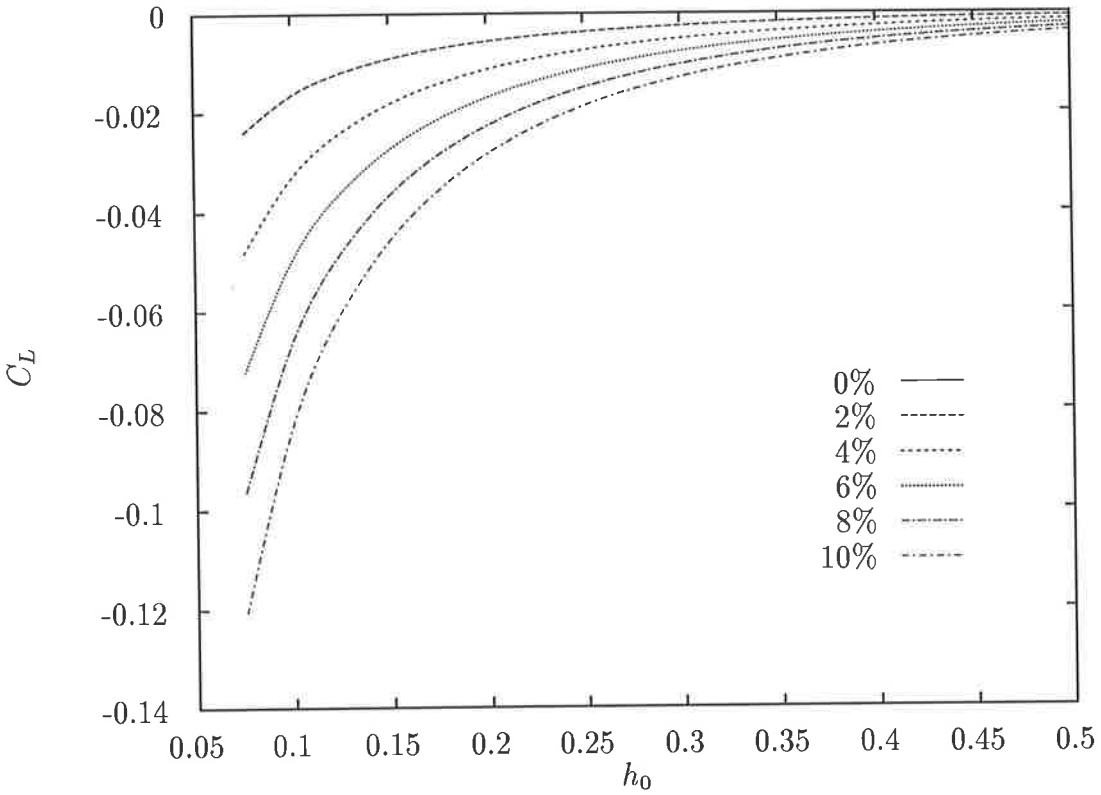

Figure 6.6: *Plots of C_L against the vertical altitude h_0 of a bare square wing in ground effect. The wing has thickness parameters $t = 0\%, 2\%, 4\%, 6\%, 8\%$ and 10%.*

6.6 Multiple Body Flight Configuration

Birds and aircraft often fly in formation. This might be for efficiency, such as the delta arrangement for large load-carrying aircraft which simulates a wing with a larger (if discontinuous) span. The addition of thickness to the wings introduces nothing to the case where all wings lie in the same plane, but when the surfaces are stacked vertically, as in some bird formations, the thickness becomes significant. The first observation is that the flow is accelerated in the diminished gap between the surfaces, thus decreasing the lift on the upper wing and increasing the lift on the lower wing. The relative location of the wings can significantly effect the coupling due to thickness. Having established the thickness properties of endplates in previous sections, we consider only multiple wing interaction in free air. In particular, we consider the case of a second wing identical to the first with a horizontal offset a and a with a vertical offset b (see Figure 6.9).

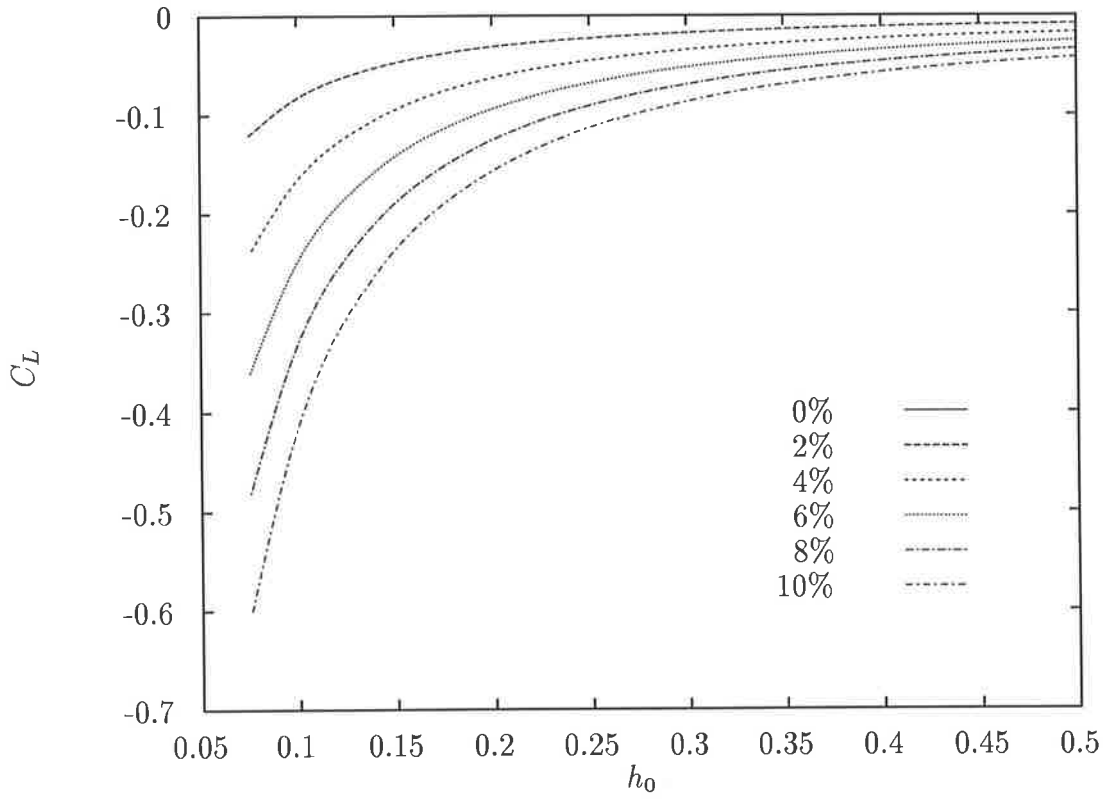

Figure 6.7: *Plots of C_L against the vertical altitude h_0 of a square wing with full-chord skirts in ground effect. The wing has thickness parameters $t = 0\%, 2\%, 4\%, 6\%, 8\%$ and 10% and the endplates have zero thickness.*

6.6.1 Horizontal Offset

For any given pair of wings at a given vertical separation, there is an optimal horizontal offset a which maximises the combined lift to drag ratio. To illustrate this, consider two unit square wings each with a NACA thickness distribution with thickness parameter t. Each wing is at an angle of attack of $\alpha_W = 5^o$. Figure 6.9 shows the variation in the ratio of lift to induced drag L/D_i for the two wing combination as the horizontal offset a between the leading edges of the two wings varies from $a = -c$, when the top wing is a full chord length in front of the lower wing to $a = c$, where it trails by a full chord. The vertical separation between the two wings is $b = c/2$. Note that there is no attempt to include skin frictional drag in this case. As biplane theory predicts (Kuchemann, 1978) for wings of zero thickness, there is an optimum when the wings lie directly on top of each other. As thickness is gradually introduced to both wings, the maximum is higher and occurs when the upper wing is forward of the lower wing.

To see what is happening to each of the two wings, we plot L/D_i as realised on each of

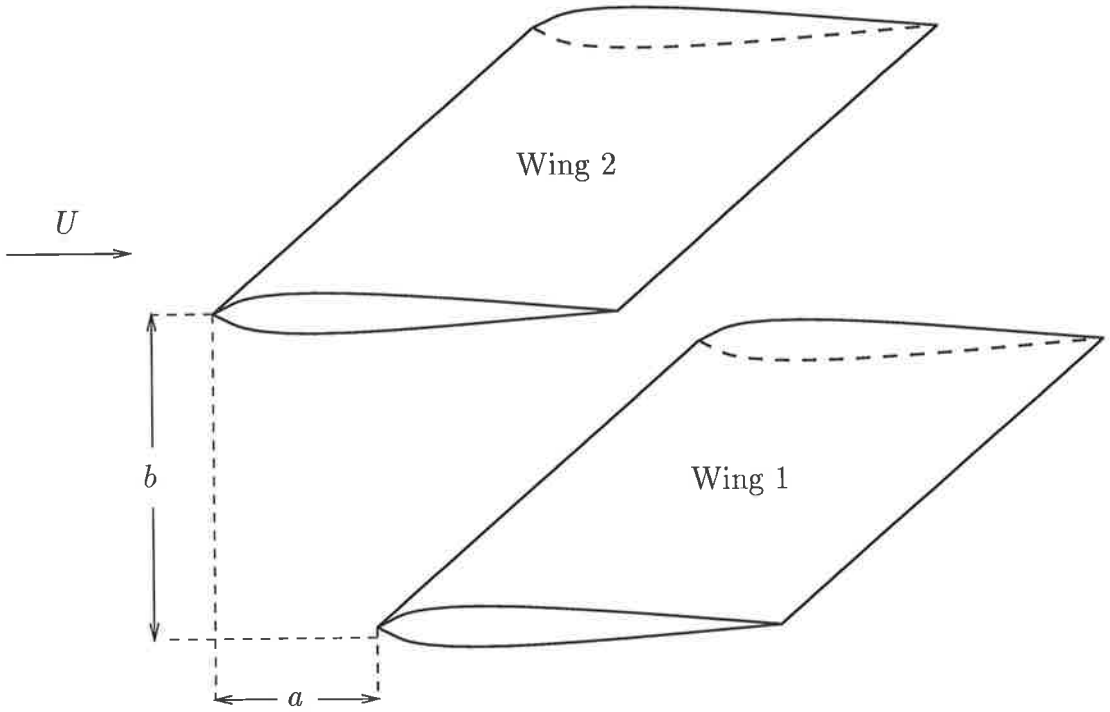

Figure 6.8: *Two identical wings with thickness parameter t and horizontal and vertical offsets a and b, respectively.*

the wings individually. Figures 6.10 and 6.11 illustrate that as the thickness parameter t is increased and the suction between the two wings correspondingly increases, the lift on the upper wing decreases. In order to reduce the drag on the upper surface it may be moved forward, thus increasing the leading edge suction. In fact for $t = 10\%$, there is a region from $-0.25 < a < -0.05$ where L/D_i on the upper wing is negative. This is not because the lift is negative, but because the suction is so strong that the upper wing is getting a free ride. This situation does not correspond to the global optimum, however!

Clearly the optimal offset a will vary with the angles of attack, span, vertical separation and thickness of the two wings. It is also clear that the variation will not be linear with any of these.

6.6.2 Vertical Separation

While there is always a well defined optimal value of a for a given vertical offset b, there is not always an advantage in utilising the straight "biplane effect." Consider the 2 square wings, again at $\alpha_W = 5^o$ with fixed horizontal separation $a = 0$ and variable vertical separation b. Figure 6.12 shows the variation in L/D_i against b for a variety of thickness

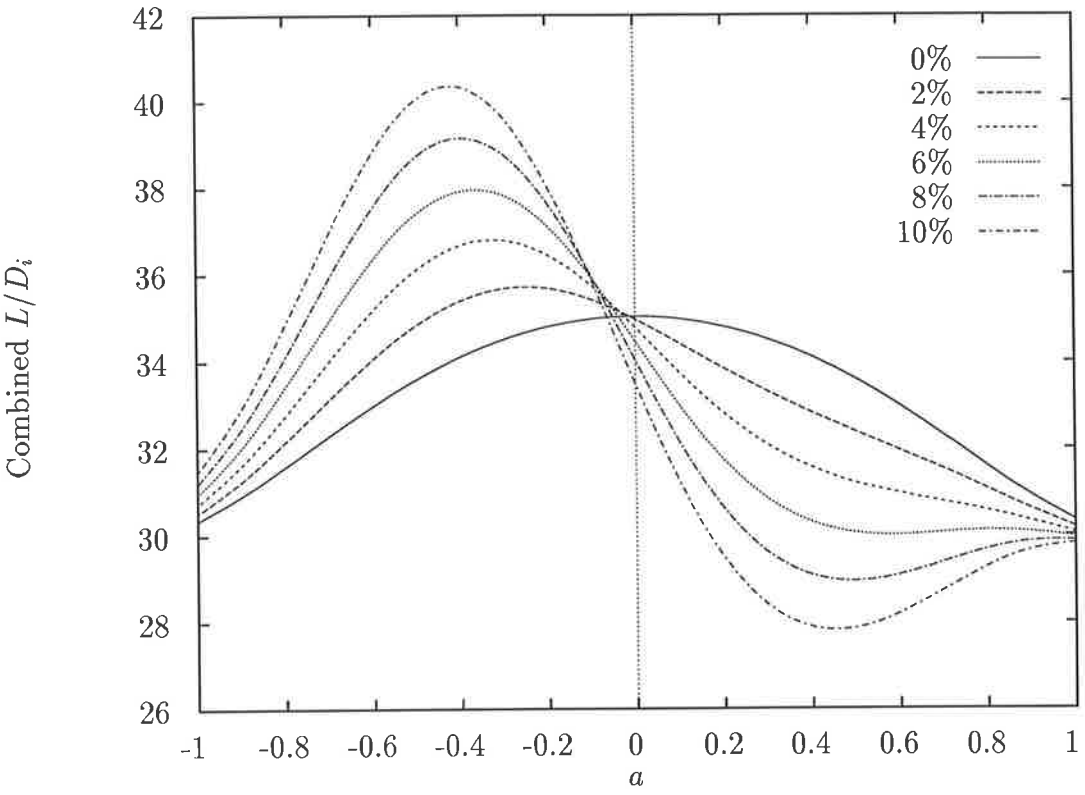

Figure 6.9: *Combined L/D_i against horizontal offset a for two unit square wings at $\alpha_W = 5^o$ and thickness parameter $t = 0\%, 2\%, 4\%, 6\%, 8\%$ and 10%.*

parameters t.

While there is a clear advantage to wings of zero thickness flying in vertical proximity, this advantage is reduced by thickness coupling. If only vertical movement is allowed, the zero thickness wings should fly with a separation of $b = 0.3c$. At a smaller separation, the loss in lift is not compensated for by the dissipation of vortex energy. Beyond a thickness of approximately $t/c = 5\%$, there is no such balance point. However, if horizontal movement were also allowed, there would be an optimal finite *pair* (a, b) that described a configuration whose performance exceeded that of the two separate wings in free air.

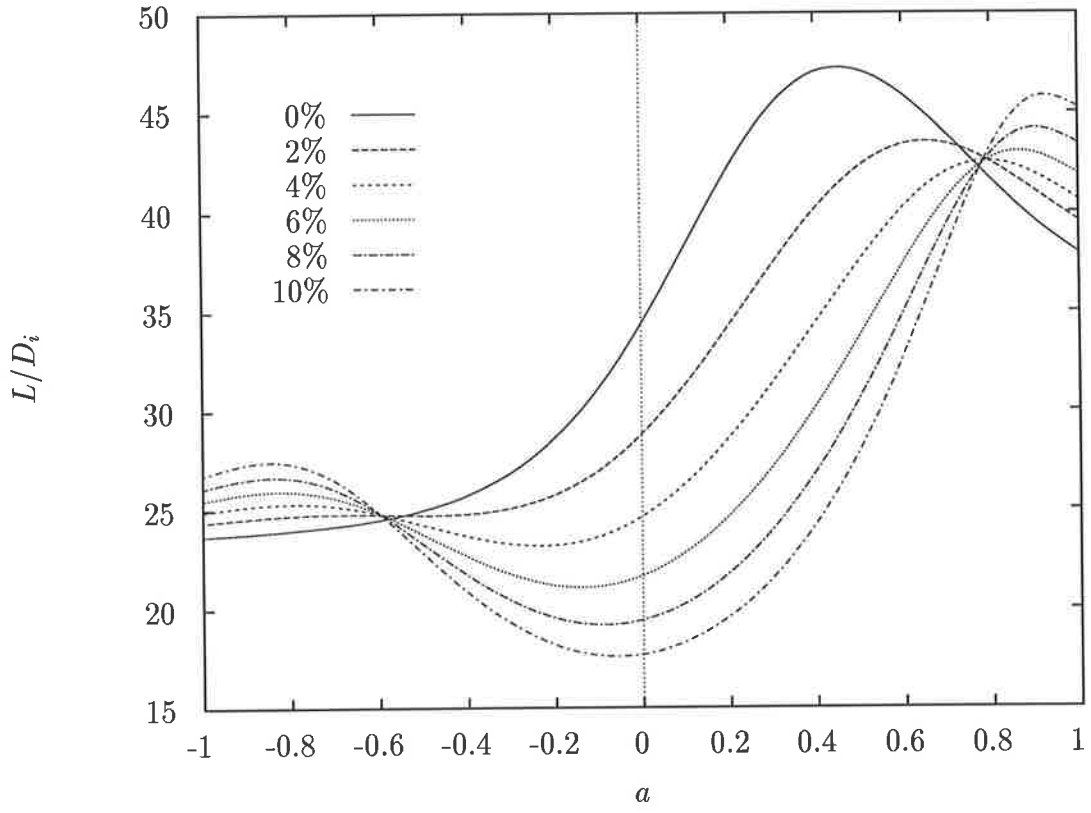

Figure 6.10: *The efficiency L/D_i for wing number 1 versus the horizontal offset a for two unit square wings angles of attack $\alpha_W = 5^\circ$ and thickness parameters $t =$* $0\%, 2\%, 4\%, 6\%, 8\%$ *and* 10%.

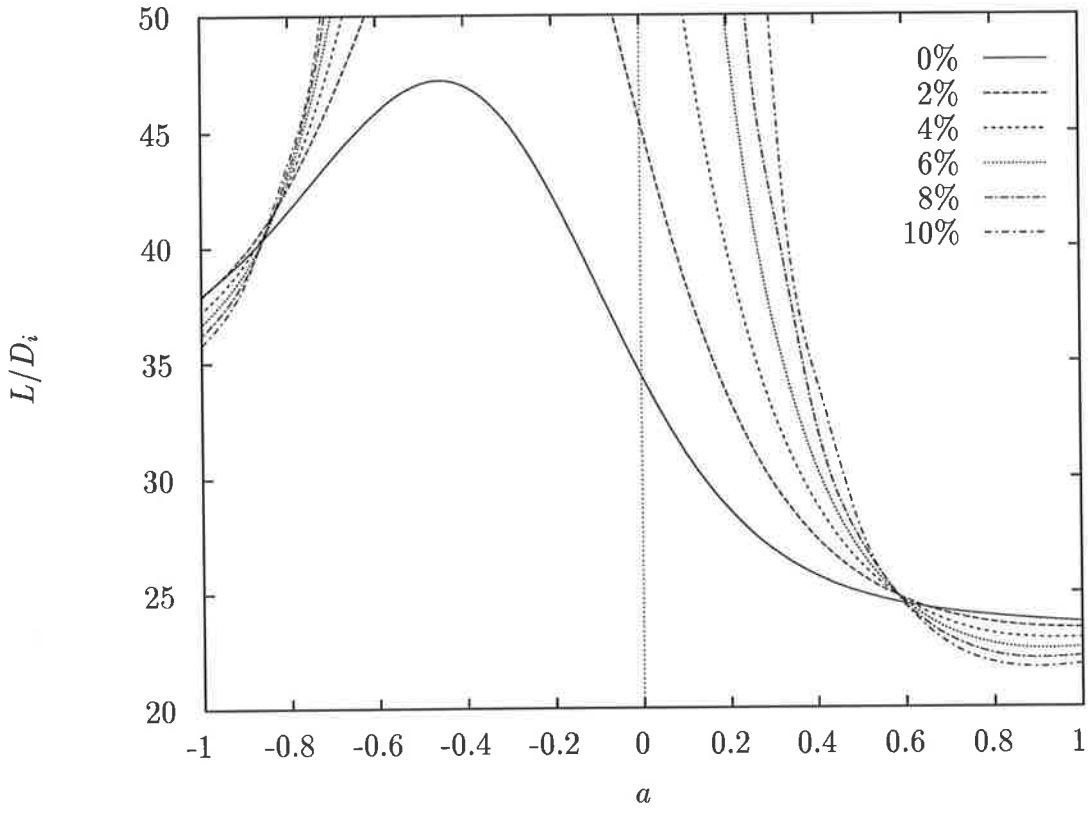

Figure 6.11: *The efficiency L/D_i for wing number 2 versus the horizontal offset a for two unit square wings at angles of attack $\alpha_W = 5^\circ$ and thickness parameters $t = 0\%, 2\%, 4\%, 6\%, 8\%$ and* 10%.

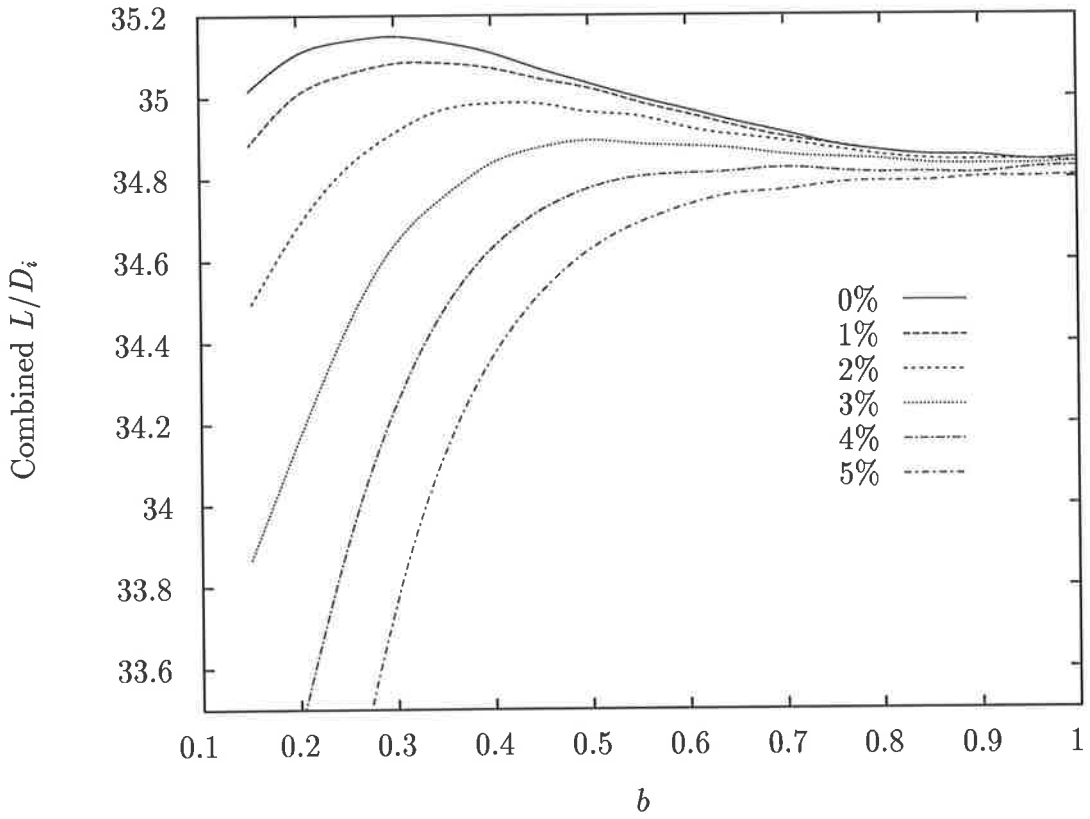

Figure 6.12: *Combined efficiency L/D_i versus the vertical separation b of two unit square wings at angles of attack $\alpha_W = 5^\circ$ and thickness parameters $t = 0\%, 1\%, 2\%, 3\%, 4\%$ and* 5%.

Chapter 7

Optimization

The theme of optimisation has been significant in many of the preceeding Chapters in this thesis, but there are issues regarding the formulation and numerical solution of optimisation problems that have not yet been explicitly addressed. This Chapter is not a comprehensive study of optimisation but contains a number of examples and separate discussions of specific problems associated with using an optimisation algorithm to improve a lifting configuration.

7.1 Introduction

The designer of an algorithm for calculating the forces on general lifting surfaces may start with a pre-conceived notion of what sort of 'general' planforms will be input to the program. It may be expected that the boundary will be quite smooth, except at a small number of points (maybe cusped wingtips) and the likely optimal shape will in all likelihood be a sleek object. However, the automatic search does not know this. Even a very clever algorithm for generating shapes needs to have a representation that allows geometric flexibility but will not trip up the numerics. In other words, the designer of the optimal search should be aware of all the possible shapes that will be input to the lifting surface program, but should not pre-empt the results.

Another approach to the structural optimisation problem involves the determination of the loading of a structure and the subsequent removal of material with loading below a critical value (Xie and Steven, 1993). This approach has been successfully used to optimise Michell trusses and other mechanical structures. Its strength lies in the ability

to use information from the function evaluation to guide the search direction. It may be useful to include a similar feature to the present algorithm, though it must be noted that such an algorithm used alone would not correctly predict the location of the leading edge on a lifting configuration, as material would never be removed from the leading edge to relocate it.

7.1.1 Finite Geometric Representation

Much effort has been devoted recently to the development of global optimisation algorithms that seek to find which of the possible values of an input vector $\boldsymbol{I}$ of either binary or real values will maximise a given function $F(\boldsymbol{I})$. These algorithms may go under the broader category names of Genetic Algorithms or Simulated Annealing, but the common feature is that they should have limited or zero functionality that is specific to the system that they are optimising.

While it is expected that certain search parameters may be tuned either externally or by a so-called meta-algorithm, only algorithms with 'heuristic' components have any problem-specific functions. All they have to do is be able to call a function to evaluate F. The way in which $\boldsymbol{I}$ represents the state of the system at hand is the only mechanism by which we may influence the direction of the search. The particular choice of representation may be unimportant or crucial to a given problem.

Consider the maximisation of the lift coefficient C_L/α_W for a wing geometry. Let the real-valued vector $\boldsymbol{I}$ specify the leading edge $LE(y), 0 < y < s$ and chord $c(y), 0 < y < s$ functions over the wingspan s at a discrete set of points, namely the spanwise collocation points $y_i, i = 1, \ldots, n$. Hence the input vector is given by $\boldsymbol{I} = (s, c_1, \ldots, C_n, LE_1, \ldots, LE_n)$ and we can run a standard real vector optimizer.

We might expect to find that the optimal input vector $\boldsymbol{I} = \boldsymbol{I}^*$ defines a circle or a square or maybe an infinite AR ellipse, but these geometries will not be found by the genetic algorithm. There is no natural limit to the size of the wing in this pseudo-random search, so there are infinitely many geometrically similar wings with the same aspect ratio. It is very likely that the optimizer will never converge, because of the *genetic drift* that frequently occurs when a problem is under-specified or under-constrained.

One solution is to prevent this from happening at the function evaluation stage by normal-

izing all vector entries with respect to the largest value. Now the optimiser will quickly start increasing the span s. This is because s is the single vector entry that has the greatest immediate effect on the lift coefficient. To have the same effect as increasing the span, all chord length entries would have to decrease in unison, the probability of which is very small. The optimiser returns a wing with a very large aspect ratio, but very little useful information about the chord length distribution, which will be effectively random.

Of course it is not reasonable to seek the wing with optimal lift coefficient C_L/α_W, because practically the span will be limited by structural considerations. We need to fix both the span and the planform area in order to have a workable problem.

7.1.2 Grid-Scale Oscillation

Many algorithms require an estimate for the downhill gradient of an optimisation cost function. For example, a popular general optimisation routine GMRES has been used to modify standard NACA airfoil profiles to improve their performance (Vossinis, 1995). However, not all functions are so numerically well behaved. A discussion of a number of "Industrial Strength" optimisation problems is presented in Davis (Davis, 1996).

There are often grid-scale oscillations in the search space that are artificial products of the discretisation scheme, quite distinct from the order of computational accuracy, that introduce an artificial sub-structure to the global optimisation problem. To illustrate this point, Figure 7.1 shows the variation in the lift coefficient C_L/α_W of a unit square wing versus the horizontal offset a of a small 1/4 by 1/4 square endplate that is vertically centered on the wing. The number of points chosen to represent the geometry is deliberately small, with $m = 12, n = 12, m_p = 6$ and $n_p = 12$.

Standard gradient methods are likely to find this troublesome, so we choose to implement a simple genetic algorithm for the search.

7.2 A Simple Genetic Algorithm

Much work has been done recently on the tuning of genetic algorithms for specific applications. In this section we do not endeavor to examine the rate of convergence of the genetic algorithm beyond a level of interest motivated by the present study of aerodynamics.

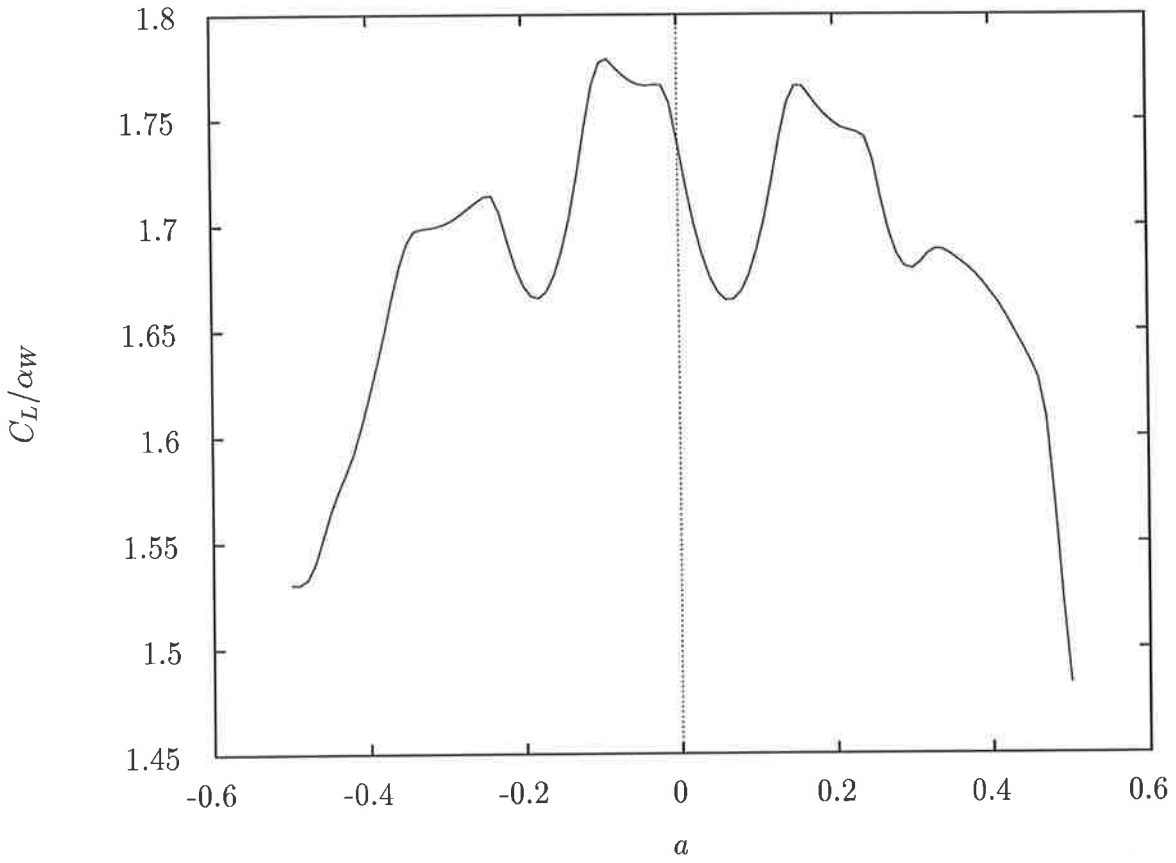

Figure 7.1: *Grid-scale oscillations in the object function C_L/α_W for a unit square wing versus the horizontal offset a of small, vertically centered square endplates.*

The present algorithm operates on a population of N_p "chromosomes" $c_j, j = 1, .., N_p$, each of which consists of N_g "genes" $g_i, i = 1, .., N_g$, or real numbers describing the geometry to be optimised. Each new generation of the population is produced by creating N_c "children" from the N_p "parents." These new $N_c < N_p$ chromosomes replace the chromosomes of the existing population which have the lowest *fitness*. The fitness is the external function to be optimised. The children are produced by one of four randomly selected operations:

- *mixed crossover*, whereby each gene in the child chromosome is randomly selected from the corresponding genes in each of two randomly selected parents.
- *random perturbation*, where the genes in a single parent chromosome are randomly either increased or decreased by 5%.
- *averaging*, whereby the corresponding genes in two parent chromosomes are averaged to produce a child, and

- *smoothing* whereby each gene in a parent chromosome is replaced by the average of its two neighbouring genes *if* their basic role in the chromosome is the same.

The last operation is the only one of this list which is function-dependent, because the genetic algorithm must have some information about the role of each gene in determining the geometry of the wing-endplate configuration. Ideally, there should be no such operations, but this one has been found to significantly increase the rate of convergence. The algorithm ceases producing new generations when the highest fitness in the population has converged to within an acceptable tolerance of the optimal solution.

Determining the optimal values of N_p and N_c for a particular problem is very difficult and usually varies as the generation number increases. The number of original chromosomes retained at each generation, $N_p - N_c$ is known as the *generation gap*. If all but one of the current population is replaced ($N_p - N_c = 1$), the system is known as *elitist*. In general, a large generation gap results in early convergence (Brown, 1997), while a small generation gap allows good *schemata*, or successful small-scale sub-structures within the chromosomes that are later assembled into complete solutions, to remain in the population. According to Davis (1989) the most effective population size is a parameter that is dependent on the problem being solved, the representation being used and the operators manipulating the representation. Other researchers in the field of genetic algorithms agree. It could take longer to derive parameter values tailored to one's problem than the time available for solving the problem itself (Davis, 1989, p61). There is very little likelihood of finding globally correct answers to questions such as the choice of population size and crossover operators (De Jong and Spears, 1990, p47). At present genetic algorithms are as much an art as a science Davis (1991). For the purposes of this simple genetic algorithm, we shall use a population $N_p = 8$, without any formal justification other than that it is small enough for the present computing capacity to make some headway and large enough to maintain some genetic diversity within the population.

7.2.1 Optimal Wing Planform

In this section, we consider a limited optimisation of the planform geometry of a wing with limited aspect ratio $AR = 1$. In order to further limit the search space, the wing will be assumed to be fore-aft symmetric. Thus the only variables are the local chord

lengths at a finite number of stations. We choose stations to coincide with the Chebyschev collocation points on one half of the wing, such that $N_g = n/2$.

In order to determine the optimal number of children N_c at each generation number, we repeat this test case for $N_c = 2, 4$ and 6 corresponding to generation gaps of $G_g = 6, 4$ and 2 respectively. The results are shown in Figure 7.2

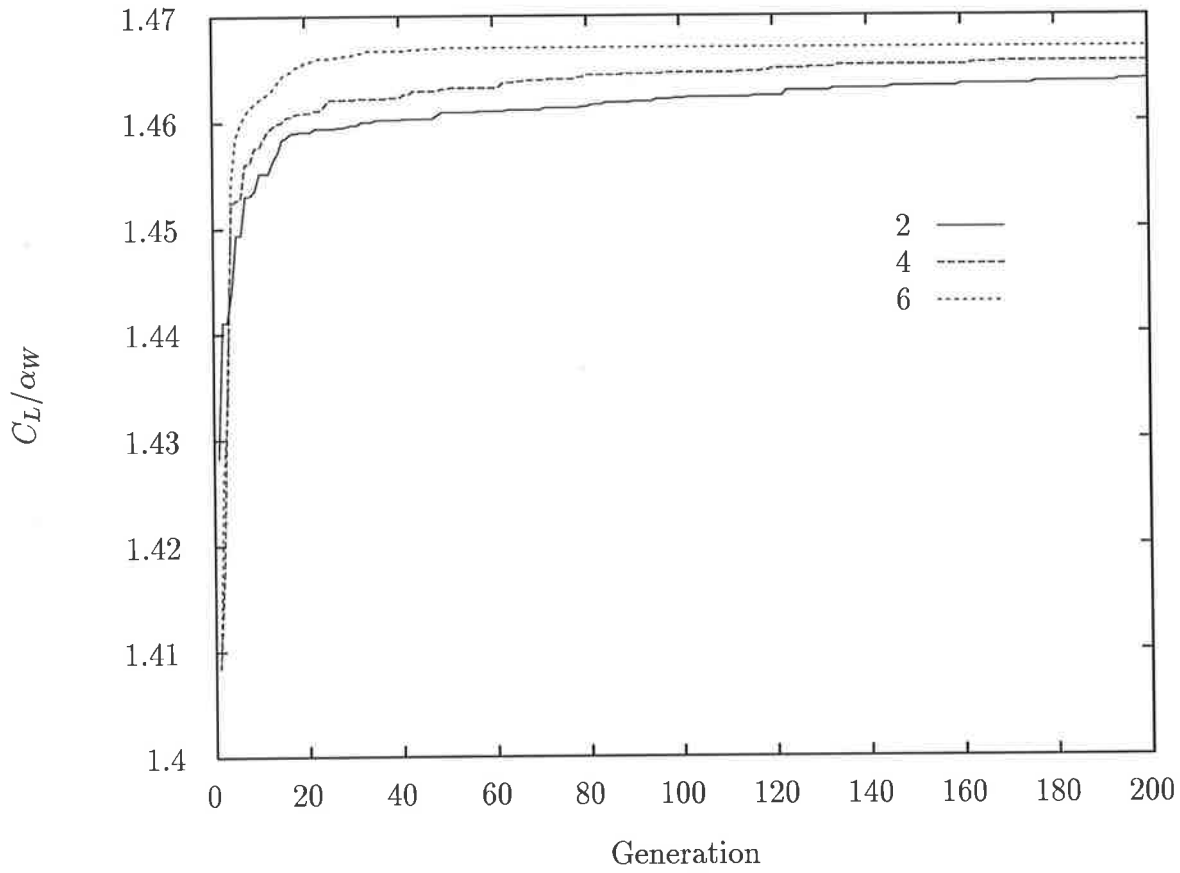

Figure 7.2: *The rate of convergence to the optimal wing planform with constant downwash versus the generation gap $G_g = N_p - N_c = 2, 4$ and 6. Clearly a small generation gap is preferable in this case.*

The optimal lift coefficient $C_L/\alpha_W = 1.467$ is somewhat greater than the lift coefficient for the square wing $C_L/\alpha_W = 1.460$ and for the elliptic wing with unit aspect ratio $C_L/\alpha_W = 1.460$, not to be confused with the elliptic wing of aspect ratio $4/\pi$, a circle. Interestingly, the optimal chord-length distribution is a hybrid of the two.

7.2.2 Optimal Endplate

A slightly more complicated optimisation problem is the addition of endplates to a square wing as considered for rectangular endplates in Chapter 3. In this chapter, we consider

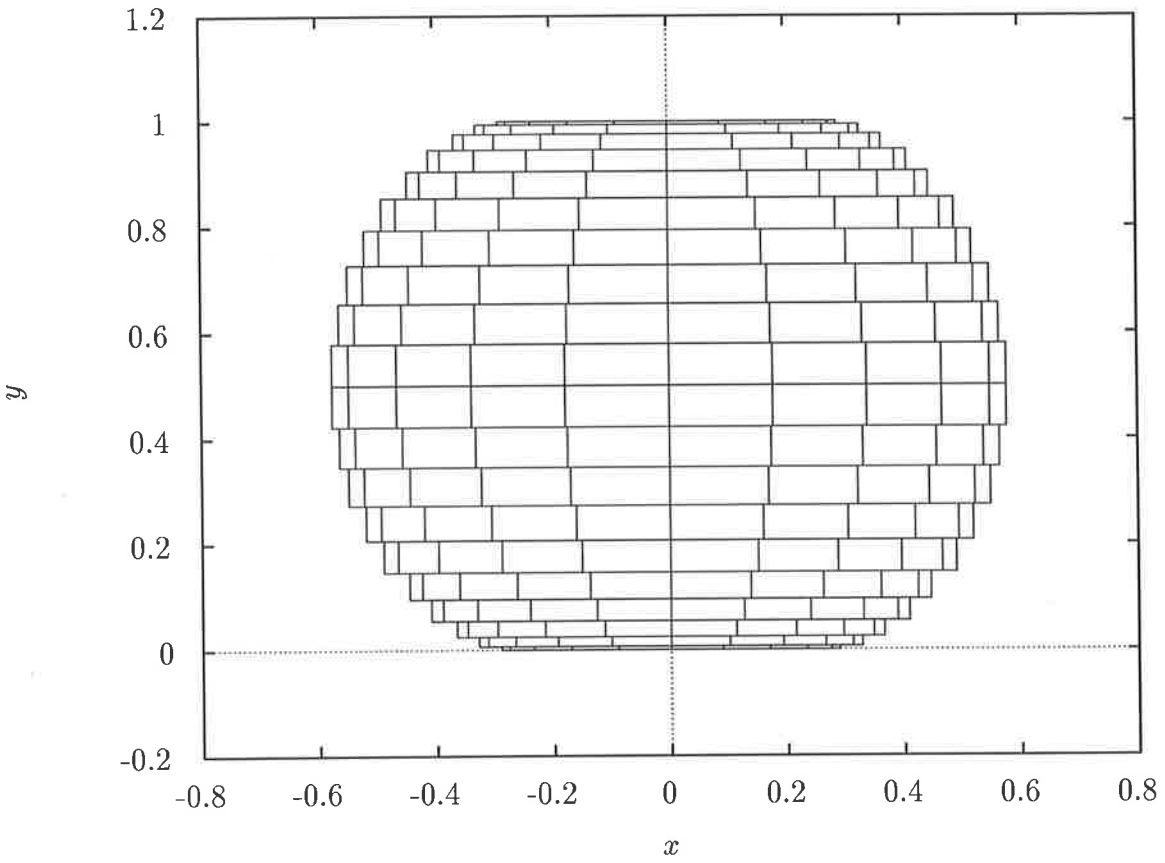

Figure 7.3: *The finite solution produced by the simple genetic algorithm for maximising the lift coefficient C_L/α_W of a planar wing with constant downwash and aspect ratio $AR = 1$. The function evaluation is made by the present lifting surface panel method with $m = 10$ and $n = 20$.*

generally-shaped endplates but we restrict the endplate to be fore-aft symmetric about the wing mean chord, although it need not be vertically symmetric. The chromosome is chosen to represent $[h_b, h_t, g_i, i = 1, \ldots, n_p]$ where h_b is the height of the lower section of the endplate, h_t is the height of the upper section of the endplate and g_i are the chord lengths of the endplate, again measured at the Chebyschev collocation points. The function evaluation is used with $n = m = 18$ on the wing and $m_p = 6$ and $n_p = 12$ on the endplate, giving $N_g = 14$ genes per chromosome. The generation gap is retained at $G_g = 2$. The rate of convergence is significantly slower than for the planar wing. Figure 7.4 shows the convergence of the lift coefficient C_L/α_W over 1500 generations.

The converged value of the lift coefficient is $C_L/\alpha_W = 1.913$ whereas the previous optimum obtained using rectangular endplates was 1.84. It is interesting to also plot the convergence rates for the individual genes. For clarity, we present only the rates for h_b, h_t and $g_i, i = 1, \ldots, 6$ in Figure 7.5. The rates for the chord-lengths on the upper portion of

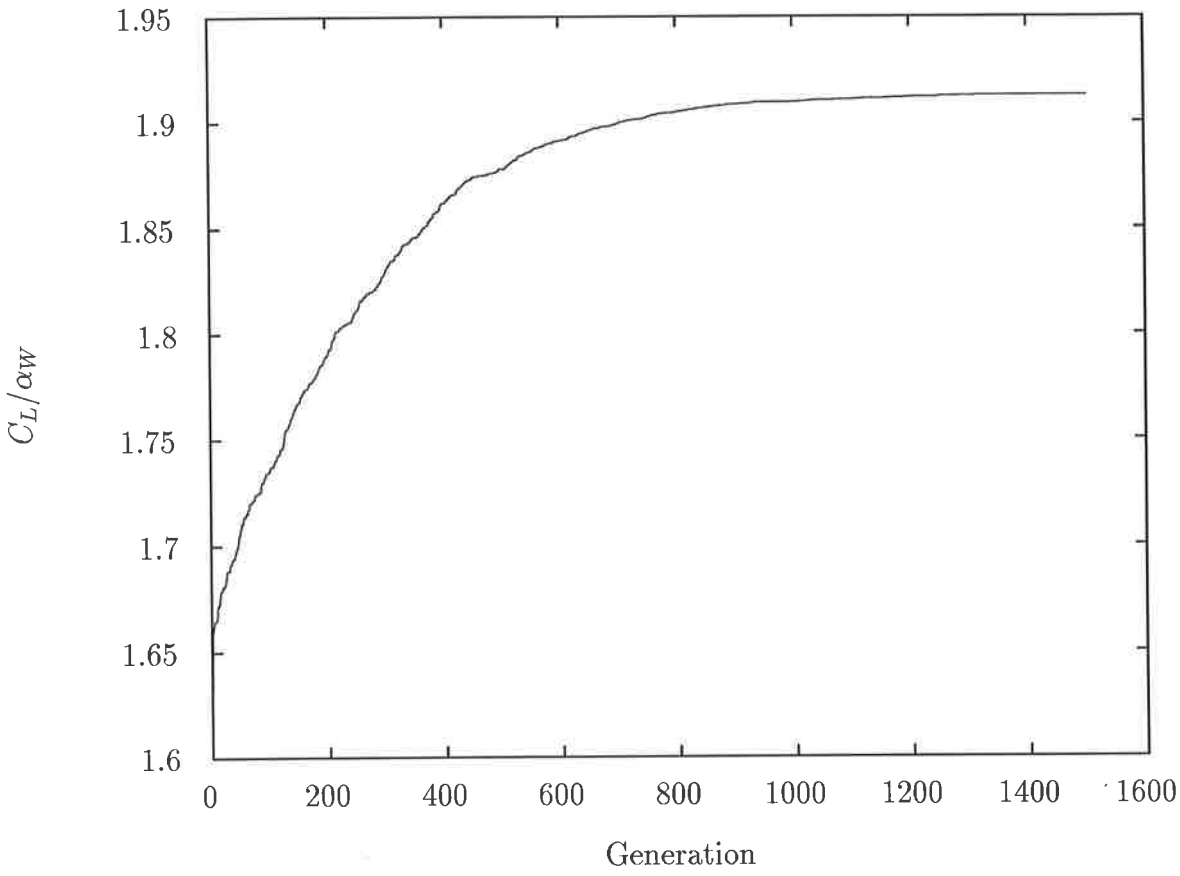

Figure 7.4: *The rate of convergence to the optimal horizontally centered endplate at zero angle of attack on a unit square wing.*

the endplate are similar. It takes far longer for the tipmost values to converge than the values representing chordwise strips near the wing. This is because the tipmost values are relatively less significant than the values near the wing. The section heights h_b and h_t do not converge as fast as the difference between them, indicating that vertical asymmetry is strongly penalised. The actual optimal geometry is illustrated in figure 7.6.

The endplates appear to be cusped, and in the limit as the number of panels on the plate increases, we expect that the endplate will be a fairing between the wing and an efficient, centrally located endplate with area zero and infinite aspect ratio, namely a line.

The colour map is a useful visualisation of the optimisation task. Clearly the high-lift regions on the wing shown in red need to be maximised. Hence placing the endplate far forward is in a sense redundant because there is already high loading there. Similarly, placing the endplate towards the rear of the wing reduces the load on the endplate because of the lower pressures there, so the optimal location is central. That the location appears to be exactly central is intriguing.

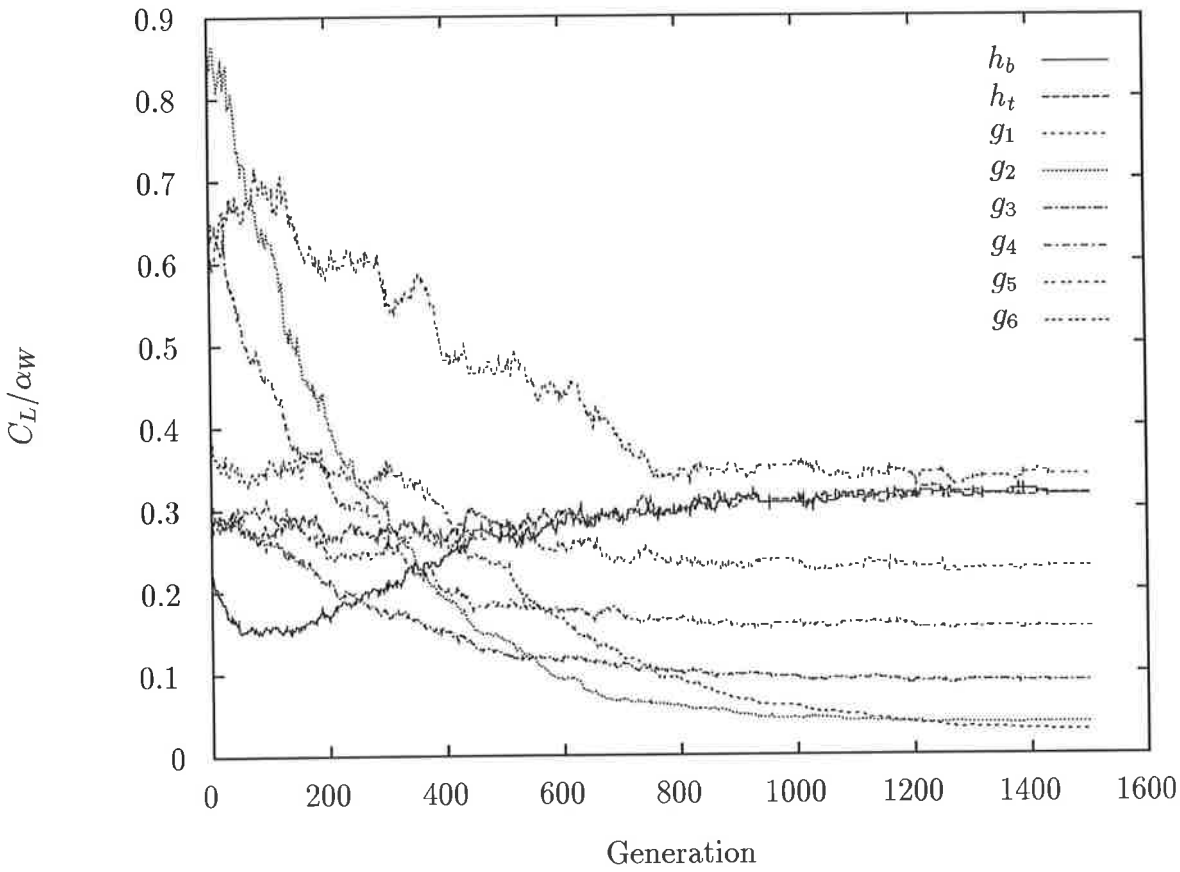

Figure 7.5: *The rate of convergence to for individual genes representing the endplate. The chord length genes start at the bottom of the endplate such that g_1 is the chord length near the tip of the lower endplate and g_6 is the chord length near the wing of the lower endplate.*

7.2.3 Full Wing-Endplate Optimisation

As with the optimisation presented in Chapter 3, we shall consider the optimisation of a wing-endplate geometry for values of the flow parameter $C_f/\alpha_W^2 = 0.1, 0.2, 0.5, 1, 2, 5$ and 10. Because the nature of the optimal solution changes dramatically when the endplates are allowed to flare, we present a series of optimal designs, generated by the present genetic algorithm operating on the chromosome $[\boldsymbol{w}, h_b, h_t, \boldsymbol{p}]$, where $\boldsymbol{w}$ is a vector of real values describing the location of the wing leading-edges and chord-lengths at six Chebyschev-located spanwise collocation positions and $\boldsymbol{p}$ gives the leading-edge and chord values for six Chebyschev-spaced heightwise collocation points on the endplate.

Adding a gene to represent the endplate flare angle dramatically increases the number of generations required to obtain convergence. This may be because of the strongly dependent roles of this gene and the genes representing the height and location of the

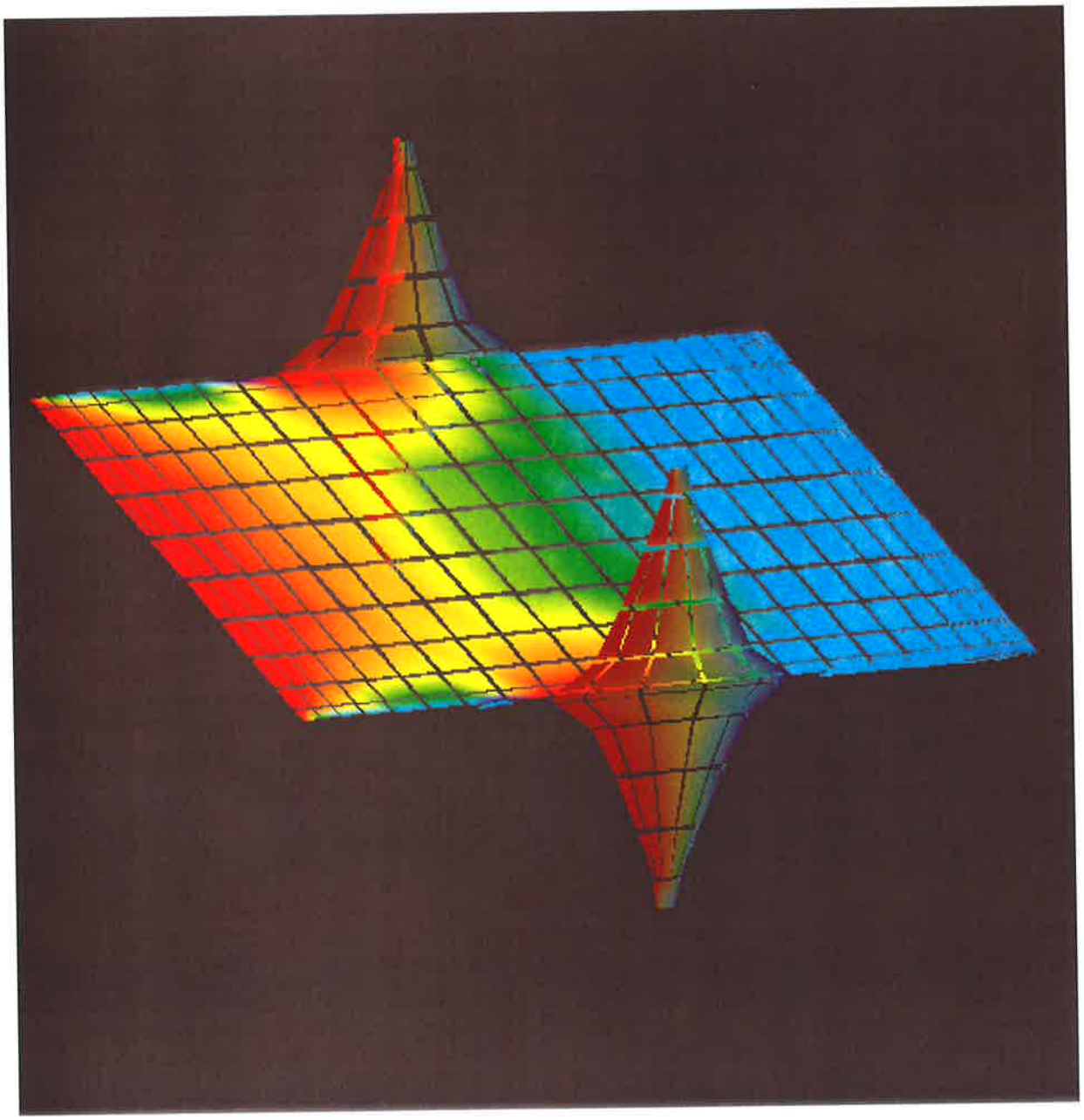

Figure 7.6: *The optimal horizontally centered endplate at zero angle of attack for a unit square wing. The object function is the lift coefficient C_L/α_W and the optimal value is 1.913 as compared with the optimal rectangular endplates for the same problem, with optimal value 1.84.*

endplate. For the values of the flow parameter $C_f/\alpha_W^2 > 1$, where induced drag is penalised far less than skin friction, the natural flare angle is larger than can be accurately input to the present linear algorithm for evaluating the pressure distributions on the wing and the endplate.

Also, if the genetic algorithm is allowed to proceed with no check on the spanwise continuity of the wing and endplate geometries, there is a tendency to produce somewhat

disjoint shapes with extreme grid-scale oscillation, when the flare-angle gene is included. This may be cured by increasing the relative frequency of the genetic operation which smooths out the jagged edges on the surfaces, but it is interesting that an increased loading on the endplate favours disjoint geometries.

The present geometric scheme allows chordwise strips to move, expand and contract to represent a planform, and spanwise discontinuity on the wing surface itself in a sense decreases the effective aspect ratio of the wing. A discussion of the effect of small gaps in lifting surfaces as are produced when a chordwise strip is significantly displaced from its neighbours is presented in White (1969). By comparison, a highly-loaded endplate, for example when flare is introduced, may well be improved by a slight *feathering* effect. A full analysis of this idea is not within the scope of this thesis.

While this effect is manifest as a degeneracy in the present scheme, it highlights one of the real advantages in using psuedo-random search techniques. By blurring the interface between the user and the function evaluation, successful new solutions may be found.

For these reasons, the inclusion of a variable flare-ratio is left for future work. It is assumed that the wing-endplate configuration is symmetric about the axis $y = 0$. The angle of attack of the endplates is maintained at $\alpha_P = 0$. Additionally, thickness variation had been omitted from the present optimisation, although thickness will alter the optimal configuration and improve the overall performance.

By using a genetic algorithm with a small, but representative number of genes per chromosome, we are able to quickly isolate a successful finite wing-endplate configuration for each of the cases $C_f/\alpha_W^2 = 0.1, 0.2, 0.5, 1, 2, 5$ and 10. The trend is fairly clear, with the endplate size decreasing as area is increasingly penalised, but there are other interesting features. While none of the designs can be regarded as "fully converged" to the optimal solution, there is a distinct asymmetry in all cases between the upper and lower sections of the endplate. However, as the horizontal offset is maintained naturally throughout the search, such that the endplate sections touch leading-edge to trailing-edge at the wing, it may be more instructive to note that the endplate portion near the leading edge of the wing is, in general, vertically shorter than the rear section. For smaller values of the flow parameter C_f/α_W^2, the optimal endplate moves forward to the leading edge of the wing and the optimal wing geometry itself changes such that the leading edge is swept and the trailing edge is unswept.

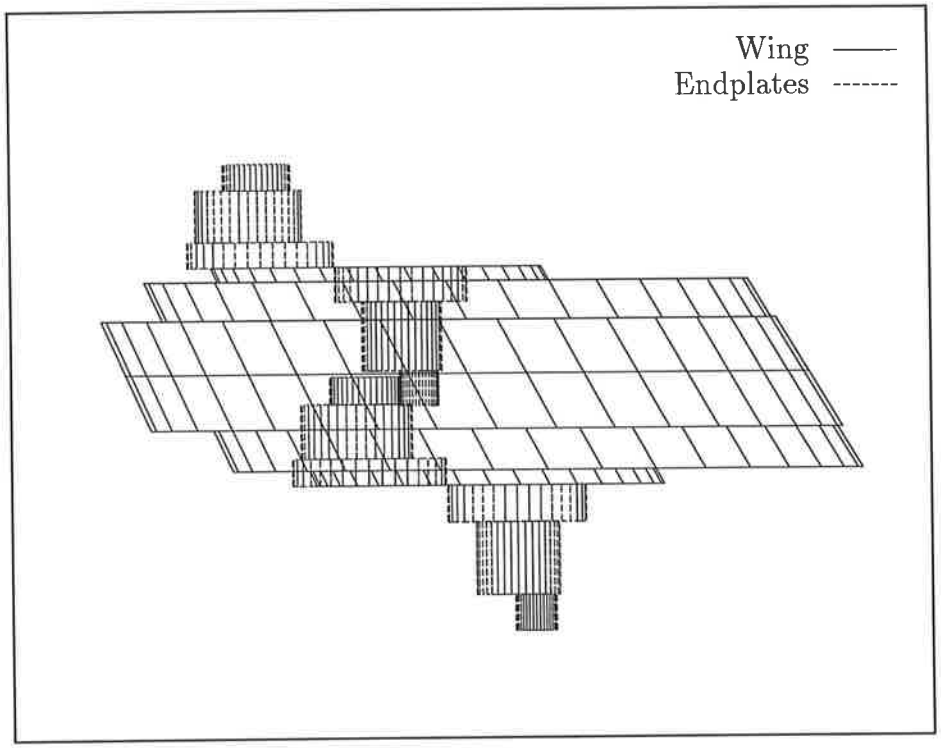

Figure 7.7: *The best discrete wing-endplate geometry found after 500 generations using* $n = n_p = 6$ *and* $m = m_p = 18$, *for the case of* $C_f/\alpha_W^2 = 0.1$.

While a calculus-based search is likely to be useful once a successful design paradigm has been identified by a genetic algorithm, it is also possible to increase the number of unknowns once an initial solution can be provided to a genetic algorithm. Figure 7.14, which also appears in colour at the front of this thesis, shows the converged solution after 1000 iterations for the wing-endplate geometry with $C_f/\alpha_W^2 = 1$ and $n = n_p = 14$ and $m = m_p = 18$.

It is interesting that the present optimal lifting surface is produced entirely randomly and *linearly*. Features such as the reduced size of the forward plate and the endplate shaping are often regarded as products of non-linear analysis.

7.3 Conclusion

Clearly the genetic algorithm is a powerful tool for identifying and optimising lifting geometries. However, there must be a balance struck between the pseudo-random search, used to avoid the solution becoming trapped in the local minima so evident in the contem-

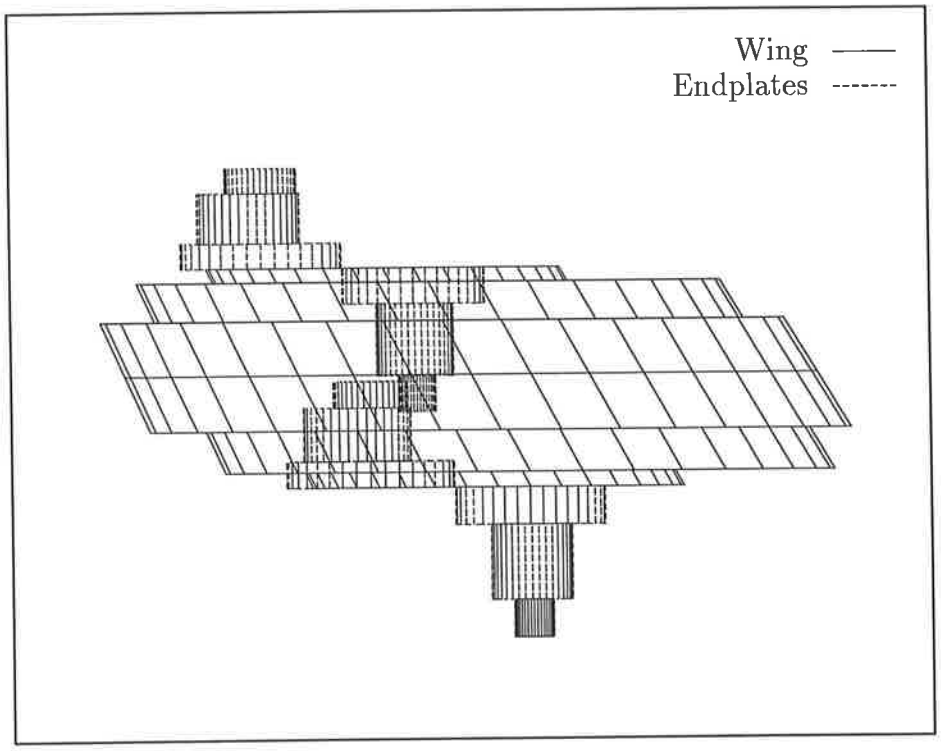

Figure 7.8: *The best discrete wing-endplate geometry found after 500 generations using* $n = n_p = 6$ *and* $m = m_p = 18$, *for the case of* $C_f/\alpha_W^2 = 0.2$.

porary panel methods, and using a calculus-based gradient scheme to optimise localised geometric features. For example, Gage et. al. (1995) present a variable-complexity algorithm which starts with a genetic algorithm and ends with a specific gradient-based scheme for the optimisation of a wing design for minimum induced drag.

In an attempt to reduce the number of grid-scale oscillations in the design during the iterative procedure, the representation was changed from assigning to the genes the leading-edge and chord value at the spanwise stations. Instead, the leading-edge and chord-length configuration were represented as Fourier-series, where the genes took the values of the Fourier coefficients. The values of the resulting functions were then evaluated at each of the spanwise collocation stations and the appropriate leading-edge and chord-length values assigned. Rather than reduce the grid-scale oscillation, it was found that the coefficients of the higher frequency modes maintained high values until convergence was reached, so no improvement was made by this particular change in representation.

Even though the search space for the optimisation of wing-endplate geometries using the present scheme undoubtably contains grid-scale behaviour that prevents the use of generic

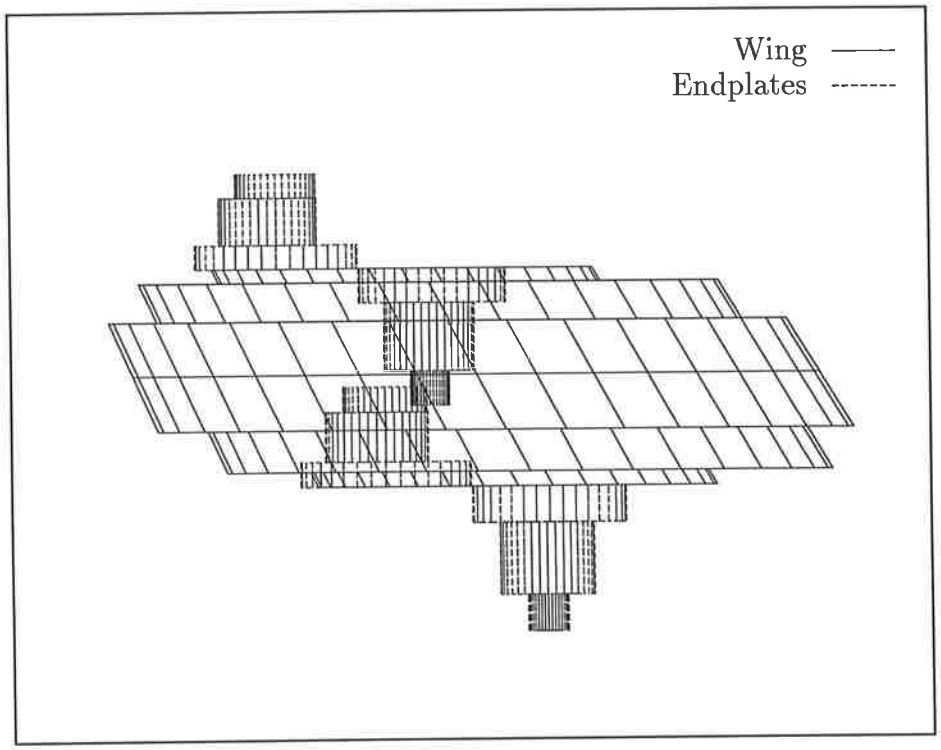

Figure 7.9: *The best discrete wing-endplate geometry found after 500 generations using* $n = n_p = 6$ *and* $m = m_p = 18$, *for the case of* $C_f/\alpha_W^2 = 0.5$.

derivative-based search procedures, the space is in many cases not so poorly behaved as to warrant a truly random search. There may be merit in introducing an acceleration or over-relaxation to the present genetic algorithm in order to speed the approach to a converged solution.

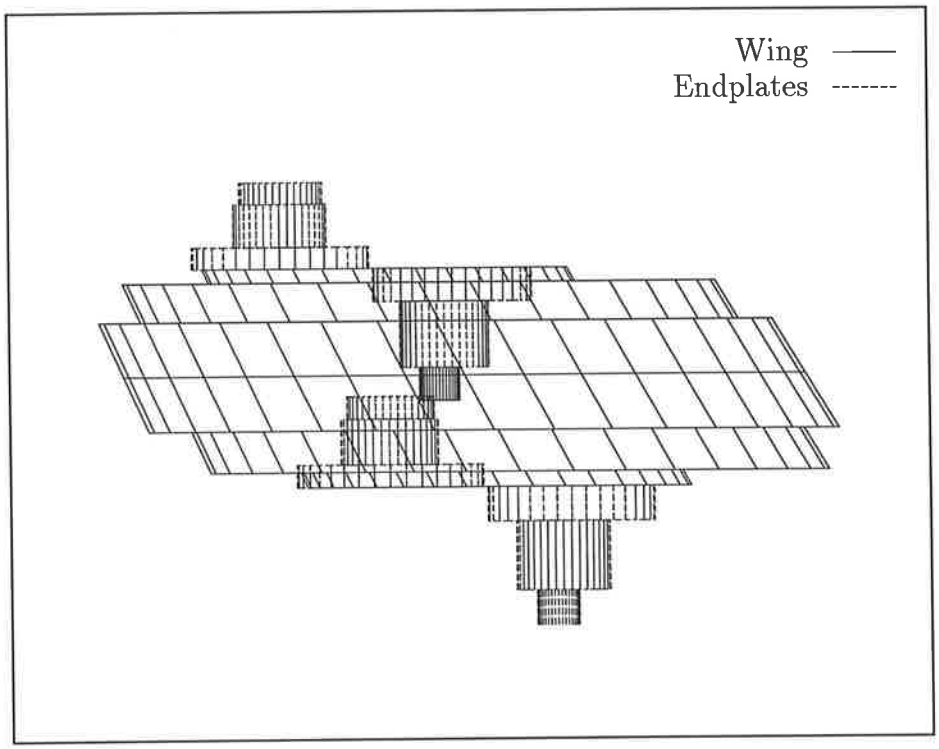

Figure 7.10: *The best discrete wing-endplate geometry found after 500 generations using* $n = n_p = 6$ *and* $m = m_p = 18$, *for the case of* $C_f/\alpha_W^2 = 1$.

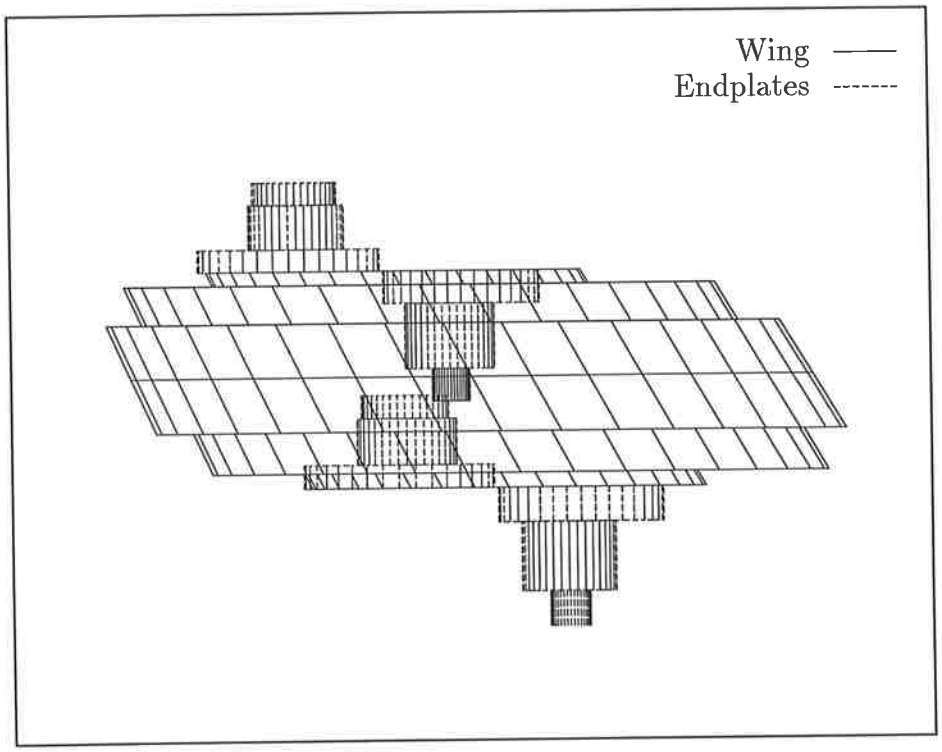

Figure 7.11: *The best discrete wing-endplate geometry found after 500 generations using* $n = n_p = 6$ *and* $m = m_p = 18$, *for the case of* $C_f/\alpha_W^2 = 2$.

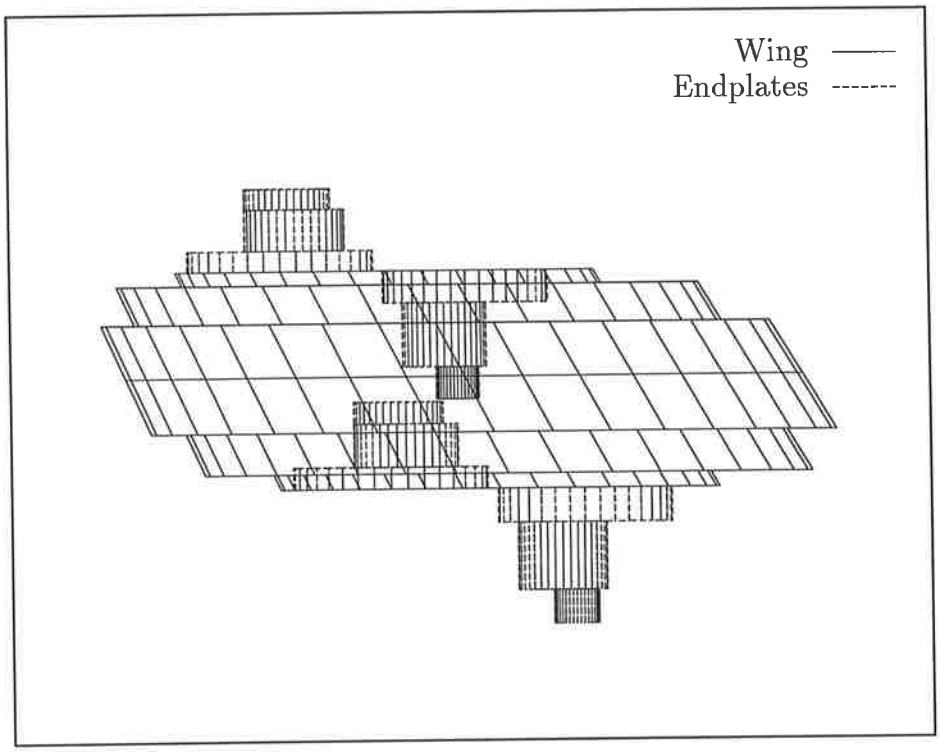

Figure 7.12: *The best discrete wing-endplate geometry found after 500 generations using* $n = n_p = 6$ *and* $m = m_p = 18$, *for the case of* $C_f/\alpha_W^2 = 5$.

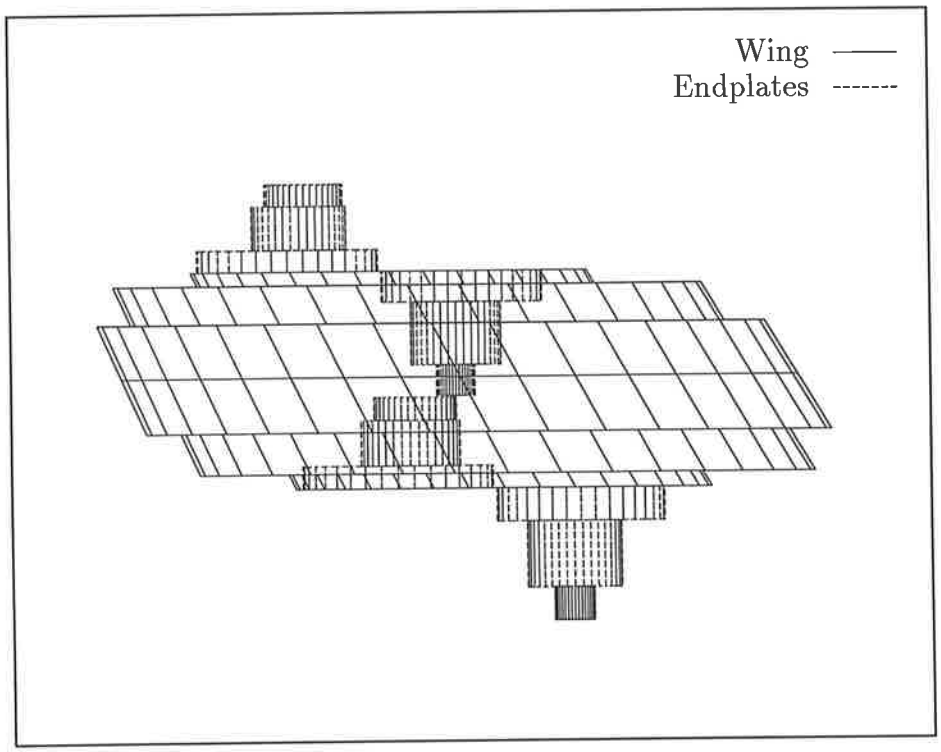

Figure 7.13: *The best discrete wing-endplate geometry found after 500 generations using* $n = n_p = 6$ *and* $m = m_p = 18$, *for the case of* $C_f/\alpha_W^2 = 10$.

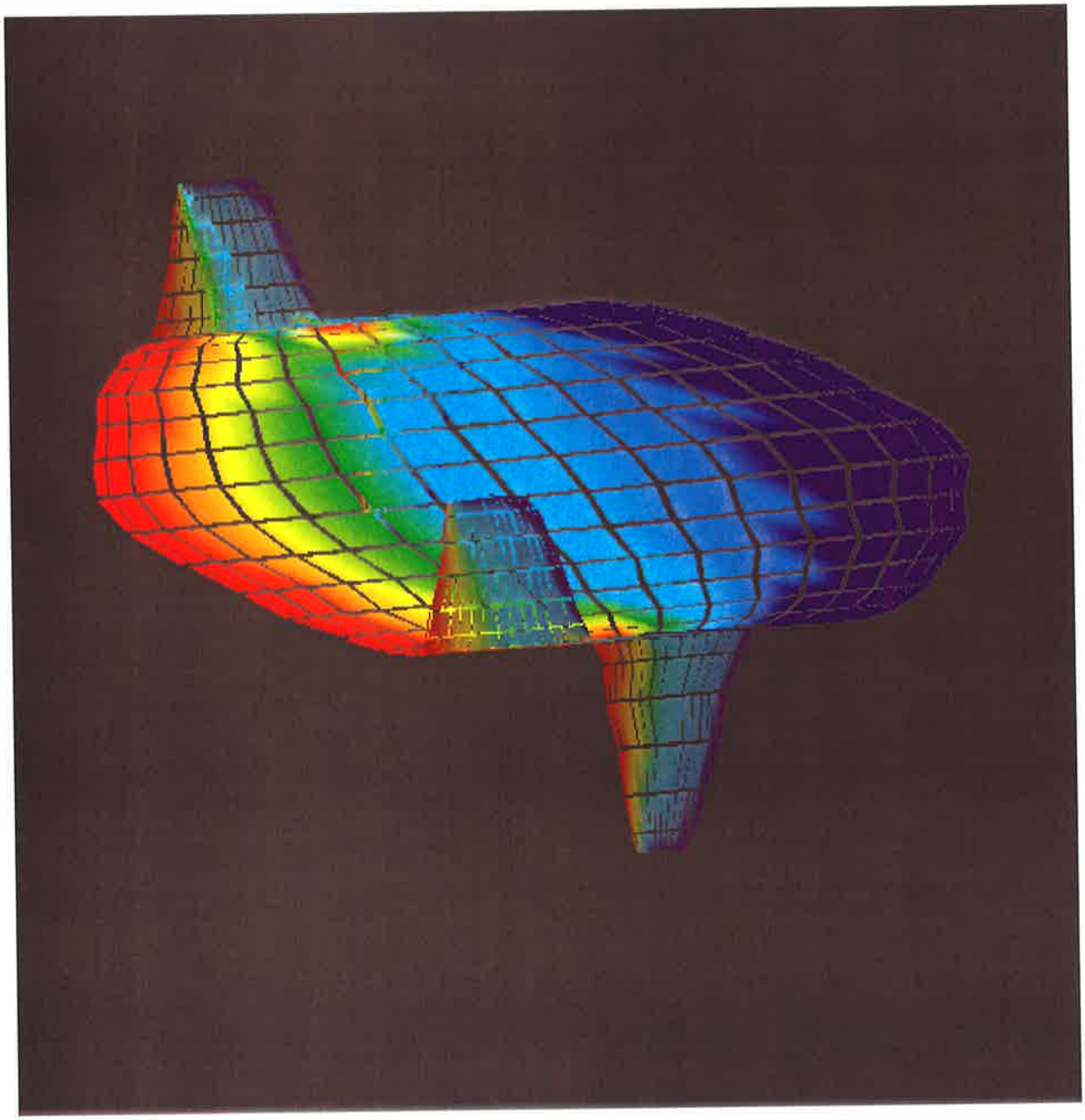

Figure 7.14: *The optimal wing-endplate configuration for a flow parameter* $C_f/\alpha_W^2 = 1$. *Generated using 1000 generations of the present genetic algorithm. The wing is forced to have aspect ratio* $AR = 1$.

Bibliography

ABBOTT, I. H. AND VON DOENHOFF, A. E. 1958. Theory of Wing Sections. Dover Publications.

ABRAMOWITZ, M. AND STEGUN, I. 1965. Handbook of Mathematical Functions. National Bureau of Standards.

ANDERSSEN, R. S. 1980. The Application and Numerical Solution of Integral Equations. Sijthoff and Noordhoff, The Netherlands.

ANDO, S. AND ICHIKAWA, A. 1983. The Use of an Error Index to Improve Numerical Solutions for Unsteady Lifting Airfoils. *AIAA Journal* 21:47–54.

ASHLEY, H. AND LANDAHL, M. T. 1965. Aerodynamics of Wings and Bodies. Addison-Wesley, Reading, Massachusetts.

BILLINGTON, A. E. 1971. On the Fiction of Leading Edge Suction. *ARL/SM-NOTE 360* .

BLACKWELL JR., J. A. 1976. Numerical Method to Calculate the Induced Drag or Optimum Loading for Arbitrary Non-Planar Aircraft. Technical Report NASA SP–405, Langley Research Center.

BOERSMA, J. 1989. Note on the Lifting-Surface Problem for a Circular Wing in Incompressible Flow. *Quarterly Journal of Mechanics and Applied Mathematics* 42:55–64.

BOGDANOV, A. I. AND MASKALIK, A. I. 1996. Some Results on the Civil Ekranoplans Certification Works. *In* Ekranoplans and Very Fast Craft, pp. 177–185, University of New South Wales, Victoria NSW, Australia.

BROWN, D. R. 1997. Optimal Design, Dimensioning & Tariffing of Telecommunications Networks. PhD thesis, University of Adelaide.

BURKETT, C. W. 1989. Reductions in Induced Drag by the use of Aft Swept Wing Tips. *Aeronautical Journal* 93:400–405.

CARTER, J. AND JACKSON, P. S. 1991. Thin-Airfoil Method for Panel Methods. *Journal of Aircraft* 29:723–724.

CONE JR., C. D. 1962. The Theory of Induced Lift and Minimum Induced Drag of Nonplanar Lifting Systems. Technical Report R-139, Langley Research Center.

CONLEY, N. 1980. Winglet Toe-Out Angle Optimization for the Gates Learjet Longhorn Wing. *Journal of Aircraft* 17:851–855.

CUNNINGHAM JR., A. M. 1971. An Efficient, Steady, Subsonic Collocation Method for Solving Lifting-Surface Problems. *Journal of Aircraft* 8:168–176.

DAVIS, L. 1989. Adapting Operator Probabilities in Genetic Algorithms. *In* J. Schaffer (ed.), Proceedings of the Third International Conference on Genetic Algorithms, pp. 61–69. Morgan Kaufmann.

DAVIS, L. 1991. Handbook of Genetic Algorithms. Van Nostrand Reinhold, New York.

DAVIS, P. 1996. Industrial Strength Optimisation at Boeing. *SIAM News* 29:1,10.

DE JONG, K. 1991. On the Optimization and the Design of Ship Screw Propellers With and Without End Plates. PhD thesis, University of Groningen, The Netherlands.

DE JONG, K. AND SPEARS, W. 1990. An Analysis of the Interacting Roles of Population Size and Crossover in Genetic Algorithms. *In* H. Schwefel and R. Manner (eds.), Parallel Problem Solving from Nature, 1st Workshop in Lecture Notes in Computer Science., pp. 38–47. Springer-Verlang.

DEJARNETTE, F. R. 1976. Arrangement of Vortex lattices on Subsonic Wings. *NASA SP-405* pp. 301–324.

DELAURIER, J. 1983. Drag of Wings with Cambered Airfoils and Partial leading-Edge Suction. *Journal of Aircraft* 20:882–886.

DOCTORS, L. J. 1997. Optimal Pressure Distributions for River-Based Air-Cushion Vehicles. *Ship Technology Research* 44:32–36.

DOCTORS, L. J. AND SHARMA, S. D. 1970. The Wave Resistance of an Air Cushion Vehicle in Accelerated Motion. Office of Naval Research 099, The Department of Naval and Marine Engineering, University of Michigan College of Engineering.

EMINTON, E. 1961. On the Numerical Evaluation of the Drag Integral. *A. R. C. R & M 3341* . National Physical Lab, Teddington, England.

ER-EL, J. AND YITZHAK, Z. 1988. Experimental Examination of the Leading-Edge Suction Analogy. *Journal of Aircraft* 25:195–198.

FALKNER, V. M. 1943. The Calculation of Aerodynamic Loading on Surfaces of Any Shape. *ARC R & M 1910* . National Physical Lab, Teddington, England.

GAGE, P. J., KROO, I. M., AND SOBIESKI, I. P. 1995. Variable-Complexity Genetic

Algorithm for Topological Design. *AIAA* 33:2212–2217.

GALL, P. D. AND SMITH, H. C. 1987. Aerodynamic Characteristics of Biplanes with Winglets. *Journal of Aircraft* 24:518–522.

GALLINGTON, R. W., MILLER, M. K., AND SMITH, W. N. 1972. The Ram Wing Surface Effect Vehicle: Comparison of One-Dimensional Theory with Free Flight Results. *Hovering Craft and Hydrofoil* 11:10–19.

GOLBERG, M. 1990. Numerical Solution of Integral Equations. Plenum Press, New York.

GRUNDY, I. H. 1986a. Air Flow Near a Water Surface. PhD thesis, University of Adelaide.

GRUNDY, I. H. 1986b. Airfoils Moving in Air Close to a Dynamic Water Surface. *Journal of the Australian Mathematical Society, Series B* 27:327–345.

GRUNDY, I. H. AND TUCK, E. O. 1987. Waves on a Static Water Surface Beneath a Layer of Moving Air. *Journal of Fluid Mechanics* 178:441–457.

GUERMOND, J. 1988. About Collocation Methods for Marine Propeller Design. *Transactions of the Society of Naval Architects and Marine Engineers* .

GUERMOND, J. L. 1989. Collocation Methods and Lifting-Surfaces. *European Journal of Mechanics, B/Fluids* 8:283–305.

GUERMOND, J. L. 1990. A Generalized Lifting-Line Theory for Curved and Swept Wings. *Journal of Fluid Mechanics* 211:497–513.

HANCOCK, G. J. 1971. Comment on "Spanwise Distribution of Induced Drag in Subsonic Flow by the Vortex lattice Method". *Journal of Aircraft* 8:681–682.

HAUPTMAN, A. AND MILOH, T. 1986. On the Exact Solution of the Linearized Lifting-Surface Problem of an Elliptic Wing. *Quarterly Journal of Mechanics and Applied Mathematics* 39:41–66.

HELTSEY, F. L. 1976. Report on the Status of a Slotted Wind-Tunnel Representation Using the Vortex-Lattice Technique. *Vortex-Lattice Utilization (NASA SP-405)* .

HEMCKE, P. E. 1927. Drag of Wings with End Plates. *NACA Report* 267:253–263.

HESS, J. L. AND SMITH, A. M. O. 1967. Calculation of Potential Flow About Arbitrary Bodies. *Progress in the Aeronautical Sciences* 8:1–137.

HOOKER, S. F. 1996. Some Thoughts on the Commercialisation of Ekranoplans and Wingships. *In* Ekranoplans and Very Fast Craft, pp. 272–294, University of New South Wales, Victoria NSW, Australia.

HOUGH, G. R. 1973. Remarks on the Vortex-Lattice Methods. *Journal of Aircraft*

(Engineering Notes) 10:314–317.

HOUGH, G. R. 1976. Lattice Arrangements for Rapid Convergence. *Vortex-Lattice Utilization (NASA SP-405)* .

HSIN , C., KERWIN, J. E., AND KINNAS, S. A. 1991. A Panel Method for the Analysis of the Flow Around Highly Skewed Propellers. *In* Propellers/Shafting 1991 Symposium, Virginia Beach, Virginia.

INCANDELA, S. 1990. The Anatomy and Development of the Formula 1 Racing Car since 1975. Haynes, Yeovil, 3 edition. 334pp.

JAMES, R. M. 1972. On the Remarkable Accuracy of the Vortex Lattice Method. *Computer Methods in Applied Mechanics and Engineering* 1:59–79.

JORDAN, P. F. 1971. Span Loading and Formation of Wake, chapter 207–227. Aircraft Wake Turbulence and its Detection. Plenum Press, New York.

JORDAN, P. F. 1973. Exact Solutions for Lifting Surfaces. *Journal of Aircraft* 11:1123–1129.

JORDAN, P. F. 1974. On Lifting Wings with Parabolic Tips. *ZAMM* 54:463–477.

KÁLMÁN, T. P., GIESING, J. P., AND RODDEN, W. P. 1970. Spanwise Distribution of Induced Drag in Subsonic Flow by the Vortex Lattice Method. *Journal of Aircraft* 7:574–576.

KATZ, J. AND PLOTKIN, A. 1991. Low-Speed Aerodynamics: From Wing Theory to Panel Methods. McGraw-Hill series in aeronautical and aerospace engineering, New York.

KERWIN, J. E. 1986. Marine Propellers. *Annual Review of Fluid Mechanics* 18:367–403.

KERWIN, J. E. AND LEE, C.-S. 1978. Prediction of Steady and Unsteady Marine Propeller Performance by Numerical Lifting-Surface Theory. *Transactions of the Society of Naval Architects and Marine Engineers* 86:218–253.

KINNAS, S. A. 1992. A General Theory for the Coupling Between Thickness and Loading for Wings and Propellers. *Journal of Ship Research* 36:59–68.

KUCHEMANN, D. 1978. The Aerodynamic Design of Aircraft. Pergamon Press, Oxford, first edition.

KUHLMAN, J. M. AND LIAW, P. 1988. Winglets on Low Aspect Ratio Wings. *Journal of Aircraft* 25:932–941.

KUHMSTEDT, T. AND MILBRANDT, G. 1995. Aerodynamic Design of Wing in Ground Effect Craft. *Proceeding of FAST 95* 2:597–608.

LAMB, H. 1932. Hydrodynamics. Cambridge University Press.

LAN, C. E. 1974. A Quasi-Vortex-Lattice Method in Thin Wing Theory. *Journal of Aircraft* 11:518–527.

LAN, C. E. 1976. Some Applications of the Quasi Vortex-Lattice Method in Steady and Unsteady Aerodynamics. *Vortex-Lattice Utilization (NASA SP-405)* .

LAN, C. E. AND MEHROTRA, S. C. 1979. Improved Woodward's Panel Method for Calculating Edge Suction Forces. *Journal of Aircraft* 16:632–635.

LAN, C. E. AND SU, I. 1987. Effect of a Round Airfoil Nose on Leading-Edge Suction. *Journal of Aircraft* 24:472–474.

LANGE, R. H. 1988. Review of Unconventional Aircraft Design Concepts. *Journal of Aircraft* 25:385–392.

LAZAUSKAS, L. V., STANDINGFORD, D. W. F., AND TUCK, E. O. 1995. On the Numerics of the Lifting Surface Equation. Technical Report Preprint, Applied Mathematics Department, University of Adelaide.

LIGHTHILL, M. J. 1969. Hydromechanics of Aquatic Animal Propulsion. *Annual Review of Fluid Mechanics* 1:413–446.

LOWE, J. D. 1988. Calculation of Lift-Curve Slope using a Wing Tip Based Vortex Distribution. *Journal of Aircraft* 25:472–473.

LOWSON, M. V. 1990. Minimum Induced Drag for Wings with Spanwise Camber. *Journal of Aircraft* 27:627–631.

LUNDRY, J. L. 1968. A Numerical Solution for the Minimum Induced Drag, and the Corresponding Loading, of Nonplanar Wings. Technical Report CR-1218, Langley Research Center, NASA.

MACCASKILL, C. C. 1977. Numerical Solution of some Fluid Flow Problems by Boundary Integral Equation Techniques. PhD thesis, University of Adelaide, Adelaide, South Australia.

MILNE-THOMPSON, L. M. 1973. Theoretical Aerodynamics. Dover Publications, New York.

MILOH, T. AND TUCK, E. O. 1993. Analytic solution of the potential flow over an elliptic planform wing. Unpublished Applied Mathematics Note, University of Adelaide.

MONACELLA, V. J. AND NEWMAN, J. N. 1967. The Pressure on the Sea Bottom due to a Moving Pressure Distribution. Department of the Navy Report 2308, David Taylor Model Basin.

NAIK, D. A. AND OSTOWARI, C. 1990. Effects of Nonplanar Outboard Wing Forms on a Wing. *Journal of Aircraft* 27:117–122.

NEWMAN, J. M. 1977. Marine Hydrodynamics. The MIT Press, Cambridge, Massachusetts.

OERTEL, R. P. 1975. The Steady Motion of a Flat Ship, including an Investigation of Local Flow near the Bow. PhD thesis, University of Adelaide.

PATTERSON, R. N. AND WATTS, K. C. 1985. The Otter Board as a Low Aspect Ratio Wing at High Angles of Attack; Some Theoretical Aspects. *Fisheries Research* 3:351–372.

POLHAMUS, E. C. 1966. A Concept of the Vortex Lift of Sharp-Edge Delta Wings Based on a Leading-Edge-Suction Analogy. Technical Report NASA TN D-3767, Langley Research Center.

PRANDOLINI, L. J. 1996. More about Ekranoplans. *Engineers Australia* pp. 17–17.

REYNOLDS, P. T. 1979. Winglets Introduced on Business Jets. *Society of Automotive Engineers, Inc* 87:44–47.

ROSENHEAD, L. 1963. Laminar Boundary Layers. Oxford University Press.

ROZHDESTVENSKY, K. V. 1992. Matched Asymptotics in Aerodynamic Analysis of WIG Vehicles. *In* Proceeding of the Intersociety High Performance Marine Vehicles Conference and Exhibit (HPMV'92), pp. WS 17–27, Arlington, Virginia.

ROZHDESTVENSKY, K. V. AND SYNITSIN, D. N. 1993. State of the Art and Perspectives of Development of Ekranoplans in Russia. *Proceeding of FAST 93* 2:1657–1670.

RUBBERT, P. E. 1964. Theoretical Characteristics of Arbitrary Wings by a Non-Planar Vortex Lattice Method. *D6-9244, The Boeing Co.* . Renton, Washington.

SIEKMANN, J. 1965. Note on the Calculation of the Suction Force. *SIAM Review* 7:349–355.

SMITH, S. C. AND KROO, I. M. 1993. Computation of Induced Drag for Elliptical Wings and Crescent-Shaped Wings. *Journal of Aircraft* 30:446–452.

SPILLMAN, J. J. 1978. The Use of Wing Tip Sails to Reduce Vortex Drag. *Aeronautical Journal* 82:387–395.

STANDINGFORD, D. W. F. AND TUCK, E. O. 1994. Wingtip Phenomena. *In* Australian and New Zealand Industrial and Applied Mathematics conference, Hunter Valley, Australia.

STANDINGFORD, D. W. F. AND TUCK, E. O. 1996a. Lifting Surfaces in Ground Effect.

In L. J. Prandolini (ed.), Commercialisation of Ekranoplans and Very fast Craft, pp. 230–243, University of New South Wales, Sydney.

STANDINGFORD, D. W. F. AND TUCK, E. O. 1996b. Optimal Rectangular End Plates. *Journal of Aircraft* 33:623–625.

STARK, V. J. E. 1971. A Generalized Quadrature Formula for Cauchy Integrals. *AIAA* 9:1854–1855.

STRICKLAND, J. H. 1979. A Vortex Model of the Darrieus Turbine: An Analytical and Experimental Study. *Transactions of the ASME* 101:500–505.

THWAITES, B. 1960. Incompressible Aerodynamics. Oxford University Press.

TRICOMI, F. G. 1965. Integral Equations. Wiley, New York.

TUCK, E. O. 1971. Irrotational Flow Past Bodies Close to a Plane Surface. *Journal of Fluid Mechanics* 50:481–491.

TUCK, E. O. 1974. Unstable Squat from Lateral Motion of Ships in Shallow Water. *Journal of Ship Research* 18:50–55.

TUCK, E. O. 1975. On Air Flow Over Free Surfaces of Stationary Water. *Journal of the Australian Mathematical Society, Series B* 19:66–80.

TUCK, E. O. 1978. Unsteady Small-Gap Ground Effects. Engineering Science Report 78-1, California Institute of Technology.

TUCK, E. O. 1980. A Non-Linear Unsteady One-Dimensional Theory for Wings in Extreme Ground Effect. *Journal of Fluid Mechanics* 98:33–47.

TUCK, E. O. 1981. Steady Flow and Static Stability of Airfoils in Extreme Ground Effect. *Journal of Engineering Mathematics* 15:89–102.

TUCK, E. O. 1982a. Linearized planing-surface theory with surface tension. Part I : Smooth detachment. *Journal of the Australian Mathematical Society, Series B* 23:241–258.

TUCK, E. O. 1982b. Linearized planing-surface theory with surface tension. Part II : Detachment with discontinuous slope. *Journal of the Australian Mathematical Society, Series B* 23:259–277.

TUCK, E. O. 1982c. Two-Dimensional Leaflet Valves with Maximum Reverse-Flow Moment. *Journal of Engineering Mathematics* 16:47–57.

TUCK, E. O. 1983. Nonlinear Extreme Ground Effect on Thin Wings of Arbitrary Aspect Ratio. *Journal of Fluid Mechanics* 136:73–84.

TUCK, E. O. 1984. A Simple One-Dimensional Theory for Air-Supported Vehicles Over

Water. *Journal of Ship Research* 28:290–292.

TUCK, E. O. 1987. Wave Resistance of Thin Ships and Catamarans. Technical Report T8701, University of Adelaide, Department of Applied Mathematics.

TUCK, E. O. 1989. The Wave resistance Formula of J. H. Michell (1898) and its Significance to Recent Research in Ship Hydrodynamics. *Journal of the Australian Mathematical Society, Series B* 30:365–377.

TUCK, E. O. 1992. Lifting Surfaces with Endplates. *In* M. R. Davis and G. J. Walker (eds.), Proceedings of the 11th Australasian Fluid Mechanics Conference, pp. 219–222, University of Tasmania, Australia.

TUCK, E. O. 1993. Some Accurate Solutions of the Lifting Surface Integral Equation. *Journal of the Australian Mathematical Society Series B* 35:127–144.

TUCK, E. O. 1994. The Planing Splash. *Workshop on Water Waves and Floating Bodies* Ninth International Symposium. Kuju, Oita, Japan.

TUCK, E. O. 1995. A Double Integral That Should (?) Vanish but Doesn't. *Australian Mathematical Society Gazette* 22. page 58.

TUCK, E. O. AND BENTWICH, M. 1983. Sliding Sheets : Lubrication with Comparable Viscous and Inertia Forces. *Journal of Fluid Mechanics* 135:51–69.

TUCK, E. O., HELFGOTT, A., AND YEUNG, R. W. 1982. Cambered Valve Leaflets that Maximise Initial Rate of Closure. *Journal of Fluid Mechanics* 121:517–529.

TUCK, E. O. AND STANDINGFORD, D. W. F. 1997. Numerical Solution of the Lifting Surface Integral Equation. *In* J. I. Frankel, C. A. Brebbia, and M. A. H. Aliabadi (eds.), Boundary Elements Technology and Applications Conference, pp. 195–204, Knoxville, Tennessee.

TURRILL, D. 1992. Wings and Free Speed. *Open Wheel Magazine* p. 63.

VAN DAM, C. P. 1981. Effect of Winglets on Performance and Handling Qualities of general Aviation Aircraft. *Journal of Aircraft* 18:587–591.

VAN HOLTEN, T. 1981. Concentrator Systems for Wind Energy, with Emphasis on Tip-vanes. *Wind Engineering* 5:29–45.

VAN OOSSANEN, P. AND JOUBERT, P. N. 1986. The Development of the Winged Keel for Twelve-Metre Yachts. *Journal of Fluid Mechanics* 173:55–71.

VOSSINIS, A. 1995. Shape Optimization in Aerodynamics using Non-Linear Generalized Minimal Residual Algorithm. *Optimal Control Applications & Methods* 16:229–249.

WANG, H. T. 1974. Comprehensive Evaluation of Six Thin-Wing Lifting-Surface Com-

puter Programs. Ship Performance Department Research and Development Report 4333, Naval Ship Research and Development Center, Bethesda, Md. 20034.

WEHAUSEN, J. V. AND LAITONE, E. V. 1960. Surface Waves, volume 9 of *Handbuch der Physik*, chapter 6. Springer-Verlag, Berlin.

WHITCOMB, R. T. 1976. A Design Approach and Selected Wind-Tunnel Results at High Subsonic Speeds for Wing-Tip Mounted Winglets. Technical Report TN D–8260, NASA, Langley Research Center.

WHITE, R. B. AND LANDAHL, M. T. 1969. Effect of Gaps on the Loading Distribution of Planar Lifting Surfaces. *AIAA Journal* 6:626–631.

XIE, Y. M. AND STEVEN, G. P. 1993. A Simple Evolutionary Procedure for Structural Optimization. *Computers & Structures* 49:885–896.

ZHU, D. M. 1981. A Computational Method for Cycloidal Propellers. *International Shipbuilding Progress* 28:102–111.